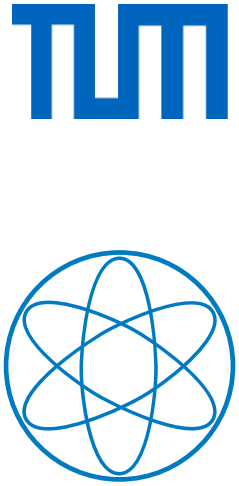

Fakultät für Physik

E66 - Precision Measurements at Extreme Conditions

PanEDM at SuperSUN

David Wurm

Vollständiger Abdruck der von der Fakultät für Physik der Technischen Universität München zur Erlangung des akademischen Grades eines

Doktors der Naturwissenschaften (Dr. rer. nat.)

genehmigten Dissertation.

Vorsitzender:	apl. Prof. Dr. Norbert Kaiser
Prüfende der Dissertation:	
1.	Prof. Dr. Peter Fierlinger
2.	Prof. Dr. Laura Fabbietti

Die Dissertation wurde am 7.10.2021 bei der Technischen Universität München eingereicht und durch die Fakultät für Physik am 6.12.2021 angenommen.

Abstract

Precision experiments offer a complementary path towards new physics, which is currently inaccessible by accelerator experiments. In particular, searches for the electric dipole moment (EDM) of the neutron are a promising tool to test for unknown manifestations of time-reversal invariance violating effects beyond the standard model of particle physics (T. E. Chupp et al. 2019). Although ongoing for 70 years, new searches for the neutron EDM are very well motivated, with the next generation of experiments aiming to lower the current experimental upper bound of $(0.0 \pm 1.1_{\mathrm{stat}} \pm 0.2_{\mathrm{syst}})\,10^{-26}$ ecm (Abel et al. 2020) by one to two orders of magnitude. The panEDM experiment (Wurm et al. 2019) uses trapped ultra cold neutrons (UCN) exposed to controlled magnetic and electric fields. Applying Ramsey's method of separated oscillatory fields (Purcell and N. F. Ramsey 1950) creates an interferometer in time with a small phase proportional to the EDM. The phase is encoded in neutron spin polarization and recovered by simultaneous spin state detection. The two key experimental challenges are the statistical sensitivity limited by available UCN densities and a strong understanding of systematic false effects originating from unknown magnetic and electric fields. The panEDM stores UCN in two room temperature material cells for simultaneous parallel and antiparallel E- and B field runs. The experiment targets a sensitivity of $d_n = 2 \times 10^{-27}$ ecm combined with the first stage of SuperSUN, a new UCN source based on superfluid ^{4}He at the Institute Laue-Langevin, Grenoble. This thesis describes the matching of panEDM to SuperSUN including major instrumental changes and characterizations. Most notably, the fitting of the apparatus to the extremely soft UCN spectrum of the source while ensuring stable systematic performance. Within this thesis, it was possible to move all large hardware components and rebuilt the UCN optics with a new diameter. All UCN switches were redesigned from scratch or upgraded. A solenoid polarizer was built and extensively characterized, both as a magnet and as a UCN polarizer. A new deuterated diamond-like carbon coating viable for panEDM was developed and experimentally tested.

List of acronyms

BSM	beyond standard model	4
CMH	current measurement housing : Abbrev. for the large high voltage enclosure of the high voltage system of panEDM.	32
DLC	diamond-like carbon	44
dPE	deuterated polyethylene	52
EDM	permanent electric dipole moment	4
FRMII	research neutron source Heinz Maier-Leibnitz (Forschungsreaktor München II, Neutron Spallation Source in Munich, Germany operated by the Technical University Munich	26
GM	guide manifold Part of the panEDM UCN guide system. It connects the solenoid polarizer with the two three-way switches. See figure 2.3	21
HFS	high field seeker UCN for which the spin is aligned anti parallel the magnetic field and UCN are attracted to high fields.	12
ILL	Institute Laue-Langevin , Grenoble, FR	4
LFS	low field seeker UCN for which the spin is aligned along the magnetic field and UCN are repelled by high fields.	21
MSR	magnetically shielded room	18
nEDM	neutron electric dipole moment	4
SF	spin flipperdevice to reverse the alignment of spins.	24
SM	standard model of particle physics	5
SP	solenoid polarizer : panEDM UCN beam polarizer	22
SuperSUN	new superthermal UCN source	4
SW	source switch . Part of the panEDM UCN guide system. It links SuperSUN to panEDM or diverts UCN to a monitor detector.See subsection 4.6.1	22
TOF	time of flight See also (Steyerl et al. 1986)	44
TW	three-way switch Part of the panEDM UCN guide system. Rotary switch with three beam ports. See subsection 4.6.2	22
UCN	ultra cold neutrons (UCN is used within the community as abbreivation for singular an plural inconsistenly.)	4

Contents

1 Introduction

1.1 Motivation

Ultra cold neutrons (UCN) are a unique tool to address fundamental physics questions. They are the rare example of subatomic particles which can be manipulated for more than 100 s in experiments. Their interaction with matter is systematically clean which makes them ideal probes for precision experiments. A prominent example of a UCN precision experiment is the search for the neutron electric dipole moment (nEDM). Current searches, while consistent with zero, probe new physics residing at an energy scale currently inaccessible to high energy physics. A finite permanent electric dipole moment (EDM) would break time-reversal symmetry and thus be a source of CP violation under CPT conservation. As EDMs appear in a wide range of beyond standard model (BSM) theories, the search is well motivated.

Combined with the new superthermal UCN source (SuperSUN), the panEDM experiment targets to search for an nEDM with a sensitivity of 3×10^{-27} ecm in its first phase and 4×10^{-28} ecm in phase II. panEDM combines Ramsey's method of separated oscillatory fields (Purcell and N. F. Ramsey 1950) with trapped UCN to gain sensitivity from long coherence time of storage measurements. The high sensitivity of the experiment mandates strong control over systematic false effects which takes up much of the experimental effort. The panEDM is currently under construction at the Institute Laue-Langevin (ILL) and is set to start data production runs in 2022.

The experiment has been designed and built for a different type of UCN source at the Technical University Munich. The author's task was facilitating the relocation and substantial refitting of panEDM for the new UCN source at the ILL. This process presented the opportunity to improve existing panEDM subsystems. The thesis presents the accomplished progress along with the description of the current experimental state in the first two chapters. Chapter 4 discusses selected aspects of UCN transport-related upgrades in detail.

The thesis makes use of an extended citation style for the benefit of readers unfamiliar with the field. Footnotes highlight caveats to statements, specify or detail aspects but are not essential to the procedural understanding of the text. Plots rely on color information. A digital version of this thesis can be obtained from `http://mediatum.ub.tum.de/603821`.

1.2 Underlying physics

A permanent electric dipole moment of a particle is an electric charge separation aligned with its spin. (Purcell and N. F. Ramsey 1950) first discussed the neutron EDM as a source of parity-symmetry violation (P-violation) more than 60 years ago. Later it was found that EDMs also break time-reversal symmetry and - assuming CPT invariance - EDMs are also CP-violating. (Tureanu 2013) found that EDMs are a signal of T violation

arising in any relativistic field theory.

CP-violation is a necessary ingredient for baryon generation in the early universe, as famously stated in the so-called Sakharov conditions (Sakharov 1967). Three sources of CP violation for the standard model of particle physics (SM) are known: In the strong interaction CP violation appears in gluon $G\tilde{G}$ contribution which is proportional to the parameter θ (Callan et al. 1976). This parameter is heavily restricted by current nEDM limits as $\mathrm{d_n} \sim \theta \cdot 10^{-16}$ ecm (Pospelov and Ritz 1999) and $|d_n| < 1.8 \cdot 10^{-26}$ ecm (Ayres et al. 2021) to $\theta < 10^{-10}$. This is also called the strong CP problem.

CP violation in the SM is also found in the weak sector in the weak decay of neutral kaons (Christenson et al. 1964) and in neutral B decays (Aubert et al. 2001). It is described by a complex phase δ in the Cabibbo-Kobayashi-Maskawa matrix (CKM)(Kobayashi and Maskawa 1973). CP violation in the weak sector is currently best measured and also insufficient to solve the CP problem. (Group et al. 2020). In the lepton sector, a complex phase in the Pontecorvo-Maki-Nakagawa-Sakata matrix (Maki et al. 1962) is a potential source of CP violation which would allow baryogenesis via leptogenesis (Luty 1992). Known sources of CP violation are not sufficient to account for the matter- antimatter asymmetry in the early universe, thus new sources of CP violation are searched for. The nEDM in the standard model is dominated by higher-order loops as shown in fig. 1.1. The predicted SM value ($\sim 10^{-32} e \cdot cm$) (Fukuyama 2012) is a few orders of magnitude smaller than the current best limit.

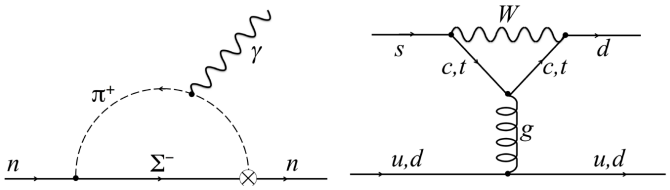

Figure 1.1: (Left) higher-order SM loop contributing to the nEDM. (right) CP-violating ΔS=1 vertex.

The next generation of searches are thus motivated by predictions from BSM theories which predict larger CP violation (T. E. Chupp et al. 2019). Next-generation nEDM experiments are currently approaching the sensitivity to test supersymmetric models. Next-generation neutron and electron EDMs can exclude, for example, scenarios of electroweak baryogenesis in minimal supersymmetric extentions (MSSM) of the SM. Figure 1.2 depicts the Higgsino mass scale $\mathrm{M_1}$ and the corresponding mixing angle φ_1 in a scenario for higgsino masses close to the bino soft supersymmetric breaking (Li et al. 2009). The allowed band of parameters for mass stop is in reach for next-generation electron EDM and 2^{nd} generation nEDM experiments.

Another extension to the SM are proposed particles that can transform leptons into quarks and vice versa, which are called leptoquarks. (Dekens et al. 2019) summarized the impact of EDM measurements on leptoquark couplings, wherein the up-quark interactions are limited by the nEDM. The nEDM offers a rather 'clean' probe compared to diamagnetic systems. When using a leptoquark model to address current anomalies in B flavor measurements[1], (Dekens et al. 2019, page 36) find:

> .. that this scenario remains consistent with current EDM experiments ...

[1] (Lees et al. 2013; Hirose et al. 2017)

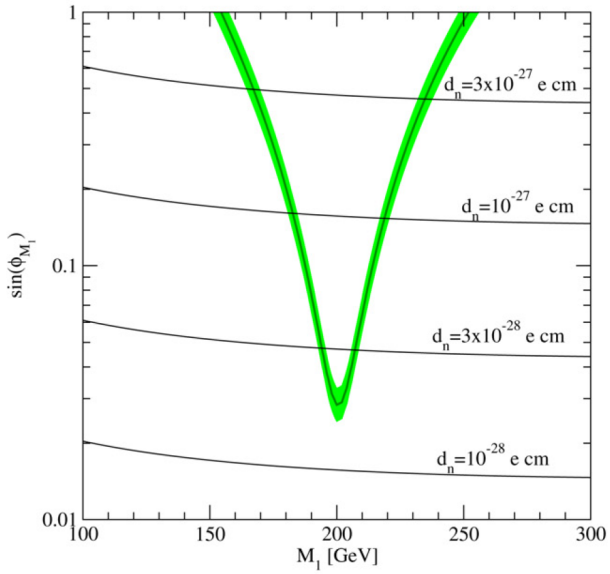

Figure 1.2: Example of nEDM informing BSM physics: This figure from (Li et al. 2009) shows the allowed region of electroweak baryogenesis in Minimal Supersymmetric extension of the Standard Model (MSSM). M_1 corresponds to the Higgsino mass scale close to the bino soft supersymmetry breaking masses with φ_1 as the corresponding mixing angle. Next-generation nEDMs are sensitive enough for full exclusion of such scenarios.

> but predicts a signal in the next generation of neutron EDM experiments. This example shows that EDMs can play an important role in the study of leptoquark models.

Permanent EDMs appear in many systems. They are accessible in paramagnetic systems (Cs,YbF, ThO, ..), diamagnetic systems (^{129}Xe,^{199}Hg, TIF, n) and particles like muons, tauons and deltas. The observed EDMs have contributions from different hierarchies of theory which makes complementary searches necessary to disentangle the origin of EDMs.

A model-independent framework for EDMs is an effective field theory (T. Chupp and Ramsey-Musolf 2015). At its core one assumes that BSM particles reside on a high mass scale such that their effects can be described with operators and the SM fields. Low energy (<hardronic scale $\Delta_{\text{had}} \sim 1\,\text{GeV}$) coefficients weight these operators and link the experimental results to Wilson coefficients of underlying theories:

> At lowest nontrivial order, one obtains the electron EDM d_e, scalar, pseudoscalar, and tensor electron-nucleon interactions (C_S, C_P, and C_T), short-range neutron and proton EDMs ($\bar{d}_n^{sr}$,$\bar{d}_p^{sr}$), isoscalar, isovector, and isotensor pion-nucleon couplings ($\bar{g}_\pi^{(i)}, i = 0, 1, 2$), and a set of four-nucleon operators (T. E. Chupp et al. 2019).

In global analysis, the neutron EDM is a valuable clean system compared to the paramagnetic systems (ThO,YbF) and diamagnetic ^{199}Hg, which have superior EDM discovery potential. In particular, electron EDM measurements in molecules suffer from uncertainties in atomic and nuclear theory to extract a dipole moment. These uncertainties

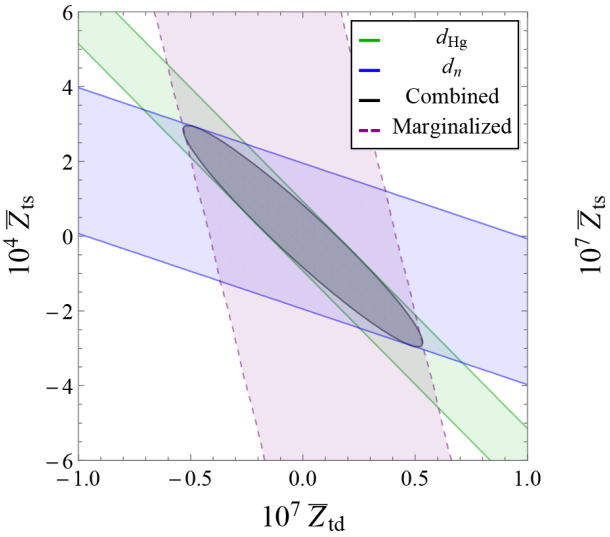

Figure 1.3: Di-quark coupling for scalar leptoquarks with limits posed by Hg and neutron EDM from (Dekens et al. 2019)

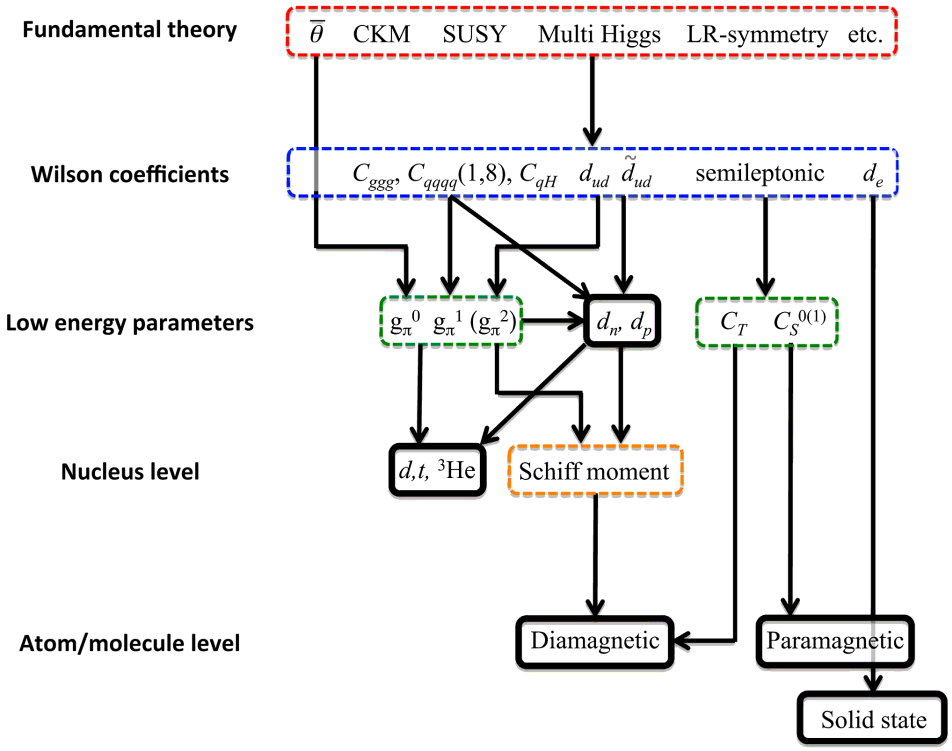

Figure 1.4: The connections from a fundamental theory at a high-energy scale to an EDM in a measurable low-energy system. The dashed boxes indicate levels dominated by theory, and the solid boxes identify systems that are the object of current and future experiments. The fundamental CP-violating Lagrangian at the top, a combination of SM and BSM physics, is reduced to the set of effective-field-theory Wilson coefficients that characterize interactions at the electroweak energy scale of $\approx 300\,\mathrm{GeV}$, the vacuum expectation value of the Higgs (T. E. Chupp et al. 2019).

include the magnitude of intermolecular electric fields (Andreev et al. 2018) and uncertainties in atomic theory to compensate for electron shell screening (Schiff's screening) (Schiff 1963; Flambaum and Kozlov 2012). Regardless of particular BSM theories, a wide range of physics lies between the current experimental limit and the SM prediction ($10^{-26} - 10^{-32}$ ecm) where new physics or a large SM-θ must exist. nEDM searches thus have virtually guaranteed discovery potential.

1.3 Ultra cold neutron properties

The field of UCN physics started with the theoretical prediction of the possibility to store to extremely low energetic neutrons could be 'trapped' for times on the scale of their lifetime (Zel'dovich 1959). Later (Shapiro 1968) showed that such particles could be used for highly sensitive nEDM searches (Purcell and N. F. Ramsey 1950), which had become a topic of focus in the 1960s. The first UCN were observed simultaneously by (Lushchikov et al. 1969) and (Steyerl 1969). With the progress of sources and improvements in storage techniques, UCN physics has become an active field and moved beyond investigating the neutron itself (Steyerl 2020). UCN are for example used to test for short-ranged forces, the free neutron lifetime or search for the neutron EDM.

The defining property of UCN is a kinetic energy low enough to be reflected from a material container under any angle of incidence. This is the case[2] for neutrons with $E_{\text{kin}} < 335\,\text{neV} \sim 8\,\text{m}\,\text{s}^{-1}$.

At such low energies, UCN trajectories are significantly affected by gravity. The gravitational potential can be rewritten as $\text{V}_\text{g} = 102\,\text{neV}\,\text{m}^{-1}$.

The neutron has no electric charge[3] and a finite magnetic moment of $\mu_n = -9.662\,365\,1 \times 10^{-27}\,\text{J}\,\text{T}^{-1}$ (CODATA 2018). μ_n is commonly expressed as a potential $60.3\,\text{neV}\,\text{T}^{-1}$, which shows that the technically accessible field are similar to the total kinetic energy. This can be used to manipulate spin statistics of UCN or built magnetic bottles to confine UCN.

The interaction of UCN with bulk material is dominated by the strong interaction with the nuclei in the wall. The deBroglie wavelength of UCN is large compared to inter-atomic spacing in solids, with

$$\lambda = \frac{1}{h}\sqrt{2m_n E_{kin}} > 100\text{nm}. \tag{1.1}$$

Thus for smooth surfaces, the UCN-wall interaction is described by elastic, coherent scattering. For UCN, incoherent scattering and in particular inelastic scattering is almost always the result of surface contamination with different nuclei than the bulk. A rigourus discussion of neutron scattering can be found in (Turchin 1965),while a condensed treatment on the scope of UCN is provided in (Golub et al. 1991).

Without further justification we define a shallow, fictitious pseudo-potential, the Fermi potential, which allows us to use the framework of perturbation theory for the UCN-wall interaction. This is counter-intuitive, as the depth of nuclear potentials $|V(r)| \gg E_{kin}$ and the wave function of the incident neutron does, in fact, change significantly upon interaction. But "The aim is to replace the nuclear potential V(r) by a fictitious

[2] The energy and critical velocity given fluctuates in the literature, depending on the choice of material bottle. Here ^{58}Ni was chosen which is, however, of little practical use as a UCN bottle material.

[3] $(-2 \pm 8) \times 10^{-22}\,\text{e}$ (CODATA 2018)

potential U(r) such that the scattering amplitude f(ϑ) can be derived from the Born approximation applied to U(r)"(Oliver Zimmer 2004). To this end the Fermi potential uses experimentally obtained scattering lengths and is defined by:

$$V = \frac{2\pi\hbar^2}{m_n} Nb, \tag{1.2}$$

where m_n is the free neutron mass, N the material number density, b the bound coherent scattering length. The interactions follow the reflection of a wave on a step function with total reflection for $E_{kin} < U_F$. As the wave function penetrates into the classically forbidden region on the scale of a few wavelengths, the UCN can be lost from inelastic up-scattering or nuclear absorption. This loss can be accounted for by adding an imaginary potential W to our pseudo potential V. We can use this simple treatment, given that both effects have vanishing probability of a reverse transition. Any inelastic interaction with the wall will increase the neutron energy above the wall potential, and down-scattering is negligible due to the small density of states in the UCN regime. We now get our complex Fermi potential to be:

$$U_F = V - \imath W, \quad V = \frac{2\pi\hbar^2}{m_n} Nb, \quad W = \frac{\hbar}{2} N\sigma_l v, \tag{1.3}$$

where σ_l is the total neutron loss cross-section and v the neutron velocity. σ_l is proportional to $1/v$, so loss is velocity independent overall. Using this potential we can evaluate the reflection probability to (Golub et al. 1991, eqn 2.71):

$$|R|^2 = \frac{E_\perp - \sqrt{E_\perp}\sqrt{2\alpha - 2(V - E_\perp)} + \alpha}{E_\perp + \sqrt{E_\perp}\sqrt{2\alpha - 2(V - E_\perp)} + \alpha}, \quad \alpha = \sqrt{(V - E_\perp)^2 + W^2}, \tag{1.4}$$

where $E_\perp$ is corresponding to the energy of the normal component of the velocity [4]. For UCN stored in a container with some degree of diffuse reflection, the directions of UCN will be randomized and the UCN behave like an isotropic gas[5]. Under these assumptions, we get for the mean loss per bounce $\bar{\mu}(E_{kin})$:

$$\bar{\mu}(E_{kin}) = 2\eta \left(\frac{V}{E_{kin}} \sin^{-1} \sqrt{\frac{E_{kin}}{V}} - \sqrt{\frac{V}{E_{kin}} - 1} \right), \tag{1.5}$$

where $\eta = W/V$. For energies $E_{\text{kin}} > V$, loss per bounce is on the order of 1 and UCN and UCN are lost after few wall collisions. Thus these UCN are irrelevant for our purpose. Eqn. 1.5 is plotted for kinetic energies below the Fermi potential in fig. 1.5. This relation is the reason for spectral softening of stored UCN. UCN with an energy close to the trapping potential have a higher loss probability than those with smaller kinetic energy.

Wall losses calculated from these relations are very small in theory, but experimentally tested surfaces have never reached the low loss values anticipated. This is part of a larger discrepancy in the field often referred to as 'anomalous losses' for UCN on surfaces. It is widely believed that hydrogen on the surface is a source of inelastic, incoherent up-scattering as well as additional absorption. Attempts to model this process

[4] Sometimes incorrectly referred to as the normal component of the energy.
[5] This is where the effect of gravity has to be accounted for in macroscopic experiments

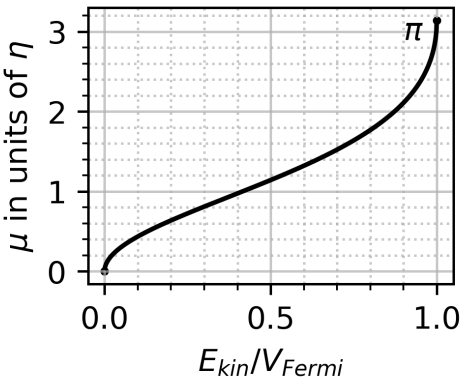

Figure 1.5: Loss per bounce $\bar{\mu}$ in units of η vs. E_{kin} as a fraction of V_{fermi}.

have not yielded the desired results (Steyerl 2020, chap.7), but workable experimental understanding has grown in the field.

Instead of loss per bounce, many experimental setups are characterized by their UCN storage time τ_{n}. It has multiple contributions which can be described as time constants:

$$\frac{1}{\tau_n} = \frac{1}{\tau_\beta} + \frac{1}{\tau_{\text{wall loss}}} + \frac{1}{\tau_{\text{surface impurities}}} + \frac{1}{\tau_{\text{slits}}}. \tag{1.6}$$

The free neutron lifetime of $\tau_\beta = (880.2 \pm 1.0)\,\text{s}$ (CODATA 2018) limits the free precession time fundamentally. $\tau_{\text{wall loss}}$ combines eqn. 1.5 with the mean wall collision rate (a geometry-dependent quantity). Experiments that intend to operate close to the neutron lifetime have to rely on magnetic and gravitational confinement of UCN in very low-pressure vacuums. In material bottles, UCN-wall interactions generally dominate the storage time.

1.4 Neutron EDM measurement principle

The Hamiltonian of a neutral particle (or compound system) with EDM is given by (J. M. Pendlebury et al. 2004):

$$H_{ext} = -\frac{\mu}{J}\boldsymbol{J}\cdot\boldsymbol{B_0} - \frac{d}{J}\boldsymbol{J}\cdot\boldsymbol{E}, \tag{1.7}$$

where J is the total spin angular momentum and μ and d are the magnetic and electric dipole moments. Both magnetic and electric dipole moment are oriented with respect to the angular momentum[6]. In Fig. 1.6 the transformation of both terms in the Hamiltonian for P- and T-inversion are shown. While the magnetic field and the spin transform like axial vectors, the electric field transforms like a polar vector.[7] Thus the term associated with the EDM is T-odd and P-odd. The full Hamiltonian can only be P- and T-invariant if $d = 0$. Assuming CPT conservation, an EDM would then also violate CP conservation [8]. For a neutron the magnetic term in eqn. 1.7 is much larger than the electric and

[6] This can be justified using a symmetry argument: No other direction or feature is available. Another argument which uses a classical framework would be based on averaging: An EDM at an angle to the spin would average to a projected value along the spin anyway.

[7] P: $V_{axial} \to V_{axial}$, P: $V_{polar} \to -V_{polar}$, T: $V_{axial} \to -V_{axial}$ and T: $V_{polar} \to -V_{polar}$.

[8] Quoted from (Wurm 2015)

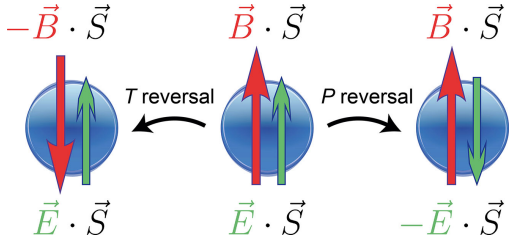

Figure 1.6: An illustration of T- and P-inversion behavior of a neutron with a magnetic moment μ aligned to the angular momentum and a permanent electric dipole moment (EDM) d. (Printed with permission from (Patton et al. 2013))

we define[9] by convention a static holding field B_0 to be along the vertical z-axis as our quantization axis. Initially, the spin, and thus the magnetic moment, is aligned with the holding field. A pulse of transverse magnetic field in the non-adiabatic limit of eqn. 4.12 can now rotate the spin in the traverse plane. We take the magnetic interaction from eqn. 1.7:

$$H = -\boldsymbol{\mu}\cdot\boldsymbol{B} = -\gamma\boldsymbol{B}\cdot\boldsymbol{J} = -\gamma\left(\sum_{i=x,y,z} B_i\hat{J}_i\right) \rightarrow \boldsymbol{B} = B\hat{z} \rightarrow H_s = -\gamma B\hat{J}_z, \tag{1.8}$$

with an associated time evolution operator U which we can apply on a spin pointing towards an arbitrary initial direction (θ_0, ϕ_0). We yield

$$U(t,0) = exp\left(-\frac{\imath H_s t}{\hbar}\right) = exp\left(-\frac{\imath(-\gamma Bt)\hat{J}_z}{\hbar}\right) \tag{1.9}$$

$$|\Psi,0\rangle = \cos\frac{\theta_0}{2}|+\rangle + \sin\frac{\theta_0}{2}e^{\imath\phi_0}|-\rangle \tag{1.10}$$

$$|\Psi,t\rangle = U(t,0)\,|\Psi,0\rangle \tag{1.11}$$

$$= e^{+\imath\gamma Bt/2}\left(\cos\frac{\theta_0}{2}|+\rangle + \sin\frac{\theta_0}{2}e^{\imath(\phi_0-\gamma Bt)}|-\rangle\right). \tag{1.12}$$

We can ignore the overall phase and yield a time evolution around the z-axis with the angle $-\gamma Bt$. This is the classical limit of a macroscopic magnetic dipole following Bloch equations:

$$\frac{\partial}{\partial t}\langle\boldsymbol{m}\rangle = \gamma\langle\boldsymbol{m}\rangle\times\boldsymbol{B}, \tag{1.13}$$

where the spin also precesses with:

$$\omega_L = -\gamma\cdot\|B_z\|\,. \tag{1.14}$$

ω_L is the so-called Larmor frequency where the magnetic moment is conveniently given as $-29.164\,694\,3\,\mathrm{MHz\,T^{-1}}$ (CODATA 2018). We can express this in terms of the magnetic moment using $\mu = \gamma J$:

$$\omega_L = -\frac{\mu}{\frac{1}{2}\hbar}\cdot B, \tag{1.15}$$

$$\hbar\omega_L = -2\mu B. \tag{1.16}$$

[9] Using the naming convention of NMR experiments.

We consider the effect of the electric field acting on the electric dipole moment analogously and yield an extension to eqn. 1.14:

$$\hbar\omega_L = 2\mu \cdot B + 2d \cdot E. \tag{1.17}$$

To extract the value of the dipole moment, one compares the precession of neutron for $E \uparrow\uparrow B$ and $E \uparrow\downarrow B$. We calculate the difference of eqn. 1.17 for both configurations by changing the signs of E and B correspondingly and yield:

$$|\omega_{L\uparrow\uparrow}| - |\omega_{L\uparrow\downarrow}| = \frac{1}{\hbar}\left(\underbrace{2\mu(B_{0\uparrow\uparrow} - B_{0\uparrow\downarrow})}_{=0} \pm 4dE\right), \tag{1.18}$$

where $|\omega_{L\uparrow\uparrow}| - |\omega_{L\uparrow\downarrow}|$ is the difference in the free precession rotation rate. To determine the electric dipole moment d, the two magnetic field contributions in both E-B configurations has to cancel perfectly. This is a critical prerequisite of an EDM measurement, as any unaccounted B field difference increases the uncertainty σ_d.

The result from eqn. 1.18 agrees with a more general formulation found in (T. E. Chupp et al. 2019, eqn 5):

$$|\Delta\omega| = \frac{dE}{\hbar J} \tag{1.19}$$

if we add the neutron spin (1/2) for the total angular momentum J and add a factor of two from the difference of two measurements.

1.5 Ramsey's method of separated oscillatory fields

In the previous section, we linked the EDM to the Larmor frequency for a single neutron, which is not a readily accessible observable. The density of UCN is typically too small for direct observation of the ensemble magnetization with nuclear magnetic resonance (NMR) methods. It is, however, possible to extract the alignment of a UCN spin in an external magnetic field with spin-sensitive detection. This means that any experiment with UCN is blind to the intermediate phase and the spin is detected - like the neutron - only destructively at the end.

PanEDM uses Ramsey's method of separated oscillatory fields (Purcell and N. F. Ramsey 1950) to create an interferometer in time. Here we observe the phase built up over a long free precession time projected onto an ensemble distribution of UCN spins in just two states. Initially, we fill spin-polarized UCN adiabatically into a measurement cell exposed to a vertical magnetic and electric field (B_0 and E). Thus all spins are aligned with the magnetic holding field. Without loss of generality, we assume[10] all spins are aligned with Z+. A transverse, magnetic pulse B_1 is applied, gated from a precise clock signal (See also figure 1.7). Pulse frequency and length are chosen such that in the rotating frame of the neutron,[11] a transverse component is present which flips the spin by $\pi/2$ into the horizontal, transverse plane. For a measurement time T the spin precesses following eqn. 1.17 which ends with a second $\pi/2$ transverse pulse, coherent with the first. In the absence of an EDM, all spins would flip to the Z- direction as the spins have completed an integer number of revolutions. A finite EDM d would add an

[10] In practice all spins are anti-parallel to the magnetic field, as only high field seeker (HFS) are filled into the experiment.

[11] Rotating with $\omega = -\gamma B_0$ in the holding field.

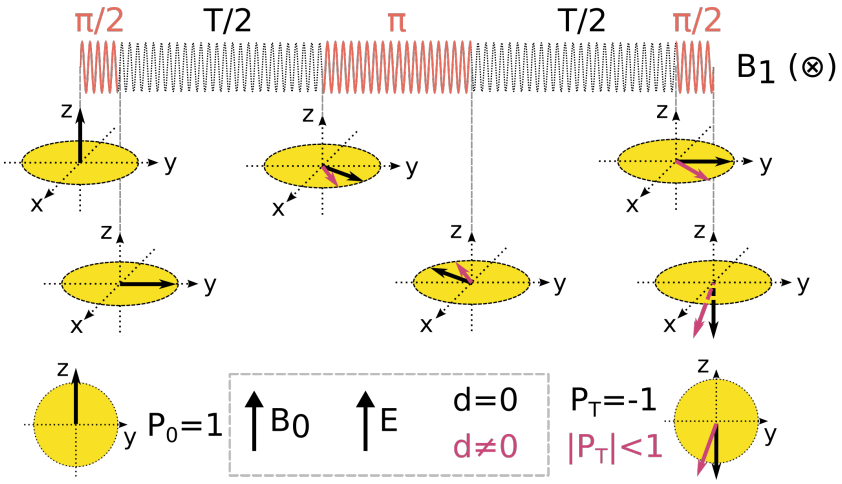

Figure 1.7: Ramsey's method of separated oscillatory fields applied at panEDM with a spin-echo pulse scheme: UCN are polarized/spin aligned initially in a holding field $B_0 \parallel z$. A transverse pulse B_1 rotates the spins by $\pi/2$ into the transverse plane where they precess as a result of the magnetic (and potential electric) dipole moment. After $T/2$, a coherent π pulse is applied to invert the dephasing of the first half. A second B_1, $\pi/2$ pulse flips the spin into $-Z$ direction for $d = 0$. A finite electric dipole moment $d \neq 0$ would cause a small phase to accumulate leading to an incomplete second flip. The EDM can then be detected in a deviation of final polarization of the UCN ensemble.

additional phase ϕ,causing a fraction of spins to be in the opposite final state:

$$\phi = \Delta\omega T, \tag{1.20}$$

where ϕ is the phase, $\Delta\omega$ the shift from pure Larmor precession and T the free precession time. Alternatively: The second flip only captures a fraction of the precessing population, as the spins are off-resonant by the phase ϕ. The final polarization is given by

$$P_{\mathrm{T}} = -P_0 \cdot \cos\phi = \frac{N_\uparrow - N_\downarrow}{N_\uparrow + N_\downarrow}, \tag{1.21}$$

where P_{T} is the final polarization, P_0 the initial polarization, *phi* the phase from eqn. 1.20, $N_\uparrow$ the number of UCN with spin up and $N_\downarrow$ the number of UCN with spin down. Eqn. 1.21 links the change in the precession frequency to of final spin state which can be gathered from spin-sensitive detection at the end of the measurement.

If we assume the effects of the magnetic field to cancel perfectly to 0, the statistical uncertainty of the electric dipole moment hinges on the uncertainty of the frequency shift. We get from eqn. 1.18:

$$\sigma(d) = \frac{\sigma(\Delta\omega_L) \cdot \hbar}{4E}, \tag{1.22}$$

for a small phase *phi* the uncertainty of the Larmor frequency shift $\Delta\omega$ is approaching[12]

$$\sigma(\Delta\omega) = \frac{1}{T}\sigma(P_z) \rightarrow \sigma(P_z) \propto \frac{1}{\sqrt{N}}. \tag{1.23}$$

[12]This corresponds to the steepest slopes on Ramsey fringes close a frequency detuning of 0.

If we combine this result with equation 1.22, we get a simplified upper bound for the sensitivity of an EDM measurement

$$\sigma_{d_n} = \frac{\hbar}{2\alpha ET\sqrt{N}}, \tag{1.24}$$

where we have replaced P_0 with α, which encloses the overall polarization contrast in the measurement.

1.6 Geometric phases

For this thesis, only this key systematic effect is discussed in more detail. An extensive treatment of neutron EDM systematics expected also for panEDM can be found in (J. M. Pendlebury et al. 2015). A reason why systematic effects are difficult to address in current nEDM searches lies in the intrinsically 'clean' nature of UCN as a physics probe. For the purpose of EDM experiments, it has no hidden degrees of freedom[13] which could obscure the measurement. Systematics generally arise during the blind time evolution of UCN. A neutron carries one bit - in the technical sense - of information: The spin alignment. One could argue, that even the kinetic energy is no direct observable, as conventional UCN detection is not energy-sensitive. The fact that the UCN itself provides almost no handles to provide trust in the yielded results, gave rise to numerous auxiliary systems discussed later in this thesis. The geometric phases in UCN measurements are non-vanishing Berry's phases (Berry 1984) and first described by (J. M. Pendlebury et al. 2004). As UCN move inside the trap they sample the non-uniform fields. In the rest frame of the UCN these are rotating fields proportional to the electric field. Such rotating field modify the Larmor precession via the Ramsey-Bloch-Siegert shift (Norman F. Ramsey 1955) which is related to the buildup of a geometric phase. To first order this shift is given by:

$$\Delta\omega = \frac{\omega_{xy}^2}{2\left(\omega_0 - \omega_r\right)}, \quad \omega_{xy} = -\gamma B_{xy}, \quad |\omega_r| \approx \frac{|v_{xy}|}{R}, \tag{1.25}$$

where ω_0 is the ideal Larmor frequency, ω_{xy} is the rotation that arises from transverse fields B_{xy} and ω_r is the orbital trap motion given by the mean UCN velocity and R the geometric radius of the EDM cell. Crucially the shift is proportional to the square of the transverse fields. Three sources of transverse fields should be discussed here.

- Any vertical magnetic field like B_0, which has[14] a vertical gradient also has transverse components given by:
$$\boldsymbol{B_{0xy}} = -\frac{\partial B_{0z}}{\partial z}\frac{\boldsymbol{r}}{2}. \tag{1.26}$$
- Particles with spin moving in an electric field $\boldsymbol{E}$ acquire a term from Lorentz transform of
$$\boldsymbol{B_v} = \frac{\boldsymbol{E}\times\boldsymbol{v}}{c^2}. \tag{1.27}$$
- Small static magnetic contamination on the inside surface of the storage cells adds magnetic dipole fields.

[13] of which we know of.
[14] This is a simple consequence of $\nabla B = 0$.

The last item is particularly relevant for a mercury co-magnetometer, as geometric phases for $|\omega_r| > |\omega_{\text{Larmor}}|$ are enhanced (Harris and J. M. Pendlebury 2006; Pignol and Roccia 2012). For panEDM a magnetic dipole of 1 pT at 3 cm distance consumes the full error budget of 1×10^{-27} ecm. In the simplest case the transverse field has two contributions from the linear vertical gradient and the motional field (J. M. Pendlebury et al. 2004)

$$\boldsymbol{B_{xy}} = \boldsymbol{B_{0xy}} + \boldsymbol{B_v} = -\frac{\partial B_{0z}}{\partial z}\frac{\boldsymbol{r}}{2} + \frac{\boldsymbol{E}\times\boldsymbol{v}}{c^2} \tag{1.28}$$

$$\omega_{xy}^2 = \gamma^2 \boldsymbol{B}_{xy}^2 = \left(\frac{\partial B_{0z}}{\partial z}\frac{\boldsymbol{r}}{2}\right)^2 + \left(\frac{\boldsymbol{E}\times\boldsymbol{v}}{c^2}\right)^2 + 2\frac{\partial B_{0z}}{\partial z}\frac{\boldsymbol{r}}{2}\cdot\frac{\boldsymbol{E}\times\boldsymbol{v}}{c^2}. \tag{1.29}$$

The mixed term is linear in the electric field and mimics the effect of a dipole moment which is indistinguishable from a nEDM. This is the strongest single systematic effect in panEDM. As an aside, it is a curious fact that a relativistic effect is the source of the dominant systematic false effect for particles moving at few meters per second. Furthermore, this also means, that the magnitude of the geometric phases scales with the mean UCN energy which is experimentally accessible. The effect also scales with the size of the gradient and the size of the cell - which both decrease for smaller cell sizes in practice. [15] The cell size is thus a trade off between large volumes for high UCN counts or small volumes and cleaner systematic effects.

1.7 Overview about ongoing searches

Neutron EDM searches are an active research field. Table 1.1 lists selected ongoing nEDM searches. Most experiments use room temperature Ramsey spectrometers which have yielded the best limits in the past decades. nEDM searches at panEDM, PSI, PNPI, TUCAN and LANL all share a common experimental concept, consisting of storage cells inside magnetic shielding and simultaneous spin detection. PNPI and panEDM use designs without Hg co-magnetometer, while it is planned or used in all the other mentioned searches[16]. TUCAN intends to enhance the capability of their co-magnetometry by adding ^{129}Xe as third species next to neutrons and mercury (Masuda et al. 2012). This would allow to disentangle the vertical gradient and isolate the false effect from geometric phases. ^{129}Xe would be filled into the cells pre-polarized and read out optically via a two-photon transition.

All of these searches target a similar sensitivity of about 1×10^{-27} ecm, which is roughly an order of magnitude improvement over the current limit. One reason why these approaches and the targeted sensitivities are similar lies in the maturity of the used technologies. Simultaneously, the community depends on the improved performance of UCN sources. The current nEDM limit has a systematic uncertainty five times smaller than the statistical uncertainty. While some progress was made in storage times (typically $\sim 100 - 300$ s), these are fundamentally limited by the neutron lifetime (880.2 ± 1.0) s. Also, polarization contrast or electric field strengths cannot improve beyond tens of percent upon the current limit. This means that the currently dominant experimental approach will likely not continue past 1×10^{-28} ecm.

[15] Gradients close to the center of shield rooms are particularly small - this is also true for the panEDM MSR.

[16] EDM at PNPI uses BeO and Be wall coating which have a particular low Hg polarization lifetime (May 1998). Using a Hg co-magnetometer would require a major redesign and sacrifice the high trapping potential.

Experiment Source	Method	Published EDMs [10^{-26} ecm]	Target Sensitivity [ecm]
panEDM @ ILL (Wurm et al. 2019)	RT UCN storage superthermal ^{4}He		$2 \cdot 10^{-27}$ ($3 \cdot 10^{-28}$)
nEDM @ PSI (Ayres et al. 2021)	RT UCN storage superthermal pulsed D_2	$0.0 \pm 1.1_{stat} \pm 0.2_{syst}$ (Abel et al. 2020)	$1 \cdot 10^{-27}$
nEDM @ ILL/PNPI	RT UCN storage Steyerl turbine	0.56 ± 3.04 (Serebrov et al. 2016a)	$1 \cdot 10^{-27}$
SNS nEDM (Wei 2020)	Cryo UCN storage in-situ prod. cold beam		$3 \cdot 10^{-27}$ ($2 \cdot 10^{-28}$)
TUCAN @ TRIMUF (Ahmed et al. 2019)	RT UCN storage superthermal ^{4}He		$1 \cdot 10^{-27}$
nEDM @ LANL (Ito et al. 2018)	RT UCN storage superthermal pulsed D_2		$4 \cdot 10^{-27}$ ($2 \cdot 10^{-27}$)
neutron beam EDM (Piegsa 2013)	Cold Neutron Beam		$1 \cdot 10^{-24}$ ($1 \cdot 10^{-26}$)

Table 1.1: Selected list of ongoing neutron EDM searches. The target sensitivities are given for later project stages (for example phase II panEDM) in brackets. RT: Room temperature.

A notably different approach is pursued by the SNS collaboration at Oak Ridge National Laboratory. At SNS, the apparatus converts UCN directly inside the EDM apparatus in liquid He. This eliminates losses from UCN transport which at panEDM add up to about a factor of 4 in UCN number. In addition ^{4}He has a exceptionally high dielectric strength which allows for large electric field to be applied. The collaboration recently demonstrated a prototype with more than $80\,\mathrm{kV\,cm^{-1}}$ across a large electrode (Phan et al. 2021) compared to $20\,\mathrm{kV\,cm^{-1}}$ at panEDM[17] and $15\,\mathrm{kV\,cm^{-1}}$ at PSI (Ayres et al. 2021). The electric field improves the EDM sensitivity linearly which leads to a factor of 4 improvement above state of the art. ^{3}He is used as a spin-dependent absorber which allows in-situ detection. While the SNS EDM experiment design is conceptually elegant, the technical challenges lie in realizing a full cryogenic experiment.

Cold beams are typically many orders of magnitude more intense than UCN sources. For example: The total UCN[18] flux at the ILL/PF2 source is $\sim 2.6 \times 10^4\,\mathrm{cm^{-2}\,s^{-1}}$ (ILL 2021). The polarized cold beam facility ILL/PF1B has a polarized[19] flux of $\sim 3 \times 10^9\,\mathrm{cm^{-2}\,s^{-1}}$ (ILL 2021). The neutron beam EDM (Piegsa 2013) attempts to capitalize on the larger flux densities of cold beam sources by revisiting the original measurement from Norman Ramsey (Purcell and N. F. Ramsey 1950). In a nEDM beam measurement, a polarized neutron beam passes through an electric and magnetic field. Coils placed at the beginning and the end of the flight path provide the spin flips which initiate and end the Ramsey cycle. The time of EDM phase buildup T is defined by the physical length of the E- and B-field region and the cold beam velocity and is typically on the order of milliseconds. As T improves the sensitivity linearly, a large number of cold neutrons is

[17] planned
[18] Here defined as $v_z < 6.2\,\mathrm{m\,s^{-1}}$.
[19] Typical wavelength 0.4 nm and degree of polarization of 99.7 %.

necessary to compensate for short precession time. The collaboration designed modular elements such that a long beam path could be built from smaller, separately built units and targeting a final length of $\sim 30\,\mathrm{m}$. The length linearly improves the time of flight and thus also linearly the EDM sensitivity. This approach is currently 2 orders of magnitude off the current sensitivity but has in theory potential to be scaled up.

2 The panEDM experiment

The panEDM experiment is a room temperature UCN double cell storage experiment to search for the neutron EDM. The majority of component development has happened at the Technical University Munich,Germany and the location of the main experimental site at the ILL in Grenoble, France.

The design, as mention in the previous section is among five experiments with roughly similar experimental approaches. A key development made within the collaboration was the improvement of magnetic shielding above state of the art and degaussing (equilibration for non-zero final fields) (I. Altarev et al. 2014; I. Altarev et al. 2015; Igor Altarev et al. 2015). This resulted in very low residual magnetic fields and excellent drift behavior. For magnetic monitoring non-magnetic, all-optical Cs magnetometers where developed which provide unprecedented clean and cross-talk free magnetic field information. Both developments improve the understanding of magnetic field in the apparatus and allow for the omission of the mercury co-magnetometer, a key difference to three other ongoing nEDM searches.

Originally the experiment was designed and built for a different type of UCN source at the Research Neutron Source Heinz Maier-Leibnitz (FRM II) in Munich (I. Altarev et al. 2012). Starting in 2017 the apparatus was disassembled and has moved to the SuperSUN source at ILL22. This chapter will provide an overview of the experiment design overall, while the following chapters will discuss changes to the experiment related to the UCN source.

A simplified schematic of the core panEDM configuration is shown in fig 2.1. A central electrode applies high-voltage of both polarities which creates opposing electric field in the UCN cells. The electric fields are respectively anti-parallel outwards or inwards. The walls of the cells are made from a single, coated quartz insulator ring each. The top and the bottom of the cells are made from coated aluminum electrodes. The outer, ground electrodes have a small central opening for filling and extraction of UCN. This EDM cell stack has a diameter of 480 mm and a height of 262 mm. It is placed in the center of a large multilayer, magnetically shielded room (MSR) and a set of cos-θ coils which provide the vertical magnetic bias field B_0. UCN in both cells simultaneously test $E \uparrow\uparrow B$ and $E \downarrow\uparrow B$[1]. The magnetic field is monitored by two[2] mercury magnetometers on top and bottom of the EDM cell stack. Eight fiberized all-optical Cs magnetometers provide additional magnetic field information.

2.1 Target statistical sensitivity

Recalling eqn. 1.24, we can determine the statistical reach of panEDM using the design specifications: panEDM stage I is designed towards an electric field of E=20 kV cm^{-1},

[1] Or $E \downarrow\uparrow B$ and $E \uparrow\uparrow B$, $E \uparrow\downarrow B$ and $E \downarrow\downarrow B$ or $E \downarrow\downarrow B$ and $E \uparrow\downarrow B$ depending on the configuration of HV polarity and the sign of B_0

[2] Potentially three, with one Hg cell placed in the HV electrode

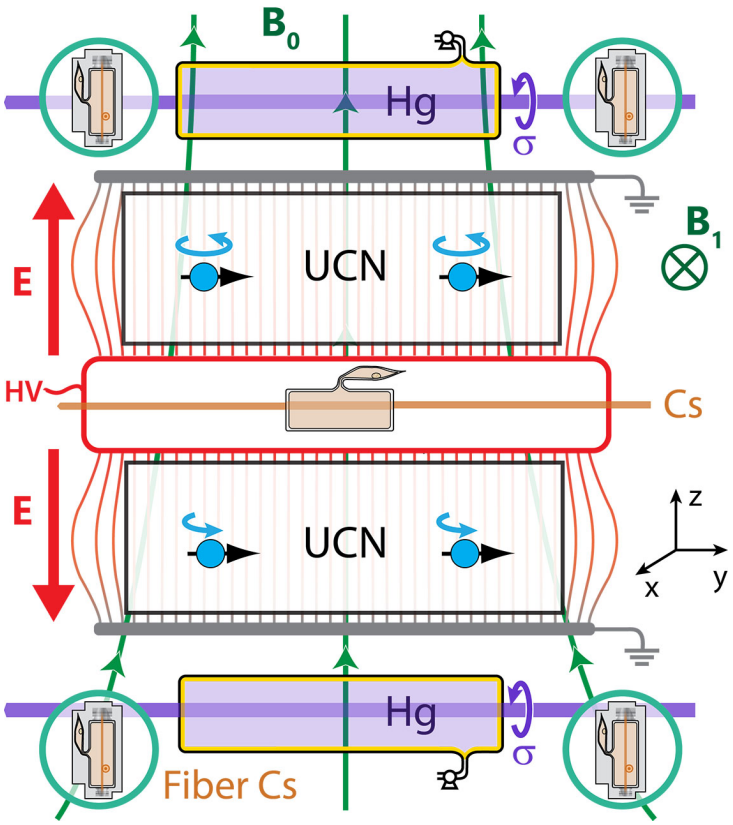

Figure 2.1: Central components of the panEDM. Two cylindrical storage cells are filled simultaneously with UCN and subject to a magnetic field $|B_0| \approx 1.3\,\mu\mathrm{T}$. A HV electrode generates anti-parallel electric fields with $E \approx \pm 2\,\mathrm{MV\,m^{-1}}$. Optical magnetometers based on laser spectroscopy of ^{199}Hg and ^{133}Cs are arranged around the UCN storage cells and inside the hollow HV electrode to monitor the field and its gradient.

a free precession time T=250 s, a visibility $\alpha = 0.85$ and a final neutron count per cell N=27 000 The visibility α is a dimensionless quality factor that encapsulates all contrast reducing effects. An ideal apparatus with an ideal spin polarizer, analyzer and perfectly non-depolarizing walls would have $\alpha = 1$.

For stage II SuperSUN receives a magnetic trap to increase the effective trapping potential (O. Zimmer and Golub 2015). The trap also accumulates polarized UCN which eliminates the need for a polarizer and increases the number of UCN by a factor of 2. Changes in the mean UCN energy and the omission[3] of foil polarizer altogether improve the transfer loss for stage II. Table 2.1 summarizes all factors and presents the expected statistical reach for the targeted 100 days of data recording. The numbers given here differ slightly from those reported in (Wurm et al. 2019) as a result of changes to the EDM measurement sequence (see sec. 2.5).

panEDM statistical sensitivity

	stage I	stage II
SuperSUN saturation density [cm^{-3}]	333	1667
Transfer loss factor [1]	4	1.5
Source saturation loss factor [1]	2	2
Polarization loss factor [1]	2	1
Density EDM cells [cm^{-3}]	4.0	111
No. of Neutron ($t = 0$) per cell	7.04×10^4	1.88×10^6
E [V m^{-1}]	2.15×10^6	2.15×10^6
α [1]	0.85	0.85
T [s]	250	250
No. of Neutron ($t = T$) per cell	25 900	690 000
$\sigma_{\text{1 cell, per run}}$ [ecm]	4.48×10^{-25}	8.68×10^{-26}
$\sigma_{\text{2 cell, per run}}$ [ecm]	3.17×10^{-25}	6.14×10^{-26}
$\sigma_{\text{per day, M=196}}$ [ecm]	2.26×10^{-26}	4.38×10^{-27}
$\sigma_{\text{100 days, M=196}}$ [ecm]	2.26×10^{-27}	4.38×10^{-28}

Table 2.1: Estimation of the panEDM statistical reach based on eqn 1.24. M is the number of runs which fit into a full day.

2.1.1 Extended statistical sensitivity

A simple upper bound of the statistical sensitivity was given in eqn. 1.24 which we shall now expand to include aspects of the wall interaction and storage time. We know from eqn. 1.6, that UCN in a material bottle are lost through various mechanisms. We can replace N, the final number of UCN from eqn. 1.24 with

$$N = N_0 e^{-T/\tau_n}, \tag{2.1}$$

where N_0 is the initial number of UCN and τ_n the EDM cell storage lifetime. This makes clear why a finite, optimal free precession time T must exist. Similarly we can

[3] For stage I saturated iron layers on aluminum foils are used in the simultaneous spin detection. These should be replaced with compact high field magnetic barriers.

parameterize[4] the depolarization of UCN over time by adding the polarization lifetime T_2:

$$\alpha = \alpha_0 e^{-T/T_2}. \tag{2.2}$$

If we insert eqn. 2.1 and eqn. 2.2 into eqn. 1.24, we obtain:

$$\sigma_d = \frac{\hbar}{2ET\alpha_0 e^{-T/T_2}\sqrt{N_0 e^{-T/\tau_n}}}, \tag{2.3}$$

where again E is the electric field, T the free precession time, α_0 the initial visibility upon filling[5], T_2 the spin coherence time, N_0 the initial number of UCN and τ_n the UCN storage time. This equation helps to weigh the impact of design changes to the experiment sensitivity, which will be the subject of later sections.

2.2 UCN optics

Conversion, polarization, precession and detection of UCN is spatially separated. The guide system - usually referred to as UCN optics - which facilitates the transport is described in this section. The complete panEDM UCN optics are shown in fig. 2.2.

UCN are extracted vertically from the SuperSUN converter volume and exit SuperSUN via a 50 mm stainless steel guide (extraction guide). A VAT shutter marks the transition to panEDM where a $\sim$ 7.5 cm stainless steel guide section adjusts for the guide mismatch between SuperSUN and panEDM. Currently, a vertical mismatch of 9 mm has to be compensated. The MSR has settled by a few m since the original placement in 2017. A similar effect is to be expected for SuperSUN with its even heavier lead shielding. The section between VAT valve and source switch (SW) is foreseen to change along with the relative motion of SuperSUN and panEDM.

The SW is a two-position switch (see subsection 4.6.1) which either diverts the beam downwards to a ^{3}He counter or passes it to the solenoid polarizer (SP). In regular panEDM operation both VAT valve and SW are set to transmission, the ^{3}He counter is mainly used for SuperSUN maintenance.

The SP creates a large magnetic field barrier which prohibits one type of spin alignment (low field seeker (LFS)) from entering the setup. As spins approach the gradient inside the guide, spins aligned with the magnetic field lines are repelled (LFS). If the magnetic barrier is higher than the maximum total kinetic energy of the incoming UCN beam, near-perfect polarization can be achieved (see section 4.5). Inside and downstream of the SP only non-depolarizing wall materials can be used for UCN optics. In the case of panEDM the majority of guides is made of $\sim$500 nm NiMo (85/15) coated glass[6] guides. Smaller sections are made of hand-polished copper, like the guide section inside the SP and the junction blocks in the SW and the TW. The high field seeker (HFS) which pass the SP enter the guide manifold (guide manifold (GM)).

The GM splits the path of UCN into an upper and lower branch separated by 340 mm. The GM is a rather delicate nine-segment UCN distributor made from precision-cut glass (see fig. 2.3).

[4] The terminology of the transverse coherence time T_2 has been lifted with some liberties from the nuclear magnetic resonance community.
[5] Basically the degree of polarization
[6] Schott DURAN Borosilikatglas 3.3, ID 50 mm, OD 60 mm

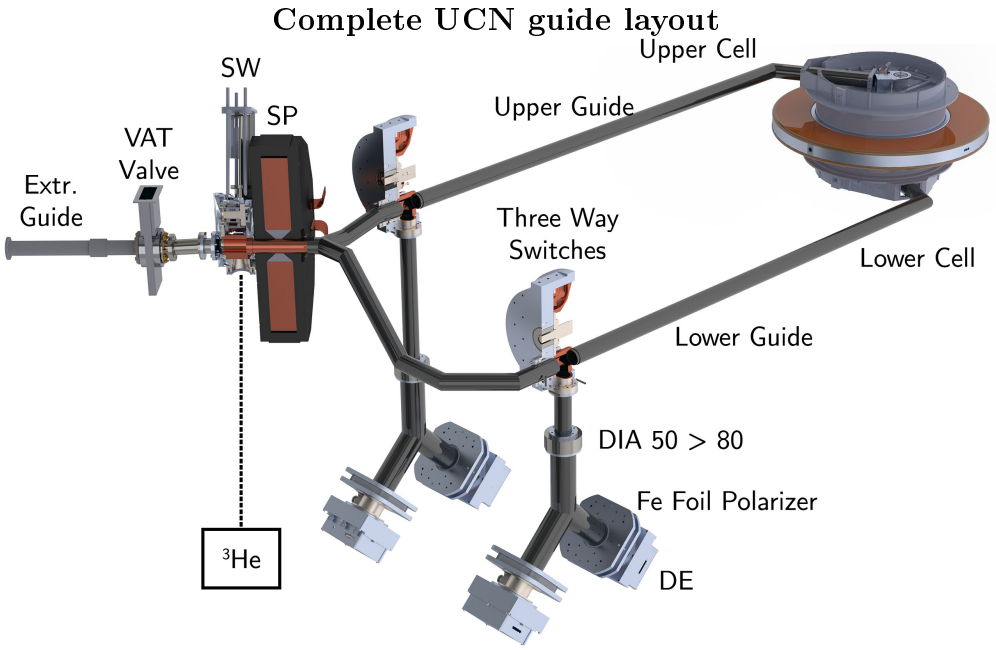

Figure 2.2: Rendering of the complete panEDM UCN guide layout. UCN enter through the extraction guide (left), pass through the vacuum separation valve (VAT) and enter the source switch (SW). UCN can be diverted to a monitor detector or passed through the solenoid polarizer (SP) and via the guide manifold into both three-way switches (TWs). For the filling, the upper (lower) guide is connected to the upper (lower) cell valves (not shown). For the emptying, the UCN propagate back to the TWs and are directed downwards to the Y-shaped simultaneous spin detection with two detectors (DE) each. DIA 50>80: Transition to guides with ID 80mm below this element.

The upper and lower branches are analogous and symmetric, hence only differences will be remarked further on.

The GM feeds into two three-way switches (TWs), one for each cell. These are rotary switches which places one of four junction blocks between the GM, the upper guide connected with the EDM cell, and the vertical guide leading to the simultaneous spin detection. There is a straight, horizontal junction block used for filling UCN, and two 90° bends to either connect the GM to the simultaneous spin detection (for background and detector drift tests) or to connect the cell to the simultaneous spin detection for counting at the end of the Ramsey sequence. A detailed description of the TW can be found in subsection 4.6.2.

The upper and lower horizontal guides exiting the TW connect to the upper and lower EDM cell valves respectively. These valves seal the EDM cells during Ramsey cycles and connect to the feed guides when open. The cell valves are described in subsection 4.6.3.

At the end of a Ramsey sequence, the ratio of both spin states has to be determined. To this end, the UCN are guided back through the cell valves and the TW. Each unit consists of a Y-shaped glass section. UCN accelerate while descending and randomly enter either end of the 'Y'. Both legs terminate with an iron foil polarizer and are equipped with an adiabatic spin flipper. Adiabatic spin flipper almost perfectly reverse the spin while UCN fly through, regardless of flight direction. The iron foil polarizer transmits only

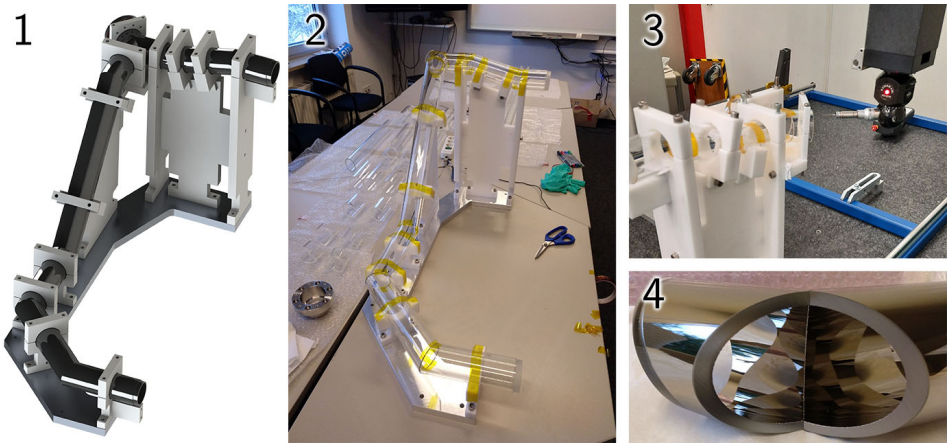

Figure 2.3: The guide manifold (GM) which splits the UCN path exiting the solenoid polarizer (SP) into two branches for the upper and lower EDM cell.(1) Rendering of the GM, (2) Test assembly of cut glass parts to determine best fit configurations. (3) Micro-meter mapping of output ports for the assembled GM (4) Picture of two NiMo coated guide elements.

spins anti-parallel to the magnetic field (HFS and reflect spin parallel to the magnetic field LFS [7]

The function of the full system is best explained following an example scenario. Fig 2.4 shows two UCN with initial spin up (purple, HFS) and spin down (blue, LFS) entering from the top. Both randomly propagate towards the left Y-branch where the HFS passes through the foil polarizer and is counted in the left UCN detector. The LFS is reflected on the foil and propagates to the right Y-branch. While passing through the spin flipper, the UCN spin get flipped and the UCN can pass the right foil polarizer and is counted in the right UCN detector.

Thus the two UCN have been sorted to a UCN detector dependent on their initial spin alignment. If we consider that both UCN would have entered the right Y-branch first, we get the same result: Both UCN spins would have been flipped. The blue UCN would have passed as a HFS and be counted on the right UCN detector, while the purple UCN would have been a LFS and get reflected on the right foil polarizer. When reflected back towards the left branch, the spin would be flipped again and the purple UCN could pass the left foil polarizer as a HFS. If the left spin flipper instead of the right is turned on, the assignment of the initial spin state and UCN detector is flipped. Likewise, if the spin flipper on the top guide is turned on, the assignment flips again. These permutation degrees are necessary to determine detection- and spin flip efficiencies in the two detectors and three spin flippers. A detailed experimental test of a simultaneous spin detection system was done in (Zechlau 2016). A detailed discussion of the development of UCN detectors is provided in (Meichelböck 2019; Pieler 2021).

While the UCN lifetime inside the guide section can be effectively long and spin flippers virtually perfect, the iron foil polarizers are in practice limiting the performance of the spin detection. Two potentials exist inside the foil: The material potential of iron and the spin-orientation-dependent magnetic potential. This means below a certain energy threshold UCN get partially absorbed and reflected, but none transmitted. In

[7] In a particular band of kinetic energies. See later in the same section.

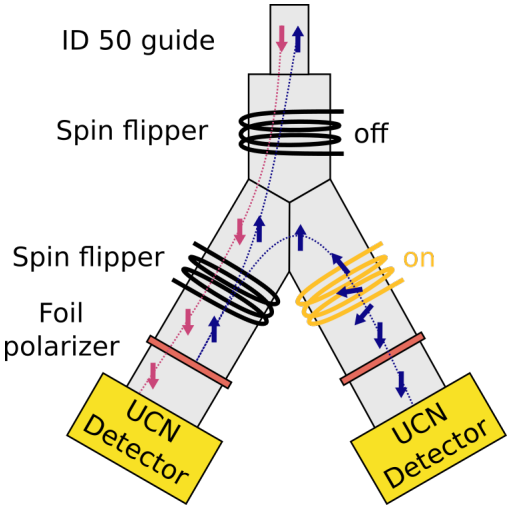

Figure 2.4: Schematic of simultaneous spin detection. To count one spin orientation per detector, one of two spin flipper (SF) in either leg must be switched on. Spin down UCN pass through are transmitted by the foil polarizer, spin up UCN get reflected and can only pass the foil placed after a running SF. The top SF and swapping the operation state of the two bottom SF allows determining the efficiencies of all SF and the foil polarizer.

an intermediate kinetic energy window, LFS are reflected and HFS transmitted while a fraction of both species is lost to absorption. For higher kinetic energies, both species get transmitted with some background of absorption and reflection. Thus the vertical position of the foil polarizer has to be set with respect to the initial UCN energy such, that all UCN reaching the foil reside within the intermediate kinetic energy range. This in turn depends on the strength of the magnetic flux density in the iron and varies strongly for individual foils. For stage II the magnetic barrier provided by superconducting coils instead of saturated iron foils. This will eliminate the loss inside the foil, widen the intermediate energy range to the maximum of the UCN spectrum and thus provide near-perfect and loss-less spin selection.

2.3 Combined magnetic field measurement

The magnetic bias field is in principle an auxiliary quantity that does not even appear in the sensitivity estimate. Its properties are entirely governed by minimizing systematic uncertainties. The field has to be reversible with respect to gravity to disentangle geometric phase effects. The magnitude of $|B_0|$ defines the frequency of free precession for neutrons via the gyromagnetic ratio of $(-29.164\,69\,\mathrm{Hz}\,\mu\mathrm{T}^{-1})$. A natural choice are so-called magic fields (Pignol 2019), where the magnitude of the field is chosen such that the false EDM in a mercury co-magnetometer vanishes. We express the false EDM effect by:

$$d_{\mathrm{n}}^{\mathrm{false}} = \frac{\hbar\,|\gamma_n \gamma_{Hg}|}{2c^2} \int_0^\infty \langle B_x(0) v_x(t) + B_y(0) v_y(t) \rangle \cos \omega t dt, \tag{2.4}$$

where γ_n,γ_{Hg} is the gyromagnetic ratio of neutrons and mercury, c is the speed of light, B_x,B_y the transverse magnetic field components, v_x, v_y the transverse velocity com-

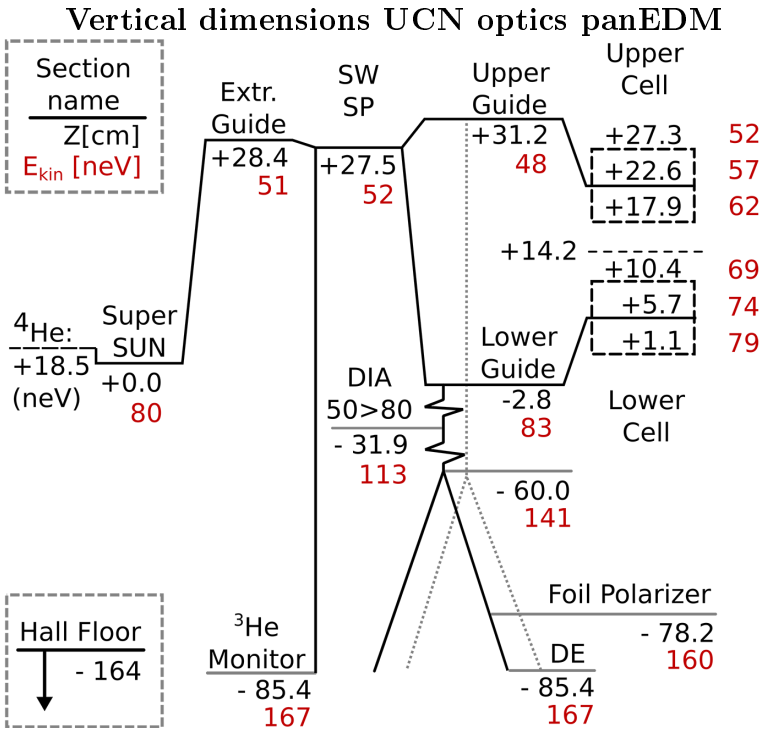

Figure 2.5: Vertical offset of UCN guides and volumes in the panEDM apparatus. The vertical dimensions have correct relative scale, for each section the offset from the SuperSUN converter vessel center is given in cm and the corresponding E_{kin} for the expected mean energy of SuperSUN. For the upper and lower EDM cell the vertical position and kinetic energy for the top, the middle and the bottom of each cell are given. From this schematic, it is apparent, that the mean kinetic energy in both cells is $\Delta E_{\mathrm{kin}} = 17\,\mathrm{neV}$.
SW: Source Switch, SP: Solenoid Polarizer, DE: Detector EDM, DIA 50>80: Transition to guides with ID 80mm below this line.

ponents, ω the angular frequency of mercury and $\langle x(0)v_x(t)\rangle$ the correlation function between velocity and position. This correlation function is independent of the cell geometry for short timescales, but dominated by the horizontal diffusion of mercury. As it turns out, both regimes have a different slope of $\langle x(0)v_x(t)\rangle$ which when combined with different ω in eqn.2.4 cause the integral to switch from a large positive value to a negative value at some ω - the magnitude of the magic field. For panEDM the magic field value is given by (Pignol 2019, eqn. 11):

$$B^{\mathrm{lin}}_{\mathrm{magic}} \approx \frac{100\mathrm{cm}}{D} \times \left[0.9 + 0.84\frac{H}{D}\right] \times 8.8\mu\mathrm{T} \rightarrow B^{\mathrm{lin}}_{\mathrm{magic,panEDM}} = 19.5\mu\mathrm{T}. \tag{2.5}$$

Generating such high fields is possible but deteriorates the field stability. This can be understood by considering the bias field generation. Homogeneous bias fields in panEDM are provided by so-called cos-θ coils for B_0 and B_1 (see also fig. 2.6). The coil is composed of a high-permeable (mu-metal) horizontal cylinder with coils wound around in a toroidal configuration with one distinct change: The coil is split vertically and both left and right[8]

[8] +x and -x

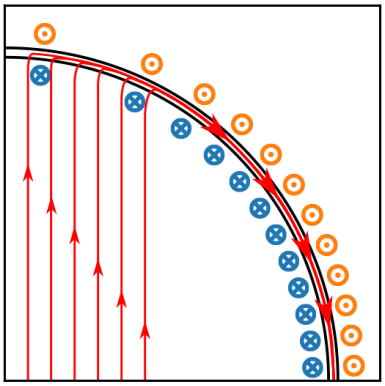

Figure 2.6: Schematic of a cos-θ coil. The coil is wrapped around a mu-metal cylinder at a density $\propto \cos(\theta)$. Field lines are forced out of the mu-metal cylinder and form a highly uniform vertical field. From (Stuiber 2018).

half generate an opposing flux. Hence the field lines do not circle around in the mu-metal cylinder, but 'collide' in the vertical X-Z plane[9].

The field lines which are forced to exit the mu-metal and pass vertically through air provide the B_0 bias field. Careful selection of the wire density allows optimizing the homogeneity of the field. This design allows creating fields with a homogeneity of $< 10^{-4}$ inside a very confined space. This is critical to avoid cross-talk to the high permeability layers of magnetic shielding of the magnetically shielded room (MSR) which hosts the bias field coil. The presence of highly non-linear magnetizable materials means that temporal stability, repeatability, and robustness against vibrational disturbances decrease rapidly for larger bias field magnitudes. This means that operating with a co-magnetometer and magic magnetic fields would increase the source of the very systematic effect which would be significantly smaller otherwise. For panEDM the optimal value for the bias field is expected close to 1.3 µT. This value avoids excess noise generally observed close to 50 Hz (1.7144 µT) and is small enough for homogeneous bias field generation. The chosen bias field magnitude also affects the low pass filtering of fast varying signal from the Ramsey pulses where - again- higher frequencies which are damped stronger require excess signal power which increases systematic uncertainties. The final value is chosen based on in-situ measurements once the apparatus is near completion. The mechanical resonance frequencies of the MSR are similar to the targeted neutron precession time. However, the mechanical eigenmodes of the MSR and their subsequent effect on the field are difficult to predict. The field generation for B_0 and the pulse generation for B_1 is prepared for a wider range of potential bias field values.

Outside magnetic field perturbations are damped by an inner ('insert') and outer magnetic shield (MSR). The combined damping exceeds $6 \cdot 10^6$(I. Altarev et al. 2014) at 10 mHz. The relative field homogeneity is better than $5 \cdot 10^{-4}$ and the temporal stability better than $10\,\mathrm{fT\,m^{-1}\,s^{-1}}$ (Lins 2016). A cut through the magnetic shielding is shown in fig 2.7. Next to UCN statistics, the leading limitation of current nEDM searches is the quality of magnetic fields via geometric phases.

At the experimental site at research neutron source Heinz Maier-Leibnitz (FRMII) an active coil compensation system outside the MSR suppressed slow varying fields by up

[9] Here the MSR coordinate system is used where Z points vertically upwards, Y inwards from the MSR door towards the back and X to the right.

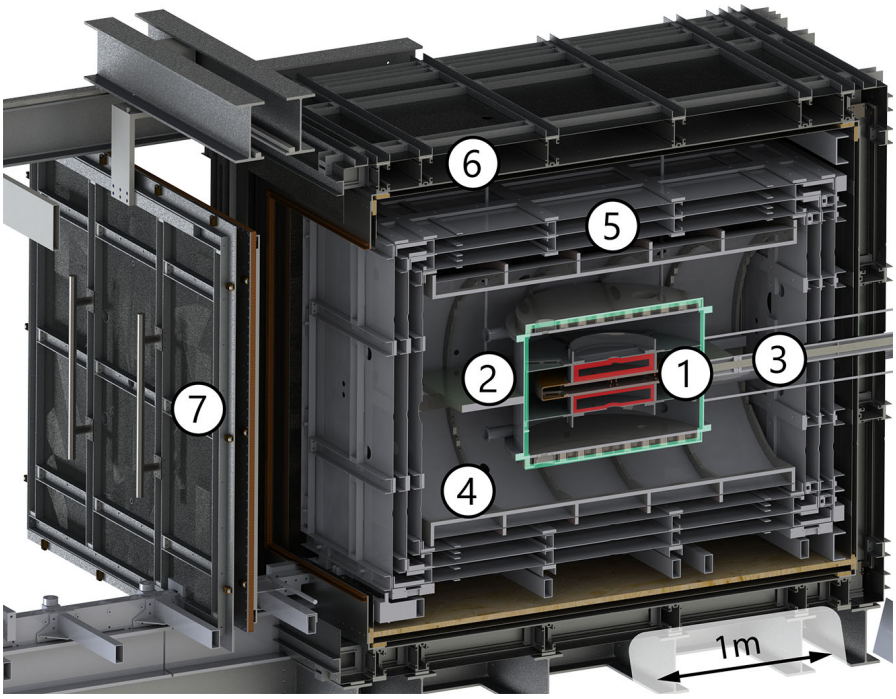

Figure 2.7: PanEDM magnetic shields and central components. 1: UCN cells, 2: vacuum chamber, 3: high-voltage insertion, 4: cylindrical shield and field coils (not shown) for B_0 and B_1, 5: three-layer inner magnetic shield (Insert), 6: outer magnetic and RF shield (MSR), 7: MSR door. Taken from (Wurm et al. 2019)

to one order of magnitude. The experimental site at ILL cannot host such a system, thus panEDM has to rely on passive shielding which has performed above the initial specifications.[10] Before the experimental runs, detailed spatial maps are recorded. The mapping campaign was largely comprised of manual measurements in the past (Stuiber 2018). The first generation of mechanical mapper can no longer be used at ILL due to the changes in the experimental site. In addition, the mechanical tolerances of the mapper limited the quality of field maps. This is a result of the particular field shape. The small transverse gradients of the holding field are crucial to characterizing the field. These components are three orders of magnitude smaller than the vertical leading field B_0. Field probes like fluxgates (Janosek 2017) have a sensitive axis, thus a small unknown angular misalignment causes a large measurement uncertainty. Field magnitude sensors, like the Cs magnetometers, are generally insensitive to heading errors[11] but require a dense grid of points to reconstruct field gradients.

Regardless of the quality of field maps, there is no substitute for magnetic monitoring during Ramsey cycles. Over the span of 250 s temperature changes for example can change the hysteresis of the mu-metal and cause magnetic field drifts. UCN in Ramsey's method are blind during phase accumulation. This means that the measured UCN data does not resolve unexpected magnetic field changes other than the final phase deviating

[10] The absence of the active field cage has two arguably more concerning consequences: The experiment lacks a rigid, clean buffer zone where a potential magnetic noise source cannot be placed. In addition, the active field cage doubles a climate tent that actively maintains stable temperature and humidity for the experiment.

[11] Only their sensitivity has an orientation. For small heading errors the decrease of SNR is $\propto \cos\theta$.

from the expected Ramsey pattern.

In the panEDM two optical magnetometer systems are used based on ^{133}Cs and ^{199}Hg which shall be briefly presented in the following sections. Both systems are based of optical birefringent vapors which arise from optical pumping. ^{133}Cs is an alkali metal with high vapor density at room temperature where an electron moment undergoes Larmor precession with $\omega_L = 3.50\,\mathrm{kHz\,\mu T^{-1}}$[12] and typical coherence times of $\tau =$ 10-150 ms (Kimball and Budker 2013). ^{199} Hg has no unpaired electrons in its outer $6s^2$ shell, thus the magnetic moment is dominated by the nucleus. Nuclear moments are suppressed by $\sim m_{\mathrm{electron}}/m_{\mathrm{nucleon}}$ but better shielded from external perturbations. Thus ^{199}Hg atoms precess with only $\omega_L = 7.590\,\mathrm{Hz\,\mu T^{-1}}$ (Afach et al. 2014) but with typical coherence times above 200 s. In practice, a mercury magnetometer can achieve higher sensitivity than Cs magnetometer at longer integration times. In addition, Hg is a suitable co-magnetometer for UCN - therefore past EDM experiments relied heavily on Hg magnetometer.

One can argue that the Larmor frequency is the fundamental bandwidth limit of a magnetometer. Magnetic field variation on faster timescales cannot be resolved. The gyromagnetic ratio of the neutron ($-29.164\,69\,\mathrm{Hz\,\mu T^{-1}}$) makes neutrons sensitive to fluctuations which might be unresolved in the mercury magnetometer. Fast events such as HV discharges can be detected with Cs magnetometer. Cs magnetometer can yield high sensitivity combined with strong spatial resolution, which is vital for tracking of higher spatial field modes.

Both systems can be pumped and interrogated optically, either with free-space beams or through optical fibers. All electronics needed for beam preparation and analysis reside outside the MSR which eliminates magnetic noise sources close the EDM cells.

2.3.1 Cesium magnetometer

A wide range of Cs based optical magnetometers have been developed over the years which allow measurements on the scale of ∼µT (Kimball and Budker 2013; Gawlik and Pustelny 2017; Weis et al. 2017). The sensors used at the panEDM experiment have been developed within the collaboration as Bell-Bloom type synchronously pumped NMOR magnetometer (Bell and Bloom 1961). Bell and Bloom first demonstrated excitation of magnetic resonance transitions driven by light intensity modulation. This removes the need for RF coils in sensor design and makes the sensor construction conceptually non-magnetic. Non-linear magneto-optical rotation (NMOR) is a particular contribution to the Faraday effect (Faraday 1846) in gases also called Macaluso-Corbino-effect (Macaluso and O. 1898). The non-linear nature arises for particular light polarization and intensities and has multiple components. In the Cs magnetometer design, NMOR is used to achieve optical rotation $\sim 10^4 - 10^6$ larger than expected for classical Faraday rotation. A detailed description of the sensor design can be found in (Sturm 2020).

The sensitive unit of the magnetometer is a paraffin coated, evacuated cell (DIA 10 mm, length 30 mm) with a reservoir containing a small drop of liquid Cs. The vapor pressure at room temperature along its axis is large enough for roughly one optical depth (1/e) of Cs vapor. For this discussion, we assume the external magnetic field to be aligned with the cell axis and the z-axis. A strong linear polarized beam of near-resonant pump light creates a non-equilibrium ground state distribution along the y axis. This is also called

[12] This is strictly speaking different for the D1 ($-3.509\,393\,68\,\mathrm{kHz\,\mu T^{-1}}$) and at the panEDM used D2 line($3.498\,228\,78\,\mathrm{kHz\,\mu T^{-1}}$ (Patton 2012).

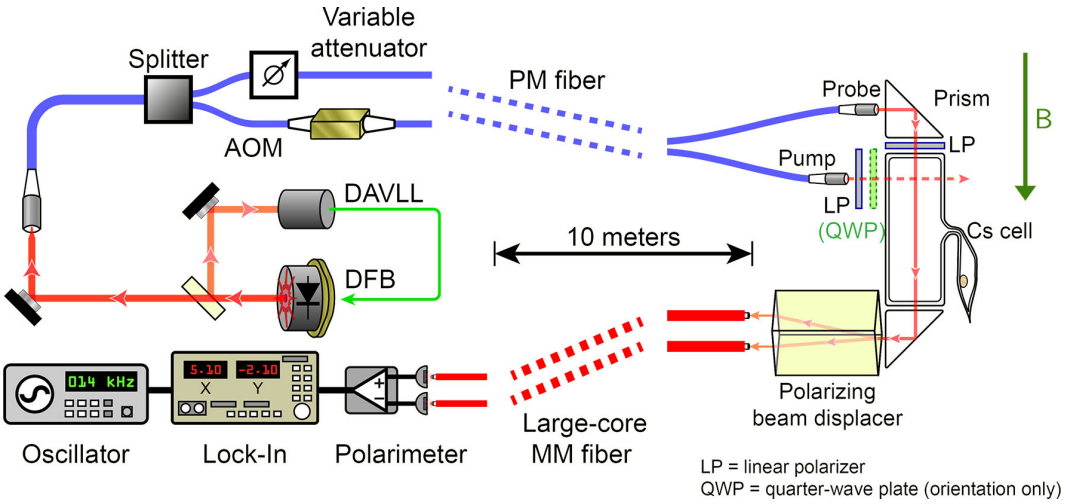

Figure 2.8: Optical schematic of Cs magnetometers. Frequency stabilized laser light is coupled into optical fibers and used as linear polarized probe light (top blue path) or chopped with an acusto-optic modulator (AOM) for transverse optical pumping (bottom blue path). The Cs vapor in the cell imprints an optical rotation signal onto the probe light which is converted into intensity modulation with a polarizing beam displacer. Two large-core multi-mode fiber return the amplitude modulated light to a polarimeter. Taken from (Patton 2015)

"pumping alignment" and creates a two-fold symmetric ground state. In the presence of the magnetic field B along the z-axis, the aligned spins precess with the Larmor frequency ω_L about the z-axis. The linear polarized probe light experiences NMOR which is modulated as the aligned spin population rotates. The transmitted light then allows for optical detection of magnetic resonance.

The optical modulation observed evolves with $2\omega_L$ due to the symmetry of the pumped spin distribution. The ensemble polarized in such a manner has no total net magnetization, which eliminates sensor cross-talk.

In general pumping and probing are sequential steps to yield free precession decay signals. A strong pump pulse[13] initiates an atomic alignment (or orientation) which precesses and slowly decays in amplitude due to relaxations mechanisms. After the signal dips below a certain SNR, a new pump pulse is triggered and another measurement cycle begins. Consecutive measurements are independent but systematically clean as only the probe light is present. In synchronous operation, pump pulses are provided continuously. A lock-in amplifier detects the phase between the frequency of the pump pulses and the modulation of the probe signal. A feedback loop locks both frequencies and allows for continuous tracking of the field. This operation mode is particularly resilient to intensity fluctuations, but field excursions limited to a small window in which the feedback loop stays locked. A simplified scheme of the optical layout of the magnetometer is shown in figure 2.8. A narrow-band laser source tuned to the Cs D2 line (852 nm) is frequency locked to a working point near the $F = 4 \rightarrow F' = 4$ transition. The light is coupled into a single-mode, polarization-maintaining fiber.[14] The light is then attenuated to the

[13] Actually a sequence of pulses roughly separated by $1/\omega_L$.

[14] Usually a special type of PM fiber called ZING fiber is used. This fiber has higher directional stress

suitable power and used as a probe beam after passing a clean-up linear polarizer at the entrance window of the cell. The pump beam is chopped with an acusto-optic modulator for synchronous pumping or the creation of arbitrary bursts. The beam is also passing through a cleanup polarizer[15]. The probe light is passing through the birefringent vapor and passed through a polarizing beam displacer which separated the two polarization components. The time-dependent circular dichroism causes the intensity of the two output beams to fluctuate proportionally to the Larmor precession. Light is returned from the sensor via two large core multi-mode fibers. The design allows the sensor head to be free of magnetic and electronic components. The typical magnetization of the sensor is on the scale of single pT, static and uncorrelated to sensor operation. A crucial figure of merit is the Allan deviation (Allan 1987; Riley and Howe 2008) which is the square root of the two-sample variance of consecutive measurements averaged over time τ. Given in simplified notation,

$$\sigma^2_{\text{Allan}}(\tau) = \frac{1}{2}\left\langle \left(\overline{y}_{n+1}(\tau) - \overline{y}_n(\tau)\right)^2 \right\rangle, \quad \overline{y}_n(\tau) = \frac{1}{\tau}\int_{\tau n}^{\tau(n+1)} x(t), \tag{2.6}$$

where $\overline{y}_n(\tau)$ are time averages of the tested quantity x(t).[16] Intuitively the Allan deviation is the expected spread of consecutive measurements of a quantity buffered for time τ. Figure 2.9 shows the Allan deviation for a typical Cs magnetometer. For short averaging times, the sample mean improves $\propto \tau^{-0.5}$ as one would expect for sampling statistics. For longer averaging times drifts within the device or from the test environment increase the variance of the reported magnetic field magnitude. At 130 s a magnetometer sensitivity of 52 fT could be demonstrated. For the relevant time of a Ramsey cycle a sensitivity of $\sigma_{T=250\text{s}} = 55\text{fT}$ was measured. The performance of the sensor itself is most likely better than this margin, as it is notoriously difficult to obtain magnetic test environments with even higher stability and known reference fields. The planned array of 8 Cs sensors with this resolution allows vertical gradient tracking with a resolution of $\sim 30\,\text{fT}\,\text{m}^{-1}$. A detailed description of the application of magnetometers in panEDM will be given in (Martin Rosner 2021).

2.3.2 Mercury magnetometer

Mercury as a co-magnetometer has a long history with EDM measurements. In the Sussex-apparatus (Baker et al. 2006) it was a critical component of the successful EDM searches in the past. Simultaneously it was a large source of systematic uncertainties. As mentioned before - mercury is among the best-suited candidates for a co-magnetometer with UCN. Only nuclear magnetic moments are shielded strong enough to provide coherence time on the level of UCN storage times. Hg is chemically inert, has a small neutron absorption cross-section and can be interrogated optically, albeit deep in the UV range.[17] Historically mercury vapor lamps were used. Now narrow band laser sources are available which promise improved systematic understanding and performance (Fertl 2013).

than PM fiber and actively polarizes the beam.

[15] For orientation mode, a quarter-wave plate is used in addition.

[16] The factor 1/2 was introduced to match the value of the Allan deviation to the standard deviation for white noise.

[17] He magnetometers (Heil 2017) rival Hg magnetometers in performance, but ^{3}He is a strong neutron absorber which makes it unsuitable as a co-magnetometer.

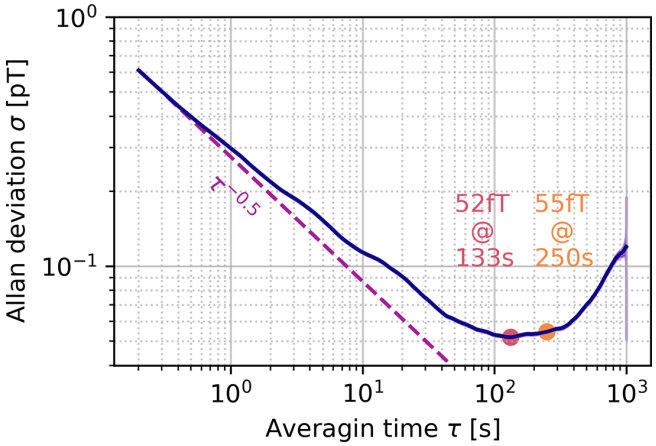

Figure 2.9: Allan deviation of Cs magnetometer. The two-sample Allan deviation expresses the repeatability of a measurement device. Under stable measurement conditions, this corresponds to the experimentally accessible sensitivity. The Allan deviation is equal to the standard deviation for pure white noise sources. σ_{Allan} improves $\propto \tau^{-0.5}$ for short averaging times. Intrinsic or external drifts ($\propto \tau^{1}$) limit the sensitivity for longer measurement times. Highlighted are the best effective sensitivities of the Cs magnetometers (52 fT @ 133 s) and for the length of a panEDM Ramsey sequence (55 fT @ 1250 s). Data taken from (M. Rosner 2021).

Of the seven naturally occupying Hg isotopes, only two (^{199}Hg and ^{201}Hg) have an odd number of neutrons and only ^{199}Hg is a I=1/2 system. Analogously to the Cs magnetometer, Hg vapor is optically pumped into a non-equilibrium ground state distribution with transverse, synchronous optical pumping. The total quantum number $F = I$ is due to the closed electronic shell. This makes the $6^1S_0 \rightarrow 6^3P_1$ (253.7 nm) transition a rare example of optically detected nuclear magnetic resonance. Once the vapor is polarized the precession signal can be obtained from the modulation of absorption of a circularly polarized probe light, or the optical rotation of linear polarized probe light. Only the first option is viable for co-magnetometer operation where enough contrast can be obtained from vapor densities below $5 \times 10^{10}\,\mathrm{cm}^{-3}$ (Taubenheim 2017).

Two systematic effects in Hg are worth highlighting in this brief discussion: Geometric phase effects in Hg are larger than in UCN due to the larger atom velocity at room temperature ($v_{\mathrm{UCN}} < 4\,\mathrm{m\,s}^{-1}$, $v_{\mathrm{Hg}} \sim 150\,\mathrm{m\,s}^{-1}$), which makes this the leading systematic in nEDM experiments. Accounting for this effect requires among other aspects, dealing with the different center of mass of Hg vapor and UCN. Any finite circular component of the readout light shifts the magnetic sublevels of the mercury atoms (m_F) akin to a fictitious magnetic field[18] - the so-called light shift effect. Light shifts (LS) generally prohibit absolute magnetic flux density determination and are a focus of magnetometer development. For a circular polarized, absorptive probe beam a remedy is tuning the laser wavelength to the no light shift point. About 8 MHz below the F=1/2 transition the effective light shift is zero but with a steep slope which mandates a lock better than 500 kHz. The absorptive scheme is prone to a variety of light shift effects due

[18] The level shift is a result of virtual and real transitions and has scalar, vector and tensor components. A detailed discussion can be found in (Happer 1972).

to the close to unity circular polarization of the probe beam. When detecting with optical rotation, no net circular component should be present. In practice, a small residual circular component from the birefringence of optics remains. In optical rotation schemes, the probe beam is tuned far away from the center of the F=1/2 transition to reduce unwanted absorption of the probe light. At large detunings, however, the light shift is significant.

The panEDM Hg system is described in detail in (Taubenheim 2017). panEDM stage I is operating without a co-magnetometer, while the apparatus maintains this capability with minor adjustments. Thus the Hg cells in use can be optimized independently of UCN requirements. This allows the use of mercury densities three orders of magnitude higher and optical rotation as readout instead of absorption. Optical rotations >1500 mrad are possible for a 30 cm long cell based on the design for the HgEDM (Swallows 2007). Signal decay caused by the probe light is reduced with off-resonant detuning. To account for the light shift, both the power of the readout light and the detuning is modulated to extrapolate to vanishing light shifts. This has to be done independently for all cells since a fair contribution of light shifts are specific to beam angle, divergence and imperfections in the optical path. Hg cells will be placed on top and bottom of the ground electrode. A sensitivity of 2 fT at a distance of 490 mm can resolve a gradient of $4.2\,\mathrm{fT\,m^{-1}}$ which, if uncompensated, corresponds to a false EDM of 1×10^{-27} ecm. A third Hg cell can be placed inside the HV electrode which extends the capability of the system to reconstruct quadratic B field shapes changes on top of linear gradient drifts. At all cell positions, no electric field is present[19] which eliminates[20] Kerr effect and Stark shifts on top of the geometric phases from $\boldsymbol{B} \times \boldsymbol{v}$.

2.4 Electric field generation

The electric field in the EDM cells is generated by shifting the potential of the central, HV electrode. Since the wall of the EDM cells are made from an electric isolator, a stable electric field between the ground electrodes and the HV electrode is established. The high voltage is generated with a modified FUG HCB 20 - 200 00 MOD[21] power supply. The supply has a reduced inline resistance of 50 kΩ and a fast analog modulation input can adjust 1 % of the full output range. The supply is connected to the current measurement housing (current measurement housing (CMH)) at the back of the MSR between the TWs which established the link to the HV electrode on the inside itself. Fig. 2.10 provides a cut view through all critical parts of the HV system.

The central electrode is charged with ±200 kV. This value is a compromise between the nEDM sensitivity, which increases linearly with the electric field and the rate of discharges and the magnitude of leakage currents. At the level of targeted nEDM sensitivity, leakage currents from HV to ground along the quartz ring causes a relevant magnetic field proportional to E. If the leakage current takes a (partially) radial path, it forms a current loop creating a field contribution parallel/anti-parallel to the bias field. This shifts the free precession frequency and causes a false EDM in analysis. A 50 pA current flowing[22] in a single loop around one cell implies a false EDM of 1×10^{-27} ecm. Thus it

[19] In particular the cell inside the HV electrode resides only in high potential.
[20] There are geometric phases still present, but independent of E and can create thus no false EDM.
[21] FuG Elektronik GmbH,Am Eschengrund 11,83135 Schechen,Germany
[22] This value was erroneously reported as 1×10^{-28} ecm in (Wurm et al. 2019).

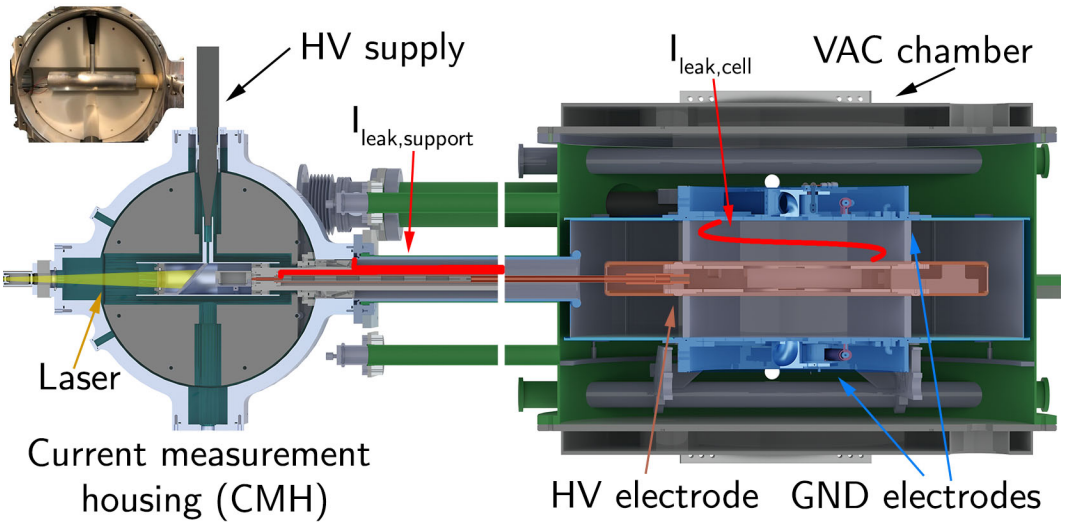

Figure 2.10: The panEDM vacum chamber with HV and GND electrodes (right) and the HV supply system (left). A HCB 200 00 MOD FuG ±200 kV, ±100 µA feeds into the current measurement housing (CMH) where an aluminum cylinder is charged up. A laser-powered ammeter relays current from the cylinder to a DIA 15 mm copper tube which is mounted to the EDM electrode. Assumed leakage currents that flow spirally across the cell walls ($I_{leak,cell}$) create a false EDM. These currents are measured entangled with $I_{leak,support}$ which flow along the only mechanical contact of the copper tube.

is vital to monitor the leakage current. An ammeter floating on high potential is placed inside an external HV enclosure(Current measurement housing CMH). It is composed of a small circuit that is powered by an external 20 W IR laser beam and measures the current between the HV supply and the copper conductor leading to the HV electrode. The circuit has a resolution of 0.5 pA and a range of ±500 pA. The ammeter has a bypass build from anti-parallel Zehner diodes which protect the electronics when the HV is ramped or a discharge occurs inside. The bandwidth of the ammeter is electronically limited to 16 Hz which is slow on the scale of analog signal electronics. The small bandwidth is a result of the large amplification needed to monitor pico-ampere currents. This cuts into the available gain-bandwidth product. Operation amplifiers with a larger gain-bandwidth product could not be used due to excessive noise or drift - both relevant for the application. In the next section, it will become clear why this small bandwidth suffices. The readings are encoded to frequency-modulated IR pulses which are again optically transmitted. A receiver circuit picks up the signal and returns a 1-10 Hz reading to the panEDM DAQ system.

2.4.1 Adjustments for panEDM at ILL

The limited physical space between panEDM and SuperSUN prohibited the operation of the original CMH of the HV system. Thus the physical dimensions of the CMH were trimmed. The original design included a voltage divider to directly measure the output voltage which is absent in the present design[23].

[23]The voltage divider would connect at the empty vertical port downwards in the CMH

Calculations and later simulations revealed the extent of AC damping from the present dielectric insulators and the dimensions of the grounded enclosure. A list of these values is given in table 2.2. The voltage divider was intended to monitor the electrode voltage fast enough for the detection of discharges. This is unfeasible with a bandwidth of $\sim$ 3 Hz, but would draw a large current from the HV supply potentially increasing drifts and noise.

After the redesign two leakage current paths remain. $\mathrm{I_{leak,cell}}$ is the unavoidable path along the quartz rings which creates false EDMs. $\mathrm{I_{leak,support}}$ is a current flowing from the HV copper conductor along the inside and outside of a ceramic insulator tube to the CMH. Current flowing along this path is attributed to $\mathrm{I_{leak,cell}}$ and increases the uncertainty on the EDM result. The path of $\mathrm{I_{leak,support}}$ is $\approx$ 1 m along the surface of the ceramic insulator and should be negligible [24]. Leakage current that originate from the supply-facing side of the ammeter do not contribute to the reported current. This is true for all currents inside the CMH which originate from the inner aluminum tube.

The new CMH allows placing an inline resistor chain in the copper conductor to further increase the low pass frequency cut off of the HV supply system. Given that the unavoidable low pass filtering prohibits fast ($\sim$ kHz) measurements, the design artificially decreases the low pass frequency to dampen ripple from the HV supply. The time needed for HV polarity reversals provides a lower bound. A useful criterion is the residual loading current (Hopf 2020):

$$\int_{t_{\mathrm{ramp}}}^{t_{\mathrm{ramp}}+t_{\mathrm{Ramsey}}} I(t)dt < 50\mathrm{pA} \cdot t_{\mathrm{Ramsey}} \tag{2.7}$$

where I(t) is the current from the supply to the electrodes, t_{ramp} is the ramping time, t_{Ramsey}=T=250 s. When a polarity reversal took place, the voltage on the HV electrode in the between the EDM cells rises proportional to the voltage difference to the supply with an exponential decay constant given by low pass filtering of the full HV system. The ramp time has to be chosen long enough, such that the total charge flow remaining within the Ramsey cycle is smaller than the acceptable error budget for a leakage current. While it is still possible to measure this effect from the ammeter reading, it cannot be distinguished from $I_{\mathrm{leak,cell}}$. For 8 GΩ inline resistance and a ramp time of 30 s the residual loading current is small enough after 44.1 s. $\mathrm{f_{3dB}}$=280 mHz (see tab. 2.2). A secondary reason to reduce the residual charging current is the associated time-dependent magnetic field (Hopf 2020).

The CMH also suppresses current ripple from the power supply. If the full specified AC ripple from the power supply of 50 mV is present on top of 200 kV, an additional gradient of $|\partial B_z/\partial z|$=3.7 aT m^{-1} causes a geometric false effect of $\mathrm{d_{af}} < 2 \times 10^{-33}$ ecm which is six orders of magnitude below the target sensitivity (Hopf 2020).

2.5 Sequence of operation during Ramsey measurement

A run is a single complete set of steps to prepare the UCN and the E and B field for a Ramsey sequence and count the UCN upon completion. The structure of a run is presented in fig 2.11.

[24] At the high voltages discussed the bulk conductivity of components is irrelevant next to surface effects. Surface cleanness is critical.

HV system capacitances

Component	C [pF]	R [Ω]
Power supply		50 k
Power supply cable	200	
Current measurement housing CMH) vacuum	33.3 (predicted) 43.1 ± 10 (measured)	
Current measurement housing (CMH) dielectric fluid[25]	71.3	
Copper conductor	63.2	8 G
EDM HV electrode	174	

Table 2.2: List of calculated values of capacitance for part of the HV supply system. The measured value is taken from (Hopf 2020).

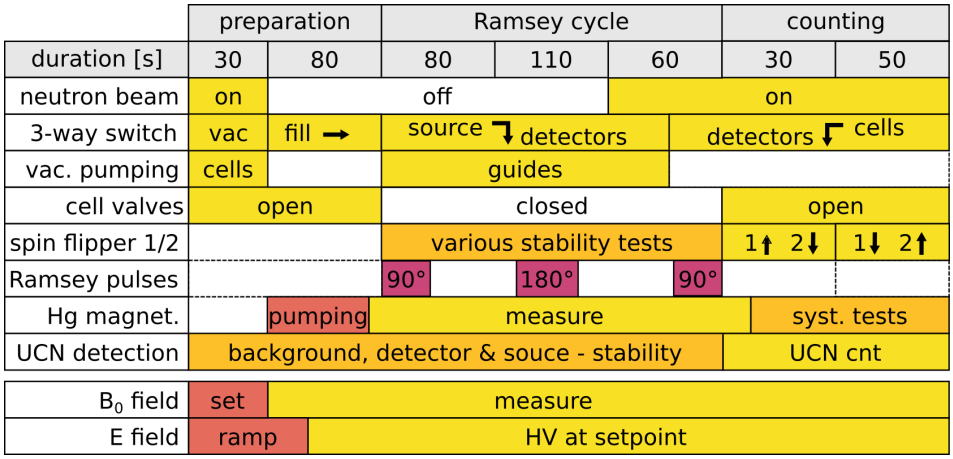

Figure 2.11: Planned sequence of operation during Ramsey measurement. The full length of a run is 440 s with a potential overlap. Shown are the activities of selected subsystems.

At the beginning of each cycle, the magnetic bias field B_0 and the polarity of the electric field E is set to the desired value. The B_0 field can be set to a new target value almost instantly, but then an equilibration (degaussing) of the magnetically shielded room (MSR) is necessary (I. Altarev et al. 2014). The high voltage takes about 45 s for a full reverse (see section 2.4). During this time the EDM cells are vacuum pumped. The buildup of UCN inside SuperSUN starts within the previous run. The source has a characteristic build-up time proportional to the storage time of the converter volume ($\sim$200 s) and is roughly exponential. Given that the total minimal runtime is about 400 s, a trade-off has to be made between source accumulation time and run repetition. A factor of two in source saturation is lost when timing the runs at the fastest possible turnaround. Owing to the exponential nature of the buildup, this is still the most optimal choice.

Once B_0 is set and the equilibration of shields are completed, the mercury in the mercury magnetometers can be pumped and UCN can be filled into the EDM cells. The three-way switch (TW) and the cell valves are placed in the 'filling' and 'open' positions respectively. After $\sim$40 s to 80 s the highest UCN density inside the cells is reached. At peak density the cell valves close and the Hg magnetometer switches to field measurement. The Ramsey sequence proper starts with the first transverse $90°/\frac{\pi}{2}$ pulse and ends with a second $90°/\frac{\pi}{2}$ pulse after time T $\sim$250 s. At $T/2$[26] a $180°/\pi$ pulse is applied, a technique also used in nuclear magnetic resonance where it is called 'spin echo' and improves the signal by compensating for dispersion due to magnetic field gradients. For UCN storage cells this was first demonstrated by (Afach et al. 2015). The core idea of this improvement can be explained by first introducing the dispersion mechanism: If a vertical magnetic gradient exists in a storage cell (as is the case for panEDM) UCN residing in higher regions of the cell precess proportional to a different field than UCN residing in lower regions of the cell. This causes dephasing of the ensemble polarization. If all UCN would sample the storage cell in a similar z-distribution, this effect would cancel out. Since UCN have different energies and those energies are comparable to the gravitational potential in the cell, higher energy UCN spend more time in higher regions of the cell than low energy UCN. Thus the combination of a vertical gradient in the magnetic field and UCN energy (due to gravity) causes striation of UCN spin precession frequencies. The dispersion of UCN spin ensemble grows linearly with time and reduces the usable signal as spins precess at different rates.

Spin echo can eliminate this effect by flipping spins halfway through the precession time. This means that spins with a faster precession rate get set back by twice the amount of their lead and spins with a slower precession rate get a boost twice the size of their phase lag. Ideally, at time T the effect is perfectly canceled and the full signal is recovered.[27]

Parallel to the Ramsey sequence, a small rate of residual UCN from the source is guided by the TW to the detectors. These UCN are used for detector stability and SF stability tests. The calculation of UCN ensemble polarization hinges on stable detection efficiencies of both spin states. For panEDM a relative detection efficiency drift between detectors on the level of $\sim 10^{-5}$ causes a systematic uncertainty of 1×10^{-27} ecm (Roehrer 2019).

[26] This is only one of multiple options.

[27] In the case of UCN, which experience energy-dependent loss at wall collisions, more insight into the evolving UCN population can be gained using spin echo. See again (Afach et al. 2015).

After the end of the Ramsey sequence, the cell valves are opened and UCN guided via the TW to the detectors for simultaneous spin detection. UCN for each cell are guided towards a top-down Y-shaped guide section. Both 'legs' have a spin flipper, a foil polarizer and a detector. SFs in legs 1 and 2 have complementary operations times, thus each combination of SF and foil polarizer transmit either spin-up or spin-down UCN. The counting time is split into two sections separated by reversing the SF operation. This allows to compensate for efficiency changes in foil and detector to be detected within each run.

If commissioning of the simultaneous spin detection proves system components to be stable over longer periods of time, this permutation of SF operation is shifted not to take place within each run, but as a permutation of consecutive runs instead. Omitting the change of SF operation also removes a short dead time. During switching, the UCN between SF and detector cannot be attributed properly and have to be discarded.

While UCN are counted, systematic tests of the Hg magnetometer can take place. This would for example include a variation of the Hg probe beam power or changes of frequency detuning to quantify the light shift.

If out-gassing in the cells is small and the vacuum maintains a pressure of $<1 \times 10^{-5}$ mbar with only short vacuum pumping, the beginning and end of two runs could overlap up to 30 s. In principle two ideal runs could overlap up to the point when emptying is directly followed be the next filling. This would improve the turnaround time but also reduce the source saturation as the accumulation of UCN gets shorter. With the currently estimated source behavior, one would attempt to shorten the runs such that the residual gas pressure in the experiment causes no relevant systematic effect or significant UCN depolarization.

Three main parameters are permutated between runs: magnetic field B ($\uparrow$ or $\downarrow$), electric field E ($+$ or $-$) and spin flipper (SF) configuration in both simultaneous spin detection systems (SF_1 on, SF_2 off or SF_1 off, SF_2 on). The permutations of these parameters should have no periodic pattern which could cause periodic external perturbations to create false effects correlated for example to the electric field - which would give rise to false EDMs. An a-periodic sequence is obtained with a simple recursive algorithm: One starts with a simple reversal ($+-$). The series is extended by inverted copies of the existing sequence.

$$(+-) \rightarrow (+--+) \rightarrow (+--+-++-) \rightarrow (+--+-++--++-+--+) \rightarrow \ldots \quad (2.8)$$

In addition to the described production runs, a small set of test runs with alterations is foreseen. To explore false effects $\propto E^2$, a set of runs with reduced electric field magnitude is intended. Quadratic effects would separate from linear effects due to their scaling. Runs with $E = 0$ would reveal if shifts and false effects are symmetric with respect to E.

2.6 Possible Analysis of a double cell configuration

Most next-generation experiments implement a vertical double chamber configuration which has been pioneered by EDM searches at the Leningrad Nuclear Physics Institute of the Academy of Sciences of the USSR (I. Altarev et al. 1981; Serebrov et al. 2016b). In this scheme, each chamber has two UCN counter for simultaneous spin detection, thus four independent measurements are obtained. As detailed in (Serebrov et al. 2015, eqn 3) from this set four quantities can be constructed: An EDM value, and three values

which encapsulate different systematics - namely electric field influences on the resonance condition, systematic neutron count rate effects and compensated variables which should be zero. This scheme does not explicitly use the mean neutron energy difference in both cells as a known quantity. This might be due to the high critical velocity ($6.8\,\mathrm{m\,s^{-1}}$) which allows use of a broad energy spectrum compared to the vertical separation of cells. Another reason might be the small effect of geometric phases ($<7.5\times10^{-28}\,\mathrm{ecm}$) compared to the statistical reach. For panEDM, in particular phase two, the soft-narrow energy distribution of UCN is similar to the energy shift from the vertical cell separation and the statistical reach matches the expected geometric phase effect. This section shows an analysis option that measures the geometric phase effect (as opposed to calculating its size from auxiliary observables) and creates a veto for magnetic contamination in the cells. As discussed in section 1.6, the expected false effect is described by (J. M. Pendlebury et al. 2004, egn. 20):

$$d_{af} = -\frac{J\hbar}{2}\left(\frac{\partial B_{0z}/\partial z}{B_{0z}^2}\right)\frac{v_{xy}^2}{c^2}\left[1-\frac{\omega_r^2}{\omega_0^2}\right]^{-1}, \tag{2.9}$$

where J=1/2 is the simple factor of the angular momentum, $\partial B_{0z}/\partial z$=1 nT m^{-1} [28] is the vertical gradient in the cell stack, $B_{0z}=1.3\,\mu\mathrm{T}$ the vertical holding field B_0, v_{xy} the mean velocity in the transverse plane, $|\omega_r| = v_x y/R$, $R=24\,\mathrm{cm}$ the cell radius and $|\omega_L|\approx\gamma B_{0z}$ the Larmor frequency. The center of both chambers is offset by 168.75 mm (see section 4.4) which corresponds to a mean energy shift of 17.2 neV. For a $E_{\mathrm{source,mean}}$=80 neV, this shifts the mean energies in the two cells to $E_{\mathrm{upper,I}}$=57 neV and $E_{\mathrm{lower,I}}$=74 neV. The expected spectrum from SuperSUN is very soft and narrow with a width of $\Delta E = 17\,\mathrm{neV}$. We can see that the geometric phase effect is directly proportional to the mean kinetic energy:

$$v_{xy} = \sqrt{\frac{2}{3}}\sqrt{\frac{2E_{\mathrm{kin}}}{m_n}} \rightarrow v_{xy}\propto\sqrt{E_{\mathrm{kin}}} \rightarrow d_{af}\sim E_{\mathrm{kin}}. \tag{2.10}$$

If we recall here, that the geometric phase effect is proportional to E and the ΔB (and changes sign with both quantities) we can design a measurement sequence where we apply an additional gradient of reverse sign. A linear fit through the geometric phase effect allows extrapolating the geometric phase effect to 0. A remaining offset would be a finite nEDM. This method also allows to integrate data from SuperSUN phase II into the experiment. The spectrum of phase II is expected to be harder - a reasonable estimate is 120 neV.[29] Thus we would yield two additional mean kinetic energies: $E_{\mathrm{upper,II}}=97\,\mathrm{neV}$ and $E_{\mathrm{lower,II}}=114\,\mathrm{neV}$. The expected statistical uncertainty are $\sigma_I = 3.2\times10^{-27}\,\mathrm{ecm}$ and $\sigma_{II}=5.9\times10^{-28}\,\mathrm{ecm}$. Fig 2.12 plots the concept with these parameter estimates. In addition, one could modulate the vertical gradient in a known fashion. If a local magnetization inside either chamber is present, it would enhance the geometric phase effect in this chamber. Through combinations of E and $\partial B_{0z}/\partial z$ unknown geometric phase sources could be evaluated from the data and act as a veto or a systematic check

[28] While we expect this value to decrease to 0.1-0.3 nT m^{-1} once all compensation coils in the MSR are used, this calculation is based on tested performance data. With respect to the analysis, it might also be of interest to artificially add a gradient of 1 nT m^{-1} scale.

[29] This is speculative at present, but motivated by (O. Zimmer and Golub 2015) and the assumptions on realistic loss coefficients, and magnetic trapping depths. Another argument would be: One might want to store UCN inside the production volume for some time to clean HFS and thus the spectrum would soften as well to - in principle - any value between the maximum trapping depth and phase I value.

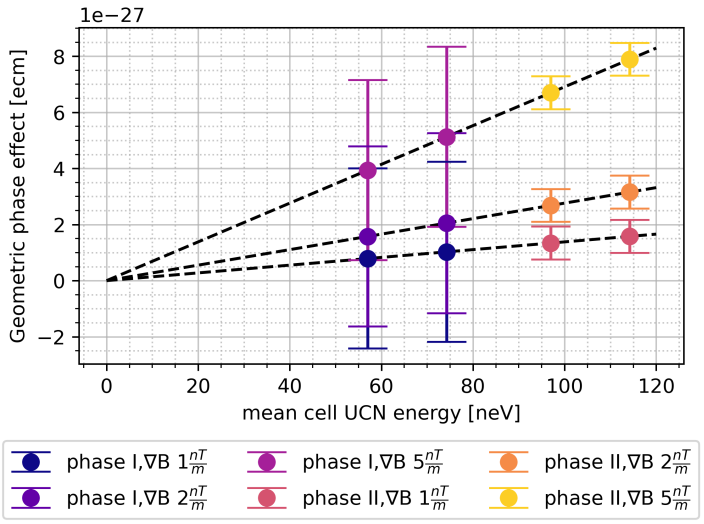

Figure 2.12: Suggested double chamber evaluation for panEDM. The different mean UCN energies result in different geometric phase contributions. Extrapolation from both chambers to 0 UCN energy would yield a finite EDM. Changes in the applied gradient would highlight local dipoles in either chamber. Both data from phase I and II could be analyzed in conjunction.

limiting the contribution of geometric phases effects in the experiment. In principle one can also build a second set of quartz rings and a secondary HV electrode with different vertical spacing. This would add two additional mean kinetic energies to the analysis. The main limitation of this method is the statistical sensitivity of UCN which is the tool to evaluate the geometric phase:

$$\sigma_{d_af|E=0} = \sigma_{d,n}\sqrt{\frac{E_{lower}^2 + E_{upper}^2}{(E_{lower} - E_{upper})^2}}, \tag{2.11}$$

where $\sigma_{d_af|E=0,phaseI}$=1.7 × 10^{-26} ecm and $\sigma_{d_af|E=0,phaseII}$=5.1 × 10^{-27} ecm. If applied the actual fit function would have to include two modifications: The term $\left[1-\omega_r^2/\omega_0^2\right]^{-1}$, was neglected in fig 2.12 and changes the shape of the fit function without impeding the analysis. The exact size of the geometric phase which scales linear with E and creates a false EDM signal is best modeled with Monte Carlo simulation.

3 SuperSUN UCN source

The number of available UCN is a major limitation of nEDM searches. As a result, experiments have to optimize their design for the source. The panEDM experiment was designed for the UCN source at the FRMII in Garching, which is a solid Deuterium source with a steady flux and a hard UCN spectrum. The SuperSUN at ILL in contrast is a ^{4}He accumulation (i.e.: discontinuous) source with a soft UCN spectrum. This chapter will discuss the difference these UCN sources and motivate the subsequent changes to the apparatus. Many components in the apparatus, while needing only minor adjustment received more structural changes to incorporate improvements made since the conception of the original apparatus. These changes include the High Voltage Supply System and the central electrodes which have been partially discussed in the previous chapter.

3.1 Classical sources

Production of UCN is a challenging endeavor. Nuclear fission, the most prominent mechanism utilized in high flux sources, generates neutrons with an approximate Maxwell spectrum centered around the temperature of the moderator. The available density of UCN in a moderated source is given by (Golub et al. 1991, p.44)

$$\rho_{UCN} = \frac{2}{3}\frac{\phi_0}{\alpha}\left(\frac{V}{k_B T}\right)^{\frac{3}{2}}; \quad \alpha = \sqrt{\frac{2k_B T}{m}}, \tag{3.1}$$

where ρ_{UCN} is the UCN density, ϕ_0 is the total thermal flux, k_B is the Boltzmann constant, T is the moderator temperature, m is the neutron mass and V is the trapping potential. This means, that for a room temperature moderator and a high Fermi Potential (V_{Be}=252 neV) only a fraction of 1×10^{-12} of the neutron flux is available as UCN. For a cold moderator such as liquid deuterium (T=25 K) the fraction improves to 4×10^{-11} While this is a very small fraction, with reactors reaching flux densities of $\phi_{\mathrm{FRM2@UCN\ source}}$=$8 \times 10^{14}\,\mathrm{cm^{-2}\,s^{-1}}$ and $\phi_{\mathrm{ILL\ source}}$=$1.5 \times 10^{15}\,\mathrm{cm^{-2}\,s^{-1}}$, UCN experiments are conceivable. In practice, the extraction of UCN into experimental setups as proven a technical challenge associated with losses on the scale of 1×10^{-3}

One of the most reliable UCN sources since multiple decades is the "Steyerl Turbine" (Steyerl et al. 1986) which vertically extracts cold neutrons from a cold source through a 13 m Ni-coated guide. A large turbine of 690 Ni coated copper blades rotating away from the beam with $25\,\mathrm{m\,s^{-1}}$ transforms the spectrum into the UCN regime which yields a flux of up to $2.6 \times 10^4\,\mathrm{cm^{-2}\,s^{-1}}$ and demonstrated density in storage experiments of $36\,\mathrm{cm^{-3}}$. Despite numerous attempts to build stronger UCN sources, this is to date a competitive UCN source with high reliability. However, next-generation EDM searches need higher UCN densities, which practically can only be reached with super-thermal sources.

3.2 Super-thermal UCN sources

An option to improve above the yield of thermal UCN sources is to use conversion instead of moderation - a dissipative mechanism to overcome the limit of Liouville's theorem. (Golub and J. Pendlebury 1975). At its core, one utilizes a low-temperature medium to remove a large amount of the neutron's energy in a single interaction (see fig. 3.2). The particle is not in thermal equilibrium and once down-scattered sits in a state where only a few up-scattering states are available. The simplest example of this mechanism is a two-level system for which we can demonstrate the principle of detailed balance (Turchin 1965, p. 110):

$$\sigma(E_{UCN} \to E^*) = \frac{E_{UCN} + \Delta E}{E_{UCN}} \cdot e^{\frac{-\Delta E}{k_B T}} \cdot \sigma(E^* \to E_{UCN}), \tag{3.2}$$

where E_{UCN} is the energy of the UCN, E^* is the exited state, ΔE the energy gap of the two-level system, k_B the Boltzmann constant, T the temperature of the converter.

For a converter temperature $k_B T \ll \Delta E$, the up-scattering cross-section $\sigma(E_{UCN} \to E^*)$ is strongly suppressed relative to the down-scattering $\sigma(E^* \to E_{UCN})$. Thus only neutrons with energy very close to the converting transition can be used to generate UCN. The strong asymmetry of relation 3.2 shifts the equilibrium UCN density to values orders of magnitude above moderation sources. Among various candidate materials only ^{4}He and sD_2 have been developed into UCN production sources.

3.2.1 Solid deuterium - FRMII UCN source

The UCN source at the FRMII (Andreas Frei 2021) is designed as a solid hydrogen premoderator (sH_2) and a solid Deuterium crystal (sD_2) as the superthermal converter. The source will be placed inside a tangential beam tube (SR6) in a region of high thermal neutron flux of $1 \times 10^{15}\,\mathrm{cm^{-2}\,s^{-1}}$. The conversion of neutron to UCN happens in a thin solid layer at the end of a cold finger. UCN generated in the crystal are emitted into a beam tube and are transported to the experiments (see fig. 3.1).

Since the first concepts for a sD_2 UCN source (Trinks et al. 2000) several conceptual improvements were discovered and tested. A premoderator significantly increases the density of UCN available for conversion (A. Frei et al. 2007). The maximum UCN production rate in the solid deuterium is yielded for an effective neutron temperature of 40 K (A. Frei et al. 2010). In the proposed sH_2 premoderator, this process is mostly facilitated by para to ortho spin-flip transitions, where the neutron losses 14.7 meV (Kai et al. 2004).

In the sD_2, it is vital to have all the deuterium in the ortho-state [1] The inelastic up-scattering cross-section for UCN in para-deuterium is about 150 × higher than in ortho-deuterium (Liu et al. 2000) which is a critical factor in the UCN lifetime inside sD_2 (Morris et al. 2002). Despite the large production rate of UCN in contrast to ^{4}He, the accumulation in bulk sD_2 is not feasible due to the short UCN lifetime, which is about 70 ms. The sD_2 crystal is provided as a thin surface layer where UCN can travel into the extraction guide. (see 3.1). A thickness of a few up to several mm is reported optimal for various sources (Lauer 2010). Larger thicknesses are less effective, as UCN moderated deep inside the crystal get up-scattered before they can exit the crystal. Due

[1] Which is the ground state in sD_2 following Bose statistics. sH_2 follow Fermi statistics where para-H_2 is the ground state.

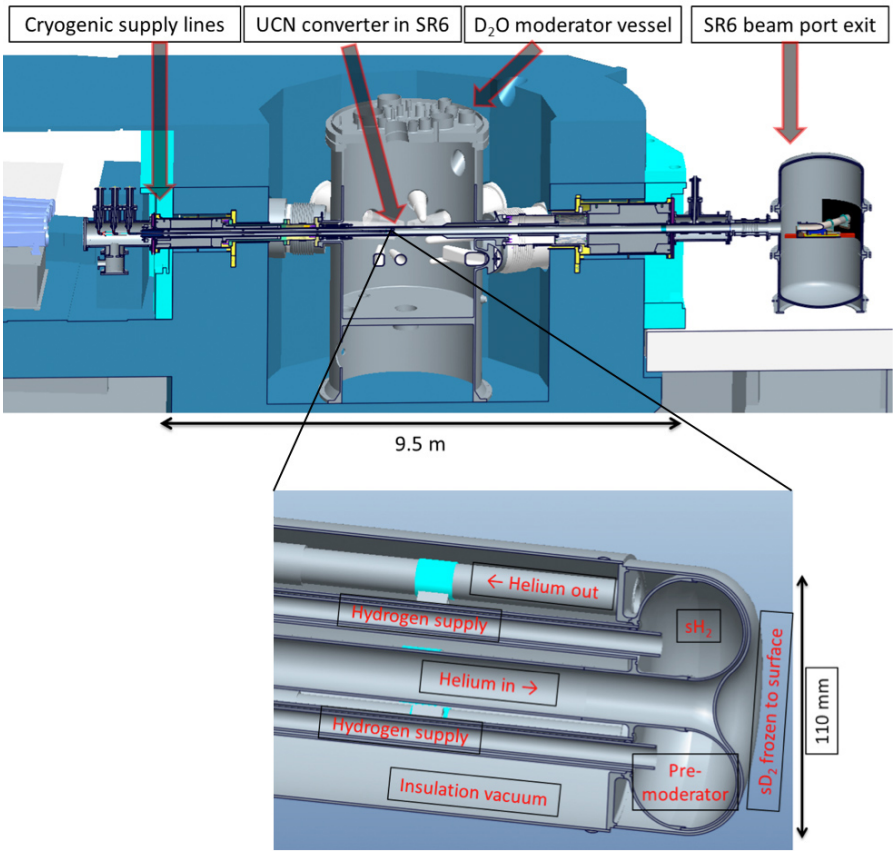

Figure 3.1: Rendering of the future UCN source at the FRMII, Garching. A tangential beamline is used to supply the cryogenics from one side and extract the UCN to the other. A solid Hydrogen (sH_2) premoderator acts as a cold source for sD_2 frozen on the UCN producing surface. Taken from (Andreas Frei 2021)

to the low thermal conductivity of sD_2 the outer layers of the crystal heat up as a result of γ-heating, which further increases up-scattering. Thermal cycling can reduce internal defects in the crystal, which shortens the effective time UCN spend inside the crystal.

When the UCN exit the crystal, they experience acceleration from the material optical potential of (99 ± 7) neV (I. Altarev et al. 2008a), which makes the spectrum from sD_2 sources intrinsically harder if used in the horizontal plane of the source.[2] This acceleration can also be seen in the velocity distribution for the UCN source at the TRIGA Mainz (I. Altarev et al. 2008b). The spectrum of sD_2 sources is strongly dependent on the detailed operation parameters such as freezing procedure, thermal cycling, crystal temperature, crystal thickness. At FRMII The projected flux at the beam tube is $6 \times 10^7\,\mathrm{s}^{-1}$ (100 neV to 230 neV)(Andreas Frei 2021).

There are a few conceptual advantages of sD_2 sources over ^{4}He. sD_2 exhibits a larger UCN production rate than ^{4}He but has a finite neutron capture cross-section. sD_2 can be operated at 5 K to 10 K, where the thermal up-scattering is small. Below 5 K temperature-independent absorption dominates which places the optimal operation temperature within range of standard closed-loop helium cooler. sD_2 converters can thus be

[2] ^{4}He has a neutron optical potential of 18.5 neV.

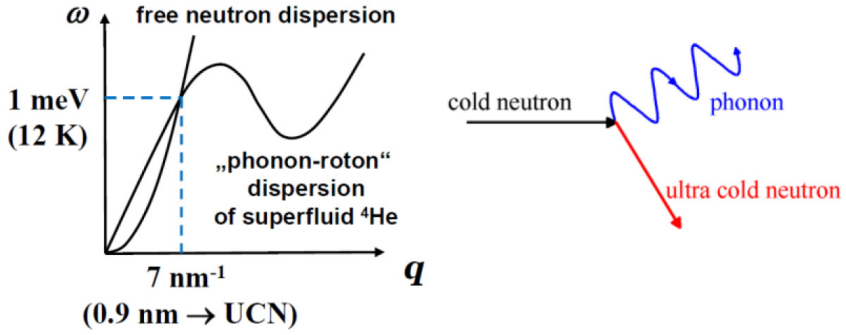

Figure 3.2: Dispersion relation (angular frequency vs wavenumber) for free neutrons and ^{4}He. At temperatures <1 K neutrons from a cold beam can lose almost their entire momentum creating single/few phonons inside a ^{4}He volume. Taken from (Degenkolb 2020)

built to accept strong external thermal loads relative to ^{4}He sources (Lauer 2010).

The sD_2 is placed within the high flux zone of the reactor, which means that UCN have to travel a long distance to the experimental sites. The high radiation load in the vicinity of the reactor fuel element also restricts some types of UCN guides. The source concept, while having large potential UCN yields is technically challenging.

3.2.2 SuperSUN - superthermal He sources

The second strong converter material candidate[3] for a superthermal process is ^{4}He (Golub and J. Pendlebury 1977). In the case of ^{4}He the $\Delta E = 1.03$ meV which corresponds to 12.0 K and is far above converter temperatures of 0.6 K to 1.6 K.^{4}He is the only known isotope with a neutron absorption cross-section of exactly 0 [4], leaves wall losses of UCN as the limitation for UCN accumulation [5]. In practice spurious contamination with ^{3}He on the scale of ^{3}He/ ^{4}He $=10^{-10}$ can dominate the storage time due to the large neutron capture cross-section of ^{3}He (Piegsa et al. 2014). In addition, the up-scattering is only sufficiently low for a converter temperature below 0.8 K and scales with $\tau_{up}^{-1} \propto T^7/100s$ (Golub 1979). Temperatures this low can only be achieved with technically challenging cooling techniques (like ^{3}He - ^{4}He - dilution fridge) which can remove only small amounts of heat. This makes a super thermal ^{4}He source impractical where large γheat loads are expected. Thus a ^{4}He converter is not feasible inside or close to the reactor. SuperSUN is placed at the end of a bent cold beam guide with a peak wavelength close to the single phonon excitation[6]. The curvature of the guide reduces γbackground from the reactor.

[3] For completeness, other superthermal candidates material are: Solid α- oxygen where spin waves or magnons could provide a mechanism for UCN production (Liu and Young 2004). Measurements indicated a production rate of about $1/5^{\text{th}}$ of sD_2 (Gutsmiedl et al. 2011). This disadvantage could be compensated with with the predicted large mean free path of UCN inside α-oxygen of 3.8 m. (Atchison et al. 2011) tested tetradeuteromethane (C_2H_4) and found ($3/4^{\text{th}}$ the production rate of s^2H).

[4] For energies far above the discussed range,a ^{5}He can be created from neutron capture of ^{4}He.

[5] And, of course, the neutron lifetime

[6] The basic idea is to match ΔE from eqn. 3.2 and the neutron wavelength. In reality, one has to consider the impact of low multi-phonon processes and the available wavelength distribution in the cold beam.

Preparing the beam to consist of useful cold UCN reduces the heat and radiation load from neutrons which cannot to contribute to the conversion process anyway.

The extraction of UCN from the conversion volume into an external experiment was associated with large losses in the past[7]. The SUN-1 apparatus (O. Zimmer et al. 2007) at the ILL employed a windowless vertical extraction system which reduced losses from extraction. Gravity would "mostly" contain the ^{4}He in the conversion volume. Since the ^{4}He is superfluid at the operating temperatures of SUN-1, a small section of the vertical extraction system is kept at a higher temperature to evaporate the ^{4}He climbing up. The ^{4}He converter is kept at saturation vapor pressure which is small enough to allow direct connection to the extraction guide vacuum. A mechanical flap valve is used to seal the converter during accumulation and opened to allow the UCN to expand into the extraction volume. The details of the flap valve and extraction design are critical to minimize the heat load into the converter (Oliver Zimmer et al. 2011; Piegsa et al. 2014) which would otherwise limit the turnaround time of the source.

In the absence of absorption and with small up-scattering, wall losses dominate the UCN lifetime in the converter. SUN-1 used[8] electropolished stainless steel for the converter volume ($V_{F,steel}$=(184 ± 4) neV) and could accumulate up to 55 UCN/cm^3. In SUN-2 (Piegsa et al. 2014) supermirrors with Be-coating ($V_{F,Be}$=250 neV) were used which improved the density to 120 UCN/cm^3. Later fomblin grease on top of Be with Ge/diamond-like carbon (DLC) resulted in a density above 160 UCN/cm^3. Adjustments to the fomblin thickness improved the converter to a density of 220 UCN/cm^3 which makes it an exceptional UCN source. In the context of this thesis, the effect of accumulation time on the UCN spectrum is of interest. UCN losses are energy-dependent wherein low energy UCN have a longer lifetime inside the converter. This is illustrated in a measurement from SUN-2 shown in fig 3.3, where the time of flight (TOF) spectrum of UCN from SUN-2 are shown for a 30 s extraction delay compared to the spectrum from PF2/TES.

SuperSUN is a new ^{4}He UCN source currently being built at the ILL. It improves upon SUN-2 in various ways. The converter volume is enlarged to 12 L (from 5 L in SUN-2)). SUN-1 and SUN-2 were supplied with a 0.89 nm beam extracted via Bragg reflection from a crystal, which is subject to large losses. The SuperSUN in contrast is placed at the end of a beam guide and supplied with a broader spectrum enabling the use of multi-phonon processes to generate UCN which adds 50% UCN production.

In phase II the SuperSUN trap is upgraded using a magnetic multipole reflector (O. Zimmer and Golub 2015). This improves the depth of the trap and removes losses from wall interaction for soft UCN. In addition, the converter will only trap[9] so-called low field seeking (LFS) UCN. Thus in phase II, SuperSUN will provide already polarized UCN to an experiment. This is particularly beneficial for panEDM which needs polarized UCN.

[7] A clever solution to this problem in the scope of nEDM searches is the concept of the SNS nEDM Oak Ridge National Laboratory (Golub and Lamoreaux 1993; Lamoreaux and Golub 2009), where the experiment is inside the converter volume. See sec. 1.7

[8] Again the trap potential is reduced by the neutron optical potential of 18.5 neV

[9] There are high field seeking (HFS) UCN also trapped, but not extracted

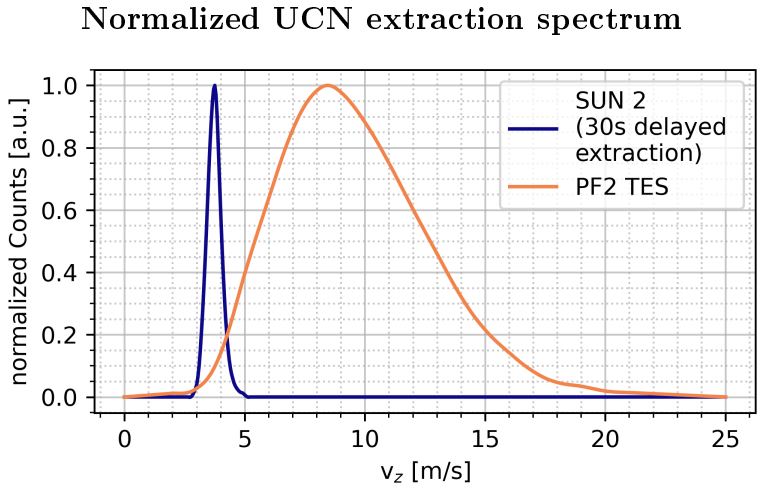

Figure 3.3: Neutron velocity distribution extracted via TOF from SUN-2 (O. Zimmer 2017) and the PF2/TES (Jenke 2021). Based on these results, SuperSUN is expected to deliver UCN between 71 neV=3.69 m s^{-1} and 88 neV=4.10 m s^{-1} with a peak value of 80 neV=3.91 m s^{-1} (Wurm et al. 2019).

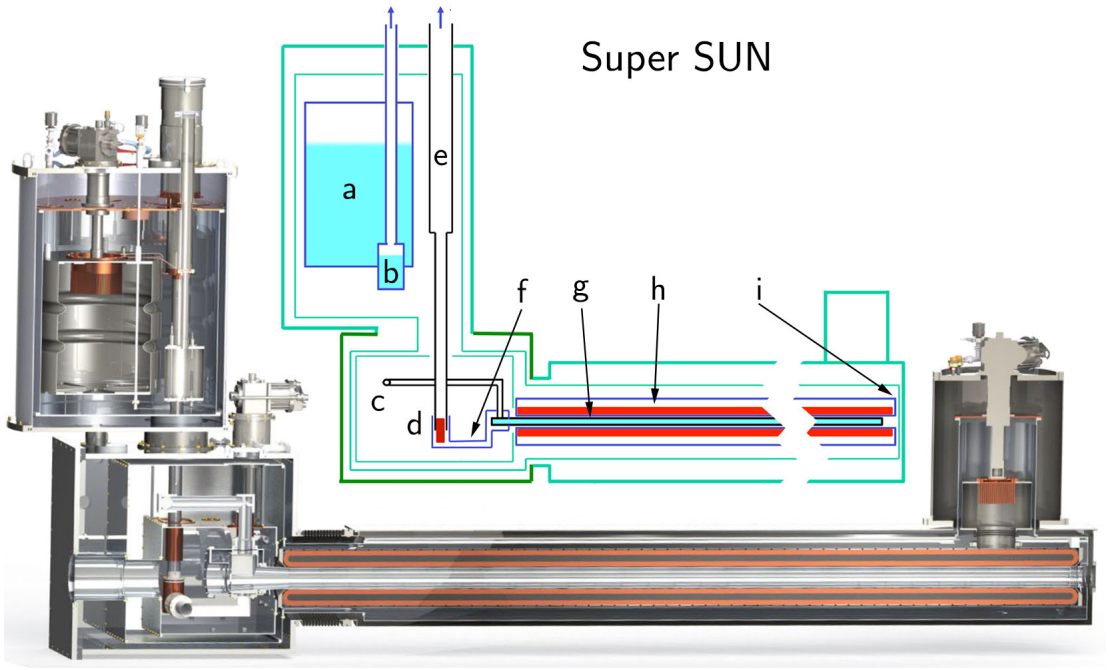

Figure 3.4: Rendering of SuperSUN. (a) 100 L ^{4}He bath, (b) '1K pot', (c) UCN extraction, (d) ^{3}He/^{4}He heat exchanger, (e) ^{3}He, (f) Superfluid ^{4}He column, (g) converter volume, (h) magnetic monopole, (i) cold beam entrance window. Taken from (Oliver Zimmer 2016; Energy 2021)

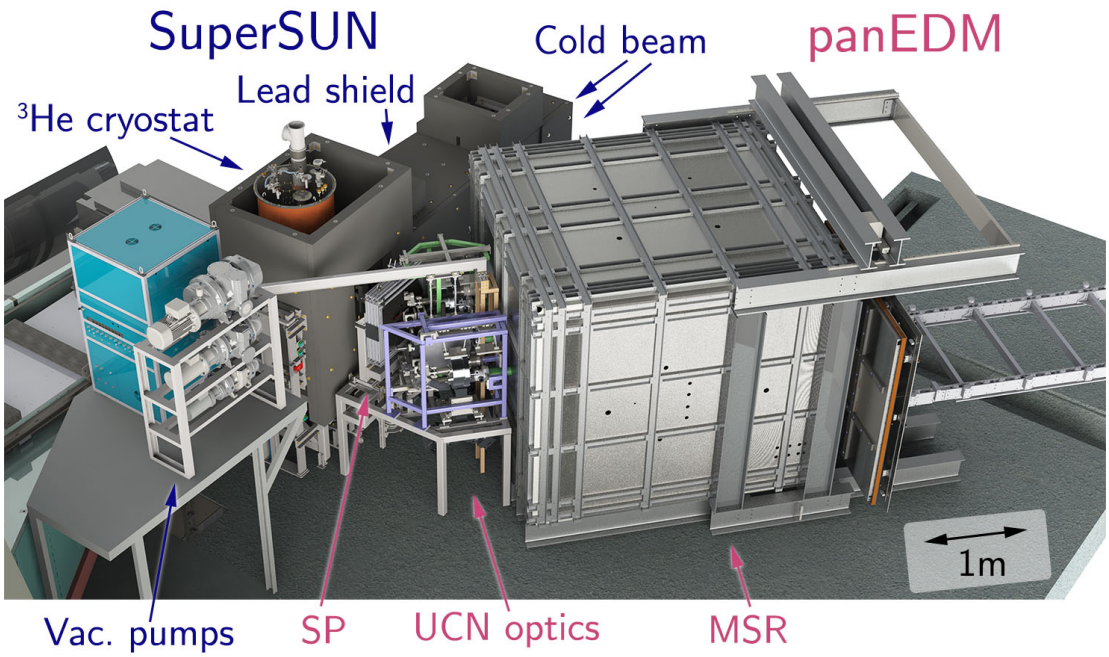

Figure 3.5: Rendering of SuperSUN and panEDM at the experimental site in ILL22, at ILL. The cold neutron beam and the converter are at an angle of roughly 45° to the panEDM. Here the compressed space between the lead shield of SuperSUN and the panEDM MSR is clearly visible where all UCN optics must be placed. All electronics and measurement control resides towards the viewer directly adjacent to the MSR in a clean room - not shown in this rendering for clarity.

4 UCN transport related upgrades

4.1 UCN optics

panEDM was conceptualized for a new beam position at the FRM2. Thus, many design choices are owed to the future sD_2 source and the layout of the guide hall east (UYM). For the setup at the SuperSUN position, these design choices were no longer optimal.

The FRM2 UCN source will operate in a continuous fashion inside the beam tube SR6. The UCNs have to travel more than 28 m (Zechlau 2016) to the panEDM. At the ILL the UCN are accumulated in the converter volume and then freely expand into the mostly empty guide system of ∼5 m length. Ignoring backflow of UCN at the destination and the source, two large mechanisms govern the amount of UCN which end up at the destination: transport loss and dilution. Transport loss is roughly the likelihood of a UCN propagating through a guide section and disappear through up-scattering, gaps or nuclear absorption. This is a steady-state quantity, where an equilibrium density inside the system is assumed. Apparently, this effect is dominant for FRM2, where the source provides UCN continuously. We coin the second effect 'dilution'. If we consider a fixed number of UCN at the moment the extraction valve inside SuperSUN opens, these UCN will eventually evenly distribute inside the available guide system. If we model the UCN as a sparse gas, the whole guide and cell volume will eventually reach an equal density. UCN which reside in the guide are effectively lost to the EDM measurement.

To illustrate the high standard of transport efficiency needed, one can simply define a relative transmission per meter and yield the UCN delivered to panEDM from:

$$T_{\text{total}} = (T_{m^{-1}})^{\frac{L}{1m}} \tag{4.1}$$

where $T_{m^{-1}}$ is the transmission per m including gaps and misalignment, $L = 28\,\text{m}$ and T_{total} the total transmission. $T_{m^{-1}}$ of $0.98\,\text{m}^{-1}$,$0.95\,\text{m}^{-1}$,$0.9\,\text{m}^{-1}$ correspond to a total transmission of 57%, 24% and 5.2%. A set of loss-less 1 m guides with 2 mm gaps per meter would yield 95% transmission. For context: UCN guides with transmission from $0.9\,\text{m}^{-1}$ to $0.98\,\text{m}^{-1}$ are now standard for ideal mounting conditions.

The relevance of the guide diameter can be modeled with diffusion theory (Golub et al. 1991, p. 93) on UCN transport in a long circular guide. Here we use the parameters obtained through a test of 15 m of NiMo (85/15 wt%) 500 nm guides built for panEDM and tested in (Zechlau 2016): $\tau_{\text{Guide}} = 37\,\text{s}$, $\tau_{\text{Guide System}} = (34.9 \pm 0.6)\,\text{s}$, $\eta = (2.7 \pm 0.3) \times 10^{-4}$,$\overline{v}$=4.88 m s^{-1} [1]. For the mean velocity, the total transmission was $(34.9 \pm 0.2)\,\%$ and $(53.1 \pm 0.3)\,\%$ including diffusely scattered UCN. From this rather complete set of measurements we can also infer, that the chance of a specular reflection in the guide was 97%. We can now extend the measured parameters to calculate the behaviour of guides made in the same process for an inner diameter of 80 mm (planed ID for panEDM@FRM2 downstream of the splitter) and 50 mm (ID of all guides of panEDM at ILL). Fig 4.1 shows for this simple transport model the losses expected (top plot, solid lines). From

[1] Extracted from $v_{\max}$ for $V_F = 221\,\text{neV}$, and $\overline{v} = 3/4 v_{max}$

this plot we confirm, that for long-distance transport, larger guide diameter is extremely beneficial.

There are - as always in UCN transport - large caveats to analytic models: Transport losses are dominated by slits and gaps for longer transports. The energy-dependent loss is softening the spectrum as the UCN propagate. While the losses from wall collisions thus also decrease, the effect of gaps and slits stays constant. The diffusion model assumes equal flux both forward and backward, which would only be the case for predominantly diffuse scattering. However, we know that effective transport in the discussed UCN guides is overwhelmingly specular. This is partially compensated by a quality factor, which is only properly motivated for straight guide sections. The diffusion model treats the guide system as an equivalent length straight guide and is therefore only a rough estimate to design impacts. The actual guide layout consists of bends and corners affect the transport on the order of unity. This can only be reasonably discussed using a Monte Carlo Simulation.

While test measurements exist for components, it is also difficult to infer from the transmission of components to a system. Usually only total count rates are easily obtainable. For an analytic combination of components, the UCN spectrum and the angular distribution for input and output would have to be known. The poor statistics of sources makes position-, angle- and energy-resolved measurements unfeasible. This is the reason why exhaustive characterization measurements of UCN components (and sources for that matter) are rare within the community.

4.1.1 UCN optics for panEDM

The UCN transport is significantly shorter at the ILL. Both panEDM and SuperSUN are placed adjacent to ILL22. SuperSUN uses an extraction system modeled after SUN-2 which includes the use of ID 50 mm extraction guides. This dimension offers smaller dilution loss compared to ID 80 mm which was prepared for panEDM atFRM2. SuperSUN will accumulate UCN while panEDM is running. At a single instance, the extraction valve is opened and UCN dilute into panEDM, which lies in direct contrast to the operation for panEDM at FRM2.

Fig 4.1 models the effect of dilution in the bottom plot. The transport losses are calculated from (Golub et al. 1991, Eqn. 4.57 and 4.78) adapting experimentally acquired parameters from the previous section. The model was then extended to DIA 80 mm and 50 mm. The highlighted length (@IlL) of 4.5 m is the distance from SuperSUN to the EDM cells which the UCN have to traverse. This is slightly shorter for the upper branch, thus the more conservative length of the lower branch is used here. The dilution is calculated from the ratio of

$$\frac{V_{\mathrm{SuperSUN}}}{V_{\mathrm{SuperSUN}} + 2 \cdot V_{\mathrm{EDM,\ cell}} + V_{\mathrm{guide}}(L)} \tag{4.2}$$

using the values from table 4.1. The highlighted length in the dilution plot (fig. 4.1, @ILL: 7.05 m) includes the total volume of both guide branches added together. This does not include the quide volume of the simultaneous spin detection system, as it will be closed during filling. Given that the guide volume with DIA 50 mm guide is small with respect to SuperSUN and the EDM cells, one can also consider reducing the cell volume. This reduces the absolute number of UCN available for the Ramsey cycle but improves other aspects of the experiment. Smaller EDM cells are subject to smaller B field gradients and

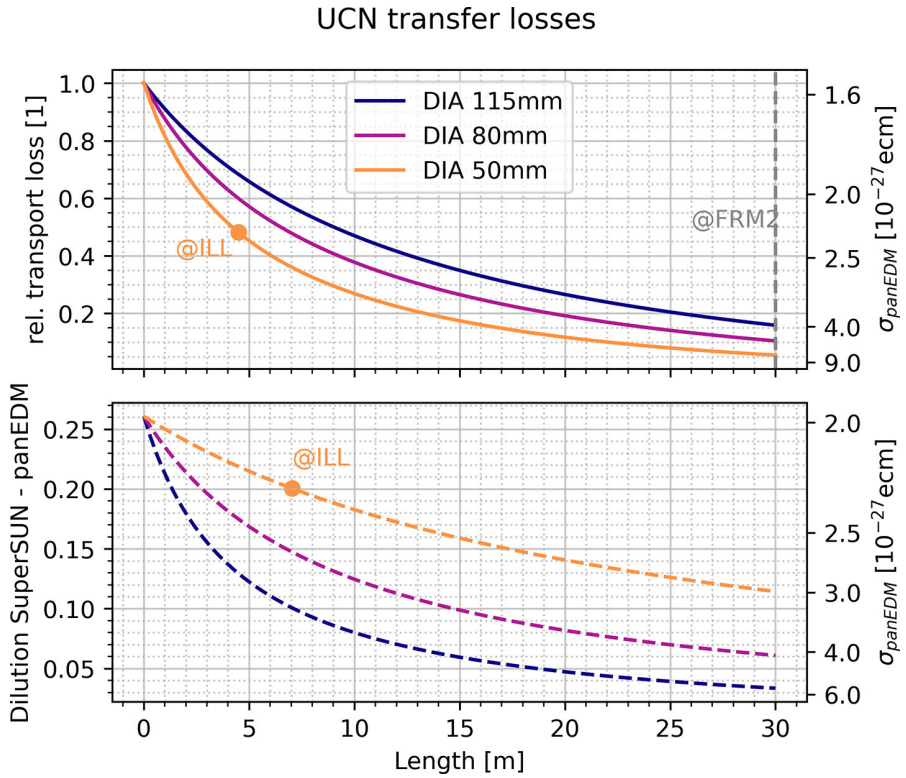

Figure 4.1: Calculated impact of UCN guides through (upper) transport loss (modeled as UCN diffusion with specular modifier) and (lower) dilution (modeled from volume ratios). For the panEDM at ILL two points are highlighted. For a filling procedure from SuperSUN into the apparatus, the UCN have to traverse 4.5 m of guide for the lower, longer path, but the total guide volume (7.05 m) has to be filled to calculate the dilution. The dilution starts at a base value derived from the volume ratio of SuperSUN and the EDM cells.

therefore geometric phase effects. Fig. 4.1 shows the case for cells made from standard 300 mm wafers instead of 480 mm diameter electrodes. See also subsection (4.4). The effect of dilution is less pronounced for the emptying process from the EDM cells into the simultaneous spin detection system. The detectors can be approximated as large absorbers which eliminates backflow and thus no diluted equilibrium is established. The emptying time is then defined by geometry and diffuse reflections and the efficiency is the sum of all other loss mechanisms compared to the detectors.

One can consider further reducing the loss from dilution in the experiment by utilizing the transient nature of the transport. Assuming a specular transport of UCN, and owing to the tight energy distribution ($E_{\text{peak}} = 80\,\text{neV}$, FWHM $\approx 17\,\text{neV}$)(Wurm et al. 2019), a large subset of UCN will arrive in a fairly defined time before diffuse scattering and backflow are relevant. Thus, it could be possible to close the EDM loading valve at a specific time and gain upon the equilibrium diluted density for the whole system volume. A similar technique was demonstrated with a pulsed UCN source (Karch et al. 2014). While the extraction time at SuperSUN is much longer than the length of a UCN burst converted from a TRIGA pulse, it still might be feasible.

panEDM UCN component volumes

Description	V [l]	Wall options
SuperSUN	12	CYTOP
source switch (SW), Solenoid polarizer	0.85	Steel, Cu
Guide manifold	2.95	NiMo or Cu
three-way switch (TW) (each)	0.17	Cu
Cell guides (each)	4.55	NiMO
Loading valve(each)	0.31	DLC on Al, Cu
EDM cells (each)	17.01	DLC, CYTOP,dPE
GY guide long	5.09	NiMo,NiP, Cu coating
GY guide short	4.43	NiMo,NiP, Cu coating
Foil polarizer - detector	0.52	Steel, ...
Wafer EDM cells (each)	5.79	DLC,Diamond,...
panEDM (w/o SuperSUN)	47.9	
panEDM (with SuperSUN)	59.9	

Table 4.1: List of panEDM components volumes given in liters with wall options. A hypothetical EDM cell made from wafers is also provided. The total volumes in the filling configurations are given in the bottom rows. Cu: copper, NiMo: nickel molybdenum, DLC: diamond-like carbon, Al: aluminum,dPE: deuterated polyethylene, NiP: nickel phosphorus

4.1.2 Transport timing estimate

It is difficult to calculate or simulate the transport time from the source volume into the cells. In contrast to the source at FRM2, the SuperSUN offers a diffuse beam profile with a narrow energy range. Fig 4.2 shows as Monte Carlo simulation for the amount of UCN traversing 4.5 m or guide assuming instantaneous release at t=0 and no backflow from the outlet. From this simulation a loading time of 15 s was assumed for panEDM. These results informed the timing of the EDM sequence (see sec. 2.5). It is worth noting, that about 10% of the UCN path are made from hand-polished copper [2]. While NiMo coated glass was demonstrated to have reliably high levels of specular transport, this is less clear for parts without a standardized production quality for surface finish. Longer sections of diffuse guides slow down and eventually 'trap' UCN. A hypothetical purely diffuse guide has a geometric mean free path of twice the radius. Thus between two wall collisions UCN travel $\sim R$. Each re-emission has the same probability of moving the UCN forward or backward. This is essentially a simple 1-dimensional random walk of stepsize R. Combined with the finite lifetime of UCN within the guide, relatively short sections of diffuse guides can make transport unfeasible.

4.2 Cell coating development

The development of suitable wall coating for UCN storage in nEDM experiments has been a central topic in experiment design. We have motivated this in sec. 1.3 and eqn. 1.5 and in sec.2.1.1 with eqn. 2.3.

[2] Such as the SP, the SW and the TWs

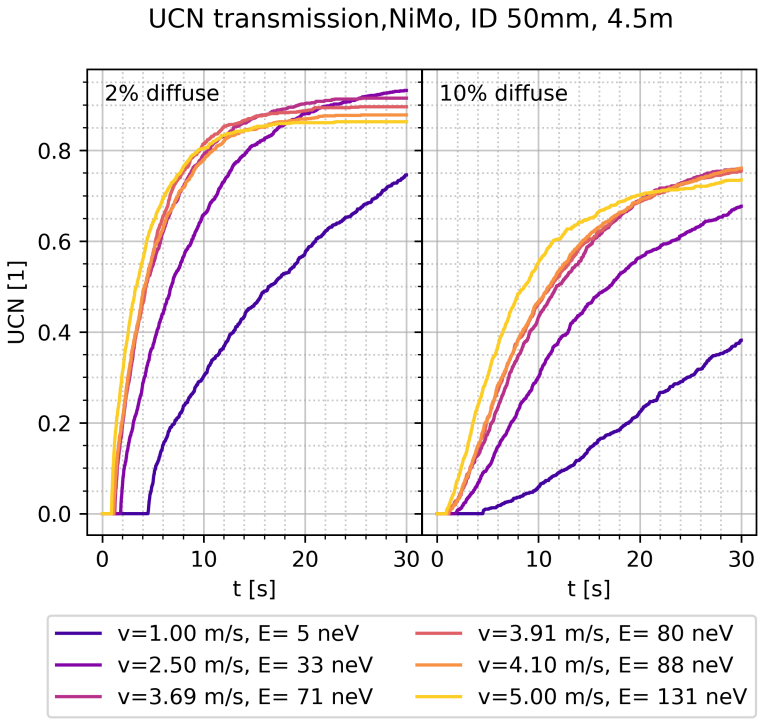

Figure 4.2: Simulated transport of UCN in a straight guide section using a diffusion model. The plot show the fraction of UCN which arrive at the exit depending on the UCN kinetic energy and the fraction of diffuse reflection of the guide. panEDM NiMo guides have $<3\%$ diffuse reflection.

(Serebrov et al. 2015) used BeO and ^{58}Ni oxide and molybdenum on the side walls where electric isolation is needed and Be on aluminum substrates for the flat sections (top and bottom). Be has extremely high Fermi potential and is therefore a natural choice. BeO, while maintaining a high Fermi potential has an electrical conductivity of $\sim 1 \times 10^{12}\,\Omega\,\mathrm{m}$ (for reference: fused quartz: 10^{16}-$1\times10^{18}\,\Omega\,\mathrm{m}$ (GmbH 2021), PS $\sim1.5\times10^{13}\,\Omega\,\mathrm{m}$ (Qi et al. 2011), PE $1 \times 10^{14}\,\Omega\,\mathrm{m}$ (Chanda 2017)) Actual coatings tend to suffer from surface effects which causes large leakage currents in BeO. Another disadvantage is the health risks associated with Beryllium. Extended handling of Be and Be-compounds can lead to a sensitization immune response and later to Berylliosis, a chronic lung disease.

The apparatus used for the measurement of the current best limit (RAL/Sussex, later at PSI) uses blank quartz on the sides and DLC coated electrodes top and bottom (Baker et al. 2014). The next-generation nEDM experiment at PSI intends to use electrodes of aluminum coated with diamond-like carbon and insulator rings from polystyrene coated with deuterated polystyrene (Ayres et al. 2021). panEDM plans the use of quartz ring coated with deuterated polyethylene (dPE) (see 4.4), which might be replaced with CYTOP. For the flat cell sections, i. e. the ground (GND) electrode substrate and the high voltage (HV) electrode substrate DLC on aluminum and diamond on quartz are considered. The investigation of the last two options shall be discussed here.

Diamond-like carbon (DLC) has been investigated as a UCN storage material more than 20 years ago (Grinten et al. 1999) and has been extensively studied (Atchison et al. 2006; Fierlinger 2005). DLC coatings are amorphous carbon layers whose Fermi potential depends on the density of carbon, ranging from 156 neV up to 305 neV for diamond. A useful quantity is the sp^2/sp^3 ratio. A perfect diamond is only comprised of sp^3 bounds or tetrahedral structure. Graphite consists of hexagonal layers, thus only of sp^2 orbitals. Pure carbon has a low loss coefficient per bounce which has never been achieved in experiments. Hydrogen contamination of DLC, both in bulk and on the surface, significantly increased the loss coefficient. (see table 4.2) Early on, this problem was addressed by replacing hydrogen with deuterium in the deposition process wherever possible. While both isotopes of hydrogen are chemically similar, its neutron absorption cross-section is vastly smaller in deuterium, which improves the loss coefficient.

The electrode substrates have a diameter of 479.8 mm which is larger than the majority of DLC coating suppliers can coat. For the production of electrodes of panEDM we investigated the patented DLC coating Adm$^{\mathrm{TM}}$010 (*Adm 010 Amorphous Diamond* 2019) from Diamond Hard Surfaces Ltd [3]. Adm 010 uses Plasma-enhanced chemical vapor deposition (PA-CVD) in ultra-high vacuum at a low process temperature of 100 °C. DLC CVDs generally operate at much higher temperatures which can cause two types of problems: The substrate deforms under thermal stress during the coating process. This would be an issue for the rather thin aluminum electrode substrates used at panEDM - which have to maintain shape on a $\sim 10\,\mu\mathrm{m}$ level. Secondly, the coating is hard compared to most substrates and has a very low coefficient of thermal expansion. During the process, when both substrate and coating are heated up, no tension exists at the material boundary. Once the piece cools down to room temperature a strong shear force appears which is stronger for larger substrates and higher temperature gradients between coating and ambient temperature. In extreme cases, this limits the size of parts that can be coated continuously at once as coatings would peel off or break. This problem was also

[3] Diamond Hard Surfaces Ltd,Caswell Science and Technology Park, Towcester,Northamptonshire,NN12 8EQ,United Kingdom

encountered at past attempts to use DLC coated parts in cryogenic environments in UCN converter. A technical solution is the use of adhesion layers between the substrate and the coating. This has its own drawbacks, in particular the fact that most adhesion materials are strong neutron absorber[4] or magnetic. The low temperature of the Adm 010 process avoids this issue. The process was adapted to reduce the chance of hydrogen incorporation in the DLC. The plasma in the process is created from a liquid precursor which contains hydrocarbons. This precursor was replaced with a deuterated, otherwise identical, precursor to create 'deuterated' DLC. A picture of a d-DLC coated high voltage electrode substrate can be found in fig. 4.8.

As an alternative poly-crystalline diamond coatings were investigated. Crystalline diamond would offer even higher Fermi potentials and potentially smaller hydrogen/deuterium incorporation. The Fraunhofer Institute for Surface Engineering and Thin Films IST [5] can deposit a few tens of nanometers to micrometer layers of poly-crystalline diamond on suitable carbide, alloys, and ceramics using hotwire- chemical vapor deposition (CVD). This process operates at temperatures of 800° to 1000° which excludes aluminum as a substrate. This process also suffers from the issues related to the mismatch of thermal expansion coefficients of DLC, but even stronger. A solution would be using quartz electrodes where the quartz itself or the diamond coating would be doped to provide enough electric conductivity to act as an electrode ($<1 \times 10^9\,\Omega\,\mathrm{m}$).

For both coatings samples were prepared for neutron reflectometry. Measurements were conducted by (Pontus 2021) at the ILL. Figure 4.3 shows the results of the reflected beam intensity versus the irradiated neutron wavelength. Neutron reflectometry is a surface-sensitive, non-destructive tool probing to the nuclear structure of the sample. Both plots show the measured values (orange crosses) and the best fitting model of a flat homogeneous material with a particular Fermi potential. The horizontal position of first drop from an intensity of unity is proportional to the Fermi potential. The fringes towards higher momentum transfer (in unit of inverse Angstrom) are a result of interference at the coating/substrate boundary and allow the extraction of the coating thickness. These fringes are only resolved for very flat samples[6]. From the depicted best model fits, the Fermi potentials were extracted $V_{\mathrm{Fermi,d\text{-}DLC}} = (205 \pm 10)\,\mathrm{neV}$ and $V_{\mathrm{Diamond}} = (290 \pm 10)\,\mathrm{neV}$. The value for d-DLC is lower than reported for similar coating by other manufacturers and lower than expected for the quoted $\mathrm{sp}^3 > 0.99$ content. This implies a lower volume density of the coating i.e. a more amorphous structure of the coating. The value of the coating is high enough to be used for panEDM. The poly-crystalline diamond value of $_{\mathrm{Diamond}} = (290 \pm 10)\,\mathrm{neV}$ is close to the theoretical value of $_{\mathrm{Diamond,\,theo}} = 305\,\mathrm{neV}$. Future measurements of the loss coefficient and for diamond are planned.

A visual representation of the impact of selected wall coatings is provided in fig. 4.4. The loss per bounce for a kinetic energy range around the expected peak value for SuperSUN (80 neV) is plotted. In lieu of experimental values for the currently developed diamond, the theoretical value for diamond is given. It should be noted, that no loss coefficient this low has been demonstrated for any carbon based coating.

[4] An issue for very thin coatings or local coating defects

[5] Fraunhofer-Institut für Schicht- und Oberflächentechnik IST,Bienroder Weg 54 e,38108 Braunschweig

[6] The sample with the diamond coating was slightly bulging in the support at the experiment, hence the fringes are not resolved.

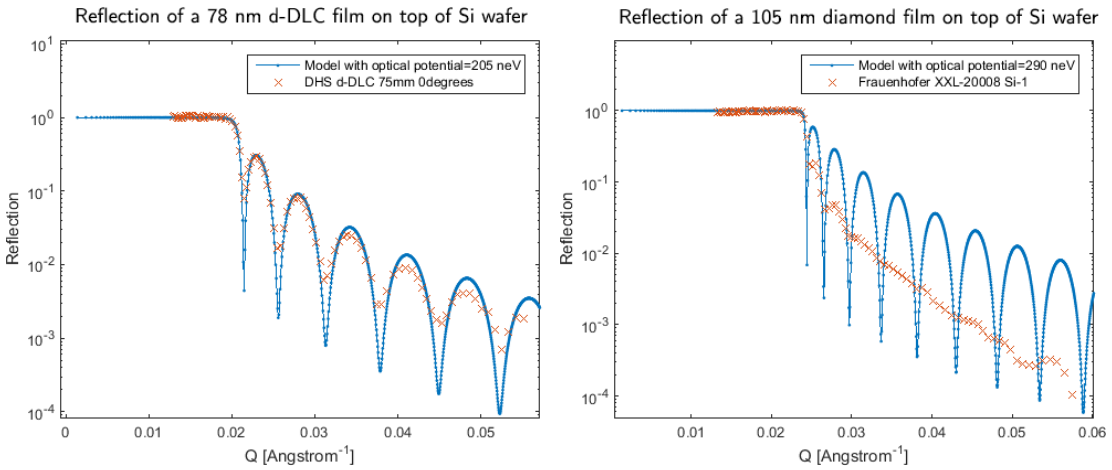

Figure 4.3: Neutron reflectometer measurements of a silicon wafer coated with deuterated diamond-like carbon (d-DLC) from Diamond Hard Surfaces (left) and for silicon wafer coated with poly-crystalline diamond from Frauenhofer IST. Shown is the intensity of the reflected beam as a function of the neuron wavelength. The position of the initial intensity drop is proportional to the Fermi potential of the material. The periodic modulations thereafter are interference effects from the thickness of the probe layer. The modulation is suppressed for the diamond data due to slight bulging of the tested sample. From this data Fermi potentials are extracted of $V_{\text{Fermi,d-DLC}} = (205 \pm 10)$ neV and $V_{\text{Diamond}} = (290 \pm 10)$ neV. Visualization taken from (Pontus 2021)

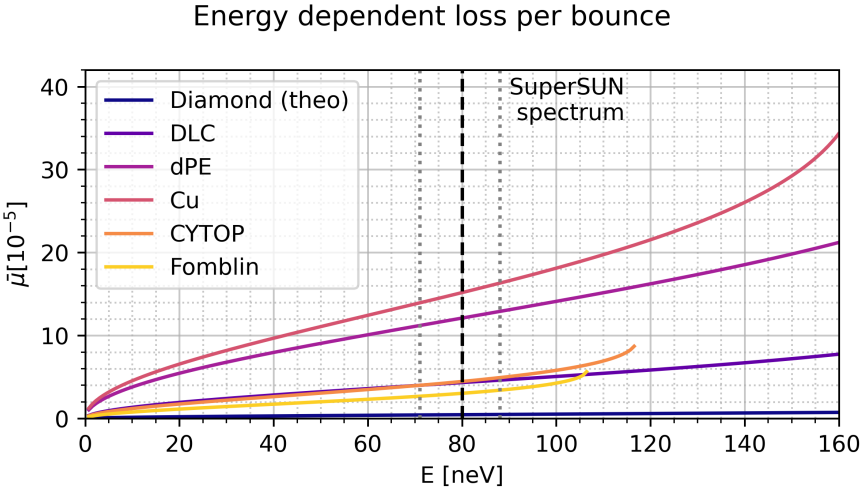

Figure 4.4: Mean loss per bounce for a storage volume with randomized UCN trajectories for selected wall materials from table 4.2. The expected mean energy from SuperSUN (dashed) and the $1\,\sigma$ width (dotted) are drawn for reference.

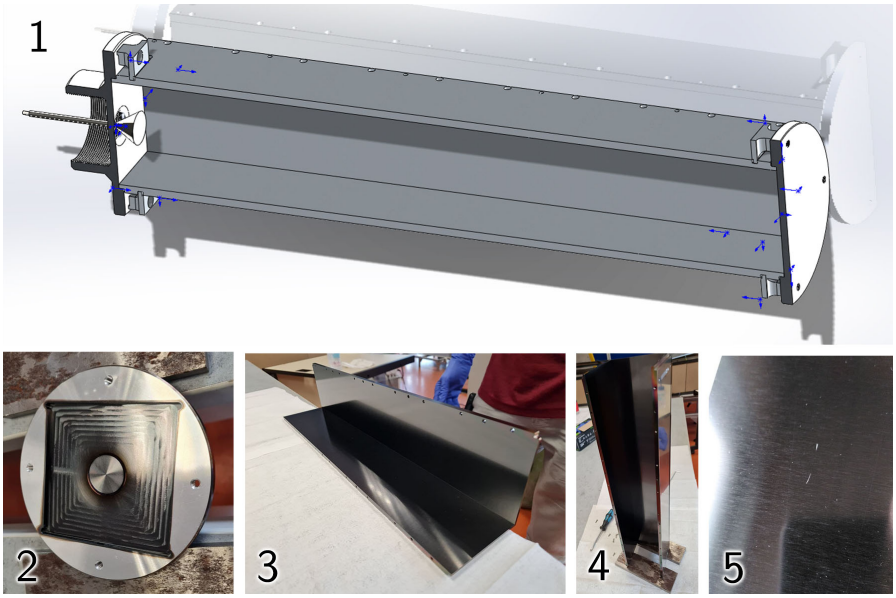

Figure 4.5: Rendered view and photos of the aluminum DHS d-DLC coated test vessel for SUN-2. 1:Cut through the $80 \times 80 \times 450$ mm vessel. The movable plug is visible on the left. 2: Picture of the coated left endcap. 3 & 4: Assembly of two (three) coated side wall elements. 5: Defects on the surface.

4.2.1 DHS d-DLC bottle measurement

The d-DLC from Diamond Hard Surfaces was tested during the ILL cycle no. 191 (Sept 2021) at SUN-2. To this end, a dedicated storage vessel from aluminum compliant with the existing experimental infrastructure at SUN-2 was built. The test vessel follows previous designs used at SUN-2. It is a rectangular aluminum vessel with inner dimensions of $80 \times 80 \times 450$ mm. The volume is filled and emptied via a stainless steel plug on one side. The side walls have unbroken, sharp edges. When the side walls are screwed together, these edges press onto coated surfaces, thus minimizing potential gaps. The endcaps push similarly against the side walls. An overview of the vessel is given in fig. 4.5.

Here we present the analysis of a storage time measurement at room temperature. We model the storage time similar to eqn. 1.6:

$$\frac{1}{\tau_{\text{obs}}} = \frac{1}{\tau_\beta} + \frac{1}{\tau_{\text{wall}}} + \frac{1}{\tau_{\text{slits}}} + \frac{1}{\tau_{\text{abs}}}, \tag{4.3}$$

where τ_{obs} is the observed storage time, $\tau_\beta = (880.2 \pm 1.0)$ s is the neuron lifetime, τ_{wall} the lifetime due to up-scattering at the d-DLC coated walls, τ_{slits} and τ_{abs} the loss contributions from slits and uncoated areas respectively.

τ_{obs} is extracted from a set of measurements where UCN are filled into the test volume and counted after different storage times. For UCN with a narrow energy distribution (such as SUN-2) the number of extracted UCN is described by a single exponential decay function with

$$N(t) = N_0 e^{t/\tau_{\text{obs}}}, \tag{4.4}$$

where N_0 is the hypothetical inital population of UCN. Fig. 4.6 shows the measurements with the DHS d-DLC coating with the extracted storage time $\tau_{\text{obs}} = (242.6 \pm 2.3)$ s and

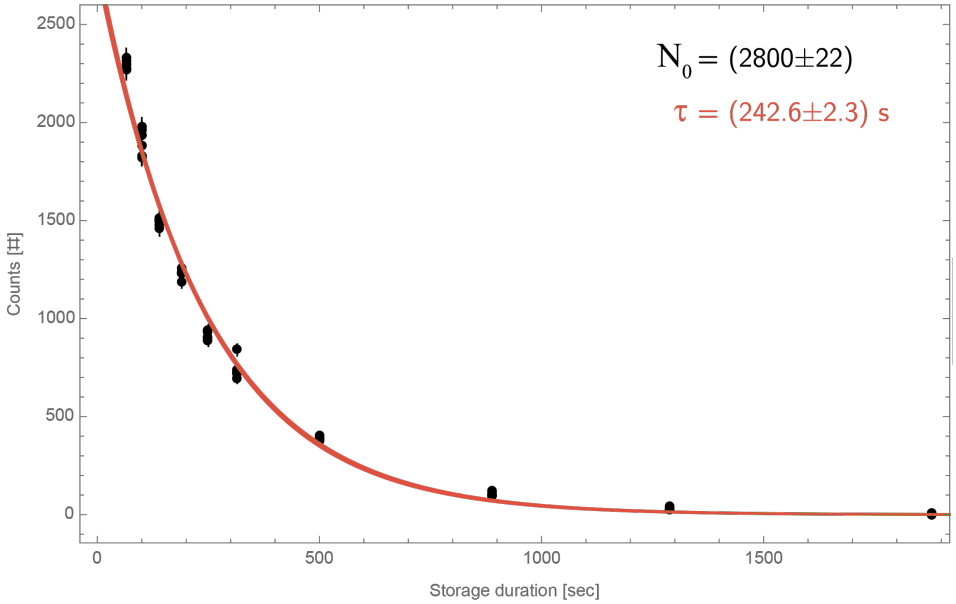

Figure 4.6: Storage time measurement of a rectangular aluminum vessel coated with DHS d-DLC at room temperature. The measures storage time constant is $\tau_{\text{obs}} = (242.6 \pm 2.3)\,\text{s}$. Taken from (Filter 2021).

an initial filling of $N_0 = (2800 \pm 22)$ UCN per run. This corresponds to an extracted density of $0.97\,\text{cm}^{-3}$.

τ_{wall} is modeled by

$$\tau_{\text{wall}} = \frac{\lambda}{\bar{v} \cdot \bar{\mu}_{\text{d-DLC}}(E_{\text{kin}})}, \tag{4.5}$$

where λ=73.45 mm is the mean free path of UCN inside the storage volume[7], $\bar{v}$ is the mean velocity and $\bar{\mu}_{\text{d-DLC}}(E_{\text{kin}})$ is the probability of a loss per bounce. Effectively this models the wall collision rate weighted with the chance of up-scattering upon wall contact. From the mean kinetic energy of SUN-2 $E_{\text{kin}} = 80\,\text{neV}$ we yield the mean total velocity $\bar{v} = 3.91\,\text{m}\,\text{s}^{-1}$. To compare the material to other surface materials we add in eqn. 1.5,

$$\tau_{\text{wall}} = \frac{\lambda}{\bar{v} \cdot \bar{\mu}_{\text{d-DLC}}(E_{\text{kin}})} = \frac{\lambda}{\bar{v} \cdot 2\eta \left(\frac{V}{E_{kin}} \sin^{-1} \sqrt{\frac{E_{kin}}{V}} - \sqrt{\frac{V}{E_{kin}} - 1} \right)} \tag{4.6}$$

such that we can extract the energy independent loss coefficient η. Here we use the measured value of the Fermi potential from section 4.2: $V_{\text{Fermi, d-DLC}} = (205 \pm 10)\,\text{neV}$.

τ_{slits} is given by the loss contributions from the gabs between the six sides[8] of the rectangular vessel and the circular gab[9] around the plug:

$$\tau_{\text{slit}} = \frac{\lambda}{\bar{v}} \cdot \frac{A_{\text{vessel}}}{\sum_i l_i \cdot d_i}, \tag{4.7}$$

[7] This value is estimated from a ideal cuboid with the vessel's dimensions and perfect diffuse/Lambertian surface emission. The effect of gravity has been omitted.

[8] $(8 \times 80\text{mm} + 4 \times 450\text{mm})$

[9] Circumference at contact: 66.2 mm.

where A_{vessel} is the inner surface area of the storage volume, l_i the length of a slit section and d_i the width of a slit section. Here we assume that the wall collision rate is uniform across the surface and all UCN incident on a slit are lost. We model the losses as a ratio of gaps over the total area. Similarly we can account for two imperfections in the coating with τ_{abs}

$$\tau_{\text{abs}} = \frac{\lambda}{\bar{v}} \cdot \frac{A_{\text{vessel}}}{\sum_i A_i}, \tag{4.8}$$

where A_i corresponds to the area of uncoated sections. For the tested vessel two small scratch marks[10] exposing he underlying aluminum where found and the d-DLC around the plug[11] is substantially thinner. We can now rearrange eqn. 4.3, such that

$$\bar{\mu}_{\text{d-DLC}} = \frac{\lambda}{\bar{v}} \left(\frac{1}{\tau_{\text{obs}}} - \frac{1}{\tau_\beta} - \frac{1}{\tau_{\text{slits}}} - \frac{1}{\tau_{\text{abs}}} \right). \tag{4.9}$$

If we assume a loss-less wall $\tau_{\text{wall}} \Rightarrow \infty$, we can calculate an equivalent uncoated surface of the same total storage time, which is $A_{\text{equiv.}} = (8.78 \pm 0.12)\,\text{mm}^2$, or $5.6 \cdot 10^{-5}$ of the total area. This means, that the area around the plug with a thinner coating thickness ($\sim$164 mm^2 behaves rather like functional coating than an uncoated aluminum. $A_{\text{equiv.}}$ can also be expressed as mean thickness along the construction edges of the vessel. In this case the mean slit width has to be smaller than (3.60$\pm$0.05) µm. Owing to the mechanical nature of the experiment we cannot determine the actual slit width reliably on this level. At present we can also not determine the detailed thickness of the coating at the rounded fillet at the plug. Thus we only subtract the contribution of the visible scratch defects for τ_{abs} and attribute the remaining losses to τ_{wall}. We then yield $\bar{\mu}_{\text{d-DLC}} = (4.33 \pm 0.07) \cdot 10^{-5}$ which corresponds to an $\eta_{\text{d-DLC}} = (4.52 \pm 0.17) \cdot 10^{-5}$. The spectrum of the used UCN in the used configuration could also consist of faster UCN. If the mean kinetic energy would increase to $E_{\text{kin}} = 120\,\text{neV}$, the results would shift to $\bar{\mu}_{\text{d-DLC,E=120 neV}} = (3.30 \pm 0.06) \cdot 10^{-5}$ and $\eta_{\text{d-DLC„E=120 neV}} = (2.55 \pm 0.11) \cdot 10^{-5}$. These values compare well to other experimentally observed loss coefficients. We can apply the measured values for Fermi potential and wall loss coefficients for d-DLC and dPE and simulate the storage time constant in the panEDM cells. Accounting for β-decay and wall losses, one would expect a mean lifetime of $\tau_{\text{simul, EDM cell}} = (278 \pm 5)\,\text{s}$. This means that up to 6.9 mm^2 inside the storage cell can be surrendered[12] to gaps and slits to maintain a storage time of better than 250 s.

4.3 Depolarization effects

The EDM signal is obtained from the ratio of UCN in both spin states (see eqn. 1.21). If undesired mechanisms change the spin alignment, signal is lost. In general such mechanisms are random and reduce the contrast. These depolarization effects are commonly parameterized by a decay time constant equal to the time it takes for the polarization to decline to 1/e of its initial value called T_2.

The terminology is lifted from nuclear magnetic resonance (NMR) where it describes the transverse relaxation time[13]. T_2 includes effects from magnetic gradients as well as

[10] each 10 mm × 0.1 mm
[11] $A_i = 164\,\text{mm}^2$
[12] or 13.7 ppm of 0.503 m^2 inner surface area.
[13] Technically what is called T_2 here is actually $T_2^* = T_2 + \text{gradients}$

depolarizing wall collisions. T_2 relaxation counters the sensitivity gained from longer free precession times. A large factor affecting T_2 is the relaxation due to gradients for the low-pressure regime (Cates et al. 1988):

$$\frac{1}{T_2} \approx \frac{4R^2\gamma^2}{175D}\left(\left|\frac{\partial B_x}{\partial x}\right|^2 + \left|\frac{\partial B_y}{\partial y}\right|^2 + \left|\frac{\partial B_z}{\partial z}\right|^2\right). \tag{4.10}$$

Modeling a diffusion constant D for the ballistic motion of UCN, gradients of better than $10\,\mathrm{nT\,m^{-1}}$ (Stuiber 2018) are necessary to achieve T_2 >250 s. This topic has been extensively covered in previous work of the panEDM collaboration (Stuiber 2018; I. Altarev et al. 2015; Lins 2016) and has no impact on panEDM cell design itself.

A second effect reducing the polarization contrast stems from UCN spin flips at wall collisions. The wall material has to be free of ferromagnetic contamination and should have no small-scale magnetic structure. Wall depolarization probability has been studied for various materials (Fierlinger 2005; Bondar et al. 2017) and is typically on the scale of $\beta \sim 10^{-6}$–10^{-5} (see table 4.2). While Nickel is ferromagnetic, a mixture of Nickel Molybdenum (NiMo 85/15 wt%) is paramagnetic and has small wall depolarization ($\beta_{\mathrm{HFS}} = (0.35 \pm 0.07) \times 10^{-5}$,$\beta_{\mathrm{HFS}} = (0.45 \pm 0.11) \times 10^{-5}$), which makes it an excellent choice for guides. However, the coating is only non-magnetic for an intact coating of defined fixture. Tests in the past have shown the strong performance of a NiMo coating, but also the risks posed by damage to the coating (Zechlau 2016). Mechanical damage, for example at the edges of guides, can release ferromagnetic dust into the experiment. High Voltage discharges deposit a large amount of energy locally on the coating. This could change the metallurgy and create a permanent dipole which would only be detected after the measurement cycle and veto a large set of data. At this time, the selection of wall materials is only weakly dependent on differences in material depolarization or happen to align with selection criteria from wall loss.

4.4 panEDM cell design

The geometry of the EDM cells has been kept from the FRM2 design: Two cells of ID 480 mm and height 93.25 mm yielding a volume of 17 L. The central electrode was made taller (in z-direction) to 75.5 mm to gain space for Hg and/or Cs magnetometer cells inside. The center of the two cells is now 168.75 mm apart. A rendering of the inner cell is shown in fig 4.7. The rings separating the HV electrode from the top and bottom ground electrodes are made from quartz which was cut from two large blocks. The quartz rings can be coated with dPE to which end a coating oven was developed in the group (Ruhstorfer 2014; Windmayer 2016; Brenner et al. 2015). The oven heats and rotates the rings while a solution is placed inside creating a thin film on the surface. Once the coated rings have cooled down, the dPE has stronger adhesion to the walls than Fomblin (grease and oil) and is less likely to diffuse into other parts of the vacuum system. dPE is suitable for the large eletric fields applied. Recently a new candiate material, CYTOP, with similar properties was tested at SUN-2 (Hingerl 2019). CYTOP is an alternative to dPE, as it may be suited for the cryogenic environment of the SuperSUN production volume.

Coating	V_F[neV]	$\eta = \frac{W}{V_F}$ [$\times 10^{-5}$]	β[$\times 10^{-5}$]
C(sp3)	$_{(\text{theo})}305^{o}$ 290^{r} 286 ± 32^{b}	$_{(\text{theo})}0.015^{o}$	
BeO	$_{(\text{theo})}260^{o}$	$_{(\text{theo})}0.016^{o}$	3.75 ± 0.33^{c}
^{65}Cu	$_{(\text{theo})}244^{a}$	$_{(\text{theo})}7.0^{a}$	
NiMo 85/15	221.4^{e}	$_{(\text{theo})}12.0^{\ o}$ 27 ± 3^{m} 20 ± 4^{n}	$0.38 \pm 0.06n$
dPE	214.8 ± 5.2^{f} 214 ± 10^{g}	13 ± 3^{f}	
NiP	213 ± 5.2^{l}	13 ± 10^{l}	(316L SS)$0.33^{+0.2}_{-0.56}$ ^{d} (Al)$0.36^{+0.2}_{-0.56}$ ^{d}
DLC	$205 \pm 10^{r,5}$ $249 \pm 14^{b,1}$ $271 \pm 13^{h,4}$	$4.52 \pm 0.17^{r,5}$ 0.015^{o} 35.2 ± 0.6^{i}	0.067 ± 0.021^{i}
SS 316 L	188^{e}	$_{(\text{theo})}9.3^{o}$	
C (sp2)	$_{(\text{theo})}\ 175^{a}$	$_{(\text{theo})}\ 0.015^{o}$	$0.59 - 1.06 \pm 0.1^{c}$
Cu	$_{(\text{theo})}165^{o}$ 188 ± 29^{b}	$_{(\text{theo})}13.6^{o}$ 15 ± 3^{n}	$0.73 \pm 0.14^{c,2}$ $1.70 \pm 0.10^{c,3}$ $0.67^{+0.5}_{-0.56}$ ^{d} 0.12 ± 0.03^{n}
C (amporh)	$_{(\text{theo})}156$	$_{(\text{theo})}0.015^{o}$ 9.45 ± 0.45^{k}	
CYTOP^{q}	$_{(\text{theo})}117^{p}$	3 ± 1^{p}	
Fomblin	106.5^{o}	(oil,theo)1.8^{o} (oil)2.35 ± 0.1^{j} (grease)1.85 ± 0.1^{j}	0.61 ± 0.13^{c}

Table 4.2: List of selected UCN surface materials of interest for panEDM. Given are measurements and theoretical predictions for the Fermi potential V_F, the loss coefficient η and the depolarization parameter β (sometimes referred to as α). The discrepancy between observed and predicted η and β is part of ongoing research. ^{a} (Golub et al. 1991),^{b} (Atchison et al. 2007),^{c} (Serebrov et al. 2003), ^{d} (Tang et al. 2016),^{e} (Daum et al. 2014), ^{f} (Brenner et al. 2015), ^{g}(Bodek et al. 2008), ^{h} (Atchison et al. 2006),^{i}(Fierlinger 2005),^{j}(Pokotilovski 2005),^{k} (Arzumanov et al. 2003),^{l} (Pattie et al. 2017), ^{m}(Zechlau 2016), ^{n}(Bondar et al. 2017), ^{o}(Steyerl 2020), ^{p}(Hingerl 2019),^{q}(CYTOP 2021),^{r} This work. 1: sp^3-content: (0.45 $\pm$ 0.05), 2: Cu 99.9% from "Good Fellow", 3: industrial Cu,4: sp^3-content: 0.67., 5: from Diamond Hard Surfaces Ltd. sp^3-content $>$0.99, mass density 3.1 - 3.2 g cm^{-3}, theory: 273 neV

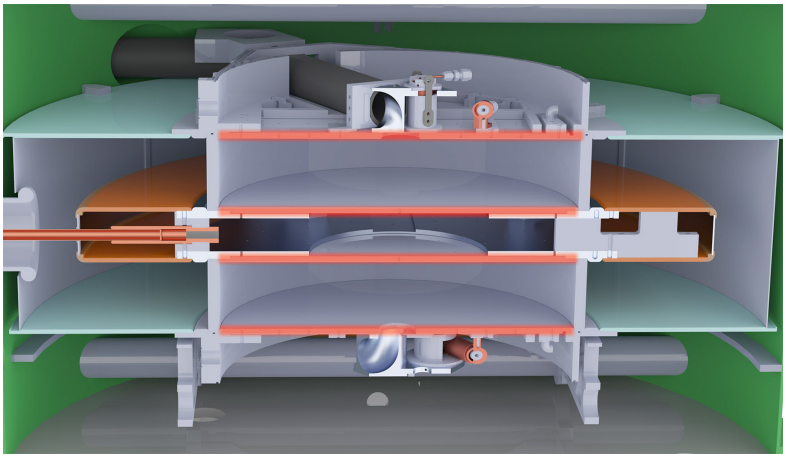

Figure 4.7: Render of the EDM cells in panEDM. The position of the exchangeable substrates is highlighted in red.

4.4.1 Ground electrodes

The original ground electrodes were machined from a single large Al block and polished on the side facing the cell. In the center an 80 mm diameter opening was prepared below the loading valve mechanism. Once the guide system transport diameter was changed from 80 mm to 50 mm, the existing GND electrodes could no longer be used as built. The problem was addressed by splitting the GND electrode into two parts: An outer, structural part and an exchangeable substrate. The substrate is a disk with DIA 479.8 mm and a thickness of 8 mm. When combined, both parts complete to the outer dimensions of the original electrode. The substrate can now be remade with a suitable central open of DIA 50 mm. This approach has additional benefits. A set of substrates can be prepared with different coatings and tested independent of the EDM central components. A coating facility must no longer be large enough to host the larger and taller GND structure, but only the substrate. One can even consider replacing the Al substrates with a different base material altogether. The HV electrodes were adapted in the same fashion to fully utilize the exchangeable substrates.

4.4.2 Wafer based EDM cell

A conceptual alternative to aluminum-capped cell are silicon wafers. Standard wafers are perfectly flat, and intrinsically clean with respect to magnetic contamination. Silicon wafers have small Johnson noise but can be easily doped to provide enough conductivity to act as electrodes. They are among the most versatile substrates for coatings and perfect, gap-free lids can be machined from wafer parts. Si wafers are however limited in size to a diameter of 300 mm which reduces the volume from 17 L to 5.79 L. The UCN density would increase from $4\,\mathrm{cm}^{-3}$ to $6.7\,\mathrm{cm}^{-3}$. The total number of UCN per cell would decrease from 70900 to 38800. This would decrease the statistical sensitivity by 26 %. In turn, improvement on systematics and access to superior coating material can extend the UCN lifetime, which enters linearly into the sensitivity.

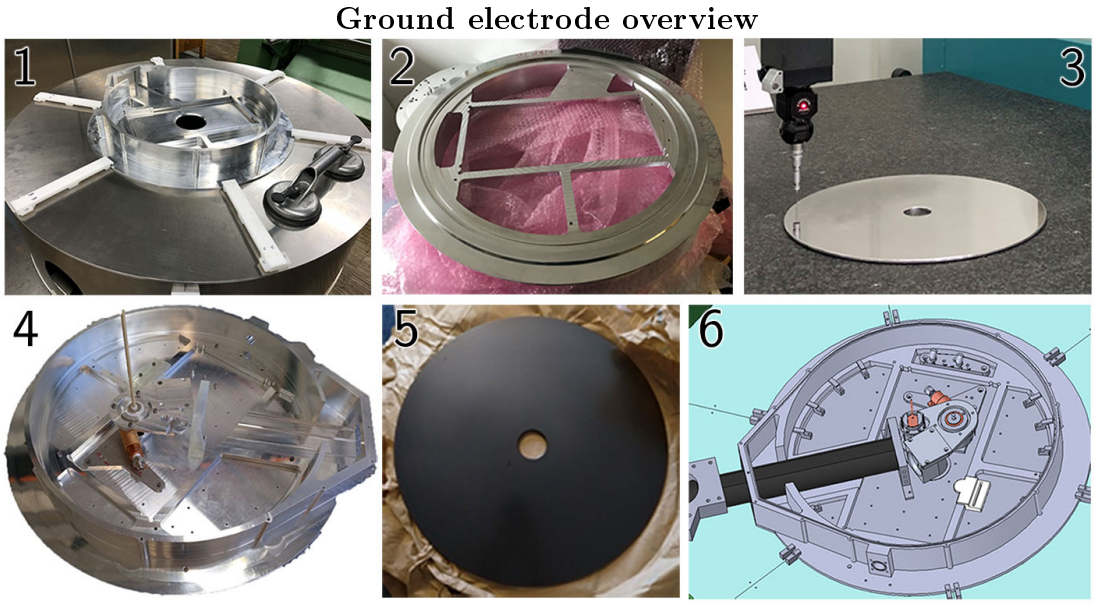

Figure 4.8: (1) Full assembly of GND electrode with DIA 80 cell opening. (2) Reworked structural part of GND electrode which supports the exchangeable substrate (3). (4)A test assembly of a loading valve with GND electrode and substrate. (5) d-DLC coated substrate. (6) Render of complete loading valve.

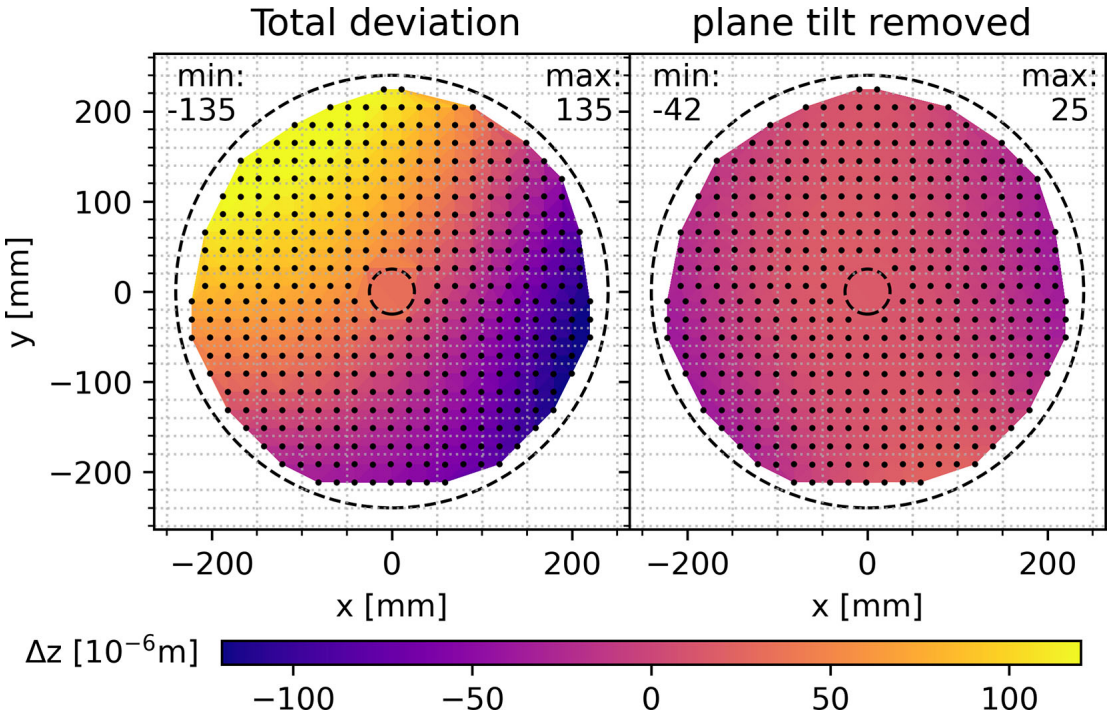

Figure 4.9: Waviness of Al electrode substrates with single-sided DLC coating. The electrode was placed force-free on a reference table and the total height was measured with a tip-probe with $<1\,\mu m$ resolution. The left picture shows the total deviation from a mean parallel plane. The right picture shows the residual waviness if the global tilt is removed.

4.5 Solenoid Polarizer

The solenoid polarizer (SP) is a compact, magnetic spin-sensitive barrier in the UCN guide system of the phase I setup of panEDM for UCN of up to 90 neV. This chapter presents the concept and design as well as the characteristics of the final component.

Polarized UCN can be obtained in multiple ways. Historically most experiments in need of a polarized beam resorted to thin iron foils that can be magnetized to saturation with small excitation fields (Harris et al. 1999). The magnetic potential adds (subtracts) to the neutron optical potential of the material for spins parallel (antiparallel) to the magnetic flux density and thus reflect (transmit) the LFS (HFS). In practice, the foils experience loss from scattering within the material and from unwanted reflection on the surface (see also sec. 2.2).

If the magnetic barrier can be generated without the use of a ferromagnetic foil, these losses are avoided. In addition, the transmitted UCN are perfectly polarized, if the barrier is higher than the largest kinetic energy of the UCN. Such designs have been used yielding significant UCN gains (Serebrov et al. 2005; Serebrov et al. 2009).[14] Many next-generation UCN experiments favor this mode of polarization (Ayres et al. 2021) and it will be used in panEDM for phase II simultaneous spin detection.

4.5.1 Component goals and design restrictions

While SuperSUN is designed to provide polarized UCN in phase II, it will only provide unpolarized UCN in phase I with kinetic energies below 90 neV (see 3.3). In order to polarize the UCN, a large magnetic gradient is placed in the trajectory of UCN which exposes the UCN to a spin-dependent potential:

$$U_m = \boldsymbol{\mu_n} \cdot \nabla \boldsymbol{B}, \tag{4.11}$$

where $\mu_n = -9.662\,365\,1 \times 10^{-27}\,\mathrm{J\,T^{-1}}$ (CODATA 2018). Expressed as potential for UCN in neV: $\mu_n = 60.3\,\mathrm{neV\,T^{-1}}$. Thus we energetically prohibit one spin state of UCN to pass through the SP if we provide a barrier of at least 1.5 T. The SP ideally provides a field higher than this level to also polarize marginally trapped UCN from SuperSUN. For short extraction delays, UCN with energies close to or above the trapping depth have not yet been "cleaned" away and contribute to the UCN yielded (see fig. 3.3). These UCN eventually disappear during the Ramsey cycle inside the EDM cells if similar wall coatings are used in SuperSUN and panEDM. However, if the trapping potential of panEDM were to change in the future, the experiment would benefit from a larger magnetic barrier. Detector stability tests running parallel to the Ramsey cycle (see fig. 2.11) are negatively impacted by a smaller degree of polarization of instantaneously extracted UCN.

The EDM measurement uncertainty improves from a higher degree of polarization linearly, while it only improves with the square root of the number of UCN. Therefore the experiment design leans towards using the highly polarized fraction of UCN. This can be achieved by stopping the cold beam and thus the production of UCN some time before the extraction.

[14] The large gains in UCN density reported (3.8× for polarized, 2× for unpolarized) arise from the practical need to have a vacuum separation foil. If this foil is placed inside the large field, the increased UCN velocity significantly reduces the loss in the material $\propto \frac{1}{v}$. The reported gain for unpolarized UCN is purely a gravitational effect from experiment design and independent of the polarization device.

Experimental restrictions

UCN guides are designed for an inner diameter of 50 mm throughout the UCN path which has to be maintained in the SP. A horizontal guide section budget of 184 mm is available for the component whereas the radial size is only weakly restricted from the apparatus. The field imposed by the SP must maintain adiabaticity for UCN transport within the SP and outside (Golub et al. 1991, Eqn 2.5):

$$\frac{1}{\tau} = \frac{1}{|B|} \cdot \left|\frac{dB}{dt}\right| \ll \frac{\mu B}{\hbar} = \omega_L, \tag{4.12}$$

where τ is the "interaction time" and ω_L is the Larmor frequency. With $\omega_L = -29\,\mathrm{Hz\,\mu T^{-1}}$ and typical UCN velocity below $5\,\mathrm{m\,s^{-1}}$ this is fullfilled for any practical field gradient for a minimum flux density of $>10\,\mathrm{mT}$ and in the absence of zero-crossings. The stray field of the SP at the outer MSR layer has to be smaller than this layer's saturation flux density, which is on the scale of 100 mT.

4.5.2 Magnet design

While superconducting magnets with large warm bores are readily available for such applications, most of these require too much space along the beam propagation and are generally expensive. With respect to the limited use until source upgrades in phase II a cheaper solution was favored. Based on experience with an existing magnet of a similar design, (see (Fierlinger 2005)) a H-type yoke with large radial and small axial dimensions was chosen. In this configuration, the main solenoid is oriented concentric around the beam. Field lines are guided by roughly radially symmetry yoke inwards towards the center and penetrate into the volume of the guide in a central section where an air gap is placed.

The H-type yoke naturally invites circular symmetry in the design. A perfect circular design is impractical due to the need for non-straight material cuts. For the iron yoke, a set of existing $42-44\,\mathrm{mm}$ thick soft iron plates were lifted from a decommissioned magnet. From the shape and size of existing parts, we determined that a twelve-sided prism would use the material best. The final segments were machined to 39 mm thickness, thus the total axial length of the magnet body would amount to 168 mm including a 90 mm long central space for the coil block. The mantle is made from 12 identical segments which lock onto the faces with a machined edge. The two faces are made from 12 interlocking segments each, which are identical up to small fixtures and holes. The magnet was designed such that the attractive forces among yoke parts lock them into shape. Under operation - in principle -the magnet would not require screws to stay assembled.

Neither the iron's magnetic behavior, alloy or grain structure was known. The target field of $>1.5\,\mathrm{T}$ is in the vicinity of saturation effects for most soft iron alloys and the concentration of field lines in the center is highly dependent on the detailed saturation behavior. While some of these parameters can be extracted with tests on small samples, these results are of limited use. Mechanical and thermal stress while machining is difficult to predict. While designing the magnet the bulk simulations were thus done both with a conservative anhysteretic soft iron model and a high saturation anhysteretic model in parallel. A full set of parts was built from the available soft iron. In case the resulting fields were too small, the central yoke pieces would be replaced[15] with a high saturation

[15] Such as VACOFLUX or PERMENDUR

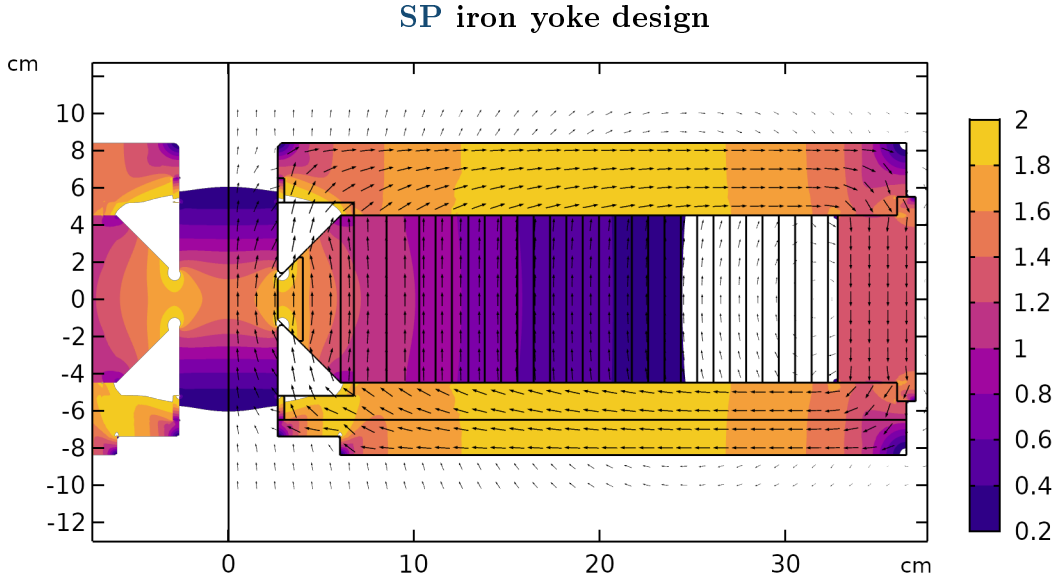

Figure 4.10: Simplified cross-section of the solenoid polarizer (SP) with the simulated magnetic flux density B [T]. The minimum of the magnetic barrier is located in the geometric center of the coil and the field cut along a radial cross-section has a saddle-shape. Figure made with COMSOL Multiphysics.

cobalt-iron alloy. See also section 4.5.4 and figure 4.18.

Simulations showed, that the 39 mm thickness of the yoke was sufficient to contain the field lines with the exception of the central region. The shape of the circular poles was the result of a parametric design study which can be seen in fig 4.11. Simulated central magnetic field flux for different pole shapes. A simplified magnet model was simulated for different gap widths and pole tip widths. The optimum is shown in black: $B_{\text{opt}} = 1646\,\text{mT}$. The final pole tip width was effectively widened due to a fillet, which causes a slight deviation from the optimum towards $B_{\text{built}} = 1643\,\text{mT}$. While it is possible to machine a sharp angle in soft iron, it can create mechanical defects in the brittle iron. Exposed sharp edges also get very hot while machining which can alter the magnetic properties unfavorably. The two poles are separated with an aluminum central piece which completes the yoke mechanically and takes the $\sim$3 t of force acting between the poles.

Coil block

The magnet consists of a coil block wound from a 4×4 mm rectangular, PTFE isolated, hollow copper guide with a 2.5 mm center bore. This dimension of the copper guide allows for easy handling and can be wound to small diameter coils with a small pitch, such that the coils can use the space inside the magnet at small radii efficiently. The coil block has a total of 20 layers with 60 turns totaling 1200 windings. The coil block is a cylinder of 88 mm[16] and extends from an inner diameter of 117.4 mm to 645.4 mm. The coil block itself is broken up into 38 individual coils with lengths from 16 m up to 55.9 m. This is necessary to allow sufficient cooling water to flow through the hollow center at

[16] While the guide itself has only 4×4 mm budgeted an extra 10 % both radially and axially.

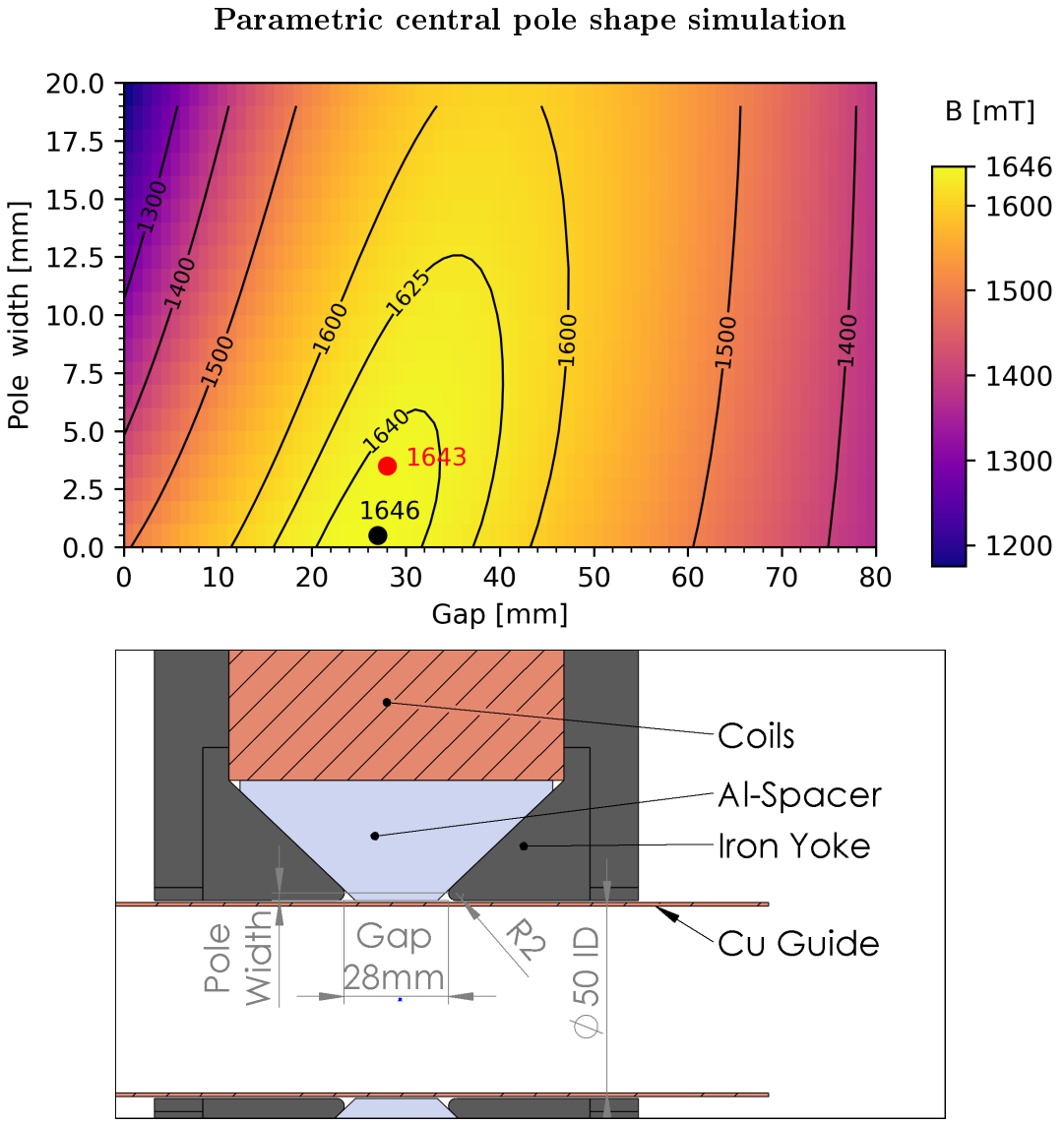

Figure 4.11: Simulated Central magnetic field flux [mT] for different pole shapes. A simplified magnet model was tested for different gap widths and pole tip widths. The optimum is shown in black: $B_{opt} = 1646\,mT$. The final pole tip width was effectively widened due to a fillet: $B_{built} = 1643\,mT$

reasonable differential pressure[17]. A detailed list of the coils and their properties is given in table 4.3.

Coil wiring

A few considerations are influencing the number and length of coils subdivided from the full 1446 m of conductor material. The shorter coils allow for larger water flow which in turn improves cooling and allows larger currents to flow through a coil. To simplify the hydraulic design, all coils operate with a shared pressure drop. Coils can only have an even integer number of windings and either 10 (half) or 20 (full) number of turns. This restriction allows inputs and output connections of coils to be placed at the same side of the magnet. In the final design, 39 coils were made with coil lengths between 16.1 m and 55.9 m. The coils are grouped by their openings in the iron yoke. Once the mechanical layout was fixed the water flow per coil could be calculated from first principle (see column theoretical coolant flow rate in table 4.3). This was later confirmed with a dummy coil wound from a spare conductor (see column heuristic model coolant flow rate in table 4.3).

Two power supplies of suitable total power were available with DC output ranges of 300A × 65V and 240A × 82V. A script was used to find the optimal configuration of parallel and serial coil links for the magnet. The script tested all possible configurations where no single coil would have a $\Delta T > 45\,\mathrm{K}$ [18] The script was further restricted to only link coils in ascending sequence within a coil group (1-16, 17-27, 28-38) to ease construction in the dense space where coils exit the iron yoke. Coil groups 17-27 and 28-38 are identical and were defined to use the same pattern.

The resulting configuration draws 300 A at 59.2 V measured (61.3 V predicted) which corresponds to 92% of the available power. The configuration is shown in fig. 4.12.

Effects of cooling water on total field generation

The contribution of each coil to the total field is different and can be observed by the magnetic excitation in table 4.3. Coils 0 to 7 generate half of the total H field. Thus a change in current ratios for parallel coils can alter the total excitation field. The steady-state temperature of cooling water flowing through the magnet has no effect the splitting ratio assuming a linear temperature dependence of conductivity.

A change in water flow rate through the magnet changes the cooling power per coil and alters the branching in parallel coils. A change of 30% in flow rate only amounts to 240 ppm changes in flux density. (see fig 4.13). This effect is mitigated as the SP has its own closed cooling water cycle which stabilizes water flow within 10 %.

Thermal expansion

The thermal expansion of the copper coils on the inside has an effect smaller than 100 ppm in the exciting H field if the coil were running in free space. With the yoke enclosing

[17] $\dot{V}^2 = \Delta p \pi^2 d^5 / 8 \lambda \rho l$ with differential pressure $\Delta p = 4\,\mathrm{bar}$,diameter d = 2.5 mm,pipe friction coefficient $\lambda = 0.0464$, fluid density $\rho = 998\,\mathrm{kg\,m^{-3}}$ and pipe length taken from table 4.3. Reynolds number 2534, surface roughness: 1.5 µm.

[18] This value originated from assumptions on the highest base temperature level in the primary coolant loop would be 20 °C such that the highest temperature leakage in the system would not cause scalding. (65 °C).

Label	Inner Diameter [mm]	Outer Diameter [mm]	# Windings	# Layers	Wire length [m]	theo. coolant flow rate [mL/s]	heuristic model flow rate [mL/s]	ΔT [K]	R [mOhm]	I_{theo} [A]	U_{theo} [V]	H_{center} [kA/m]
0	117.4	135.0	2	20	16.1	8.1	8.5	39.0	29.3	212	6.2	33.5
1	135.0	170.2	4	20	38.6	5.2	5.5	24.0	66.7	88	5.9	23.2
2	170.2	205.4	4	20	47.4	4.7	4.9	19.4	80.6	69	5.5	14.6
3	205.4	223.0	2	20	27.1	6.2	6.5	26.4	47.3	120	5.7	11.2
4	223.0	240.6	2	20	29.3	6.0	6.3	25.3	51.0	111	5.7	9.6
5	240.6	258.2	2	20	31.5	5.7	6.1	26.0	55.0	107	5.9	8.6
6	258.2	275.8	2	20	33.8	5.6	5.9	25.1	58.6	100	5.8	7.5
7	275.8	293.4	2	20	36.0	5.4	5.7	24.3	62.3	94	5.8	6.6
8	293.4	311.0	2	20	38.2	5.2	5.5	35.0	68.7	106	7.3	7.0
9	311.0	328.6	2	20	40.4	5.1	5.4	34.0	72.4	100	7.2	6.2
10	328.6	346.2	2	20	42.6	4.9	5.2	33.0	76.1	95	7.2	5.6
11	346.2	363.8	2	20	44.8	4.8	5.1	11.4	73.9	56	4.1	3.1
12	363.8	381.4	2	20	47.0	4.7	5.0	11.1	77.5	53	4.1	2.9
13	381.4	399.0	2	20	49.2	4.6	4.8	10.9	81.1	51	4.1	2.6
14	399.0	416.6	2	20	51.4	4.5	4.7	10.6	84.6	49	4.1	2.4
15	416.6	434.2	2	20	53.7	4.4	4.6	10.4	88.2	47	4.1	2.2
16	434.2	451.8	2	20	55.9	4.3	4.5	10.2	91.7	45	4.1	2.0
17/28	451.8	469.4	2	10	29.1	6.0	6.3	21.5	49.9	104	5.2	4.5
18/29	469.4	487.0	2	10	30.2	5.9	6.2	21.0	51.8	100	5.2	4.2
19/30	487.0	504.6	2	10	31.4	5.8	6.1	20.6	53.6	96	5.2	3.9
20/31	504.6	522.2	2	10	32.5	5.7	6.0	25.4	56.4	103	5.8	4.0
21/32	522.2	539.8	2	10	33.6	5.6	5.9	25.0	58.3	100	5.8	3.8
22/33	539.8	557.4	2	10	34.7	5.5	5.8	24.5	60.1	97	5.8	3.5
23/34	557.4	575.0	2	10	35.8	5.4	5.7	10.5	58.8	64	3.7	2.2
24/25	575.0	592.6	2	10	36.9	5.3	5.6	10.4	60.6	62	3.7	2.1
25/36	592.6	610.2	2	10	38.0	5.2	5.5	10.2	62.4	60	3.7	2.0
26/37	610.2	627.8	2	10	39.1	5.2	5.4	10.1	64.2	58	3.7	1.9
27/38	627.8	645.4	2	10	40.2	5.1	5.4	9.9	65.9	57	3.7	1.8
					$\sum$	$\sum$	$\sum$	$\oplus$	$\oplus$	$\oplus$	$\oplus$	$\sum$
					1446	210	222	20.9	204	300	61.3	211

Table 4.3: Properties of the individual coils in the SP. Corresponding properties of the combined coil system are listed as $\oplus$. Coils 17-27 are only half as tall and stacked twice, thus the total number of coils is 38. The theoretical flow rate assumes a turbulent flow with $\Delta p = 4\,\mathrm{bar}$

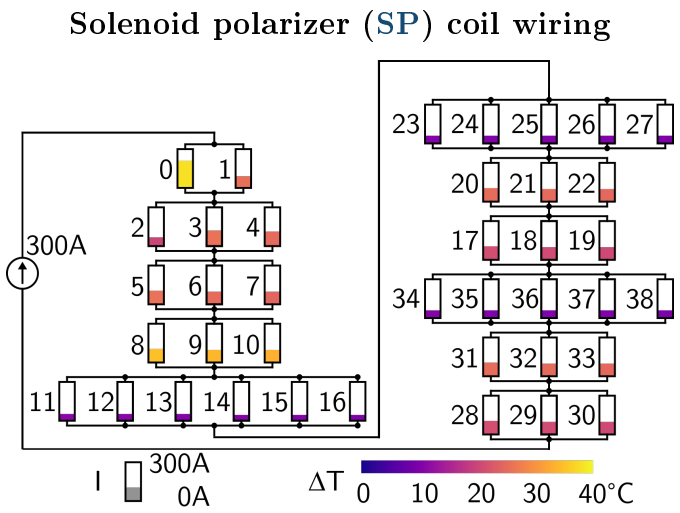

Figure 4.12: Diagram of Coil wiring. The colors indicate the mean temperature increase of each coil, the level of soild fil the fractions of current passing through the individual coil. Coil labels take from table 4.3

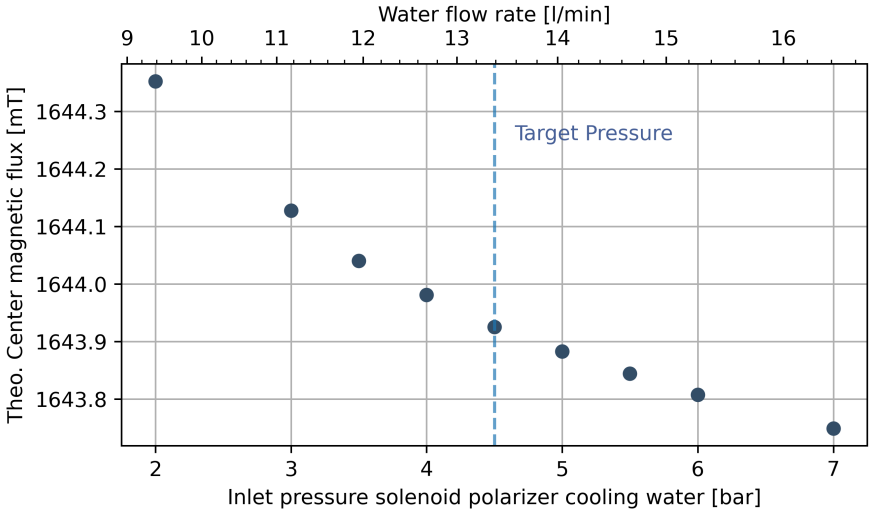

Figure 4.13: Simulation results of the projected central magnetic flux density value for different cooling water flow rates. This effect arises from slight variations in current branching between parallel coils due to changes in the conductor temperature. The simulation assumes full power operation with 18 °C input. The absolute field value is higher than elsewhere discusses due to a simplified magnet geometry used in this simulation.

the coils, this effect is strongly mitigated as all field lines collected by the yoke. For a temperature increase of the full magnet from 18 °C to 45 °C, the aluminum spacer separating the yoke poles expands by up to 0.04 mm which in turn lowers the center field value by 50 ppm.

Temperature dependence of hysteresis behavior

It is well known that ferromagnetic materials lose their permanent magnetization at the Curie temperature. Even at lower temperatures, the saturation magnetization of iron decreases on a percent level under some circumstances (Raghunathan et al. 2010; Sixdenier et al. 2016). The design of the H-type yoke implies saturation of the pole tips, thus the flux density in the guide center is sensitive to small saturation changes. These effects are difficult to model or predict even if a large set of material properties is known. For the designed SP the effect is addressed only by maintaining a constant power load and cooling water supply.

The coils inside the SP are cooled through water passing through the hollow conductors. This process reaches equilibrium within a few minutes and does not affect the magnetic flux density measurably. On the scale of 3 h, the iron yoke itself heats up which causes the field in the center to decrease in a repeatable fashion as shown in fig 4.14. The upper plot depicts the decrease of the field from 1544 mT to 1521 mT which correlates with the iron yoke temperate[19].

Radial symmetry SP

During the design of the SP, the field was assumed to have radial symmetry. This allowed the majority of calculations and simulations to be significantly simplified. Upon completion of the design, the final construction model was tested in a full 3D simulation. To limit the number of needed mesh entities, all threads and screw holes were removed. The total field in the central plane (Z=0) perpendicular to UCN flux is shown in the top plot and the deviation from a radially symmetric field in the bottom plot. This deviation is defined as $(\|B\| - B_r)/B_r$ where $B_r = \frac{1}{2\pi}\int_0^{2\pi} \|B(r,\phi)\|\, d\phi$. The two solid black circles represent the copper guide, the dotted line the dimensions of the bore in the soft iron yoke. The decreased field to the right is a result of the large cutout in the iron yoke for the exit of the inner coil group. The inner coil group has its exit very close to the center and forces field lines to circumvent the area. When comparing the inhomogeneity ($< \pm 0.3\%$)with the total field change long the radius ($\Delta B_{0\to R} \approx 25\%$, radial symmetry is a fair assumption.

4.5.3 Completed SP

The main body of the SP was built at the central mechanical workshop of the TUM Department of Physics. Wiring and assembly of the SP electronics were done at TUM. The completed SP was then shipped to ILL for a test with UCN. Figure 4.16 shows a rendering of the magnet and some of the technical details. Figure 4.17 shows the completed magnet with an automated mapping robot while mapping the inner field and pseudo color image of the surface temperature under full operation.

[19] Temperature was measured with a PT100 inside an aluminum housing placed inside a ⌀ 10 mm hole ≈ 20 cm off-center on the SuperSUN side.

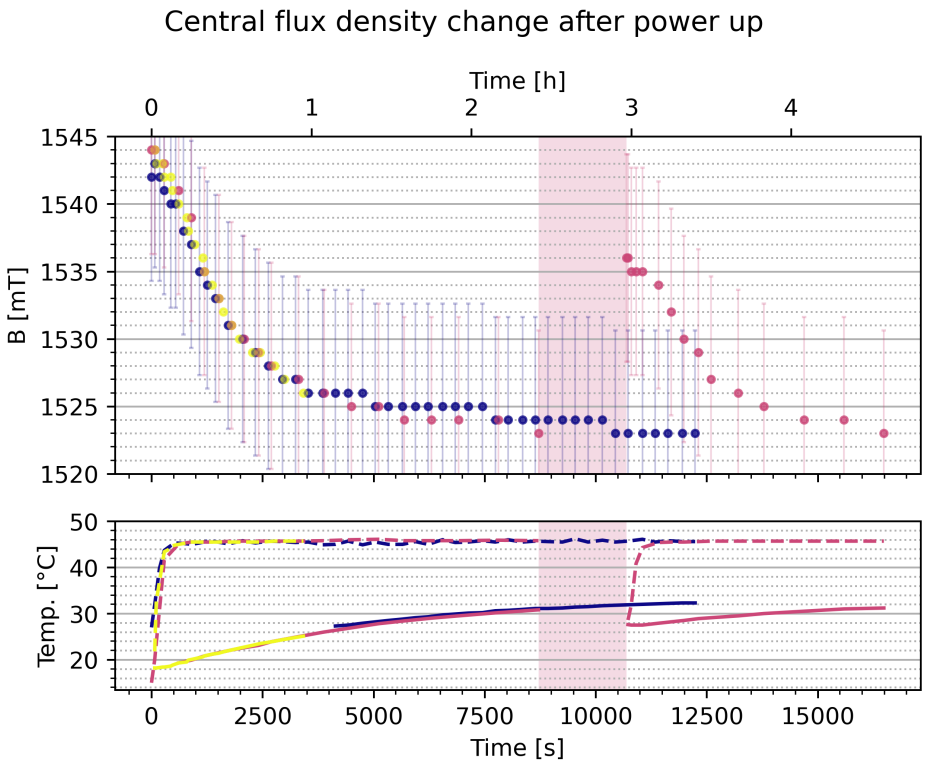

Figure 4.14: Upper plot: Three sets of measured values of the central magnetic flux density after switching on the solenoid polarizer (SP). The field falls off in a reproducible fashion from 1544 mT to 1521 mT. While the return cooling water rapidly approaches an equilibrium (dashed lines lower plot), the iron yoke itself warms up within 3 h (solid lines lower plot). The rose data set includes a 40 min break in coil current highlighting the reversible nature of the effect.

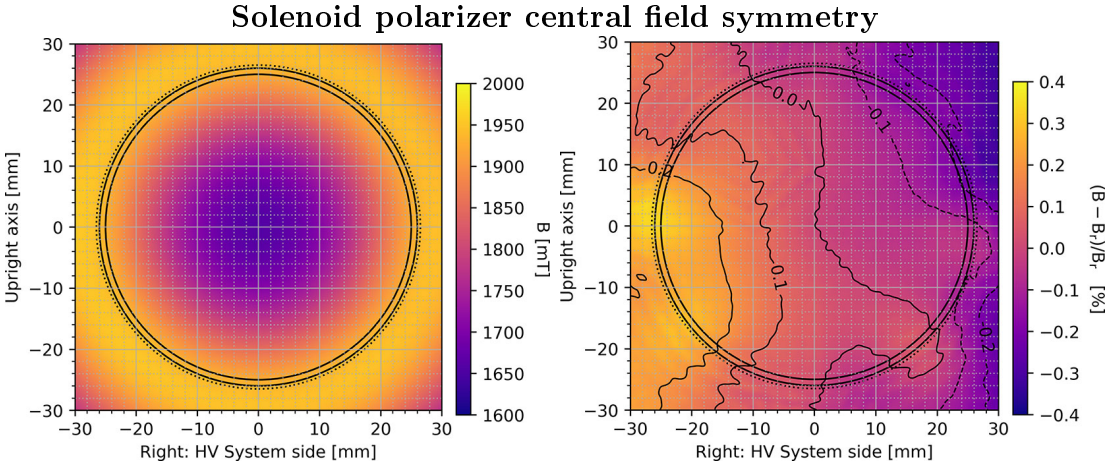

Figure 4.15: Flux density in the central plane of the solenoid polarizer (left) and relative deviation from radial symmetry (right). The simulation confirmed the working hypothesis of circularly symmetric flux density of the final design.

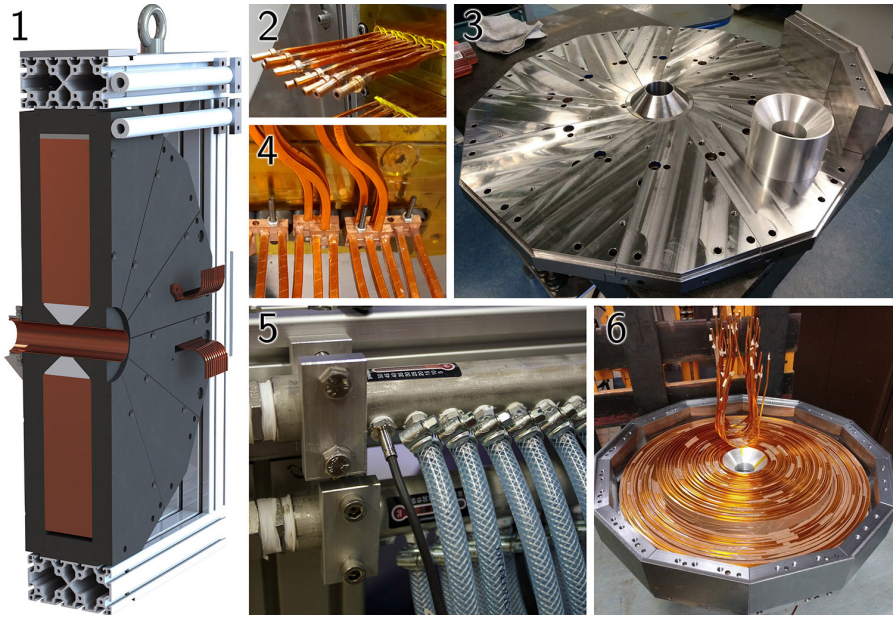

Figure 4.16: Solenoid Polarizer. Full SP rendering (1), Coils are wound from PTFE isolated holler copper conductor (2), Copper brackets link coils in parallel and attach to links (4), Iron yoke with aluminum spacer (3), Magnet with 27 of 38 coils installed (5), Cooling water distribution (6).

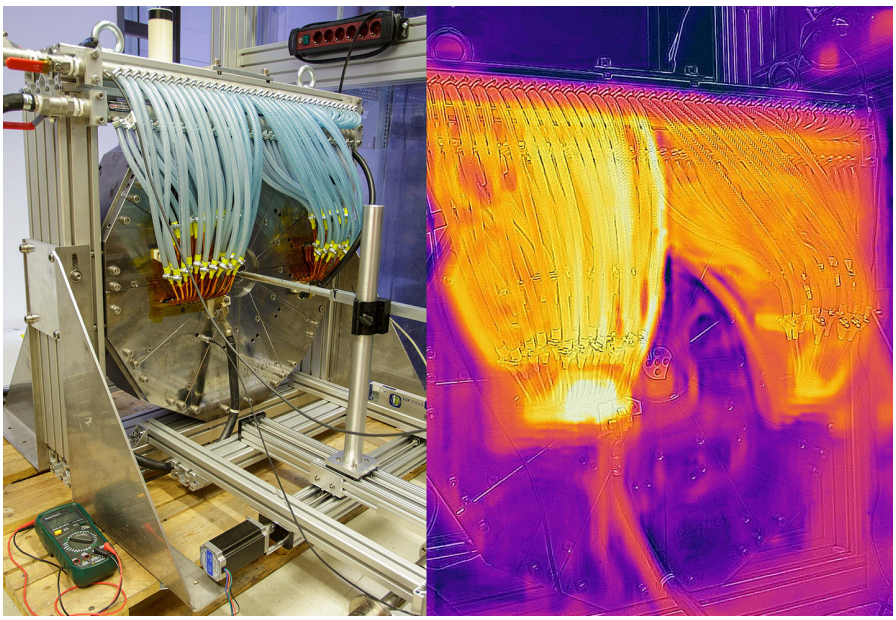

Figure 4.17: Solenoid Polarizer in operation during mapping (left) with NIR image (right). This was used to both confirm circulation in all coils as well as to confirm the relative heat load. Coil 0 (rightmost of the left group) experiences the highest temperature increase as expected.

4.5.4 Field maps

A vital step in the characterization of the magnet is the recording of field maps. This is needed to confirm the operation of the magnet as designed and to provide accurate field data for integration into panEDM. Once the SP is placed in its final position at panEDM, many relevant positions are inaccessible for magnetic field probes. Therefore a wide set of positions and distances should be covered, as future needs are difficult to predict.

Inner field

To evaluate the magnetic field near the center and inside the bore, two setups were used. The simple setup consisted of a 3D-printed guiding piece which allowed to place an axial Hall probe *AXIALSONDE HGM.A3.069.045* connected to *MAGSYS Gaussmeter HGM09* in defined axial distances and angles. This setup was well defined in R and Θ , but poorly defined along the Z-axis. Larger maps were recorded using a mapping robot that could access a large set of points in the horizontal R,Z plane with $<$0.1 mm resolution and 1 mm accuracy using the same Hall probe.

The SP is a spin-selective magnetic potential barrier. The trajectory with the lowest magnetic peak value will limit the energy of maximum UCN polarization. The flux density in the guide volume can be treated as axially symmetric (see sec. 4.5.2) and viewed in a cross-section, the flux density norm is saddle shaped (see fig.4.10). This means that the trajectory with the lowest peak value is a beam along Z=0 which has its minimum at R=0.

This was confirmed with a detailed map in the central, horizontal plane with a 1.5 mm grid of points spanning from $Z = \{-59, 59, \Delta = 1.5\}$[mm] and $R = \{-17, 17, \Delta = 1.5\}$[mm] shown in fig 4.18. The map was recorded after $>$ 4h of continuous operation when the magnet established internal thermal equilibrium. The size of the used axial field probe only allowed to map the field $\pm$17 mm around the Z-axis instead of the final inner guide radius of $\pm$25 mm[20] This is still enclosing enough of the central region to judge the field shape.

The obtained map is shown in fig 4.18. The figure also provides results from three simulations evaluated for an identical grid. The simulations were made using a detailed coil layout with coil currents taken from 4.3 and adding low permeability ($\mu = 1$) gaps of 0.5 mm between parts. The measured map reports slightly higher values than the standard iron simulation but lower than the high saturation material. This suggests that if a gain of 200 mT for the central field is needed, an upgrade of the central parts of the iron yoke would likely suffice. The target value of 1500 mT has been reached in the present configuration.

Fig 4.19 presents the simulated magnetic flux along the central axis for different fractions of the maximum current. Two measured line maps are added which comply with the simulated results. The measurement with $0.55 \cdot$I[21] map was recorded by hand which resulted in larger uncertainty of the position, but allowed to record the tails of the axis. The measurement with $1.0 \cdot$I where obtained with a motorized mapper. A practical plot with just the field value from the geometric center is provided in fig. 4.20. It highlights

[20] The bore in the iron yoke has a radius of 26.5 mm

[21] This set of data was recorded early in the magnet commissioning where safety precautions mandated operation below a certain power.

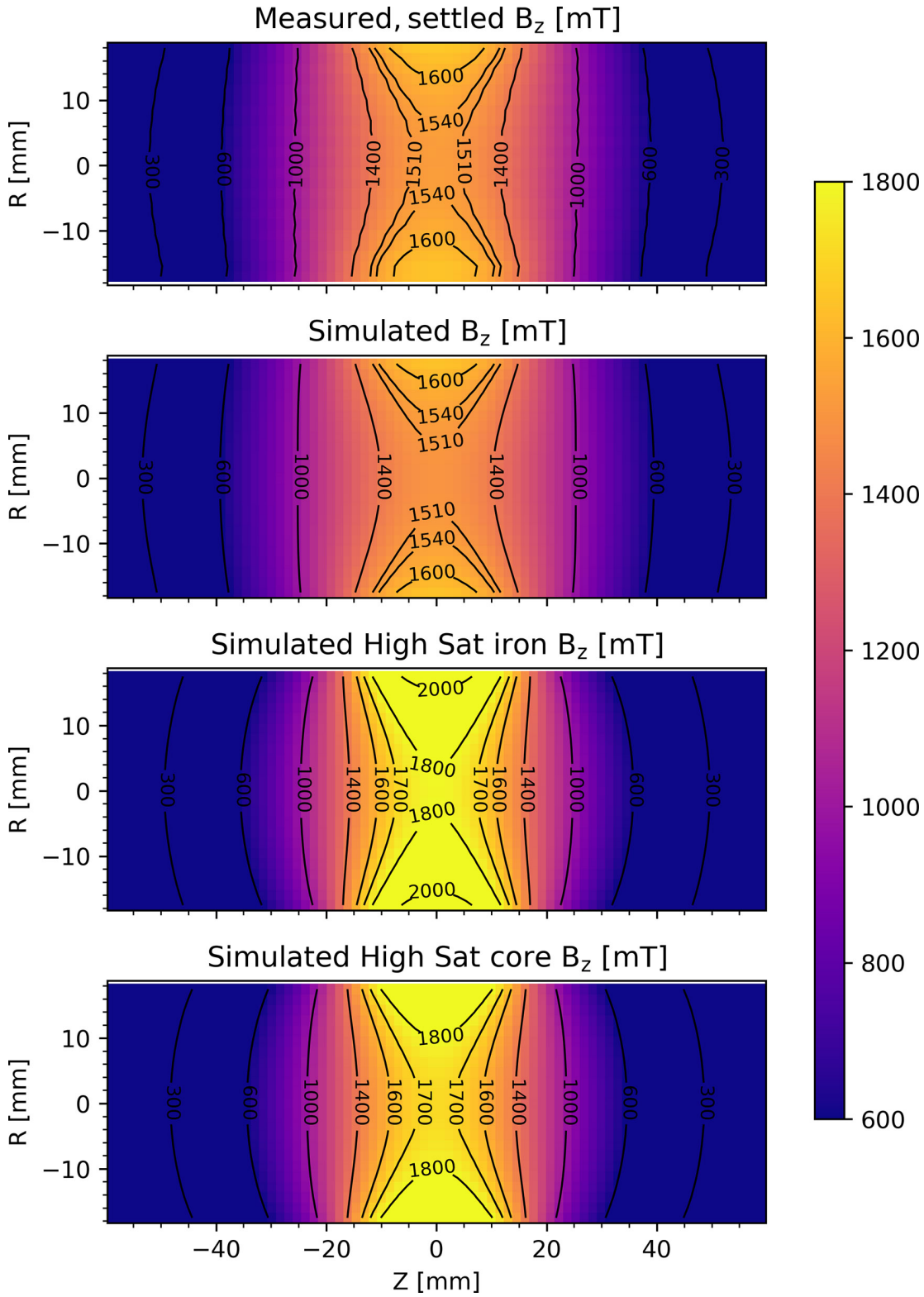

Figure 4.18: Map of B_Z on the central, horizontal plane on a 1.5 mm grid. The Z-axis points along the UCN flight direction. The R-axis is oriented to yield a top-down view. Three sets of simulated results evaluated on a matching grid are provided for reference.

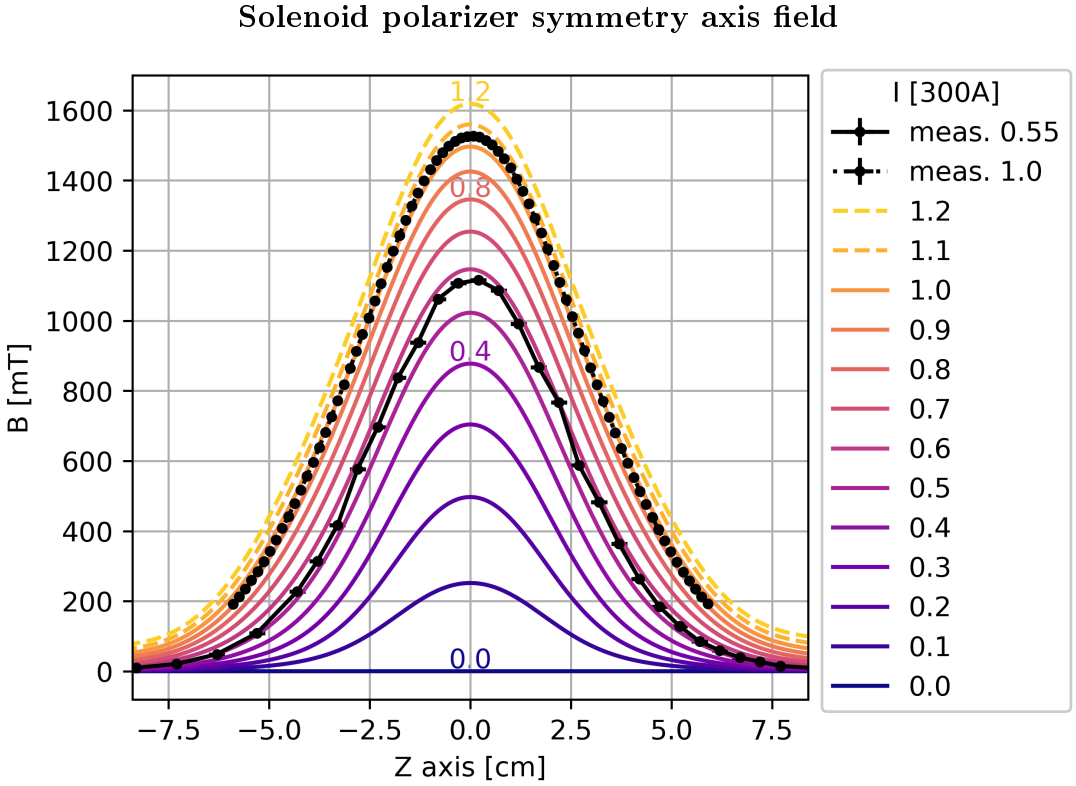

Figure 4.19: Simulated and measured line maps for the magnetic flux density along the central axis of the SP. Z-axis points along UCN flight direction.

the projected field gain for higher currents as well as the effect of high permeability upgrades. For an increase of 20% in current (and 44% in power to 26.8 kW), the center field rises 8.2% to 1618 mT (standard iron) to 9.6% to 1963 mT (high sat. iron).

Outer field and adiabaticity during transport

While the flux density in the center should be very large, the stray fields of the magnet should be small, ideally in the range of few times the flux density of the earth's field. A large stray field is a safety hazard on site as well as an unwelcome background in electronic systems nearby. In the case of panEDM if the stray field would be strong enough to saturate outer layers of the magnetically shielded room, it would deteriorate the shielding performance.

The fringe field also has a practical use at panEDM. In order for UCN to stay polarized during transport, a bias field has to be provided fulfilling eqn. 4.12 - the adiabatic transport condition. This means that changes in the observed magnetic field are slow compared to the Larmor precession of the neutron spin. UCN are by their nature slow-moving particles - in practice this criterion is fulfilled when guides are submerged in >3 times earth magnetic field ($\sim \|B_{\text{earth}}\|$ 50 µT). This is the case within about 1.2 m around the SP and covers the UCN guide layout presented.

Fig 4.22 shows the stray field norm for an axially symmetric magnet model. The ⌀ 120 mm,⩒ 10 mm recess on the panEDM side of the magnet ($+Z$) has a small local effect which we can neglect for the present discussion. The flux density falls of to 50 mT

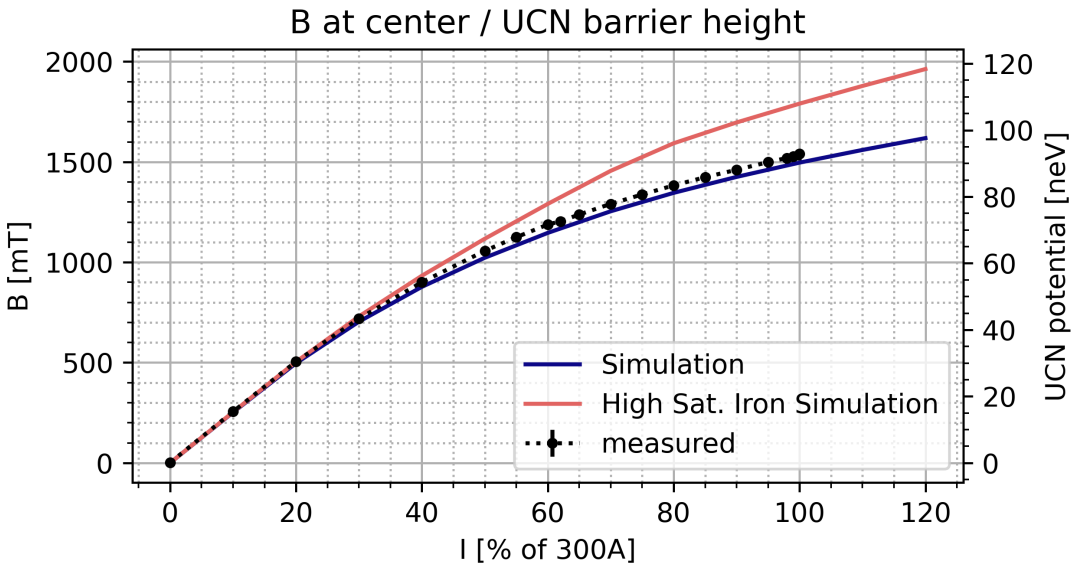

Figure 4.20: Simulated and measured instantaneous central magnetic flux density for various applied coil currents. The red line highlights the expected field for high saturation iron alloys (such as VACOFLUX or PERMENDUR) used in the central parts of the yoke. The simulation line corresponds to peak values at $Z = 0$ in fig. 4.19

on axis at the surface plane of the magnet (5). The flux density close to the surface is at largest $\|\boldsymbol{B}_{R=13cm,Z=8.5cm}\| \approx 60\,\mathrm{mT}$ and pointing radially (4). At a distance of 1 m the stray field falls below 400 µT (7,8,9) and below earth field/50 µT for any direction past 2.4 m.

4.5.5 Behavior as UCN spin selector

A large magnetic gradient has strong effects on the trajectories of UCN in the guide. As demonstrated before, the magnetic barrier is high enough to filter UCN with total kinetic energy of 91.7 neV. Above this energy the transmission probability of LFS is dependent on the field and guide geometry. SuperSUN has a fraction of UCN above this threshold, depending on the accumulation time. While some of the high-energy tail will be intrinsically cleaned in the long storage time of a Ramsey cycle, it is worth investigating the instantaneous polarization of the UCN passing the SP.

Given that the field is above 10 mT inside the whole magnet and no zero-crossings are present, we can assume adiabatic spin transport everywhere. Thus HFS and LFS can be treated as separate species for which the magnetic potential is attractive or repulsive and no exchange between these species occurs with the exception of spin-flipping wall collisions[22]. The HFS get accelerated towards $Z = 0$, $R = 25\,\mathrm{mm}$, owing to the saddle shape of the flux density. This is visualized in fig. 4.23. Thus UCN are accelerated towards the wall close to the center. The highest field on the surface of the guide is up to 2.5 T which accelerates 80 neV UCN up to 230 neV, which is well above the Fermi potential of copper (168 neV). In this section, simulations are presented which evaluate

[22] One could improve the yield of polarized UCN by adding a spin-scrambler upstream of the SP. LFS which are rejected by the barrier may be flipped and could pass through the SP.

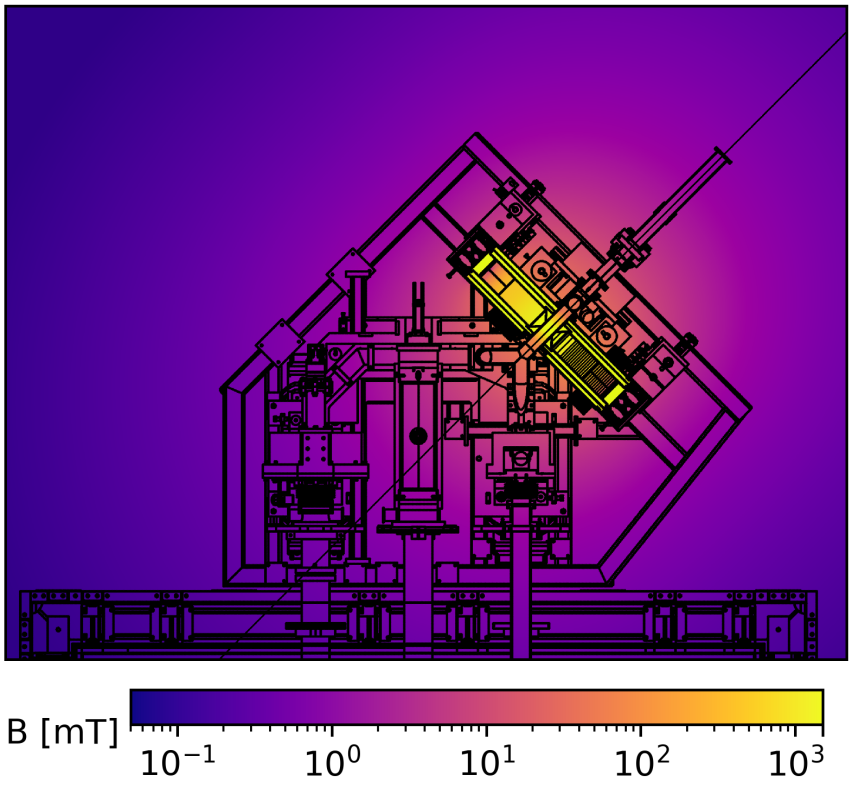

Figure 4.21: Outer field with a model cut from panEDM. The stray field serves as a holding field for UCNspins to facilitate adiabatic transport from source to the MSR.

the additional loss of HFS in the current configuration as well as discuss the fraction of LFS passing the barrier.

The setup of this simulation consists of a 500 mm tube with ID 50 mm with a copper surface ($V_{\mathrm{Fermi}} = 168\,\mathrm{neV}$, $\eta = 1.55\times10^{-4}$) where a set of 10^5 UCN with 80 neV=3.91 m s^{-1} are released following a Lambertian distribution from one side.

The reflection probability is calculated from eqn. 1.4. If the UCN is reflected from the wall, it does undergo a specular or diffuse reflection with adjustable probability[23]. If not specified otherwise a ratio of 5 % diffuse reflections is assumed. The input is modeled as a perfect diffuse reflector, which encapsulates a larger hidden set of UCN guides towards the source. The output is a perfectly absorbing detector. The UCN are released at t=0 s into an empty guide and the results of the simulation are shown for t=2 s. The impact of the magnetic field was simulated by adding a scalar potential:

$$\phi(r,z) = \left\|\overrightarrow{B}_{\mathrm{SP}}(r,z)\right\| \cdot 60.3\frac{\mathrm{nV}}{\mathrm{T}}, \quad \phi(r,z) > 0, \quad [\phi] = \mathrm{nV}, \tag{4.13}$$

which can be used to derive a force acting upon the UCN.

$$\overrightarrow{E}(r,z) = -\nabla\phi(r,z), \quad \overrightarrow{F_e}(r,z) = e \cdot q \cdot \overrightarrow{E}(r,z)), \tag{4.14}$$

[23] This is a functional, but physically incorrect model of the UCN reflection process. However, there is still no wall interaction model available which would yield better prediction based of first principles.

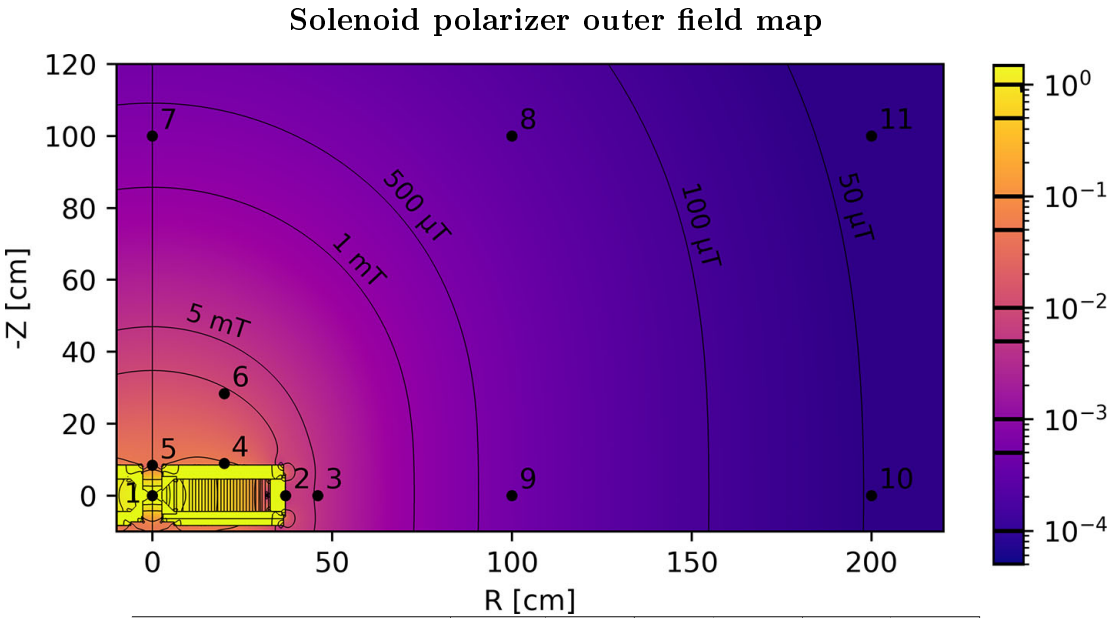

	1	2	3	4	5	6
$\|B_{\text{measure}}\|$ $[mT]$	1543	2.5	2.2	59.4	48.3	8.3
$\|B_{\text{std, simul}}\|$ $[mT]$	1497	6.10	4.5	53.4	53.2	11.0
$\|B_{\text{high sat, simul}}\|$ $[mT]$	1790	1.61	3.4	47.6	44.8	9.22

	7	8	9	10	11	
$\|B_{\text{measure}}\|$ $[\mu T]$	395	133	209	37	36	
$\|B_{\text{std, simul}}\|$ $[\mu T]$	649	190	368	48.4	40.1	
$\|B_{\text{high sat, simul}}\|$ $[\mu T]$	522	155	298	39.1	32.9	

Figure 4.22: Axially symmetry $\|\boldsymbol{B}\|$ [T] simulation with selected measurements. For high saturation yoke material, flux densities inside the magnet are higher and the stray field is lower. Measured data shows generally smaller stray field than anticipated. The earth magnetic field is $\|B_{\text{earth}}\| \sim 50\,\mu\text{T}$.

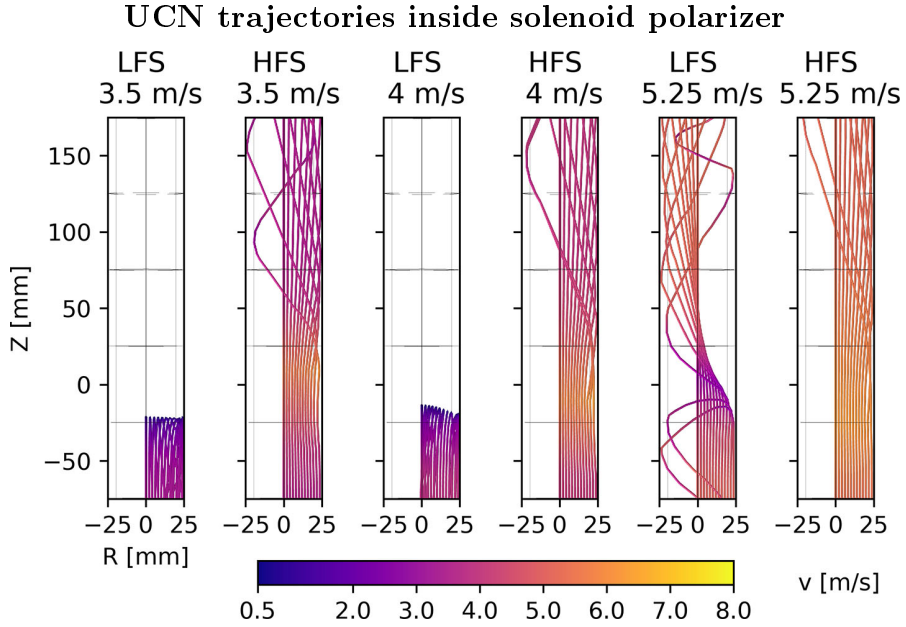

Figure 4.23: Example trajectories of UCN emitted on a line grid flying parallel to the beam axis (Z) into the solenoid polarizer (SP). Simulations are shown for both low field seeker (LFS) and high field seeker (HFS) around the expected average UCN kinetic energy of 80 neV=3.91 m s^{-1}. LFS with total veclocitities $<$4 m s^{-1} cannot pass the magnetic barrier while HFS are accelerated.

where $\overrightarrow{B}(r,z)$ is the magnetic flux density inside the SP and $\overrightarrow{F_e}(r,z)$ is the effective force simulated for particles with e=1.602×10^{-19} C the electron charge. Thus we can run the simulation for three relevant cases by defining:

$$q_{\mathrm{HFS}(\triangle)} = -1, \quad q_{B_{off}(\bigcirc)} = 0, \quad q_{\mathrm{LFS}(\triangledown)} = 1. \tag{4.15}$$

Given the small vertical span of possible positions, no gravitational potential was added and other typical loss channels for UCN (lifetime, slits,up-scattering from gas collisions) were omitted.

While this simulation does treat the full length like made from copper, this is not the case for the panEDM beampath. At panEDM, UCN travel through an electro-polished steel guide with bends, a hand-polished copper section of 86 mm, the hand and electro-polished SP guide section of 215 mm copper and then enter the Guide Manifold made from hand and electro-polished copper or NiMo coated glass. The most critical region, close to the center, is copper in both cases and thus the result should translate to the future application.

Figure 4.24 shows the results of this simulation. The guide is sectioned along the UCN flight direction (Z-axis) in 9 sections selected by the magnitude of the flux density shown in color shading. The flux density at the surface of the copper guide is shown in the bottom plot reaching from a few mT up to 2.5 T near the center. The top plot shows the number of UCN wall contacts per released UCN, per second (within the 2 s of the simulation runtime) and per cm of guide. The simulation was performed for UCN without magnetic field ($\bigcirc$), high field seeker (HFS, $\triangle$) and low field seeker (LFS , $\triangledown$). LFS are contained in the volume of the first four regions as they can't pass the magnetic

barrier. Their rate of wall interaction settles to 0 for Z>0[24]. For $B = 0$ UCN and HFS show smaller rates of wall collision as they propagate forward. This is expected as the density of UCN falls off in propagation direction due to the perfect absorber at the outlet. HFS are accelerated away from the wall initially but then diverted towards the walls in the center. This is visible in the slightly decreases wall interaction rate of $B = 0$ (◯) above HFS (△). Accordingly, in the three central regions HFS (△) wall collisions are above $B = 0$ (◯).

The middle plot shows the UCN lost from wall interaction as a fraction of the initially released number. In contrast to the top plot, this is not normalized by guide length, hence short regions are expected to have smaller total losses. The LFS loss curve tracks the wall reflection curve, as one would expect. Similarly, the $B = 0$ simulation result is a convolution of the wall interaction rate and the area of the binned region. HFS exhibit a large excess loss in the high field region, where wall collisions happen at $E_\perp > V_{\text{Fermi}}$. UCN not lost to wall interaction are either inside the guide volume (△:0.37 %,◯:0.34 %,▽:97.47 %) or propagated into the counter (△:94.05 %,◯:99.19 %,▽:0 %). A visual representation of the simulation state after 2 s is provided in fig. 4.25. The position of each UCN is marked with a dot, color-coded with the total velocity. Particles lost to up-scattering are fixed at the position of the last wall contact. In the top plot with $B = 0$, the total velocity of particles is unaffected and most particles have reached the exit (right). The density of UCN lost at the wall slightly decreases from left to right. In the middle plot, all LFS are contained in the guide volume upstream of the magnetic barrier. UCN close to the barrier have smaller velocities. In the bottom plot HFS have again mostly traversed the setup and are collected at the exit. A fraction of UCN with higher velocity was lost near the center of the SP. One can even see two distinct rings of higher loss density which correspond to the guide surface field maximum. The transmission of the SPfor HFS is thus $\approx 94\,\%$ which is significantly better than typical iron foil transmission of $\sim$ 20-40 %.

4.5.6 Distribution of velocities and angles

The previous simulation considered a single UCN velocity which was well below the magnetic barrier height and assumed a particular angular distribution of the incoming beam. As an extension to this study, a parametric simulation was made to resolve the effects of velocity and angle and additionally the degree of specular reflection in the guide. An overview of the tested parameters is given in table 4.4. The velocity and angular distribution of UCN is sampled by selected ratios of radial to forward velocity (v_r/v_z) and forward velocity (v_z). One could also have chosen energy and angle or total velocity and angle. The reason for the unusual choice of binning lies in the most prominent experimental technique of UCN velocity classification: Time of flight (TOF) measurements. A TOF measurement is only sensitive to the mean forward velocity component v_z, which is a widely reported quantity and sometimes conflated with the total velocity under the assumption that the UCN beam has small transverse components.

Simulation design The simulation uses the same geometry as presented in the previous section. A 500 mm long copper guide with DIA 50 mm is combined with the magnetic field from the SP. At the left side 10^5 UCN are released into the guide to propagate for

[24] Not visible in the log scale plot

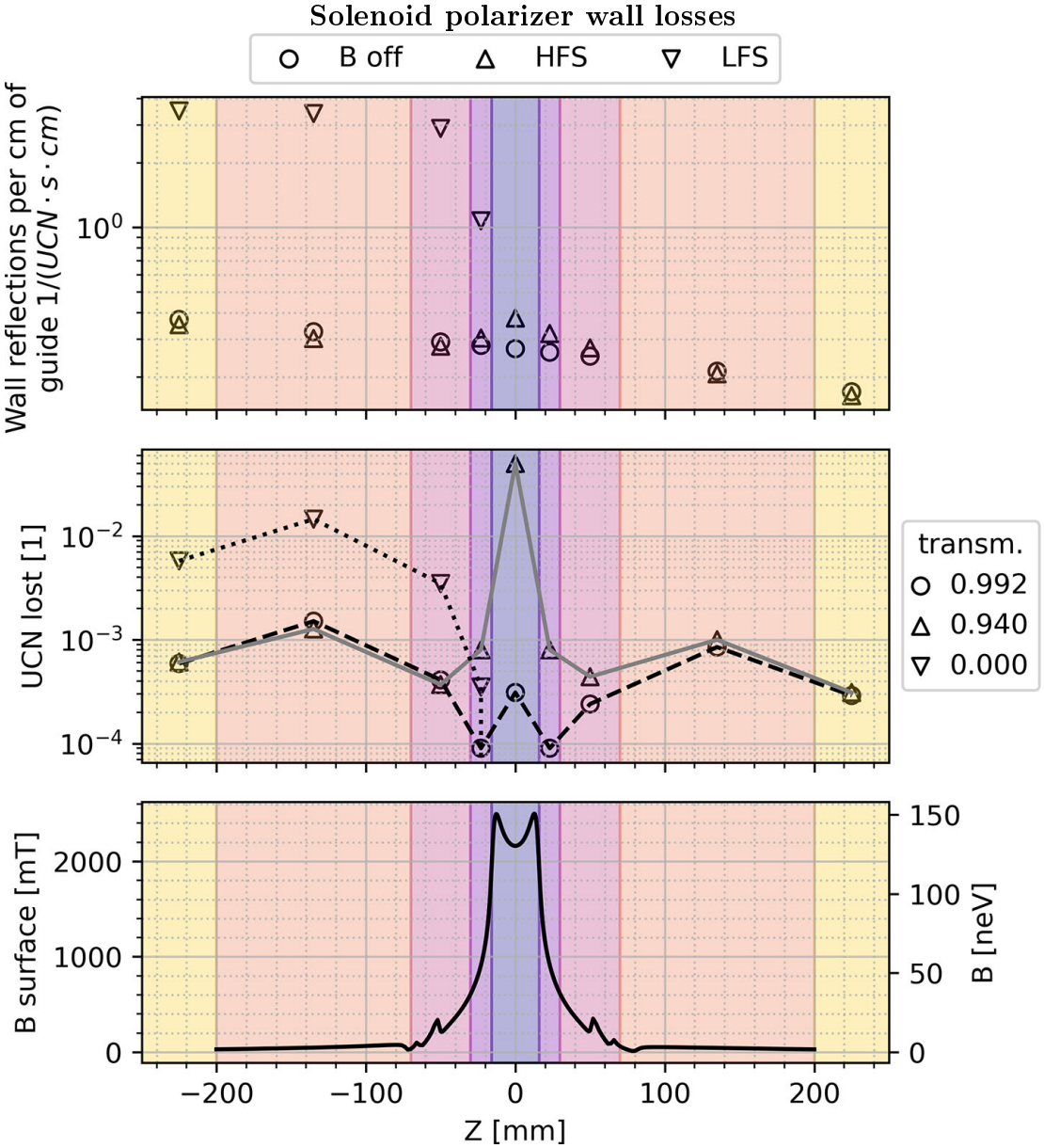

Figure 4.24: Monte Carlo simulation of 10^5 UCN with 80 neV propagating through a 50 cm Cu guide after 2 s elapsed. The simulation was run each for UCN without magnetic field (◯), High Field Seeker (HFS, △) and Low Field Seeker (LFS , ▽) . The top plot shows the number of wall collisions binned by regions inside the guide. Without magnetic field, the density of wall interactions fall of akin to the density of UCN in the guide. The LFS are confined in the $Z < 0$ region, while the HFS pass the barrier with slightly increased density of wall collisions. This leads to excess loss, as shown in the lower plot. From all UCN released at time=0, some stay in the volume (△:0.37 %, ◯:0.34 %, ▽:97.47 %) and some already passes the volume into a perfect counter (△:94.05 %, ◯:99.19 %, ▽:0 %). The fraction off the total released UCN lost in each region is shown in the middle plot. The large loss of HFS is a result of increased wall collisions and the higher loss probability per bounce at higher kinetic energy.

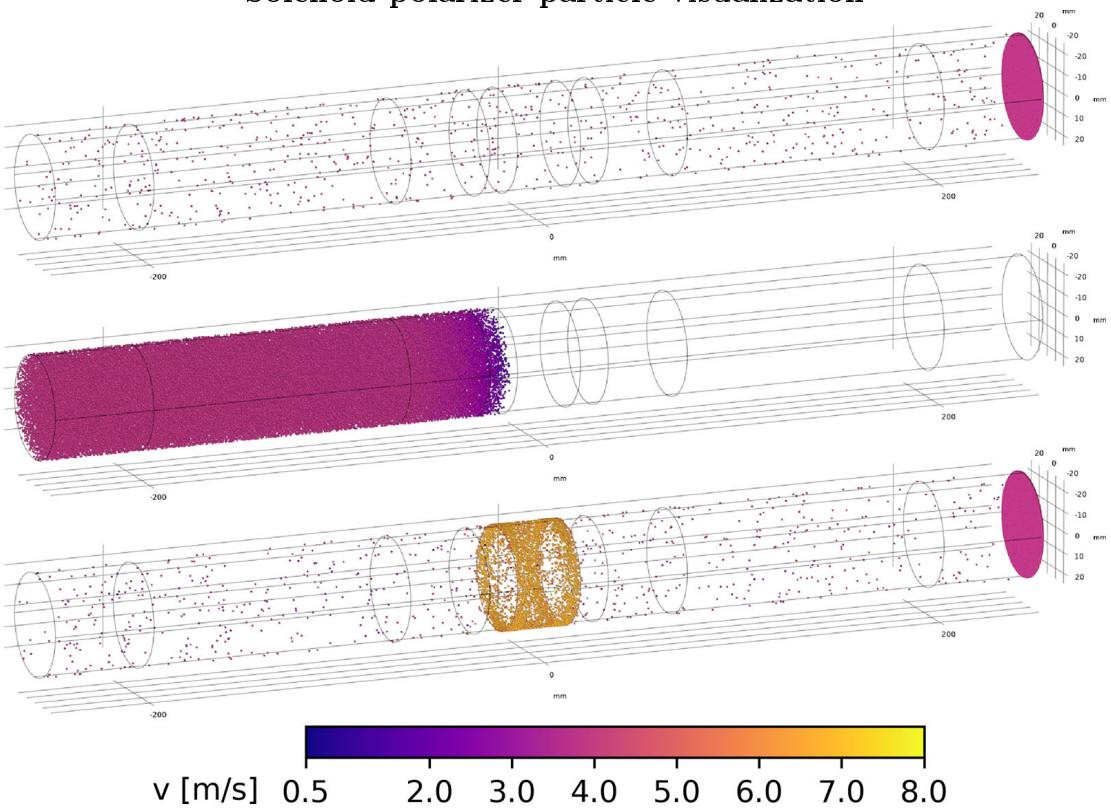

Figure 4.25: Visualization of fig 4.24. Visible is the distribution of UCN at the end of the 2 s runtime for B off (top), LFS (middle) and HFS (bottom). UCN lost are shown at the position of their last wall collision. The color scheme represents the velocity. One can see the confinement of LFS upstream of the SP field and the excess loss of HFS in the center.

Parametric simulation parameter

Parameter	Values	# Values
v_z [m/s]	0.5 to 20 with Δ= 0.5	39
v_r/v_z [1]	0, 0.05, 0.1, 0.2, 0.5, 1, 3	7
Wall specularity [1]	0.95, 1	2
Magnetic interaction	B off, HFS , LFS	3
	Sum	1638

Table 4.4: Table of all simulated parameters for a parametric treatment of UCN transmission in the UCN solenoid polarizer (SP).

$3 \times 500[\text{mm}]/v_z$. All particles start from a random position on the cross-section[25] with a fixed v_z, v_r/v_z. This means the propagation velocity was the same for all particles, as well as the angle by which the UCN "entered" the simulation. At the end of the simulation runtime, the final v_z and v_r for all particles which passed the guide were processed by a kernel density estimation (KDE) with a gaussian kernel. This created an estimate of the probability density function (PDF) of the final $v_{\text{z,KDE}}$. Gaussian KDEs is a useful method for unimodal distributions where PDFs are needed without a particular distribution model.

The magnetic interaction follows the same model as discussed in eqn. 4.15. In contrast to the previous simulation, both exits of the guide are open for UCN to exit. Meaning UCN can be lost to reverse flow, where they propagate towards the source. If UCN reach the entrance window, their chance of loss is 95% and the chance to re-emission into the guide volume is 5%. This change was made to better reflect the situation at the PF2/TES beam. For SuperSUN one can argue, that the loss from reverse flow should be smaller. An exemplary result of this process is shown in figure 4.26.

The plot summarizes the result of all runs with $v_r/v_z = 0.5$ of LFS. The full set of plots can be found in section 6.1 in the appendix. To improve clarity only half of the 39 available v_z are shown. The top plot displays the normalized PDFs of $\text{v}_{\text{z,KDE}}$ color-coded by their initial v_z. In most scenarios, the center of the distributions also happens to align with the initial velocity. UCN initially belonging to a particular velocity bin tend to leak into neighboring velocity bins with a tendency towards lower velocities. The PDFs are normalized, thus the fraction of UCN transmitted cannot be extracted from the top plot. For $v_{\text{total}}<4.19\,\text{m}\,\text{s}^{-1}$, LFS are unable to pass the magnetic barrier. The dotted vertical line indicates the minimum of the theoretical magnetic barrier of the SP for a UCN with $v_z = v = 4.188\,\text{m}\,\text{s}^{-1} = 91.7\,\text{neV}$. The solid lines show the case of an ideal guide with only specular reflection. The widening of the distribution is a result o the geometry of the guide. If a fraction of 5 % of reflections are diffuse, the distribution widens from additional random reshuffling of velocity components. It should be stressed here, that the fraction of diffuse reflections is a property of the guide surface.

The bottom plot indicates the fraction of UCN occupying one of four possible final states at the end of the simulated time. UCN which exit the guide towards the detector are 'transmitted'. Those reflected back to the source are labeled 'reverse flow'. UCN which are up-scattered at wall collisions are labeled 'wall loss' and particles which remained inside the guide volume correspondingly 'in volume. The last case is only significant for LFS which get caught in low-velocity trajectories close to the barrier. These could be eliminated from the simulation with longer runtimes, but since we care mostly about transmitted UCN we can assume these UCN to be effectively lost.

Here it is useful to recall, that UCN with a non-zero transverse component and v_z close to the theoretical value have kinetic energy high enough to pass - therefore a small fraction of UCN are shown as transmitted. For higher velocities, the velocity component normal to the wall at interactions exceeds the critical velocity of copper and UCN are lost to the wall.

In agreement with conventional observations, a small fraction of diffuse reflections can significantly alter the transport behavior of guides.

[25] This assumption is not necessarily true. Many high-velocity components stay only trapped in guide performing so-called Garland-reflection: A spiral of small-angle reflections. In this case, the density of UCN is concentrated close to the edge.

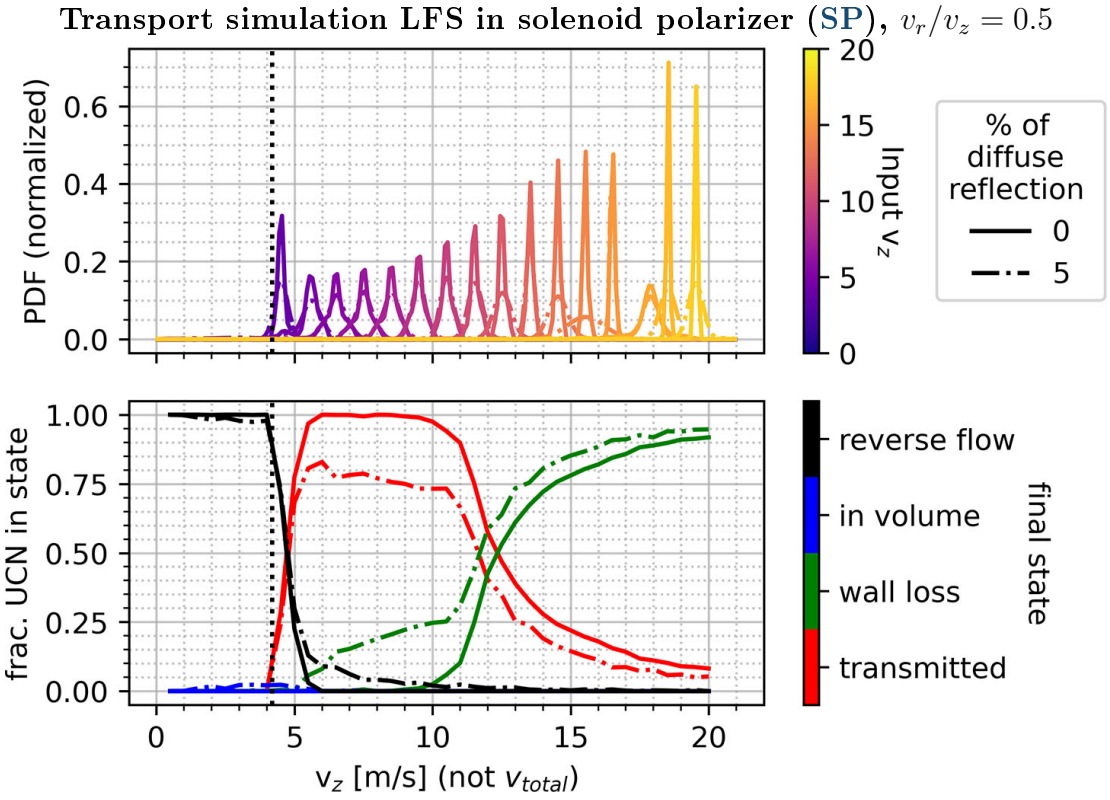

Figure 4.26: Simulation of LFS with $v_r/v_z = 0.5$ propagating along a 50 cm Cu guide and the Solenoid Polarizer. The top plot shows the widening of v_z for initially fixed v_z. The bottom plot shows the 'fate' of UCN. All solid lines correspond to purely specular UCN propagation where dashed lines correspond to a 5% fraction of diffuse wall interactions. The LFS are reflected at the magnetic barrier as expected for low velocities. Wall loss dominates once the kinetic energy exceeds the Fermi potential of the Cu guide.

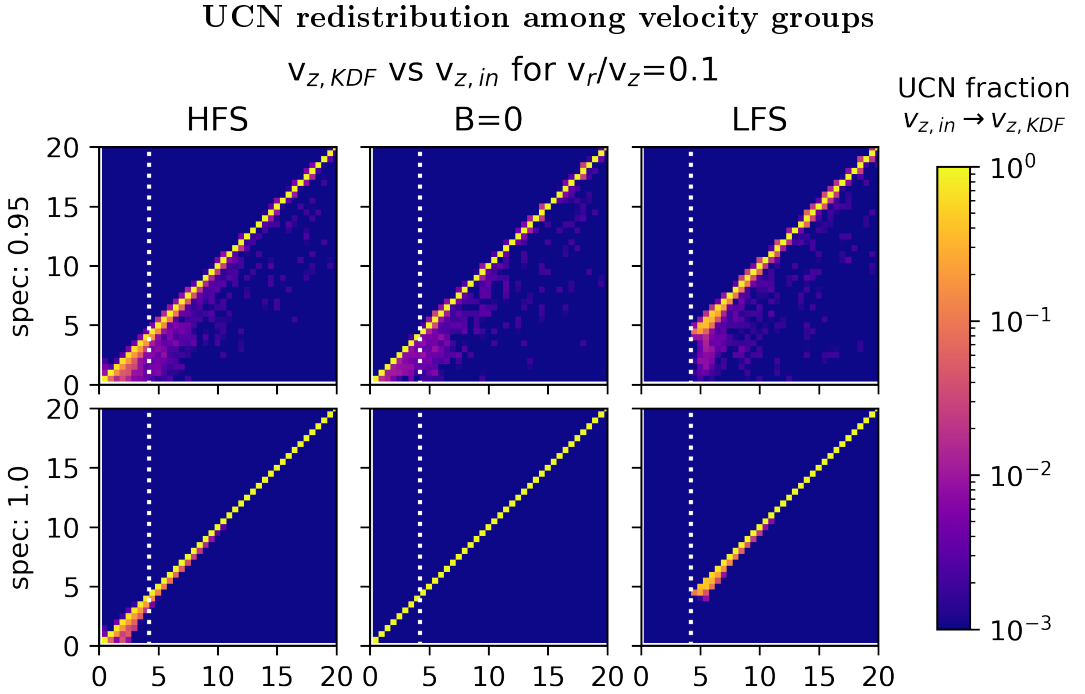

Figure 4.27: Redistribution of the longitudinal velocity of UCN passing the SP. The six plots represent a transfer matrix for a input vector of longitudinal velocities (v_z binned: $\{0.5; 20; \Delta v = 0.5\}$) to a equally binned output $v_{z,KDF}$. In the absence of a magnetic field ($B = 0$) and for perfectly specular reflection (spec: 1.0) the matrix is simply the identity matrix. Low field seeker (LFS) have not transmission below the critical velocity of the magnetic barrier (white dotted line). In the presence of a magnetic field high field seeker (HFS) and LFS are redistributed to lower output velocities.

We can now use the simulation results to create a matrix that transforms any input distribution of velocities into an output distribution without the need for new Monte Carlo simulations and gain insight into how velocity groups redistribute. Fig 4.27 is a visual representation of six transmission matrices for a fixed ratio $v_r/v_z = 0.1$. The PDFs have been weighted with the effective transmission for each entry[26], thus the sum of all matrix elements <1 and corresponds to the total transmission of the guide.

The simplest transmission matrix is the identity matrix, where each particle maintains its forward velocity. This is the case for $B = 0$, perfectly specular reflection and $v_r/v_z = 0$. For finite angles or in the presence of a magnetic field, UCN get redistributed into other velocity classes. In the particular plot, high-velocity classes in HFS and LFS visibly leak into lower velocity classes.

4.5.7 Experimental tests

The SP was tested as a UCN barrier at the ILL UCN source PF2/TES in Cycle no. 189 (March 2021) and Cycle no. 190 (May 2021) in a beamtime run by Hanno Filter. The

[26] Basically each row is the binned sum of the top plot from fig 4.26 multiplied with its corresponding 'transmitted' final state.

main purpose of this beamtime was set testing of detection methods inside high fields, utilizing the inner field of the SP. As part of the commissioning the SP transmission of an unpolarized beam was measured with a time of flight (TOF) setup for different operation currents.

Setup

The UCN are guided via 3 m of stainless steel guide (DIA 81.5 mm) from the PF2/TES port to the SP. A stainless steel adapter with a polyethylen absorber insert reduces the beam diameter from 81.5 mm to 50 mm and transitions to a 500 mm NiMo 85/15 coated glass guide which is connected to the 215 mm long Cu guide inside the SP (ID 50 mm, OD 52 mm). Downstream the SP a 305 mm long stainless steel guide connects to a time of flight setup consisting of a chopper[27], a 1016 mm, ID 81.5 mm propagation guide and a UCN detector. The setup as described uses an unpolarized UCN beam and has no polarization-dependent detection (panEDM CASCADE detector), thus any effect the SP imprints on the beam is observed in the count rate. The TOF allows classifying UCN by their travel time which is expressed in bins of wavelength of $\Delta\lambda$=4 nm from 0 to 304 nm. In this discussion, the data has been rebinned into velocity groups of v_z for a more intuitive relation to the previously discussed simulations. The chopper is a slightly modified version used in (Lauer 2010) has horizontally moving blends which open and close every 50 ms to gate a short pulse of UCN into the propagation guide. The CASCADE detector uses a trigger signal from the chopper to record the time of flight. With corrections for signal delay, one can infer on the propagation velocity of the UCN.

This method has several substantial drawbacks: The exact propagation length is geometry dependent and in particular affected by the guide diameter. The propagation time has numerous electronic and mechanical delays which can retain uncertainty[28]. The method is only sensitive to the average forward velocity component v_z[29]- as addressed by the simulation in the previous section for the SP. When the UCN propagate with a small angular spread the method is a good approximation for the total velocity and thus the energy. For longer propagation guides, smaller propagation guide diameter and larger angular distribution of UCN velocities, the TOF spectrum is no longer a reliable tool to investigate the kinetic energy of UCN.

PF2/TES has a spectrum peaking at v_z=8.4 m s^{-1} ($\bar{v_z}$=9.6 m s^{-1}) which is well above the critical velocity of the guide surfaces. After 3 m of stainless steel guide one expects a narrow angular distribution. This is in sharp contrast with the future application of the SP at SuperSUN, where $\bar{v_z}$=3.91 m s^{-1} and a Lamerbtian angular distribution can be assumed. Only 7 % of UCN have $E_{\text{kin}} < E_{\text{SP barrier}}$, thus >90 % of counts are background and exhibit systematic effects.

The TOF measurement was conducted with 7 different SP currents, i.e. 0,50,60,70,80,90 and 100 % of 300 A. The ratio of a TOF with finite current and I=0, shows the relative impact of the SP per velocity class. Naively one expects the count ratio in bins with $E_{\text{kin}} < E_{\text{SP barrier}}$ to be 1/2 and for bins with $E_{\text{kin}} > E_{\text{SP barrier}}$ to be 1. From section 4.5.5 we expect an additional loss of HFS which has an energy dependence and was

[27] Similar to the one described in (Lauer 2010)

[28] Both effects could be partially mitigated if the experiment is conducted for at least two propagation lengths. Extrapolation to zero allows removing a majority of these factors.

[29] Here we use the convention of v_z as the velocity component along a cylindrical guide and v_r as the transverse/radial component.

simulated to be $\eta_{\mathrm{HFS,80\ neV,\ loss}} \sim 6\,\%$.

Simulation

To support the understanding of the experimental results, the simulations presented in section 4.5.6 is applied to the experimental setup.

Input spectrum simulation The input spectrum is simulated based on TOF data from TES/PF2 (Jenke 2021) combined with the aforementioned setup. Fig. 4.28 provides the expected distribution of UCN at the inlet of the SP given in the parameter space established in section 4.5.6. The angular distribution of PF2/TES was simulated with a Lambertian angular distribution ($I = I_0 \cos\theta$) with $\tan(\theta) = v_r/v_z$ in lieu of available data. This is in practice of small concern, as the long stainless steel guide section dominated the shape of the angular distribution for a wide range of plausible angular distributions. This is shown in fig. 4.28 with a dash-dotted line defined by $v_r = v_{\mathrm{crit,\ SS}}$, the cutoff from the Fermi potential of steel. The strong forward concentration of the beam is also apparent in the v_r/v_z histogram bottom right. The simulation also showed velocity classes below $4\,\mathrm{m\,s^{-1}}$ gain relatively to the PF2/TES input distribution (see top left histogram).

Output spectrum We can now apply the transmission matrix from section 4.5.6 on the input spectrum and yield the expected idealized TOF signal[30] at the SP output guide. Results are provided seperatly for $B = 0$, HFS and LFS in figure 4.29 and 4.30. The top subplot shows the v_z spectrum color-coded by the longitudinal velocity of the particles at the time they left the PF2/TES output. The composition per velocity bin is given in the 'vz composition' and the bottom subplot. The latter groups all UCN into those who started with a lower ($v_{\mathrm{initial}} < v_z$), a similar ($v_{\mathrm{initial}} = v_z$)or a higher ($v_{\mathrm{initial}} > v_z$) initial velocity. To illustrate this, one can observe fig. 4.30 for LFS with $v_z < \mathrm{SP}_{\text{cut-off}}$, where all UCN present have to stem from higher velocity classes.

Results

The central result of the measurement and simulation effort is shown if figure 4.31. Depicted is the relative transmission of the SP of an unpolarized beam for different longitudinal velocities v_z. The transmission is given as a relative deviation from the TOF transmission without magnetic field. $(R - R(B = 0))/R(B = 0)$. The simulation result corresponds to $(R_{\mathrm{HFS}} + R_{\mathrm{LFS}})/(2 \cdot R_{\mathrm{B=0}}$, where R_{noB}, R_{HFS} and R_{LFS} are the v_z spectra from the top subplots in fig. 4.29 and 4.30. The measured TOF spectra are shown as colorized solid lines, uncertainties are depicted as shaded bands of matching color. The critical velocity of the SP for each current is provided as v_{cut} and marked with a dotted line in the plot.

For velocity far above the critical velocity simulation and measured results approach 0, as expected. Between $3\,\mathrm{m\,s^{-1}}$ and $5\,\mathrm{m\,s^{-1}}$ the transmission is reduced correlated with the SP current. The observed transmission reduction for the full magnetic field is only half of the simulated magnitude. This is surprising, as the contrast of the simulation is already below the naive estimate of 0.5. The weak dip in relative transmission means

[30] The TOF itself suffers from the same effects of velocity redistribution. Simulation of the use TOF geometry can be found in the appendix 6.2

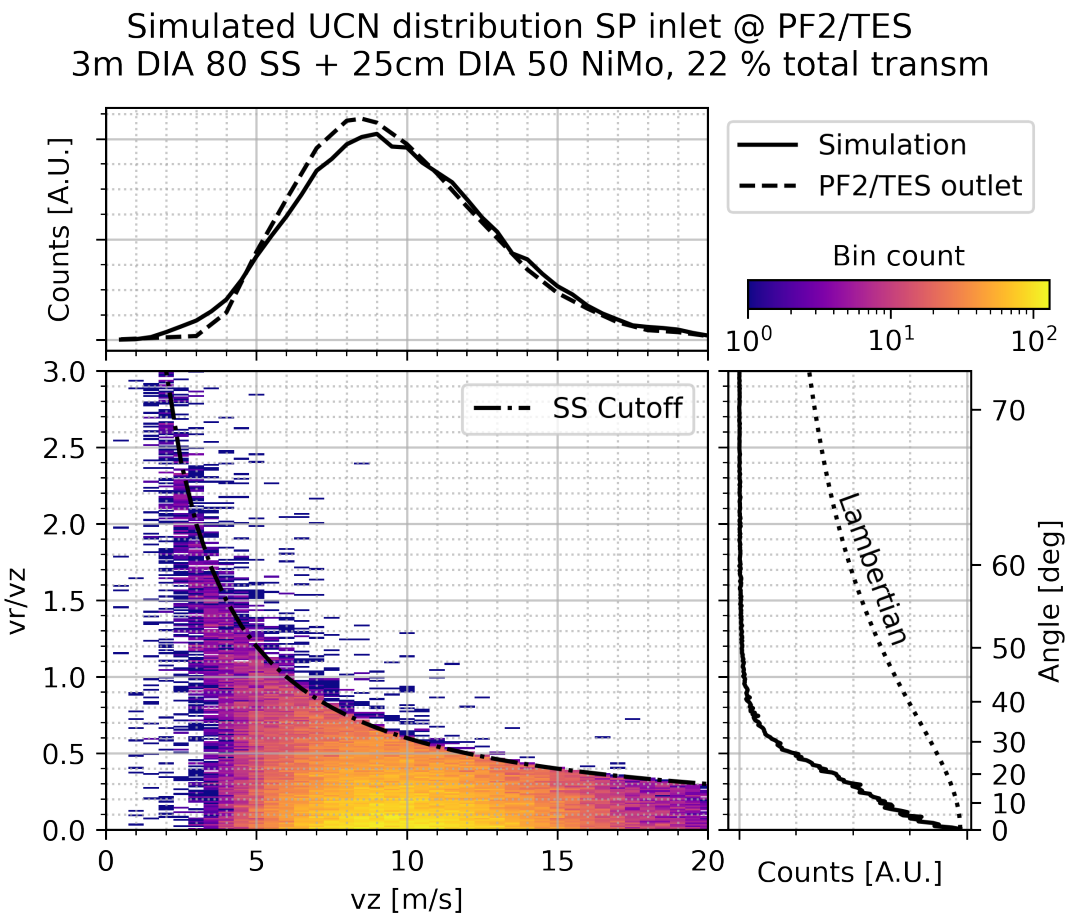

Figure 4.28: Simulation of expected UCN velocity distribution in forward direction (v_z) and radial direction (v_r) at the inlet of the SP. The central histogram shows the cutoff from the Fermi potential of the stainless steel guide section which follows directly after the PF2/TES outlet. The top histogram highlights a slight redistribution of UCN towards lower velocities. The large amount of high energy UCN paired with the fairly low Fermi potential of steel causes a strong forward filtering of the flux. UCN with large radial components are lost to the guide walls. For reference, a Lambertian angular distribution is shown which is a popular model for diffuse surface scattering.

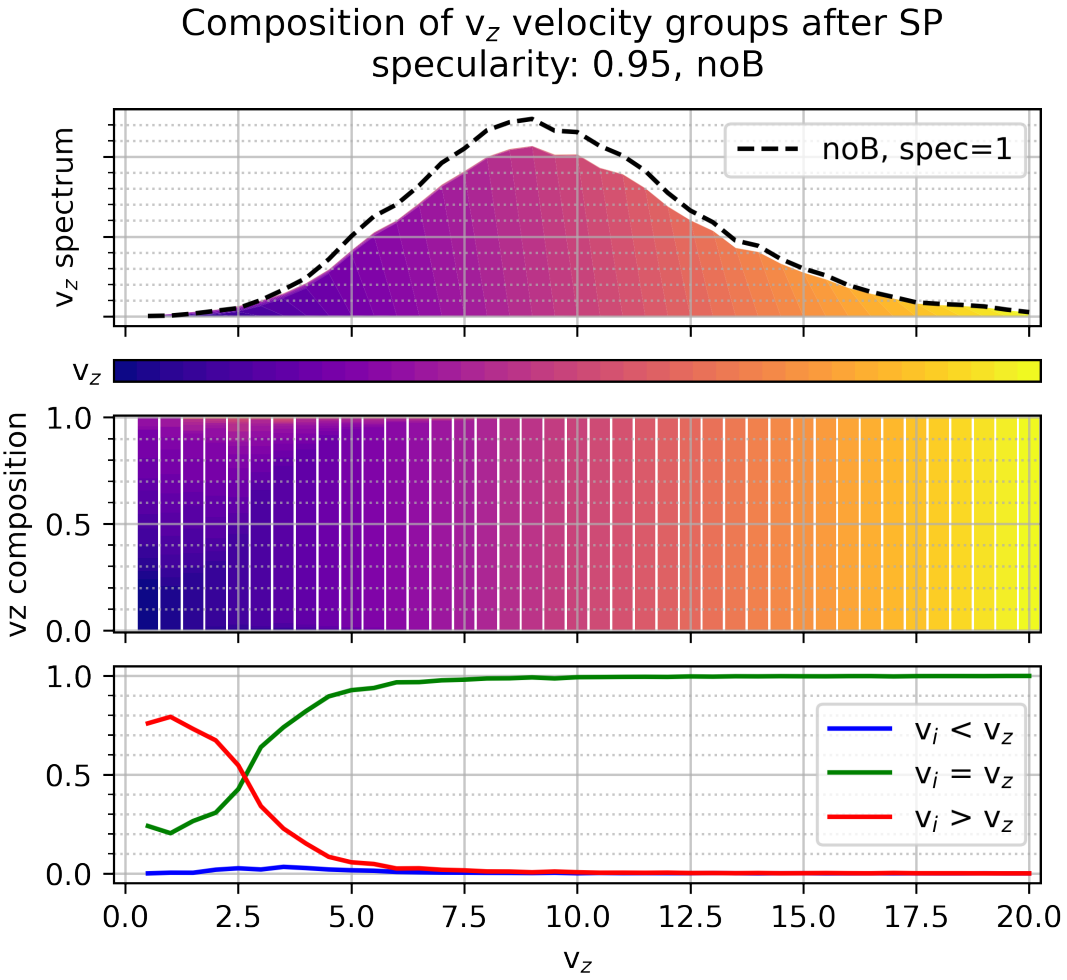

Figure 4.29: Simulated velocity spectrum for transmission of the SP when switched off (noB). This analysis highlights the mixing of velocity groups within the apparatus and the SP. The color coding in the top and middle plot refers to the initial velocity in the PF2/TES spectrum. UCN can change the velocity through diffuse scattering or geometry effects. TOF measurements are sensitive only to the average forward velocity, hence they do not identify kinetic energies. This mixing can result in artifacts for low velocities. The majority of UCN attributed to forward velocities $v_z < 2.5\,\mathrm{m\,s^{-1}}$ entered the apparatus with a higher velocity. Fig. 4.30 show similar simulation results for low field seeker (LFS) and high field seeker (HFS) respectively for a $B = B_{\max}$.

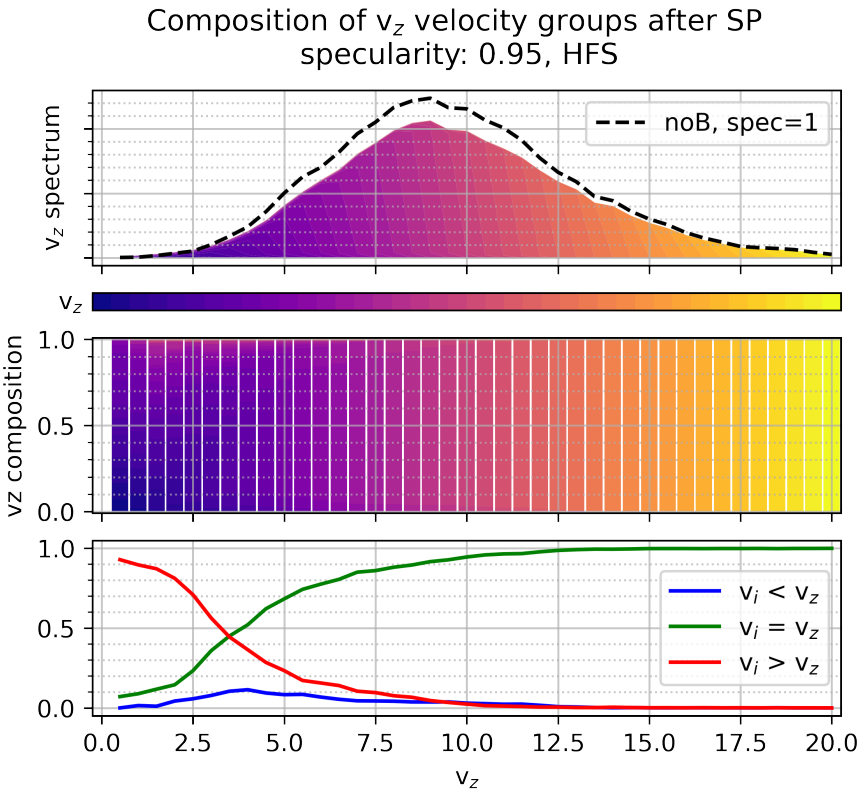

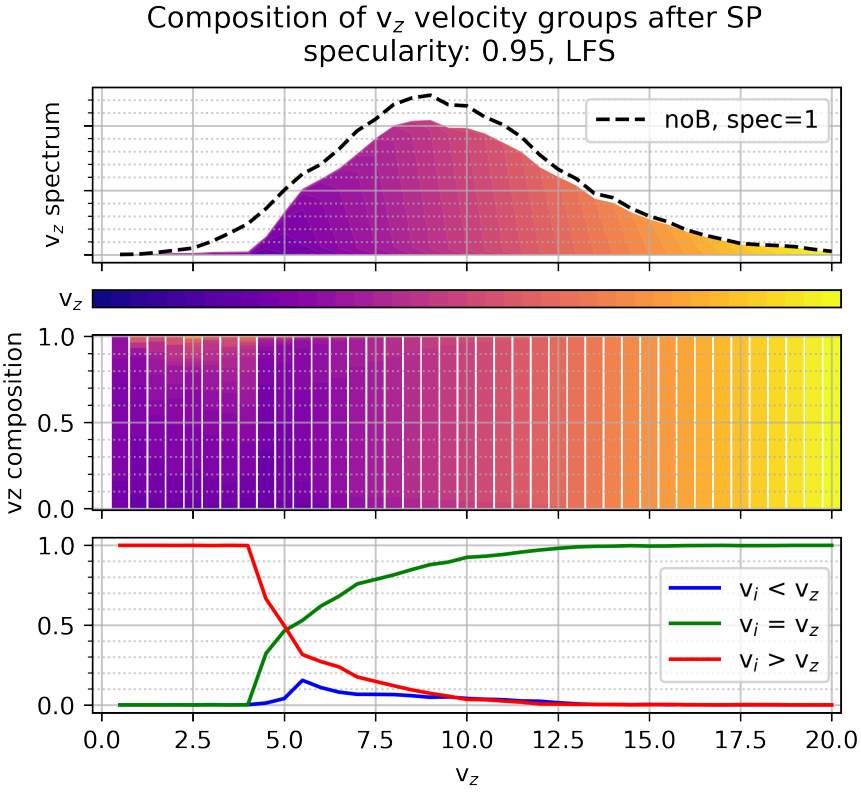

Figure 4.30: See 4.29

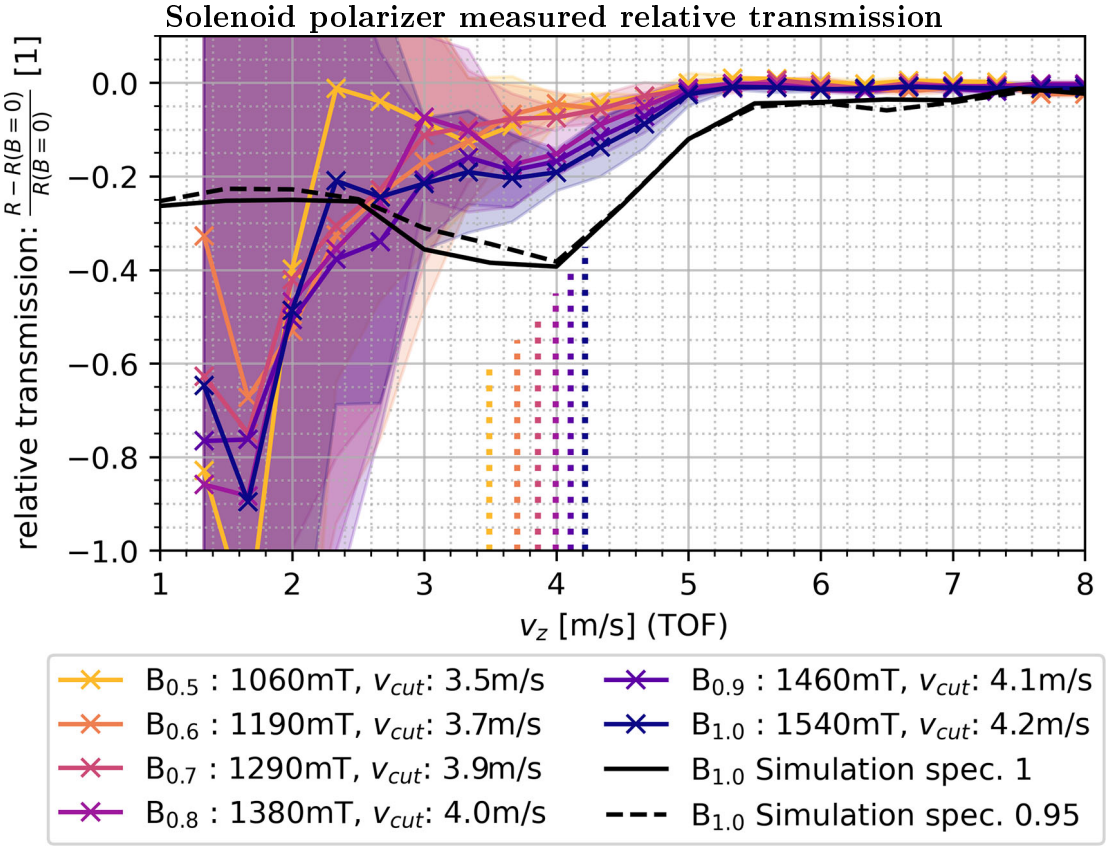

Figure 4.31: Results from testing the UCN polarizer at the PF2/TES beam. Shown is the ratio of UCN transmission rate relative to B=0 for different forward (v_z) velocities. The shaded area marks the uncertainty of measurements. The solid (dashed) black line shows the results of a full simulation of the experiment from first principle for a surface specularity of 1 (0.95). It is clearly visible that all ratios approach 0 for velocities far above the magnetic barrier - as expected. Between 3 and 5 $m\,s^{-1}$ the rising sections are shifted related to the height of the magnetic barrier.

that more UCN velocity changes occur in the apparatus than anticipated. It should be noted, that the simulation is based on the input spectra, the geometry, the magnetic field and the wall materials. It has no free parameters which could be fitted to measured transmission results. One could extend the simulations to cases with a smaller fraction of diffuse scattering of UCN. A more natural next step is a dedicated experimental setup with a polarized input beam and a spin flipper combined with a spectrum shaper for copper (V_{Cu}=165 neV,v_{crit}= 5.62 $m\,s^{-1}$). This would provide a clean probe where the transmission of LFS and HFS could be tested with attenuated contributions from velocity classes far above the SP's critical velocity. This result also adds to the list of examples where TOF results have to be interpreted with caution.

4.6 UCN switches

As previously discussed (see 4.1) one can model UCN transport as free molecular flow with highly specular wall interactions. While flawed, this model helps identify challenges

Figure 4.32: Slitless dPE UCN valve (Windmayer 2016).

in designing switches for UCN. A UCN switch should avoid strong bends and maintain the guide diameter across the switch everywhere. The mechanics should not introduce gabs and UCN facing parts have to be made from (or feasible to coat with) suitable guiding materials.

Traditionally switches and valves are based on flaps that open or seal guide sections, or revolver/interchanger designs where a guide sections are replaced. Recent examples can be found in (Bison et al. 2020; Hingerl 2019).

An alternative slit-less valve (Windmayer 2016) was developed based on a flexible guide sections made from deuterated polyethylene (dPE) (Brenner et al. 2015). A mechanical clamp squeezes the flexible hose to close the valve. (see fig 4.32). A built prototype could be operated for more than a thousand cycles without significant degradation. The key challenge for application resides with vacuum operation and the delicate mechanics which 'fold' the hose without wrinkles into the closed position and vice versa.

At present all three switches for panEDM are based on rigid mechanical guide sections interchanged at the beam path via rotation. All three switches use sections of straight pipe or $\pi/2$ fractions of a horn torus[31] made from solid metal via 5-axis milling. The resulting parts are then hand-polished to optical quality. The details of each switch are given in the following sections in the order of UCN propagation in the experiment.

A crucial common feature is the surface quality of guide sections. SW and TWs operate with solid copper blocks from which the straight or bent guide sections are milled. The parts are then polished by hand or with mechanical supports using cloth and diamond paste. The resulting surfaces are optically polished and show no defects for straight sections and minor, thin scratches for custom-shaped parts. Achieved surface roughness are R_a[32] $= 0.025\,\mu m$,R_q[33] $= 0.033\,\mu m$ and R_z[34] $= 0.215\,\mu m$. As a reference: electro-polished stainless steel DN50 sterri-tubes[35], which are a standard UCN guide tube, measured on the same device [36] have $R_a = 0.06\,\mu m$ and $R_z = 0.42\,\mu m$. Using solid copper has two advantages: Scratches and indents which occur at later handling or in operation don't reveal an UCN absorbing material. The material is stable over time

[31] Torus with R=r
[32] Arithmetic mean deviation
[33] Root mean square
[34] Mean peak to valley height
[35] STERI-Tube DN050 DIN Ø53x1.5, e-pol./K400,1.4435 DIN 11866;G. A. Kiesel GmbH, Wannenäckerstr. 20, 74078 Heilbronn
[36] ST1 Garant, Hoffmann GmbH: Surface roughness measuring tool ST1 GARANT, 2018

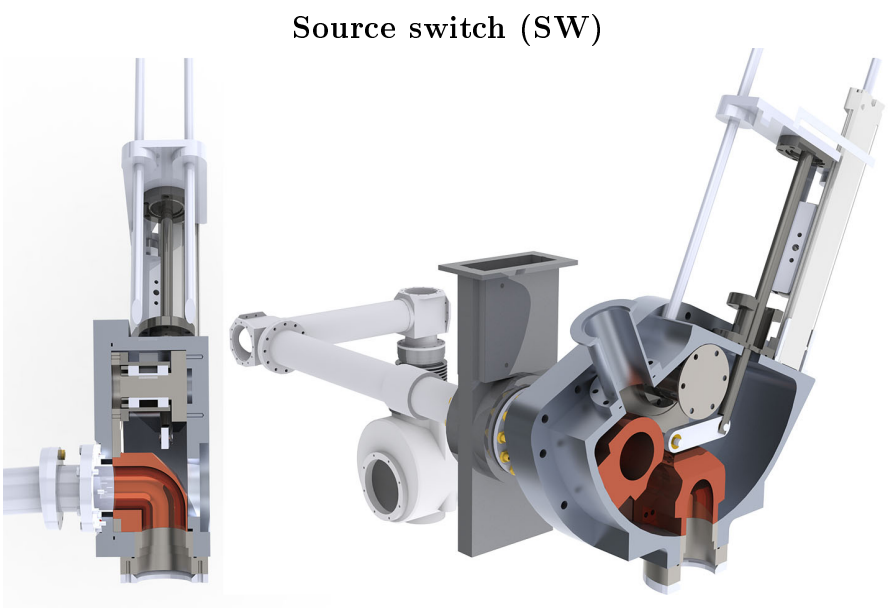

Figure 4.33: Rendering of the source switch (SW). Two copper blocks rotate about a horizontal axis to either guide UCN from the source downwards to the source monitor detector or into the panEDM apparatus. The right rendering shows parts of the extraction system inside SuperSUN.

and can be machined and easily replaced. The rather low Fermi potential is no strong detriment in an experiment with a very soft UCN spectrum.

4.6.1 Source switch (SW)

When exiting from SuperSUN, UCN might be guided down towards a ^{3}He detector (see 2.5) or forward into the SP. A rotating stainless steel support holds 2 copper junction blocks. One block has a straight DIA 50 mm bore, the second block a DIA 50 mm horn torroid 90° bend. The steel plate rotates about two oil-free, full ceramic ball bearings inside a custom aluminum vacuum vessel. An outside pneumatic actuator moves a spring bellow which drives the rotation of the steel plate, thus vacuum is maintained during operation. The two mechanical end positions of the SW correspond to the two operating points. In addition to the three guide openings, a KF 50 vacuum pump port is present to pump the switch as well as the UCN guide system for panEDM.

The switch is built and mechanically tested. Once the mechanical interface to SuperSUN is finalized it can be commissioned.

4.6.2 Three-way switches (TW)

The two three-way switches (TWs) each connect an exit of the guide manifold (GM), a UCN cell filling guide and the simultaneous spin detection branches (GY). During regular operation the switch resumes three states:

- Filling: when UCN pass from the SuperSUN through the GM into the filling guide.
- Monitoring: During he Ramsey sequence UCN from the source are guided to the

simultaneous spin detection to provide rate measurements on background levels and to quantify detection efficiency drifts

- Readout: UCN from the storage cells propagate to the simultaneous spin detection system

As a fourth option a junction block that links all three ports was added, although it is not intended for use in panEDM, but might be needed for prior tests. A revolver mechanism places one of these four junction blocks between three static ports. The TW and SW both use the same copper blocks[37]. The TW also uses ceramic ball bearings but instead of a pneumatic actuator, a magnetically coupled stepper motor rotates the steel plate which hosts the junction blocks. The plate provides a total of six mounting positions of which four are used by junction blocks and two are occupied by balance weights which place the rotor's center of mass on the axis and removed up to 0.30 N m of static torque. The mass of the full rotor is 17.5 kg, the average mass of a copper junction block is 2.56 kg. A section cut of the switch is shown in fig 4.34. The moving parts have a clearance to the ports of 0.1 mm which is remarkable. In the case of the TWs, this total clearance is maintained across five mechanical links for a rotor of ∼30 kg. The mechanical tolerance is also the gap through which UCN are lost. Thus the gap was made as small as possible for a reliable mechanism. The TW have vacuum pumping ports (ISO-K 100) where the switched themselves as well as the UCN guide system for panEDM is pumped.

Experimental tests

One of two TWs was part of a beam time for testing storage times and emptying efficiencies for panEDM (Neulinger et al. 2021). Testing of the TW was not the primary objective of this run, but two results related to the TWs could be extracted. The switch itself was successfully used a guided UCN from a horizontal incoming beam-line downwards to UCN detector. Transmission through the 90-degree forward bend (later used to connect source and detectors during background and drift measurements) was reasonable on the order of one. A proper transmission measurement could not be conducted and the uncertainty on upstream transmission properties prohibits the calculation of a credible estimate. Since the TW was used in it full configuration, the effect of the rotor position on beam transmission had to be tested. Across a series of measurements the rotor (and the 90° bend) were shifted by small angular increments, then counts were accumulated for each position. These counts were corrected by a monitor detector to account for fluctuations in beam intensity due to reactor power or source efficiency changes. Fig 4.35 shows the normalized transmission through the TW versus the angular offset from the ideal position given in microsteps and degrees. Two runs (run 5 and run 6) are shown with 1.32° (run 5) and 0.09° (run 6) incremental step size. Between run 5 and run 6 the TW moved to the internal homing position and thus we get a sample of typical positioning uncertainty. An error in positioning appears as a shift of the transmission curve along the horizontal axis which can clearly be seen in the plot insert. Measuring the average shift of both curves, one yields 0.24°. This corresponds to a relative flux uncertainty of 0.07 % and is thus of no concern in operation. While this first test demonstrates functionality under real conditions, a transmission efficiency measurement for all junction blocks and a longer endurance test are planned prior to on-site installation. An interesting tangential

[37] The block in SW and TWs are identical up to an offset in the bent- guide in the SW and a mechanical cut-out.

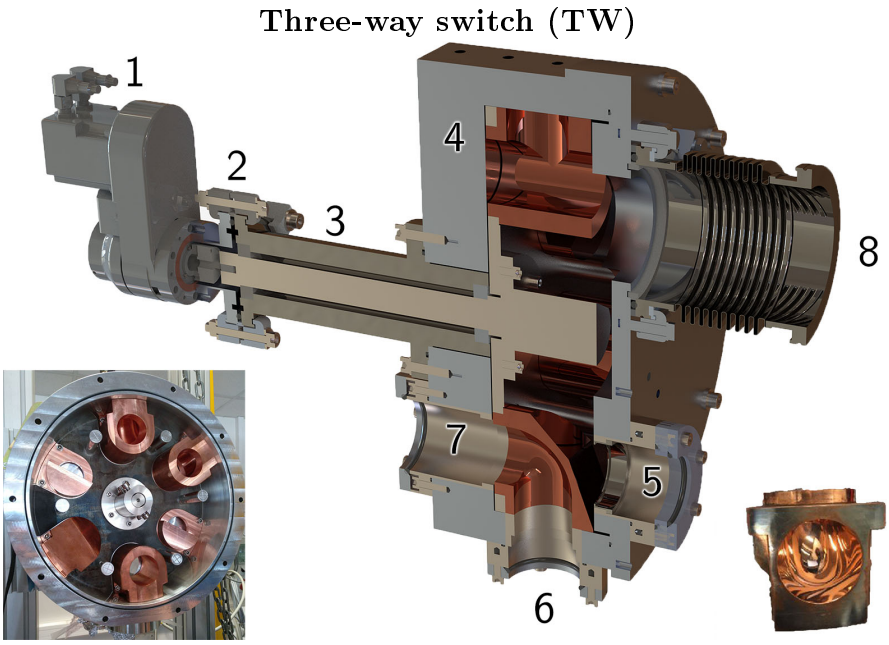

Figure 4.34: The three-way switch (TW). A stepper motor (1) rotates a horizontally suspended axle (3) which is fixed to a stainless steel disc with four copper guide elements + 2 balance weights (bottom left picture). The copper guide elements allow a combination of the three ports (5-7) to be connected. The full mechanism is running on dry Zirconium dioxide bearing in a large aluminum vacuum housing (4) which is pumped with an electrically isolated Turbomolecular pump (8). The copper guide sections are straight sections or $\pi/2$ fractions of a horn torus which are mechanically polished (bottom right).

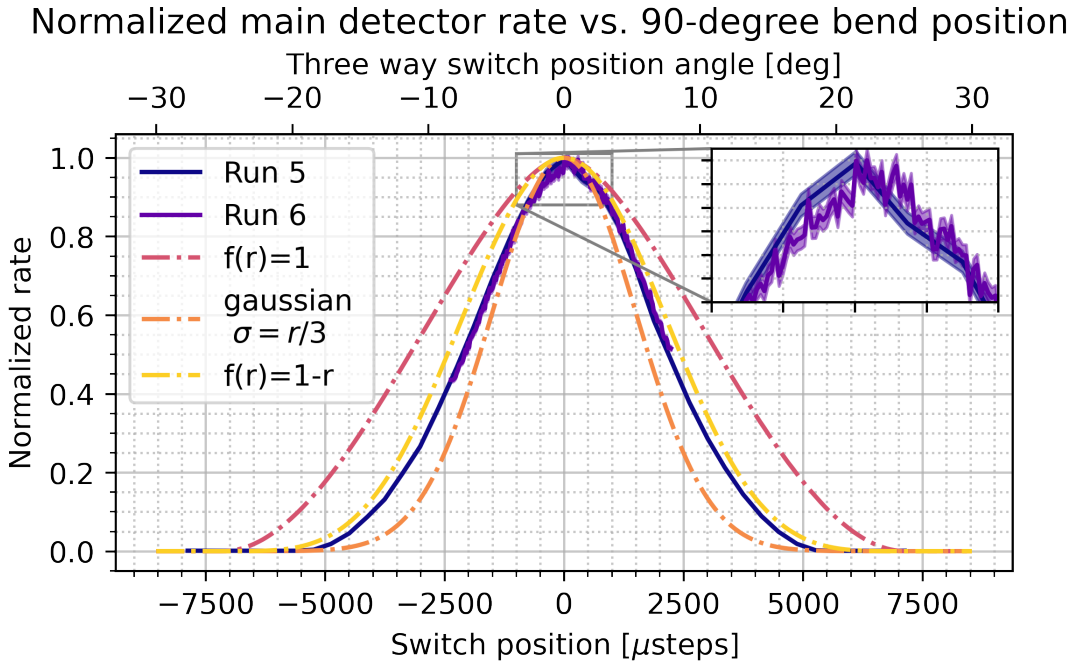

Figure 4.35: Normalized rate of UCN transmission through a 90° copper junction block in a three-way switch (TW) versus angular offset from transmission position. Two example runs (Run 5 and 6) are shown with uncertainty as shaded area. Between both runs, the TW was reset and the horizontal shift between both curves corresponds to the accuracy of the switch of 0.24°

observation can be drawn from the shape of the detector rate. One could argue,that the plot shows the convolution of the UCN beam intensity profile and the transmission profile for a lateral shift[38]. For comparison the auto-correlation of three radio-symmetric intensity profiles are shown with dashed lines: A homogeneous transmission efficiency ($f(r) = 1$) and two distributions declining with radius: $f(r) = 1 - r$ and a Gaussian profile. It is reasonable to assume an even UCN distribution across the supply beam and attribute the transmission through the bend as the defining factor. This would imply, that the 90° bend strongly favors UCN flux close to the center. This distribution - once measures for all junctions blocks - would be a valuable test for UCN transport simulations which is independent of absolute UCN transmission.

4.6.3 Cell valves

The cell valves have more design restrictions than SW and TW. The valve is directly above the EDM cell and closes off the cell during the Ramsey cycle. The parts which are exposed to UCN inside the chamber have to be suitable for UCN storage and the entire mechanism has to be strictly non-magnetic. As discusses earlier - a local dipole of few pT at this proximity causes a false effect on the level of 1×10^{-27} ecm. In addition, the mechanism has to be light enough to not deform the ground electrode substrates. The mechanism should fit within a tight vertical space -ideally within the height of the feed

[38] For a guide with r=25 mm rotating on R=155 mm this is reasonable for a small angle.

guide, such that the mercury cell above can be placed close to the EDM cell. Technically the valve has two independent functions: Establishing a connection from the feed guide to the cell and sealing off the EDM cell during Ramsey cycles. If this seal has a significant gap, UCN are lost and the effective storage time decreases (see eqn. 1.6). The presented design uses two independent actuators for each function made of a beryllium-copper corrugated tube. Pressurized air extends the tubes while elastic silicon or metal springs retract the tubes when air pressure is released. Mechanical stops limit the motion of both actuators. The first actuator rotates the switch from the open to the close position, centering either the 90° guide block or a coated lid above the DIA 50 mm hole in the EDM cell. The second actuator presses the lid against the ground electrode to seal the EDM cell or lifts the lid up by <1 mm when the switch rotates or is in the open position. The 90° guide block is made from aluminum and will be coated with DLC. The lid can be made of aluminum or cut from a wafer and receive the same coating as the EDM cell.

Within a component test beam-time, both cell valves where used to perform storage time measurements on a panEDM EDM cell replica with different coatings (Neulinger et al. 2021) While the valves did operate as intended and storage measurements could be performed, the beam-time unveiled handling deficits and sources of potential long-term failure were found. Within a 100 day panEDM beam-time the cell switches would accumulate $\sim 4.3 \times 10^4$ switching cycles. In the tested iteration, the corrugated beryllium-copper tubes were at least an order of magnitude stiffer than necessary, increasing the required spring stiffness and the necessary air pressure. This in turn added unnecessary tension mounting pins and other connection elements which should be avoided. In addition, the actuation length of the rotational movement will be decreased to reduce the relative length change in the corrugated tube and the return spring.

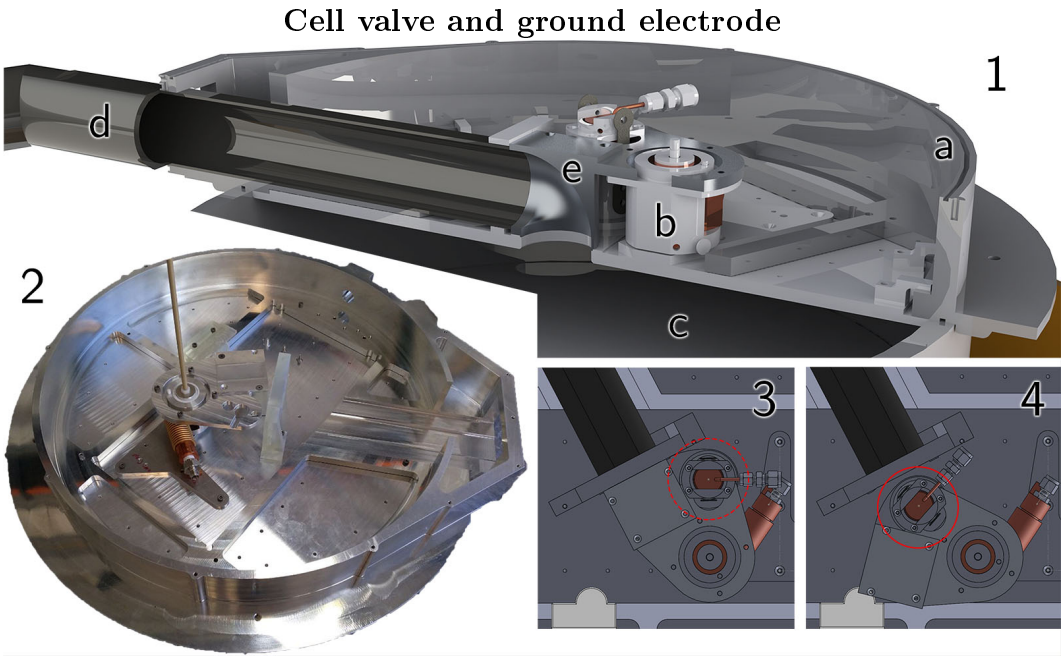

Figure 4.36: Cell valve for filling and emptying for UCN into the EDM cell. Only the top valve is shown. (1) Rendering of the ground electrode (a) with the cell valve (b) on top of the top EDM cell (c) cut along the feed guide (d). The valve is shown in the open position. A 90° section (e) connects the guide to the opening in the ground electrode. (2) Assembly with an uncoated test guide. The valve uses two pneumatic pistons. In the open position (3) the 90° guide block is rotated above the hole in the ground electrode to connect to the feed guide. In the closed position (4) a small coated lid is pressed onto the hole in the ground electrode to seal it for UCN. This lid is lifted by a fraction of a mm before the switch moves towards the open position.

5 Summary and Outlook

The panEDM apparatus and its subsystems have been disassembled and moved to the new UCN source at the ILL. This includes in particular all large hardware components such as the MSR, the vacuum chamber, the degaussing system and major components of the optical magnetometry.

Within this thesis, the UCN guide system was rebuilt to a diameter of 50 mm. Five new switches were designed and built. The new source switch (SW) is ready for test assembly. The new three-way switches (TWs) operated in a UCN test experiment and demonstrated transmission and their functionality as switches. Two new cell valves have been built and tested. While the concept stood up to expectation, the built cells do not employ the required durability and will be revised.

The high voltage and ground electrodes of the EDM cell stack were adapted to host exchangeable inner substrates. A set of high-quality aluminum substrates was built of sufficient flatness and surface finish for phase I. A deuterated diamond-like carbon coating for the electrodes was developed in collaboration with the manufacturer Diamond Hard Surfaces Ltd. The coating has a Fermi potential of $V_{\text{Fermi,d-DLC}} = (205 \pm 10)\,\text{neV}$, obtained by neuron reflectometry measurements and a loss coefficient of $\eta_{\text{d-DLC}} = (4.52 \pm 0.17) \cdot 10^{-5}$ extracted from a storage time measurement at SUN-2. From these results a UCN storage time of $\tau_{\text{simul, EDM cell}} = (278 \pm 5)\,\text{s}$ for panEDM possible which meets the design target of phase I of $\tau_{\text{EDM min}} = 250\,\text{s}$.

Poly-crystalline diamond as a coating alternative was explored which can now be developed into a future coating based on the promising demonstrated Fermi potential of $V_{\text{F, diamond}} = (290 \pm 10)\,\text{neV}$.

A normal conducting UCN polarizing magnet was designed, built and tested for the application in phase I of panEDM. The magnet slightly exceeded its design field target of B_{target}=1500 mT with B_{measured}=1521 mT. The magnetic field was mapped in detail inside the future guide volume. The solenoid polarizer also fulfills its secondary role by providing an adiabatic transport field for panEDM. The magnet operated successfully during two UCN beam experiments with good qualitative agreement of the simulated velocity-dependent transmission.

With a majority of UCN optics completed, system integration on site can move forward in preparation of UCN operation in 2022.

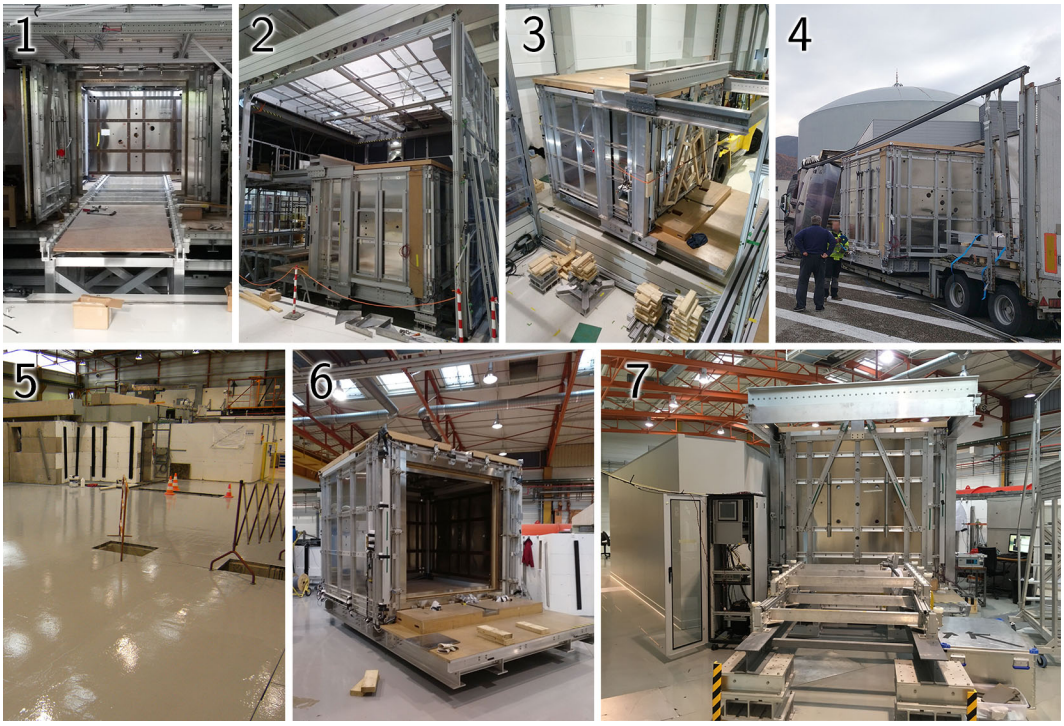

Figure 5.1: Transport of the magnetically shielded room (MSR) as part of the large hardware relocation. The MSR at FRM2, Munich (1). The coil cage was opened at a side (2) to allow a heavy-duty forklift to lift the whole room (3) and place it on an air-suspended truck to transport to ILL (4). The newly made concrete foundation at ILL22 (5), ILL where the MSR is placed (6). (7) shows the current status of the cleanroom installed.

6 Appendix

6.1 Parametric velocity simulation results

This section presents the full parameter space simulated in the guide transmission simulation discussed in sec. 4.5.6. A list of all parameters is shown in table 4.4.

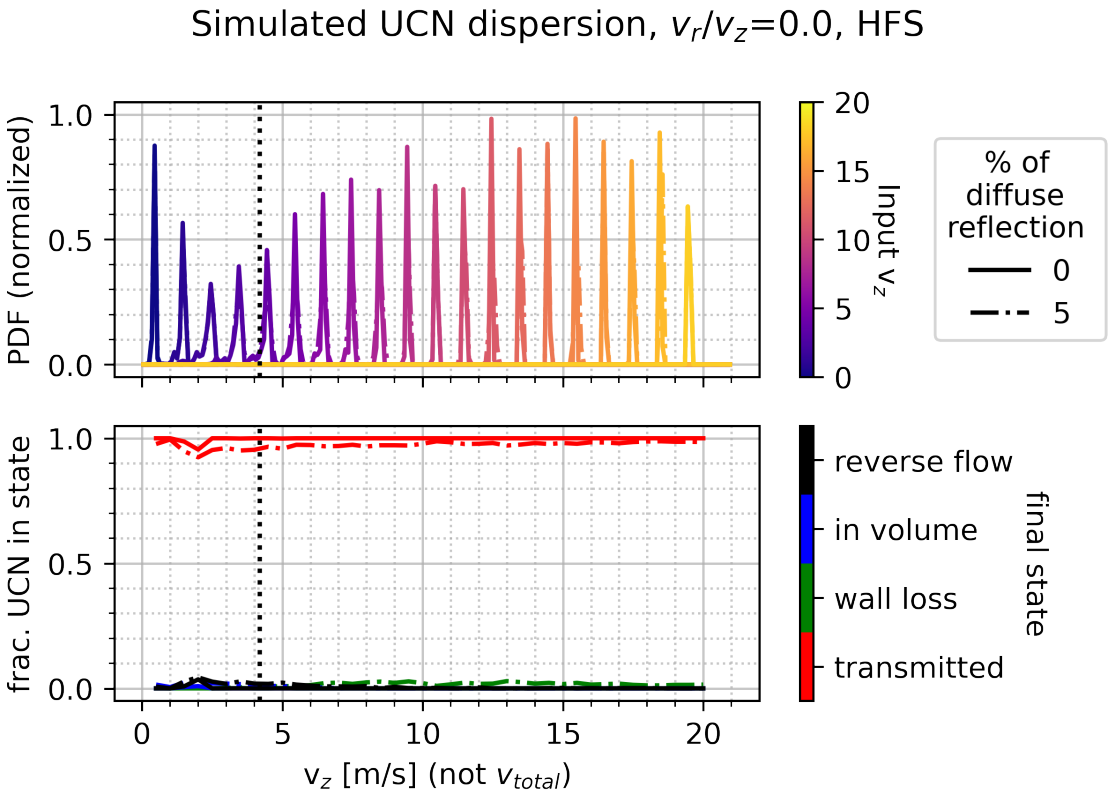

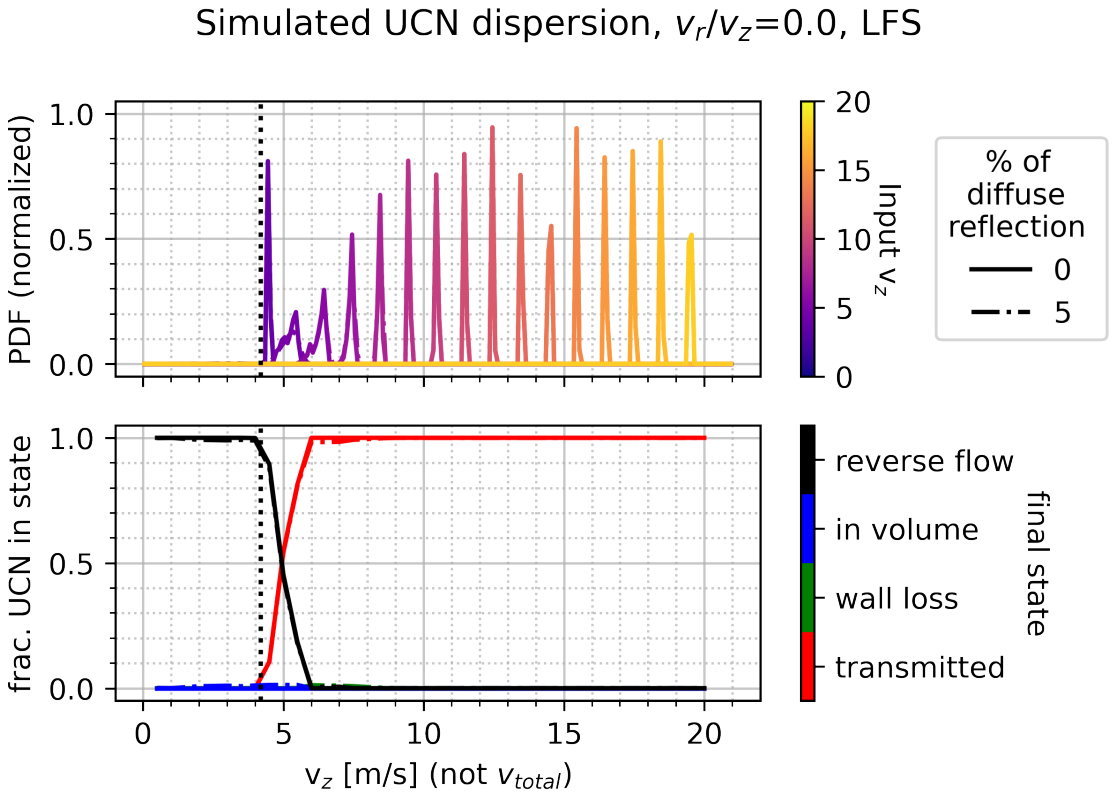
Simulated UCN dispersion, v_r/v_z=0.0, LFS
PDF (normalized)
1.0
0.5
0.0
20
15
10
5
0
Input v_z
% of diffuse reflection
0
5
frac. UCN in state
reverse flow
in volume
wall loss
transmitted
final state
0
5
10
15
20
v_z [m/s] (not v_{total})

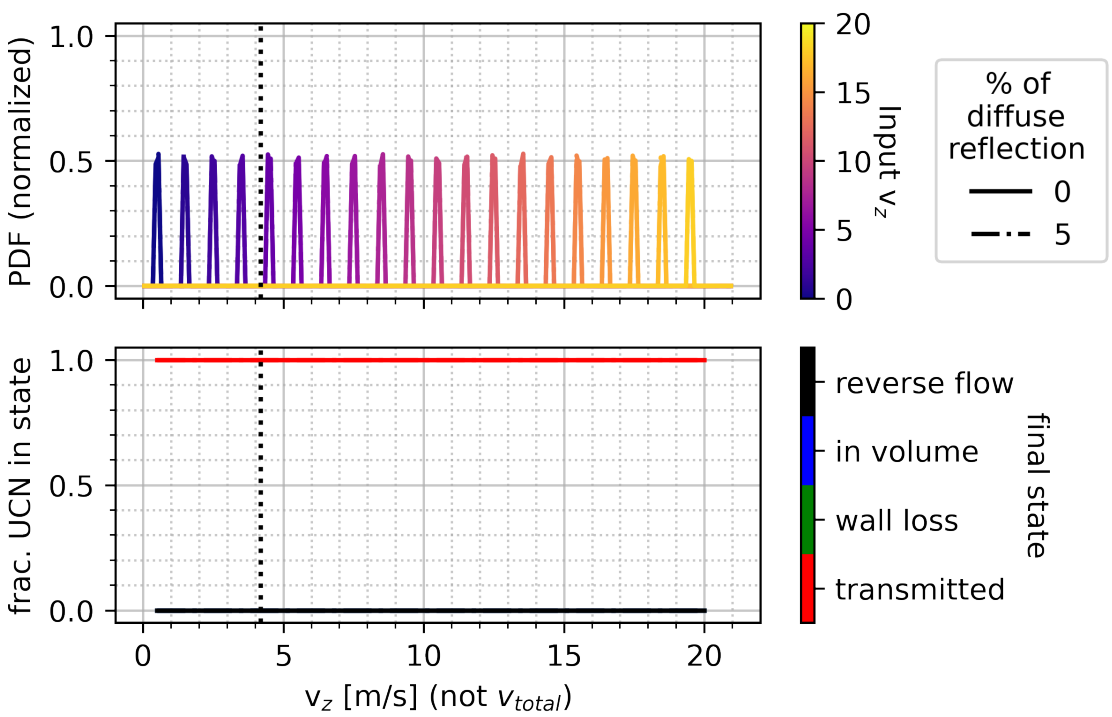
Simulated UCN dispersion, v_r/v_z=0.0, noB
PDF (normalized)
1.0
0.5
0.0
20
15
10
5
0
Input v_z
% of diffuse reflection
0
5
frac. UCN in state
reverse flow
in volume
wall loss
transmitted
final state
0
5
10
15
20
v_z [m/s] (not v_{total})

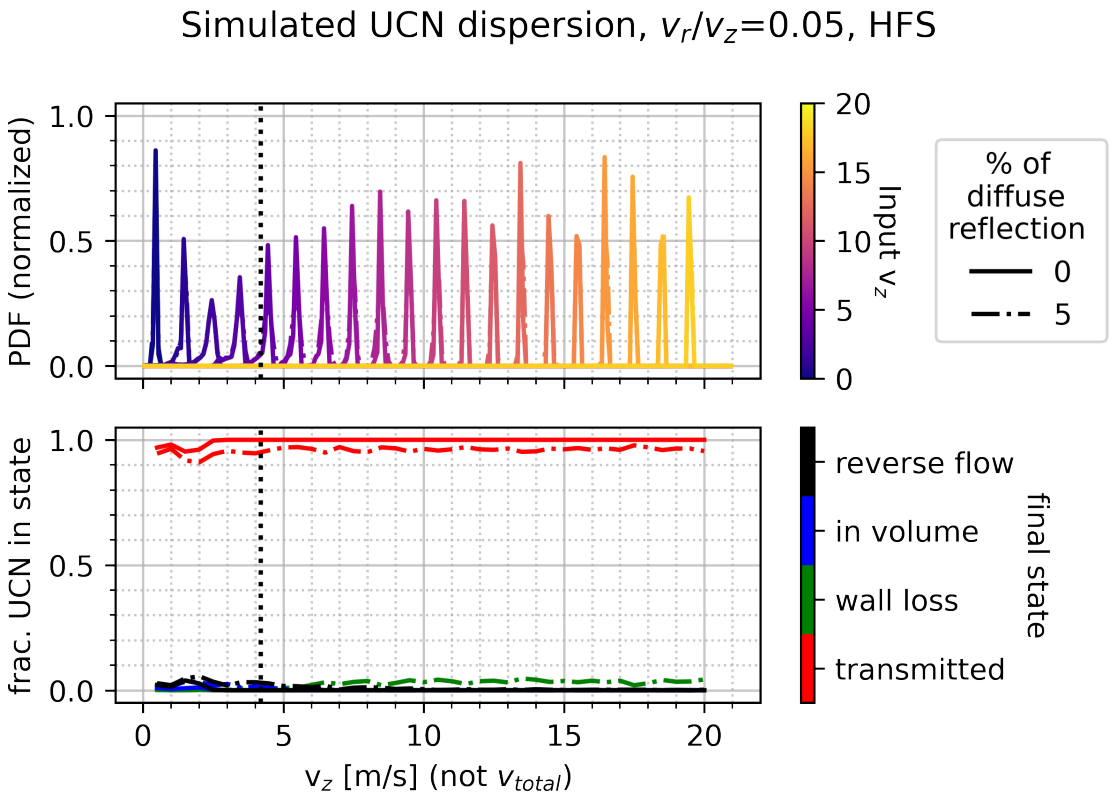
Simulated UCN dispersion, v_r/v_z=0.05, HFS
PDF (normalized)
1.0
0.5
0.0
20
15
10
5
0
Input v_z
% of diffuse reflection
0
5
frac. UCN in state
reverse flow
in volume
wall loss
transmitted
final state
0
5
10
15
20
v_z [m/s] (not v_{total})

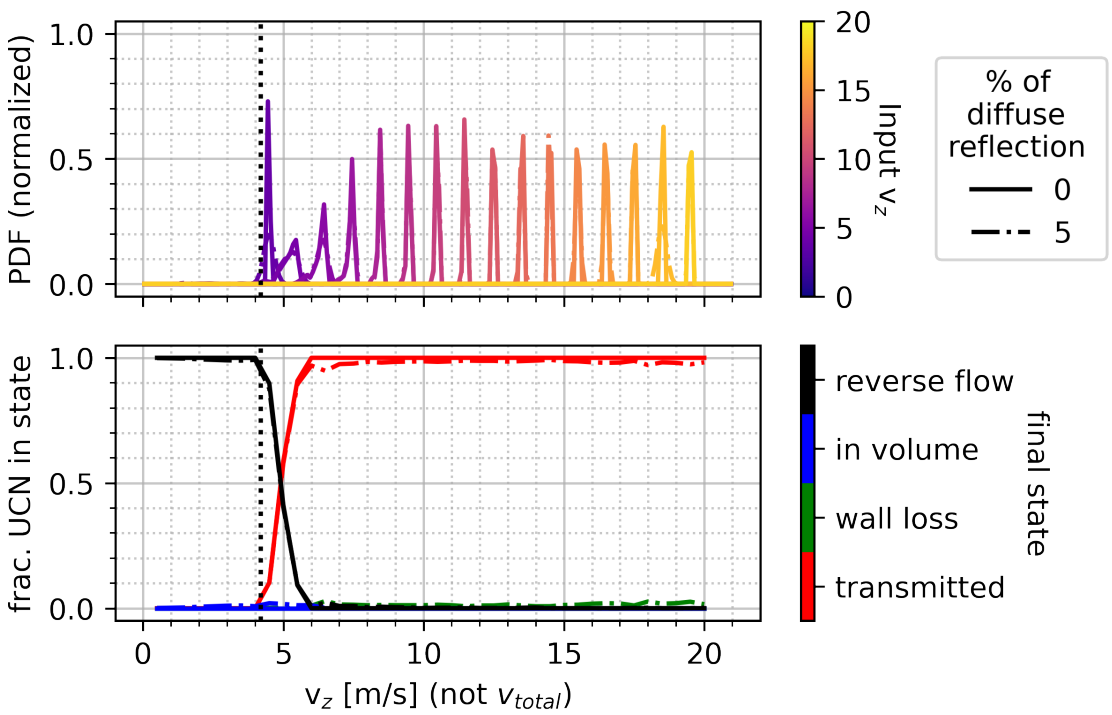
Simulated UCN dispersion, v_r/v_z=0.05, LFS
PDF (normalized)
1.0
0.5
0.0
20
15
10
5
0
Input v_z
% of diffuse reflection
0
5
frac. UCN in state
reverse flow
in volume
wall loss
transmitted
final state
0
5
10
15
20
v_z [m/s] (not v_{total})

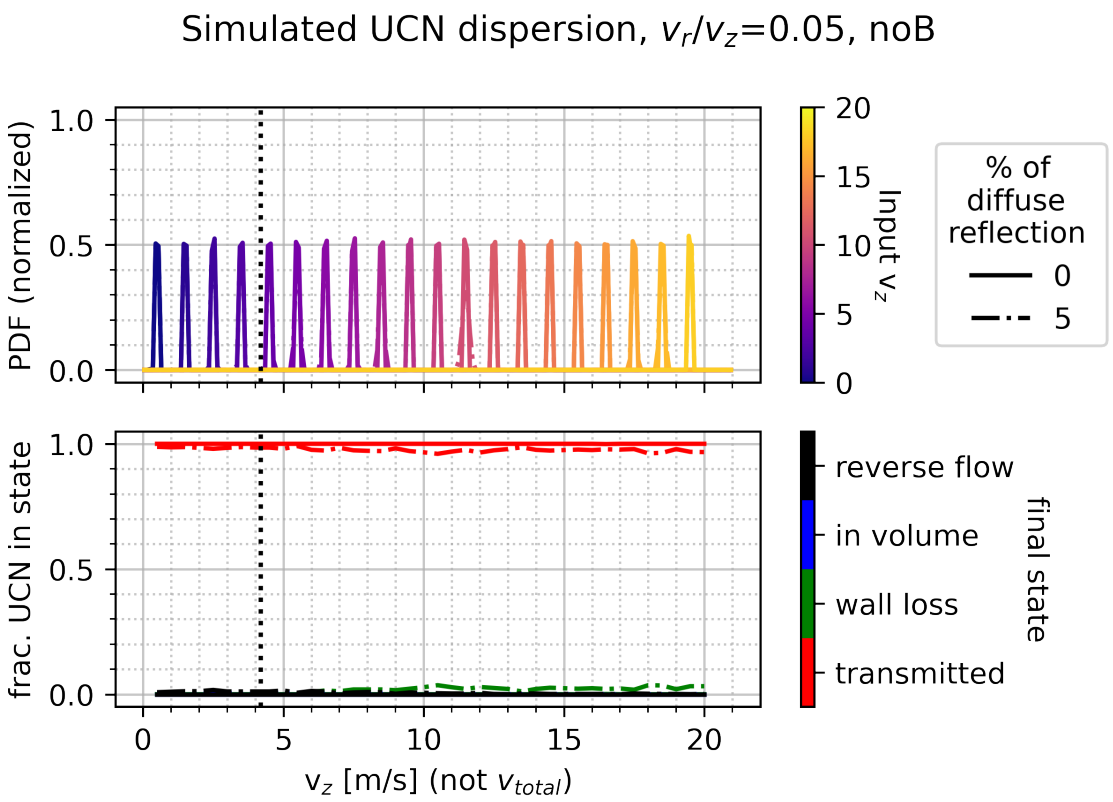
Simulated UCN dispersion, v_r/v_z=0.05, noB
PDF (normalized)
1.0
0.5
0.0
20
15
10
5
0
Input v_z
% of diffuse reflection
0
5
frac. UCN in state
reverse flow
in volume
wall loss
transmitted
final state
0
5
10
15
20
v_z [m/s] (not v_{total})

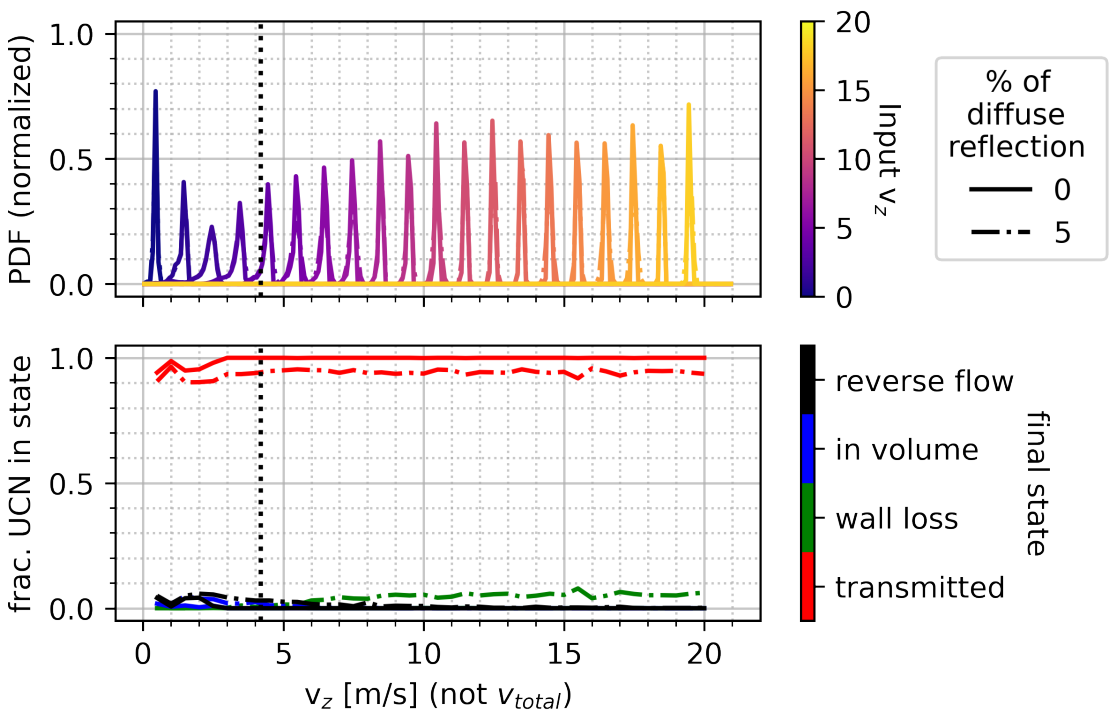
Simulated UCN dispersion, v_r/v_z=0.1, HFS
PDF (normalized)
1.0
0.5
0.0
20
15
10
5
0
Input v_z
% of diffuse reflection
0
5
frac. UCN in state
reverse flow
in volume
wall loss
transmitted
final state
0
5
10
15
20
v_z [m/s] (not v_{total})

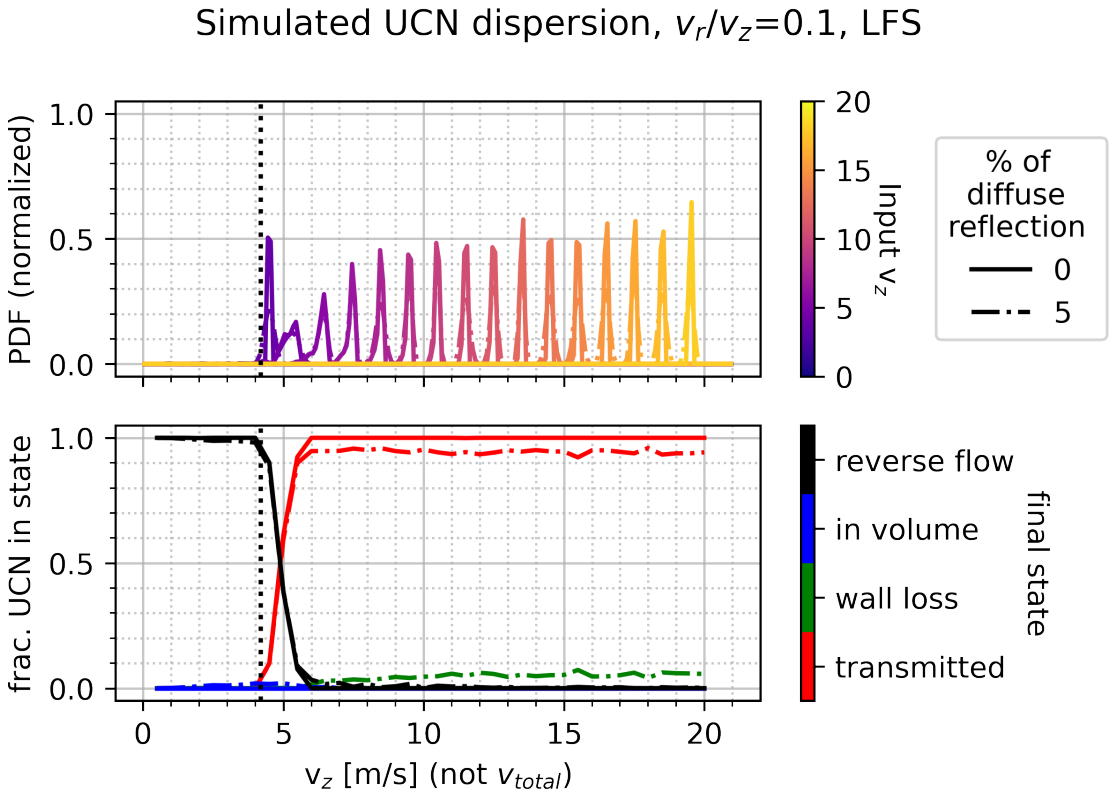
Simulated UCN dispersion, v_r/v_z=0.1, LFS
PDF (normalized)
1.0
0.5
0.0
20
15
10
5
0
Input v_z
% of diffuse reflection
0
5
frac. UCN in state
reverse flow
in volume
wall loss
transmitted
final state
0
5
10
15
20
v_z [m/s] (not v_{total})

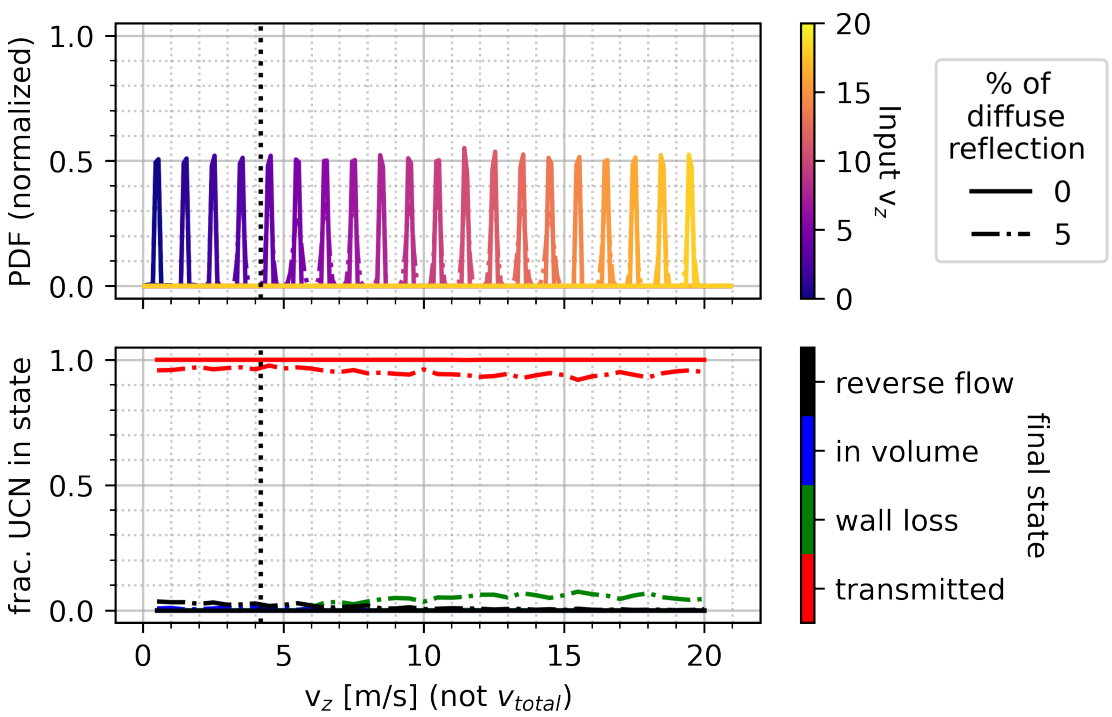
Simulated UCN dispersion, v_r/v_z=0.1, noB
PDF (normalized)
1.0
0.5
0.0
20
15
10
5
0
Input v_z
% of diffuse reflection
0
5
frac. UCN in state
reverse flow
in volume
wall loss
transmitted
final state
0
5
10
15
20
v_z [m/s] (not v_{total})

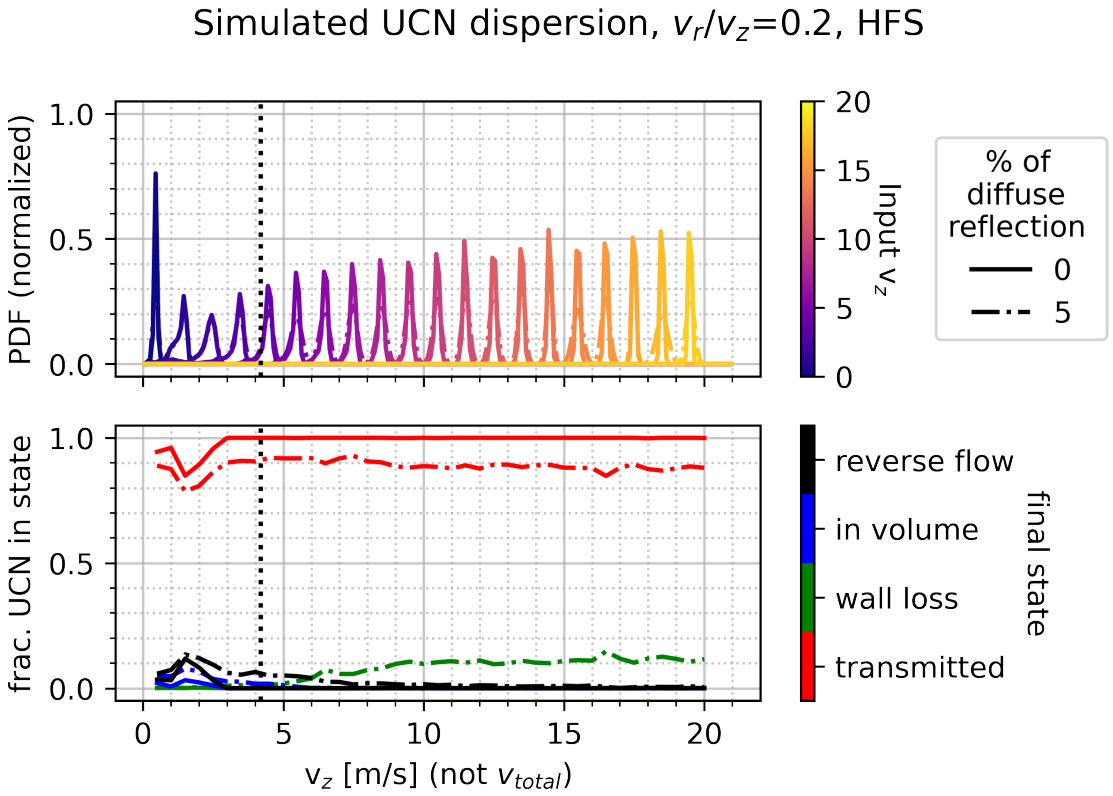
Simulated UCN dispersion, v_r/v_z=0.2, HFS
PDF (normalized)
1.0
0.5
0.0
20
15
10
5
0
Input v_z
% of diffuse reflection
0
5
frac. UCN in state
reverse flow
in volume
wall loss
transmitted
final state
0
5
10
15
20
v_z [m/s] (not v_{total})

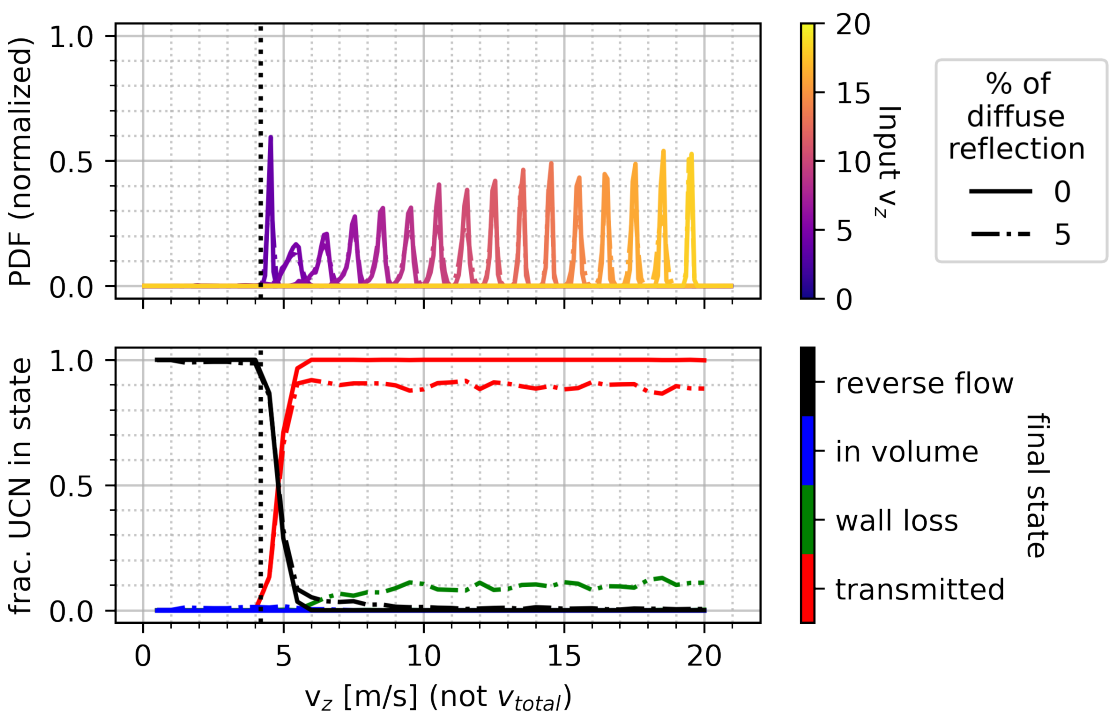
Simulated UCN dispersion, v_r/v_z=0.2, LFS
PDF (normalized)
1.0
0.5
0.0
20
15
10
5
0
Input v_z
% of diffuse reflection
0
5
frac. UCN in state
reverse flow
in volume
wall loss
transmitted
final state
0
5
10
15
20
v_z [m/s] (not v_{total})

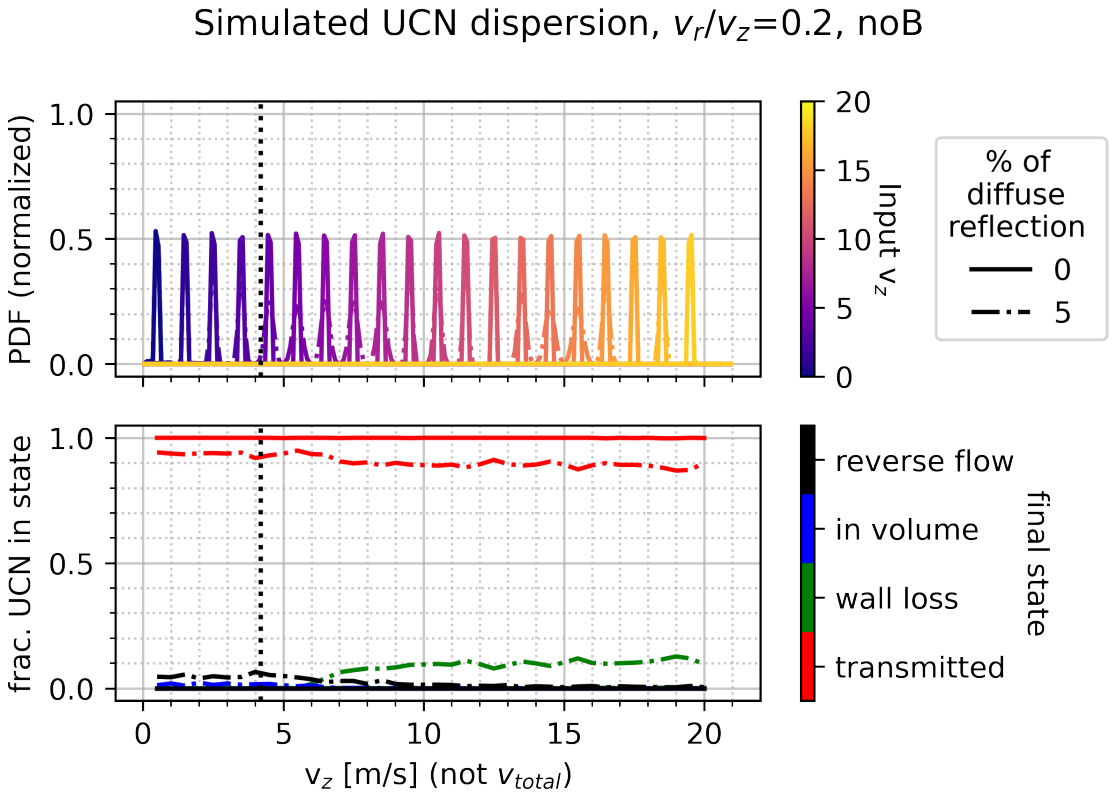
Simulated UCN dispersion, v_r/v_z=0.2, noB
PDF (normalized)
1.0
0.5
0.0
20
15
10
5
0
Input v_z
% of diffuse reflection
0
5
frac. UCN in state
reverse flow
in volume
wall loss
transmitted
final state
0
5
10
15
20
v_z [m/s] (not v_{total})

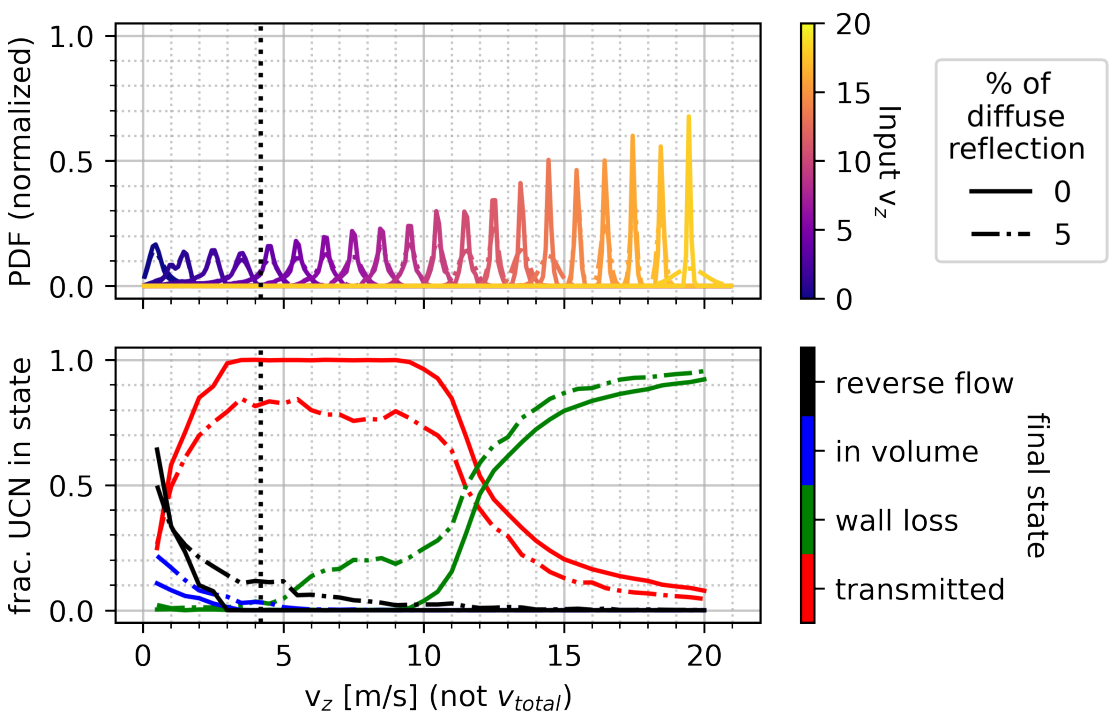
Simulated UCN dispersion, v_r/v_z=0.5, HFS
PDF (normalized)
1.0
0.5
0.0
20
15
10
5
0
Input v_z
% of diffuse reflection
0
5
frac. UCN in state
reverse flow
in volume
wall loss
transmitted
final state
0
5
10
15
20
v_z [m/s] (not v_{total})

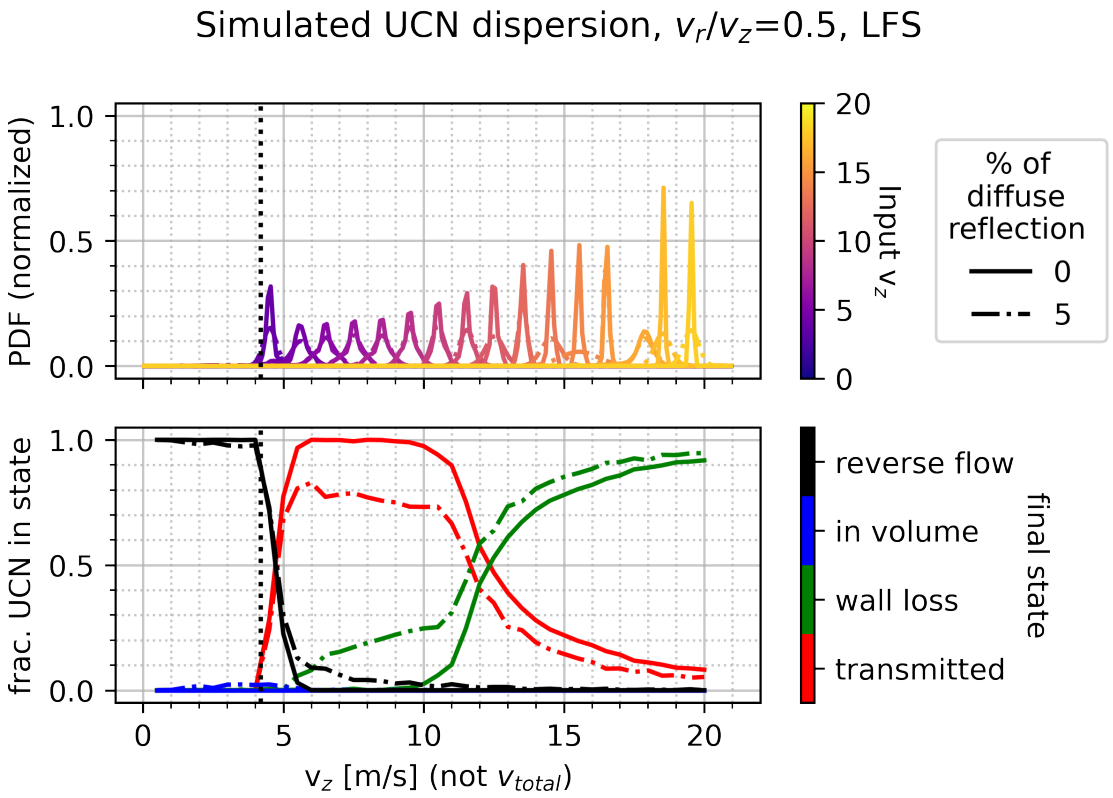
Simulated UCN dispersion, v_r/v_z=0.5, LFS
PDF (normalized)
1.0
0.5
0.0
20
15
10
5
0
Input v_z
% of diffuse reflection
0
5
frac. UCN in state
reverse flow
in volume
wall loss
transmitted
final state
0
5
10
15
20
v_z [m/s] (not v_{total})

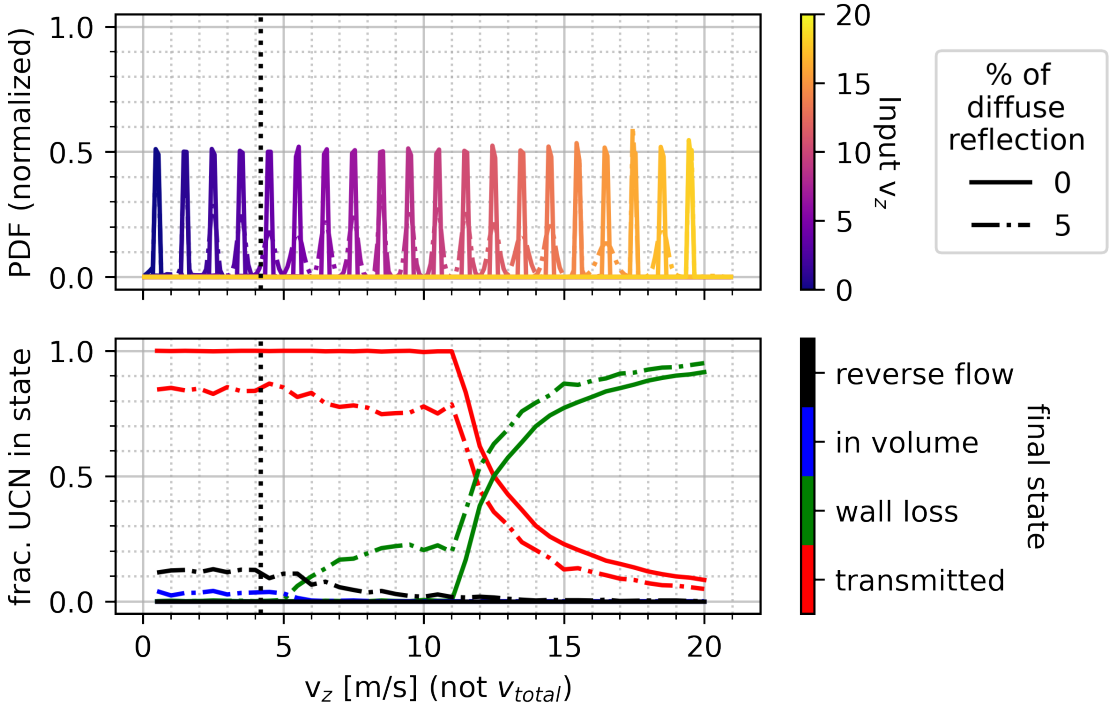
Simulated UCN dispersion, v_r/v_z=0.5, noB
PDF (normalized)
1.0
0.5
0.0
20
15
10
5
0
Input v_z
% of diffuse reflection
0
5
frac. UCN in state
reverse flow
in volume
wall loss
transmitted
final state
0
5
10
15
20
v_z [m/s] (not v_{total})

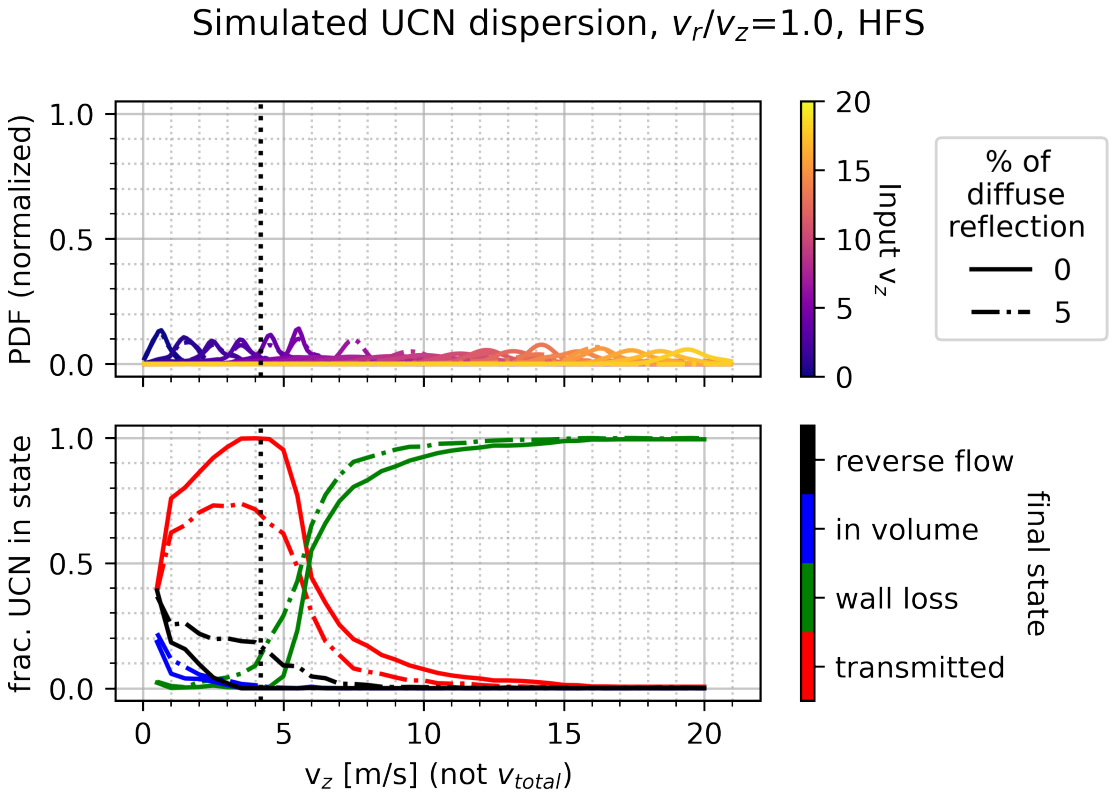
Simulated UCN dispersion, v_r/v_z=1.0, HFS
PDF (normalized)
1.0
0.5
0.0
20
15
10
5
0
Input v_z
% of diffuse reflection
0
5
frac. UCN in state
reverse flow
in volume
wall loss
transmitted
final state
0
5
10
15
20
v_z [m/s] (not v_{total})

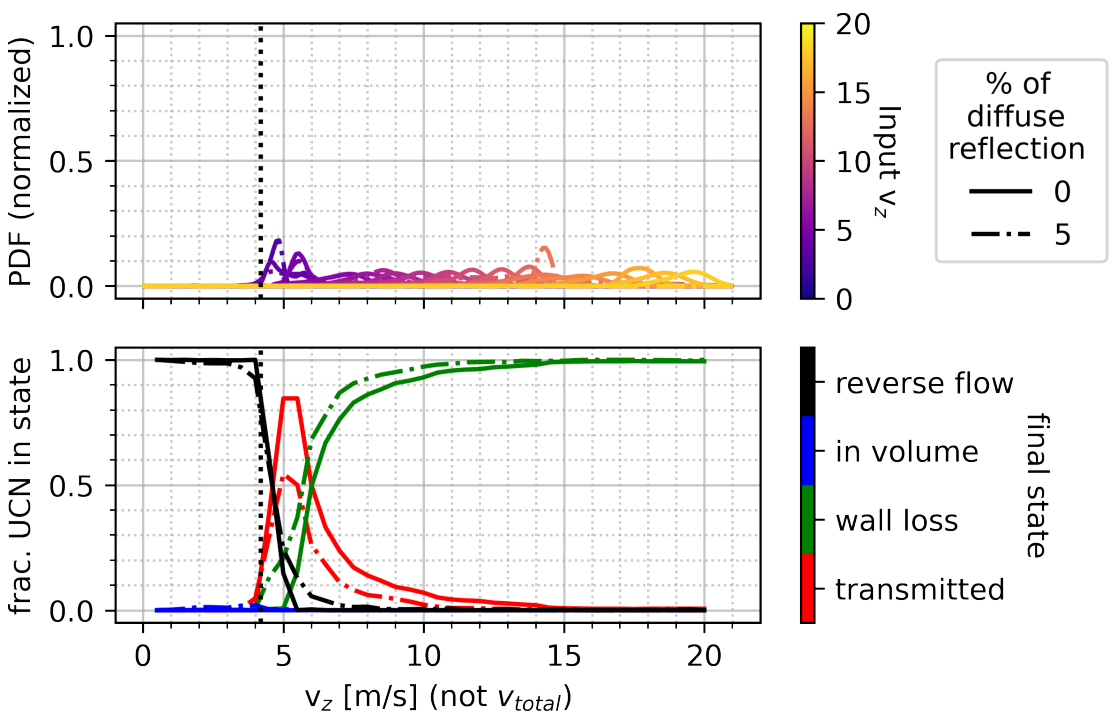
Simulated UCN dispersion, v_r/v_z=1.0, LFS
PDF (normalized)
1.0
0.5
0.0
20
15
10
5
0
Input v_z
% of diffuse reflection
0
5
frac. UCN in state
reverse flow
in volume
wall loss
transmitted
final state
0
5
10
15
20
v_z [m/s] (not v_{total})

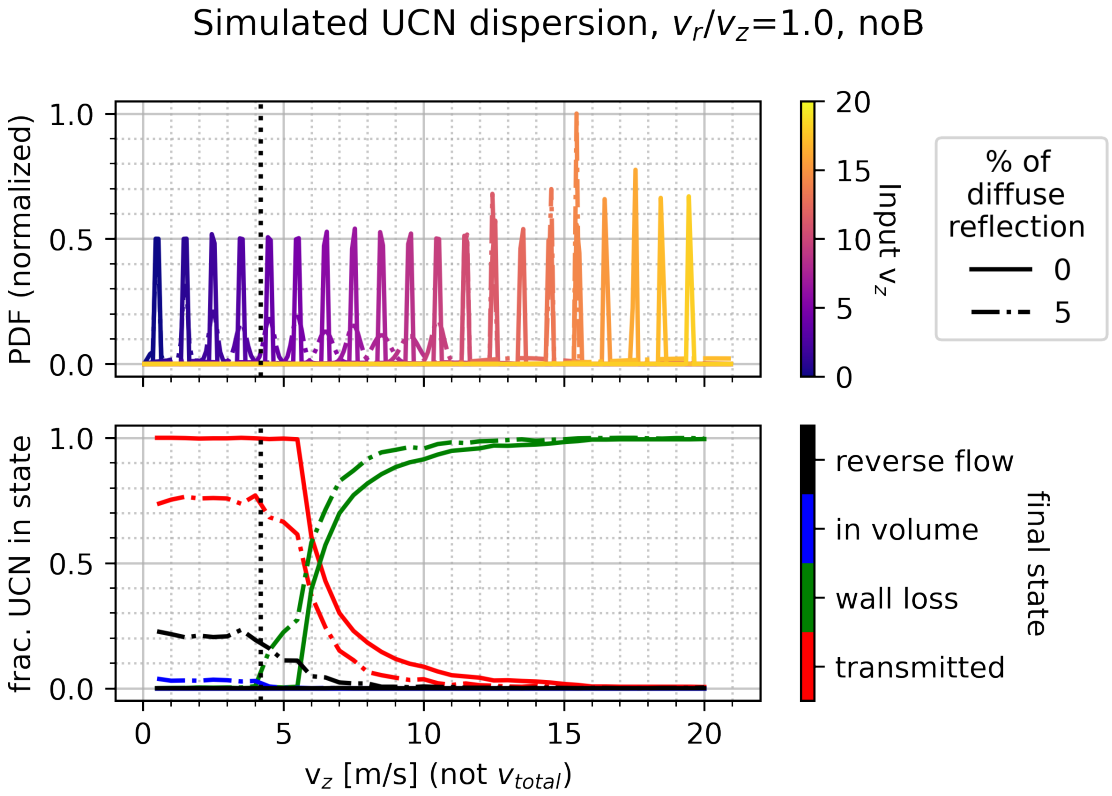
Simulated UCN dispersion, v_r/v_z=1.0, noB
PDF (normalized)
1.0
0.5
0.0
20
15
10
5
0
Input v_z
% of diffuse reflection
0
5
frac. UCN in state
reverse flow
in volume
wall loss
transmitted
final state
0
5
10
15
20
v_z [m/s] (not v_{total})

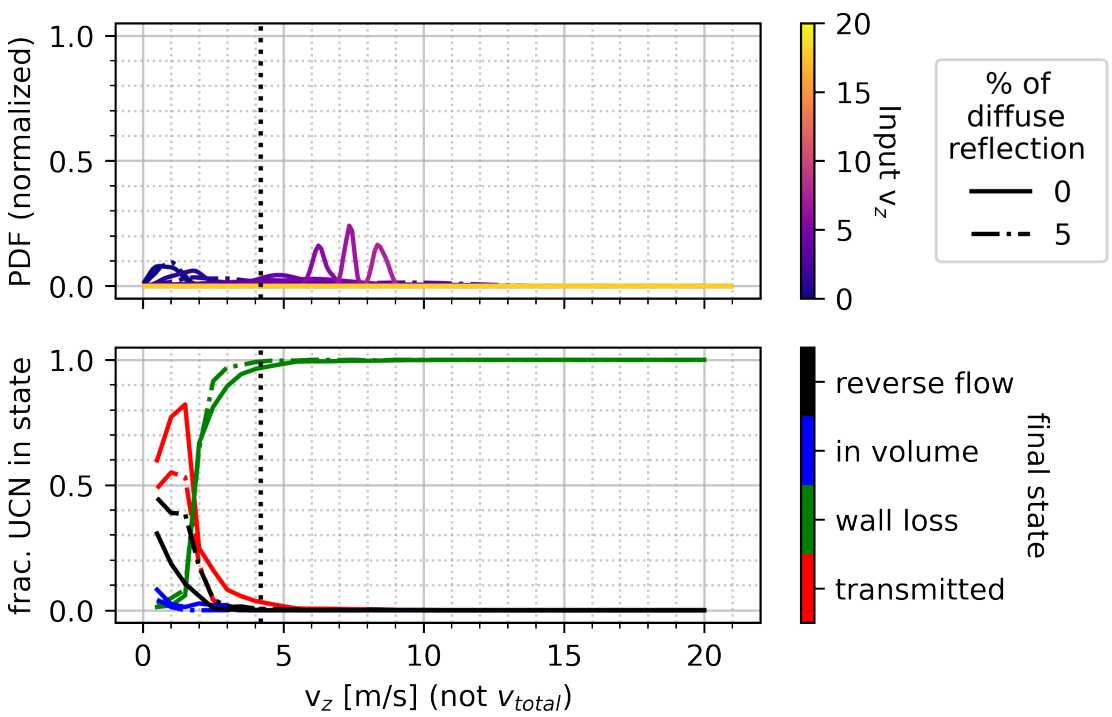
Simulated UCN dispersion, v_r/v_z=3.0, HFS
PDF (normalized)
1.0
0.5
0.0
20
15
10
5
0
Input v_z
% of diffuse reflection
0
5
frac. UCN in state
reverse flow
in volume
wall loss
transmitted
final state
0
5
10
15
20
v_z [m/s] (not v_{total})

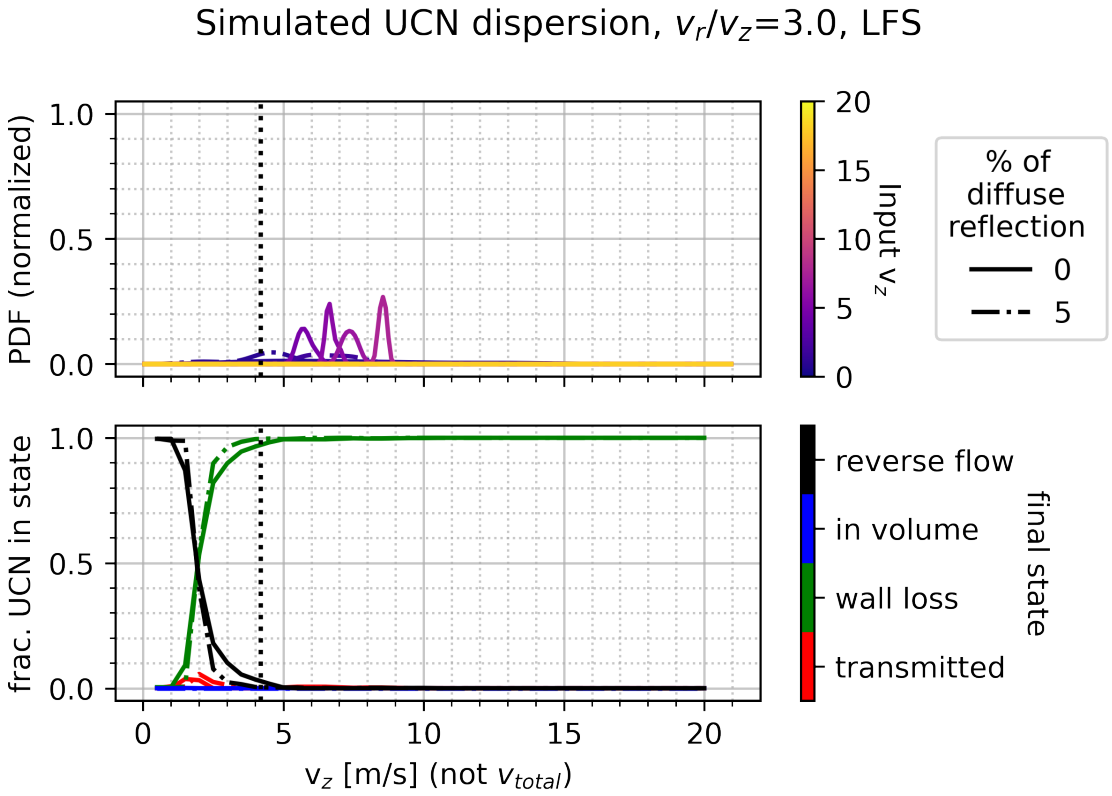
Simulated UCN dispersion, v_r/v_z=3.0, LFS
PDF (normalized)
1.0
0.5
0.0
frac. UCN in state
1.0
0.5
0.0
0
5
10
15
20
v_z [m/s] (not v_{total})
20
15
10
5
0
Input v_z
% of diffuse reflection
0
5
reverse flow
in volume
wall loss
transmitted
final state

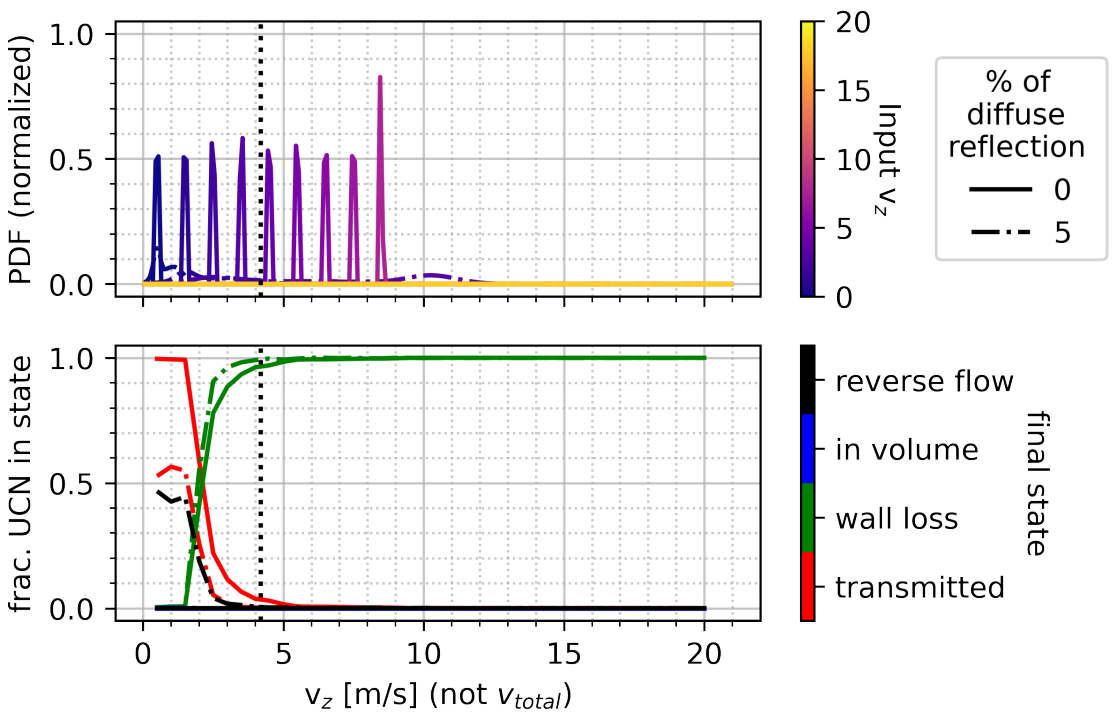
Simulated UCN dispersion, v_r/v_z=3.0, noB
PDF (normalized)
1.0
0.5
0.0
frac. UCN in state
1.0
0.5
0.0
0
5
10
15
20
v_z [m/s] (not v_{total})
20
15
10
5
0
Input v_z
% of diffuse reflection
0
5
reverse flow
in volume
wall loss
transmitted
final state

6.1.1 Transmission matrices

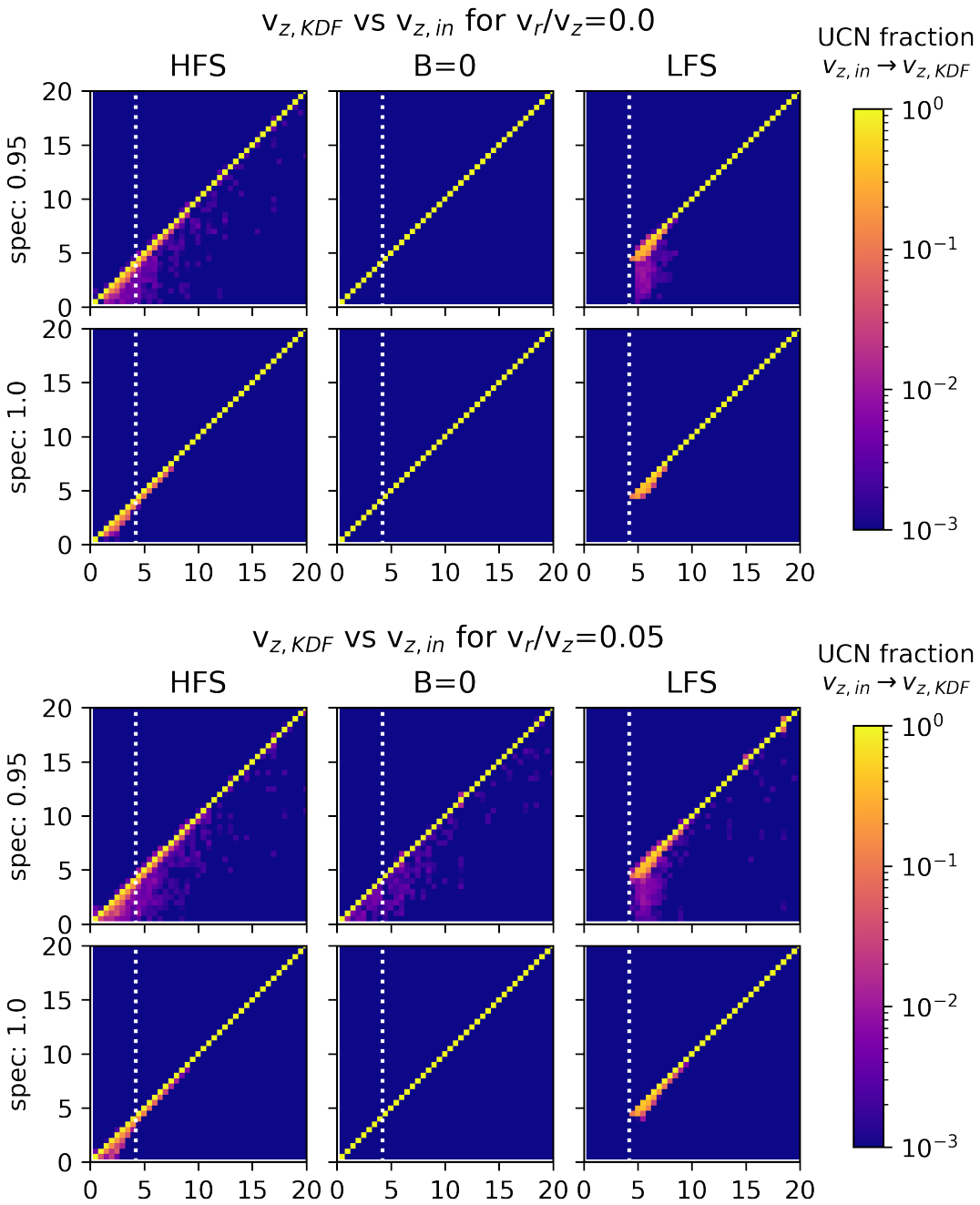

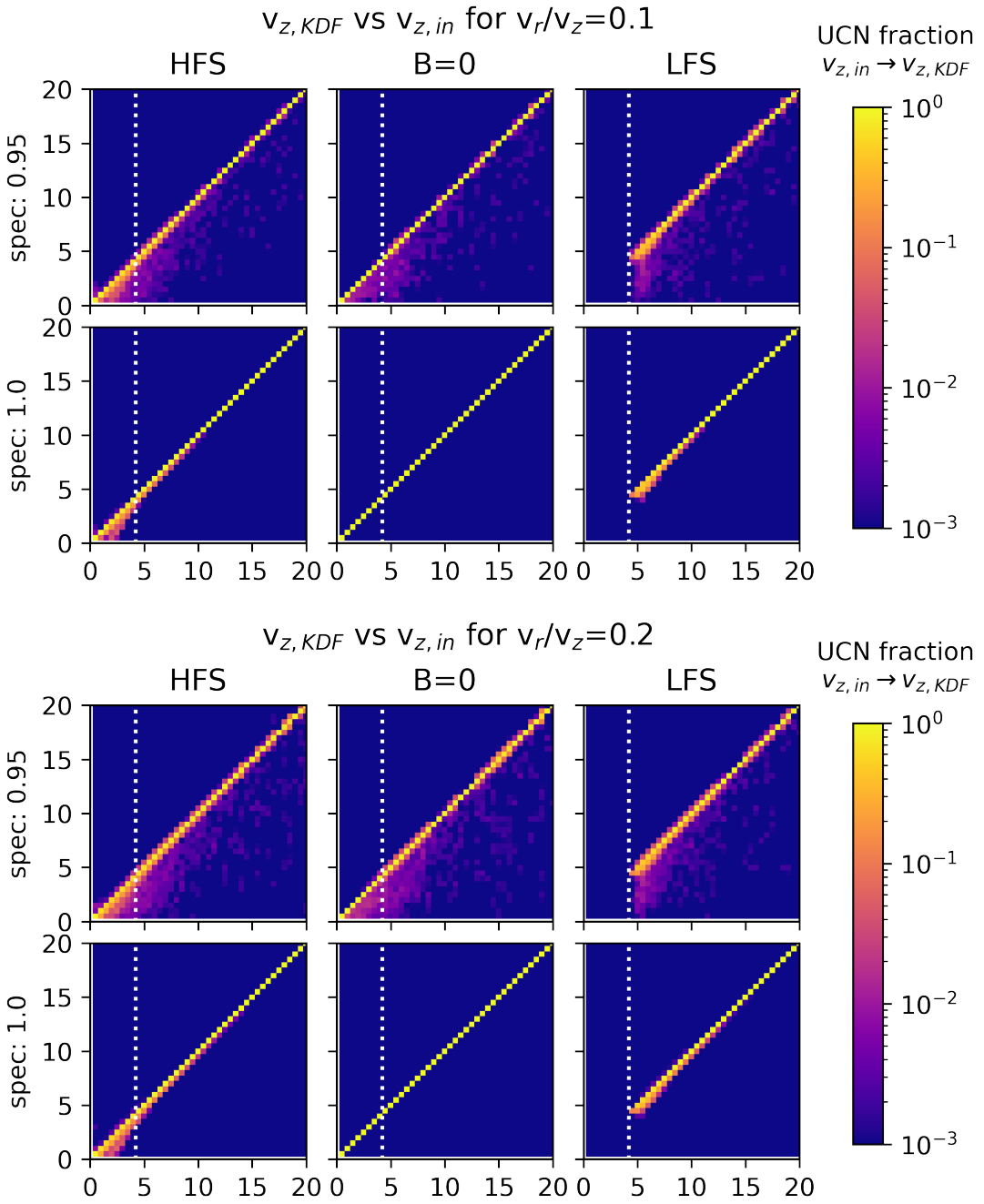
$v_{z,KDF}$ vs $v_{z,in}$ for v_r/v_z=0.1
HFS
B=0
LFS
spec: 0.95
spec: 1.0
UCN fraction
$v_{z,in} \rightarrow v_{z,KDF}$
10^0
10^{-1}
10^{-2}
10^{-3}
$v_{z,KDF}$ vs $v_{z,in}$ for v_r/v_z=0.2
HFS
B=0
LFS
spec: 0.95
spec: 1.0
UCN fraction
$v_{z,in} \rightarrow v_{z,KDF}$
10^0
10^{-1}
10^{-2}
10^{-3}

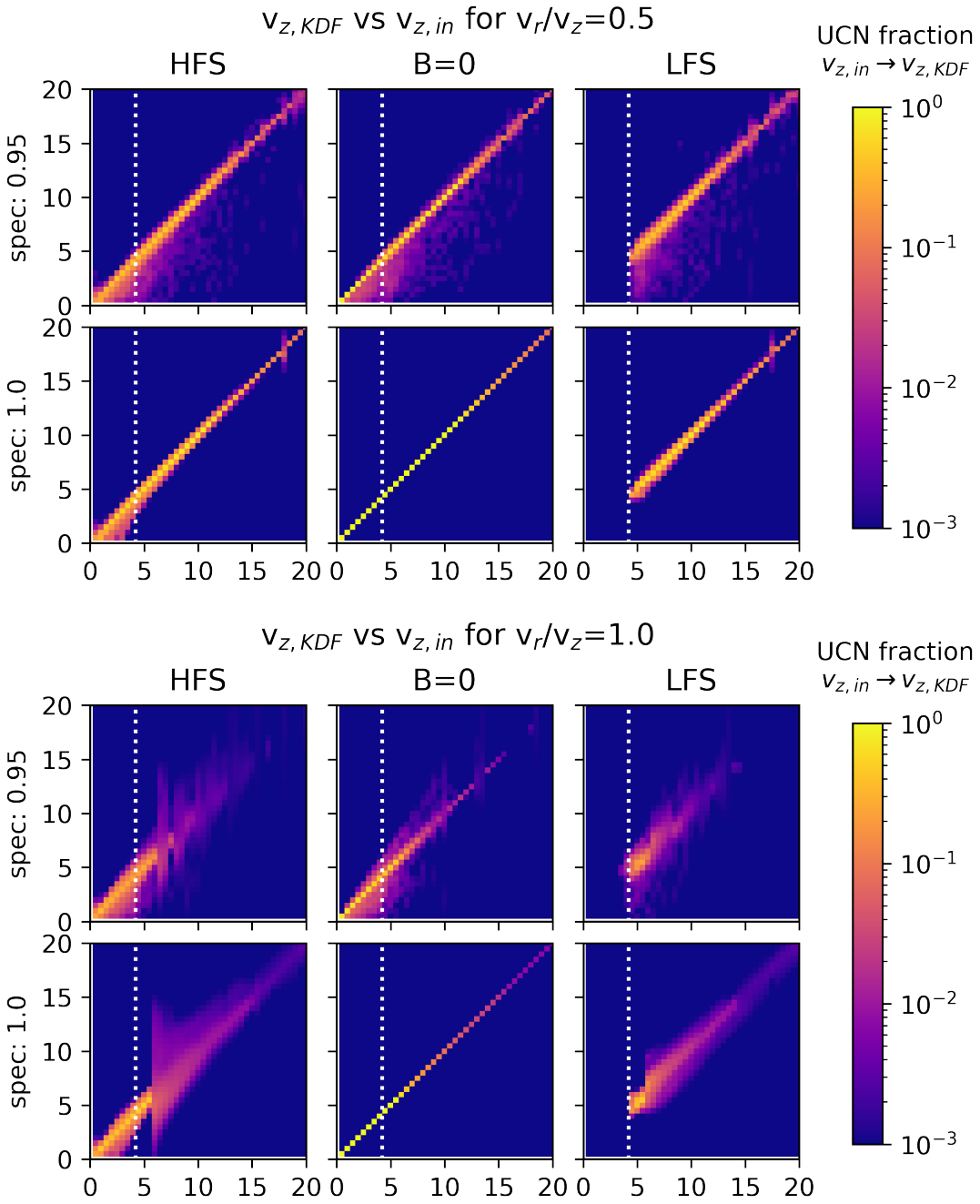
$v_{z,KDF}$ vs $v_{z,in}$ for v_r/v_z=0.5
HFS
B=0
LFS
spec: 0.95
spec: 1.0
UCN fraction
$v_{z,in} \rightarrow v_{z,KDF}$
10^0
10^{-1}
10^{-2}
10^{-3}
$v_{z,KDF}$ vs $v_{z,in}$ for v_r/v_z=1.0
HFS
B=0
LFS
spec: 0.95
spec: 1.0
UCN fraction
$v_{z,in} \rightarrow v_{z,KDF}$
10^0
10^{-1}
10^{-2}
10^{-3}

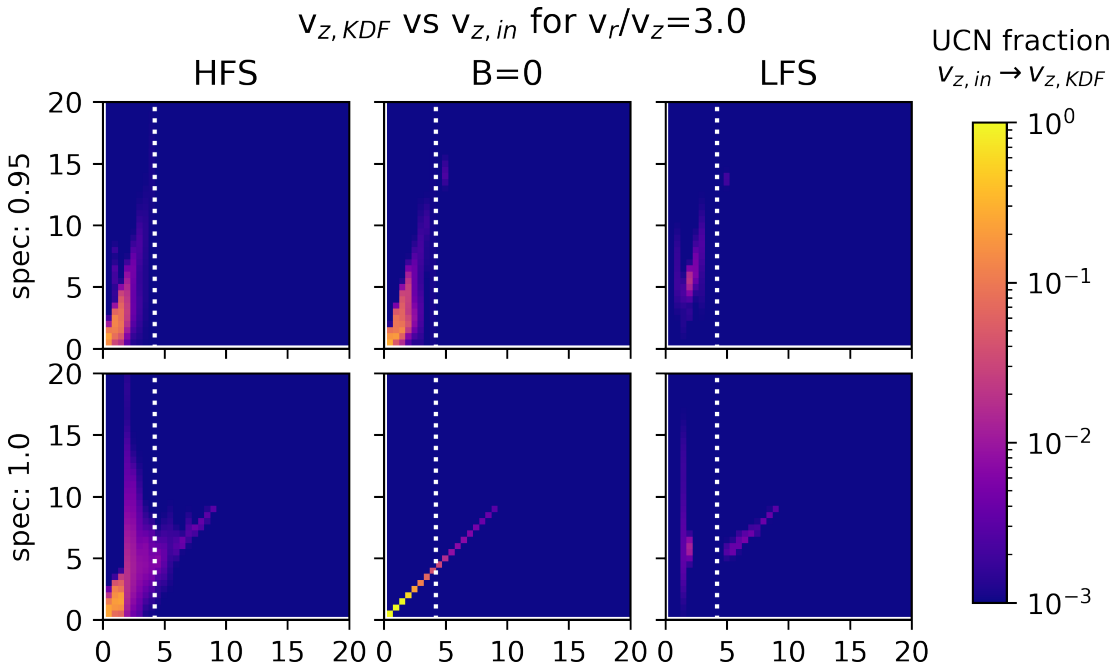

6.2 Full TOF spectra

6.3 Full panEDM cut render

6.4 Setup UCN polarizer

6.4.1 Prerequisits

- Test whether the body of the magnet - the iron yoke - is not connected to the coils. This has to be tested before the large DC cables are attached, as the power supply connects the cables to ground when not in operation.
- The Coil system itself has just 197 mΩ, which is difficult to test by hand
- The space required is: a EURO palette for the coolwater-transfer station, half of an EURO palette for the Danfysik power supply
- 2 sockets for IEC 60309, Red 3P+N+E, 6h 32A plugs (Power Supply and main pump)[1]
- 1 sockets for IEC 60309, Red 3P+N+E, 6h 16A plugs (auxiliary pump)
- 1 sockets for 230V standard (temperature monitor unit)

6.4.2 Tube and DC cable limits

- Setup the Danfysik Supply 853-6395-9604268 which can output 300A at 65V DC up to 5 m away from the cooling water station and up to 8 m from the magnet

[1] The Danfysik Supply must be connected to a 32A plug, the pumps may both be connected to 16A versions. Currently one pump has a 32A plug just due to avalibilty of plugs in Munich (we ought to change this to 16A as the pump does not even come close to pull 16A

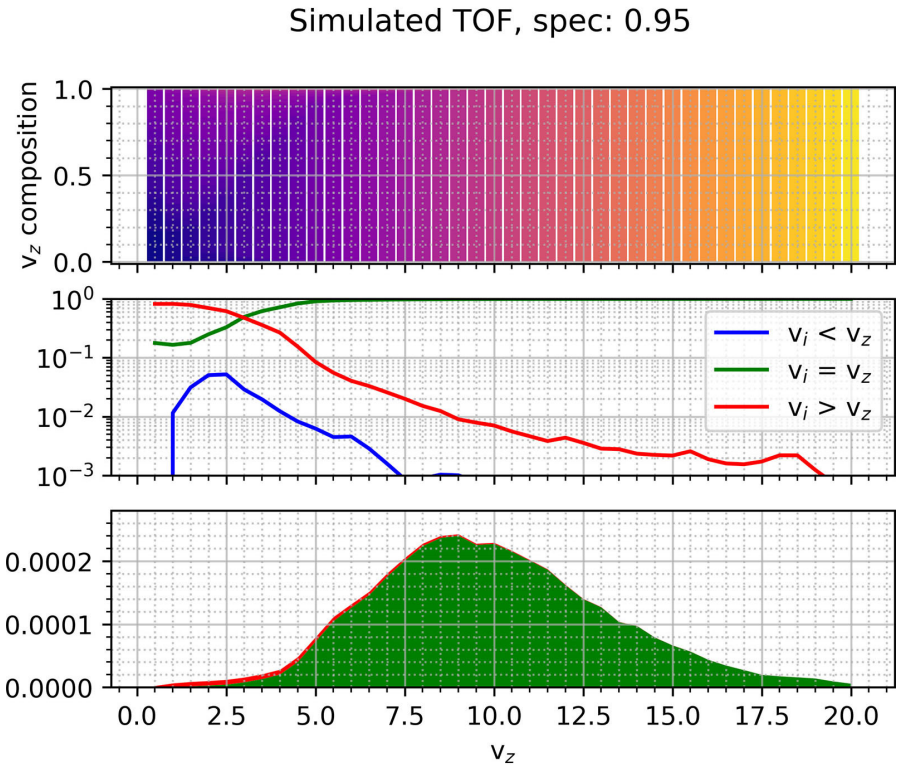

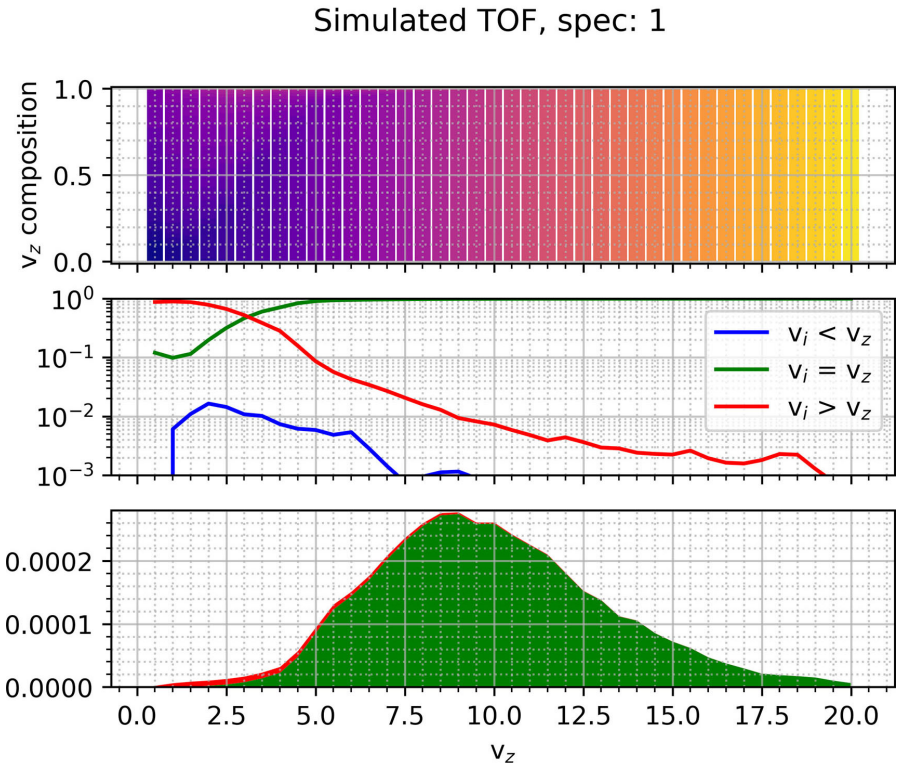

Figure 6.1: Full Simulaton TOF origns

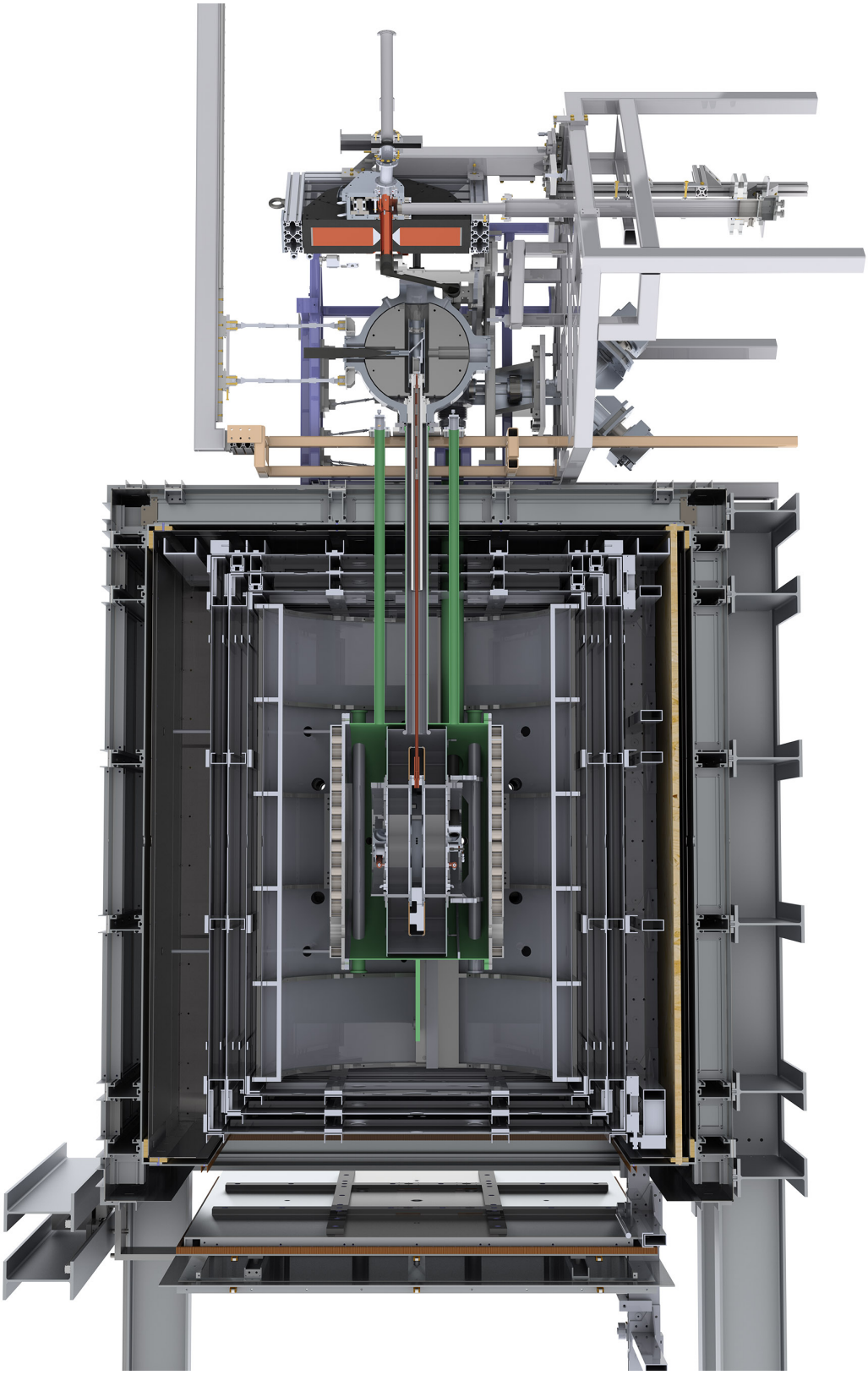

Figure 6.2: Full panEDM cut view.

Figure 6.3: Wiring SuperSUN side of magnet

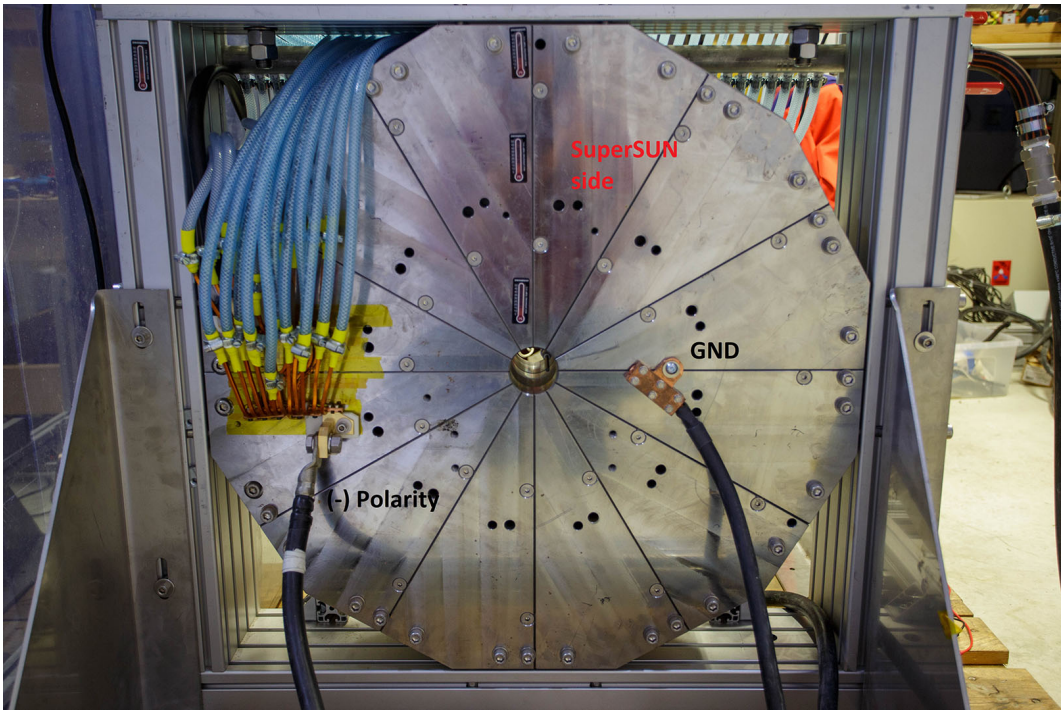

- Setup the magnet no more than 8m from the cooling water station and 8m from the power supply.

6.4.3 Wiring magnet

- The two largest cables carry 300 A of DC current and should be placed to minimize sharp bends and with care as to the stray field they produce.
- The third large cable is a protective GND connection. Connect it on the yoke (anywhere) and connect it to the housing of the Danfysik.
- The body temperature probe has to be pushed into the magnet as deep as mechanically possible
- Do not change the direction of cooling water flow. It is important that the temperature probe in the return flow measures the temperature at the outlet
- Observe the polarity of the cables.

6.4.4 Wiring Danfysik Supply

The Danfysik Power supply has two lids that can be opened. The front lid hosts the control panel and inside a connection to RS232. The back lid provides access to the connection for cooling water at the bottom, as well as the connections for the power and signal cable. The back lid has a door interlock, so it has to be closed in order to operate. Do not touch the resistor banks after 1 minute for operation. There are very

Figure 6.4: Wiring EDM side magnet

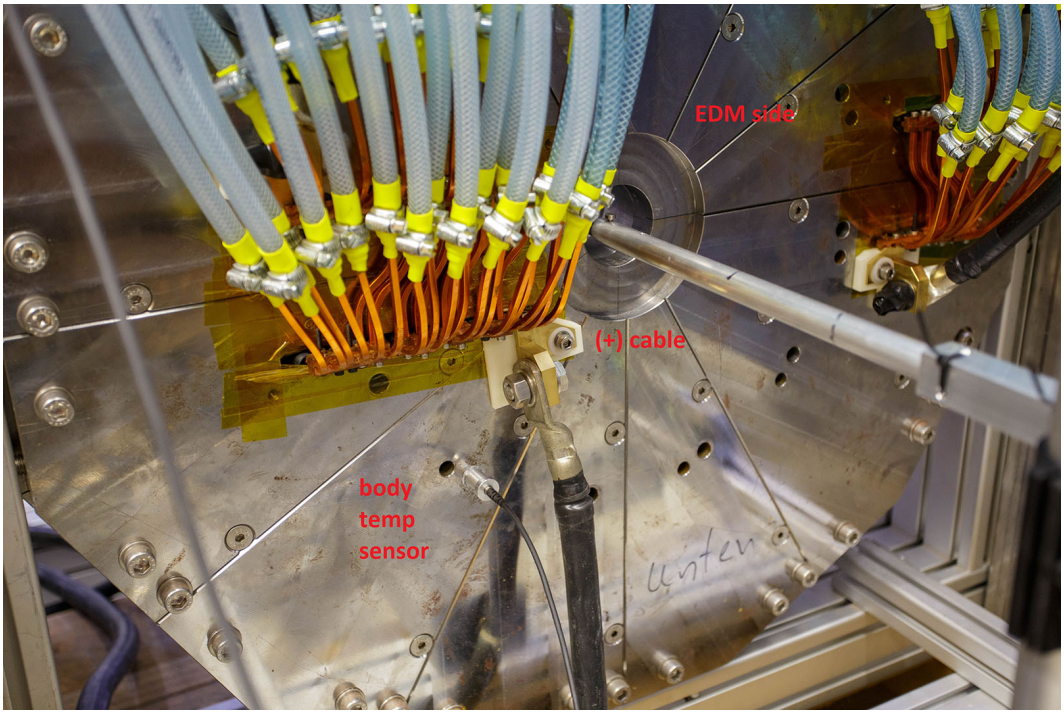

large capacitors inside and the transistor bank is on high potential. This could kill you on the spot.

The two 300 A cables connect close to the bottom left with M16 nuts on screws behind plastic lids. There are two external interlock signals, the supply needs to have in order to operate, which are connected as show in the picture. In the lower left corner, you can attach the GND cable. One of the two interlock cables is already in place with a plug at the opposite end. This connector is linked to the flow meter on the cool water station. This is a reed relay which only closes when the flow matches the desired value $\sim 10\,\mathrm{L\,min^{-1}}$. The Temp monitor unit has two free leads which have to be screwed into the other two terminals.

6.4.5 Water system layout

The cooling water system has two loops. The secondary loop is the external cooling water and only consists of a filter and two hoses. Observe the flow direction or the filter is futile and the heat exchanges does not work efficiently. The volume of this system is about 5 l.

The primary cooling loop is a single large loop passing through all devices. There are two shortcuts built in:

- Closing (8), (6) and opening (7) bypasses the ion filter. This is intended to do when the filter substrate has to be exchanged.
- (3) and (4) when open create a bypass to the magnet. If I,II,IV or V is closed then no water flows through the magnet which the pumps can run.

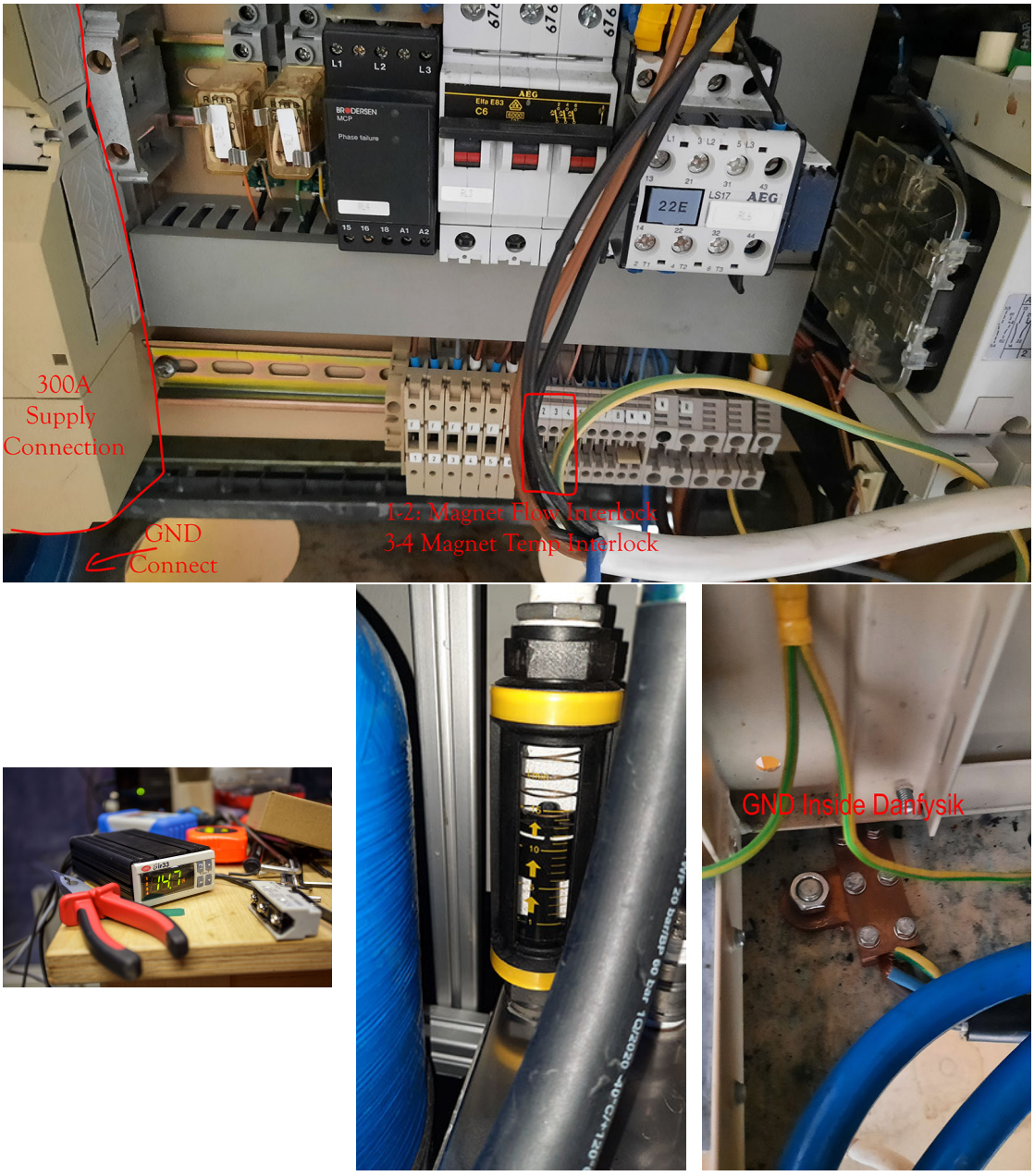

Figure 6.5: Top: wiring inside Danfysik, Bottom: Temperature Monitor, Flow indicator and interlock, grounding Danfysik for the SP body.

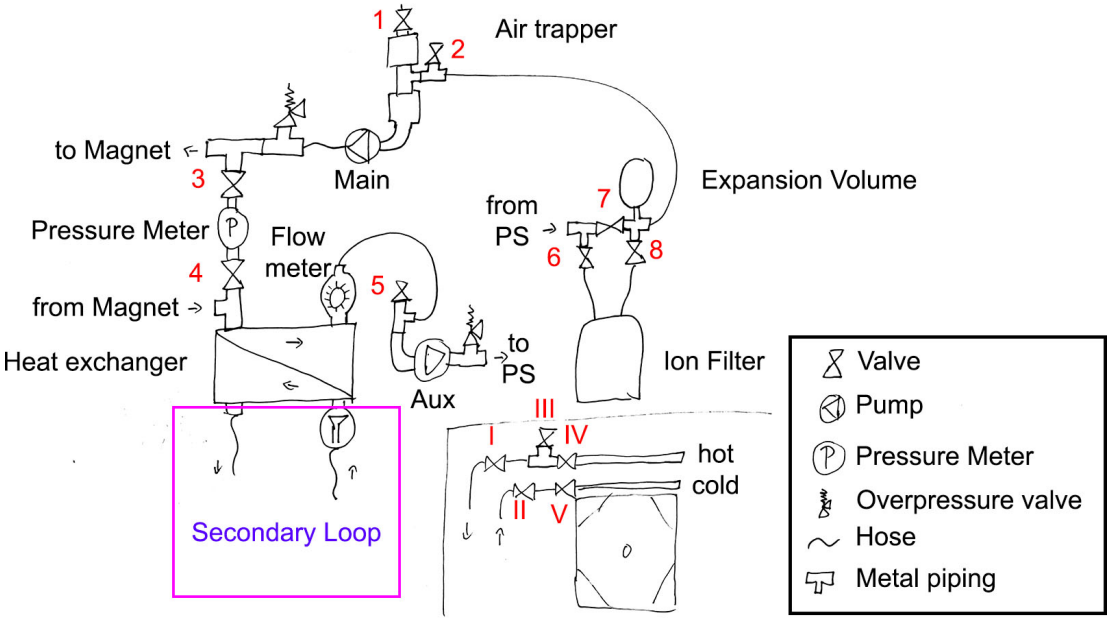

Figure 6.6: Layout cooling water system: Valves labeled 1-8 on the cooling water station. I-V on the magnet. PS means Power Supply aka Danfysik.

6.4.6 First installation cooling system

The system is delivered with some changes to the operational layout:

- The ion filter was detached
- The secondary cooling loop is connected to the primary loop at the two connections where the ion filter would be attached.
- The Magnet and the Danfysik are disconnected
- Everything is filled with 0.2 Ethanol, except the ion filter, which is filled with distilled water only.

To turn the system into operation follow these steps:

1. Get the two hoses from underneath the Danfysik and route them through the holes in the bottom. Connect the Danfysik to the primary coolant circuit. The input in the Danfysik is the hose that directly connects to the internal flowmeter.
2. Connect the magnet to the primary coolant circuit
3. Now you should have a full closed coolant circuit with this valve configuration:

Valve	1	2	3	4	5	6	7	8	I,II,IV,V	III
State	x	x	x	x	x	o	x	o	o	x

4. Switch on the main pump and check if the flow meter displays a flow of $7L/min$
5. Switch off the pump and disconnect the hose next to valve 2 at the air trapper for the main pump. This is hard to do and can take some time. Don't push or pull


to Magnet
(cold)
3
P
4
from Magnet
(hot)
from Danfysik
(hot)
7
Ion water filter connections
8
6


to Danfysik (cold)


1
2
5
Disconnect
for filling here
(on main motor)
Aux
(vertical)
Main
(horizontal)

on the piping, as it is only fixed in the pump itself. Put the end of the hose in a bucket. Close the opening with some tape or another temporary seal. Open valve 1 and pour in fresh water.

6. Switch on the main pump again and continue filling in fresh water while the system empties through the hose. About 40 L should be in the total system. If you have removed 40 L in total, the remainder of Ethanol should be no problem.

7. Reattach the hose and switch of the pump. Detach the hoses of the secondary loop from the connections near valve (6) and (8).

8. Connect the ion filter to (6) and (8), where (6) goes to the ion filter input and (8) to the output. The flow direction of the filter is marked with an arrow on the top of the black cap.

9. Make sure all hoses are fixed with metal clamps and not just pushed onto the hose barb. Once we run both pumps on full pressure, this is important.

10. If the primary loop is complete you may start both pumps. You can check the flow and also measure the pressure in the system in the forward feed for the magnet (by opening valve (3)) or alternatively the return pressure (by opening valve (4)). The flow will be below the target value at first.

11. After the pumps have been running for a minute - with both still running - add more water at the air trapper of the auxiliary (aux) pump. Carefully open valve (5) and let all the air escape. If no water rushes out, add some with a bottle.

12. Once the aux pump has no large volumes of air in it, we only refill at the main pump. The aux pump air trapper will very soon be on 1.5 bar and water will shoot out if you open (5). For the next 15 minutes, open valve 1 at the main pump air trapper and refill water up to the top. Remember, that the system can expand into the 24 L expansion volume and there are overpressure valves, so do not hesitate to refill at the main pump.

13. After some 30 minutes, while everything is running, open valve (3) and observe the pressure. It should be just below 4 bar. Walk over to the magnet and close valve I for a short time. This will cause the pump to run at its maximum pressure and the pressure gauge should move up to 5 bar. This also applies a high pressure shock to the system and helps moving air along.

14. The system should have a steady flow after some time. Before switching on the magnet. Take a small sample of water (for example from valve III) and measure the conductivity. If the ion filter has done its job, the water should have less than 4 µSi/cm.

15. Switch on the temperature monitor. It reports the temperature of the magnet return flow. One can also navigate to the magnet body temperature. Once the secondary cooling loop is working, the system should quickly take on the secondary coolant temperature also in the primary cycle. Make sure that there are at least $40\,\mathrm{L\,min^{-1}}$ of primary cooling water available.

6.4.7 Powering up DC power supply

- The Danfysik has a large switch that powers up the unit and the fans behind the back lid. Once this is switched on, close the back lid.
- The flow meter interlock closes when we have $10\,\mathrm{L\,min^{-1}}$ This value can be adjusted by moving the reed-block physically up and down. The temperature monitor breaks the interlock when the coolant exceeds 46.5 °C or the body of the magnet exceeds 50 °C.
- When the Danfysik is powered up, the front panel should be on. Press the "local" button to get the device from remote to local control. This is needed to make any other button respond.
- Press "OFF/reset" to make the Interlock errors disappear. All red interlock indicators should switch to off now. If this is not the case, test why the interlock is still tripped (Danfysik door not closed properly, connection to temperature monitor lost, ...)
- Polarity should be (PLUS) and you can press the Display button to show the voltage output of the unit.
- To run current through the magnet, press "coarse" and then "ON" After a few seconds the "Ready" green indicator should light up.
- The current is adjusted as ppm of the full range. The six digits offer a range form 0 to 999999 ppm of the full range (300 A). The knob changes the setpoint of the first two digits in "coarse" (so xx0000) and respectively the current on a percent-level, the middle two (00xx00) on medium and the last two (0000xx) on fine.
- Increase the setpoint to 10 % (100000) and wait for the (Ready) Light to come up again. The voltage should be up to 8 percent (roughly) in this case.
- Check the magnet. You should also hear a significant noise from the transistor banks. The cooling water should quickly heat up.
- Ramp up to (990000) and observe temperature and voltage. The voltage should move up to 86 % initially. After some time, once the magnet coils have warmed up (15 min) the voltage should be 91 %.
- Ramp up to (999900), this is our operational current. Voltage should level at 92 %.
- To switch off the magnet, ramp down the current with the knobs to (000000), then switch the power supply to OFF. The cooling has to be maintained for at least 10 more minutes to remove heat from magnet and power supply.

Bibliography

Abel, C. et al. (2020). "Measurement of the Permanent Electric Dipole Moment of the Neutron". In: *Phys Rev Lett* 124.8, p. 081803. ISSN: 1079-7114 (Electronic) 0031-9007 (Linking). DOI: 10.1103/PhysRevLett.124.081803. URL: https://www.ncbi.nlm.nih.gov/pubmed/32167372.

Adm 010 Amorphous Diamond (2019). Diamond Hard Surfaces Ltd., Caswell Science and Technology Park, Towcester, Northamptonshire, NN12 8EQ, UK.

Afach, S. et al. (2014). "A measurement of the neutron to 199Hg magnetic moment ratio". In: *Physics Letters B* 739, pp. 128–132. ISSN: 0370-2693. DOI: https://doi.org/10.1016/j.physletb.2014.10.046. URL: https://www.sciencedirect.com/science/article/pii/S0370269314007692.

Afach, S. et al. (2015). "Observation of Gravitationally Induced Vertical Striation of Polarized Ultracold Neutrons by Spin-Echo Spectroscopy". In: *Phys Rev Lett* 115.16, p. 162502.

Ahmed, S. et al. (2019). "First ultracold neutrons produced at TRIUMF". In: *Physical Review C* 99.2. ISSN: 2469-9985 2469-9993. DOI: 10.1103/PhysRevC.99.025503.

Allan, David W. (1987). "Should the classical variance be used as a basic measure in standards metrology?" In: *IEEE Transactions on Instrumentation and Measurement* IM-36.2, pp. 646–654. DOI: 10.1109/TIM.1987.6312761.

Altarev, I. et al. (1981). "A NEW UPPER LIMIT ON THE ELECTRIC DIPOLE MOMENT OF THE NEUTRON". In: *Physics Letters* 102B.1.

Altarev, I. et al. (Jan. 2008a). "Direct Experimental Verification of Neutron Acceleration by the Material Optical Potential of Solid $^2H_2$". In: *Phys. Rev. Lett.* 100 (1), p. 014801. DOI: 10.1103/PhysRevLett.100.014801. URL: https://link.aps.org/doi/10.1103/PhysRevLett.100.014801.

Altarev, I. et al. (2008b). "Neutron velocity distribution from a superthermal solid 2H2 ultracold neutron source". In: *The European Physical Journal A* 37.1.

Altarev, I. et al. (July 2012). "A next generation measurement of the electric dipole moment of the neutron at the FRM II". In: *IL NUOVO CIMENTO* 35.4.

Altarev, I. et al. (2014). "A magnetically shielded room with ultra low residual field and gradient". In: *Review of Scientific Instruments* 85.7, p. 075106. DOI: 10.1063/1.4886146.

Altarev, I. et al. (2015). "A large-scale magnetic shield with 106 damping at millihertz frequencies". In: *Journal of Applied Physics* 117.18, p. 183903. DOI: 10.1063/1.4919366. eprint: https://doi.org/10.1063/1.4919366. URL: https://doi.org/10.1063/1.4919366.

Altarev, Igor et al. (Jan. 2015). "Minimizing magnetic fields for precision experiments". In: *Journal of Applied Physics* 117. DOI: 10.1063/1.4922671.

Andreev, V. et al. (2018). "Improved limit on the electric dipole moment of the electron". In: *Nature* 562.7727, pp. 355–360.

Arzumanov, S. et al. (2003). "Storage of Ultracold Neutrons in Vessels Whose Walls Are Made from Graphite, Fluorine Polymer Oil, or Heavy-Water Ice". In: *Physics of Atomic Nuclei* 66.10, pp. 1820–1830.

Atchison, F. et al. (2006). "Diamondlike carbon can replace beryllium in physics with ultracold neutrons". In: *Physics Letters B* 642.1, pp. 24–27. ISSN: 0370-2693. DOI: https://doi.org/10.1016/j.physletb.2006.09.024. URL: https://www.sciencedirect.com/science/article/pii/S037026930601166X.

Atchison, F. et al. (2007). "Measurement of the Fermi potential of diamond-like carbon and other materials". In: *Nuclear Instruments and Methods in Physics Research Section B: Beam Interactions with Materials and Atoms* 260.2, pp. 647–656. ISSN: 0168583X. DOI: 10.1016/j.nimb.2007.04.253.

Atchison, F. et al. (2011). "Production of ultracold neutrons from cryogenic 2H2 ,O2 , and C2H4 converters". In: *EPL (Europhysics Letters)* 95.1. ISSN: 0295-5075 1286-4854. DOI: 10.1209/0295-5075/95/12001.

Aubert, B. et al. (Mar. 2001). "Measurement of CP-Violating Asymmetries in B0 Decays to CP Eigenstates". In: *Phys. Rev. Lett.* 86 (12), pp. 2515–2522. DOI: 10.1103/PhysRevLett.86.2515. URL: https://link.aps.org/doi/10.1103/PhysRevLett.86.2515.

Ayres, N. J. et al. (2021). "The design of the n2EDM experiment". In: *The European Physical Journal C* 81.6. ISSN: 1434-6044 1434-6052. DOI: 10.1140/epjc/s10052-021-09298-z.

Baker, C. A. et al. (Sept. 2006). "Improved Experimental Limit on the Electric Dipole Moment of the Neutron". In: *Phys. Rev. Lett.* 97 (13), p. 131801. DOI: 10.1103/PhysRevLett.97.131801. URL: https://link.aps.org/doi/10.1103/PhysRevLett.97.131801.

Baker, C. A. et al. (2014). "Apparatus for measurement of the electric dipole moment of the neutron using a cohabiting atomic-mercury magnetometer". In: *Nuclear Instruments and Methods in Physics Research Section A: Accelerators, Spectrometers, Detectors and Associated Equipment* 736, pp. 184–203. ISSN: 01689002. DOI: 10.1016/j.nima.2013.10.005.

Bell, William E. and Arnold L. Bloom (Mar. 1961). "Optically Driven Spin Precession". In: *Phys. Rev. Lett.* 6 (6), pp. 280–281. DOI: 10.1103/PhysRevLett.6.280. URL: https://link.aps.org/doi/10.1103/PhysRevLett.6.280.

Berry, Michael V. (1984). "Quantal phase factors accompanying adiabatic changes". In: *Proc. R. Soc. Lond.* A39245-57. DOI: https://doi.org/10.1098/rspa.1984.0023.

Bison, G. et al. (2020). "Neutron optics of the PSI ultracold-neutron source: characterization and simulation". In: *The European Physical Journal A* 56.2, p. 33.

Bodek, K. et al. (2008). "Storage of ultracold neutrons in high resistivity, non-magnetic materials with high Fermi potential". In: *Nuclear Instruments and Methods in Physics Research Section A: Accelerators, Spectrometers, Detectors and Associated Equipment* 597.2-3, pp. 222–226. ISSN: 01689002. DOI: 10.1016/j.nima.2008.09.018.

Bondar, V. et al. (2017). "Losses and depolarization of ultracold neutrons on neutron guide and storage materials". In: *Physical Review C* 96.3. ISSN: 2469-9985 2469-9993. DOI: 10.1103/PhysRevC.96.035205.

Brenner, Th. et al. (2015). "Deuterated polyethylene coatings for ultra-cold neutron applications". In: *Applied Physics Letters* 107.12, p. 121604. DOI: 10.1063/1.4931388.

eprint: https://doi.org/10.1063/1.4931388. URL: https://doi.org/10.1063/1.4931388.

Callan, C.G., R.F. Dashen, and D.J. Gross (1976). "The structure of the gauge theory vacuum". In: *Physics Letters B* 63.3, pp. 334–340. ISSN: 0370-2693. DOI: https://doi.org/10.1016/0370-2693(76)90277-X. URL: https://www.sciencedirect.com/science/article/pii/037026937690277X.

Cates, G. D., S. R. Schaefer, and W. Happer (Apr. 1988). "Relaxation of spins due to field inhomogeneities in gaseous samples at low magnetic fields and low pressures". In: *Phys. Rev. A* 37 (8), pp. 2877–2885. DOI: 10.1103/PhysRevA.37.2877. URL: https://link.aps.org/doi/10.1103/PhysRevA.37.2877.

Chanda, Manas (2017). *Plastics Technology Handbook*. CRC Press.

Christenson, J. H. et al. (July 1964). "Evidence for the 2-pi Decay of the K-0-2 Meson". In: *Phys. Rev. Lett.* 13 (4), pp. 138–140. DOI: 10.1103/PhysRevLett.13.138. URL: https://link.aps.org/doi/10.1103/PhysRevLett.13.138.

Chupp, T. E. et al. (2019). "Electric dipole moments of atoms, molecules, nuclei, and particles". In: *Reviews of Modern Physics* 91.1. ISSN: 0034-6861 1539-0756. DOI: 10.1103/RevModPhys.91.015001.

Chupp, Timothy and Michael Ramsey-Musolf (Mar. 2015). "Electric dipole moments: A global analysis". In: *Phys. Rev. C* 91 (3), p. 035502. DOI: 10.1103/PhysRevC.91.035502. URL: https://link.aps.org/doi/10.1103/PhysRevC.91.035502.

CODATA (2018). *CODATA Recommended Values of the Fundamental Physical Constants: 2018*. Tech. rep. NIST.

CYTOP (2021). URL: https://www.agcce.com/cytop-technical-information/.

Daum, M. et al. (2014). "Transmission of ultra-cold neutrons through guides coated with materials of high optical potential". In: *Nuclear Instruments and Methods in Physics Research Section A: Accelerators, Spectrometers, Detectors and Associated Equipment* 741, pp. 71–77. ISSN: 01689002. DOI: 10.1016/j.nima.2013.12.050.

Degenkolb, Skyler (Sept. 2020). "Searching for a neutron EDM using Superthermal Sources and Cryogenics: PanEDM, SuperSUN, and (EDM) n". In: *Workshop on Electric and Magnetic Dipole Moments*. Ed. by Tanmoy Bhattacharya et al. Accessed: 2021-05-01. Fundamental Physics in Small Experiments topical group (RF3). The publisher.

Dekens, W. et al. (2019). "The phenomenology of electric dipole moments in models of scalar leptoquarks". In: *Journal of High Energy Physics* 2019.1.

Energy, Elytt (2021). *Elytt design and manufacturing superconducting magnet for ILL*. URL: https://www.elytt.com/project/elytt-design-and-manufacturing-superconducting-magnet-for-ill/.

Faraday, M. (1846). "On the magnetization of light, and the illumination of magnetic lines of force". In: *Philos. Trans. R. Soc. Lond.* 1, pp. 104–123. DOI: https://doi.org/10.5479/sil.389644.mq591299.

Fertl, M. (2013). "A laser based mercury co-magnetometer for the neutron electric dipole moment search". PhD thesis. ETH Zurich.

Fierlinger, Peter (2005). "Losses and Depolarization of Stored Ultra Cold Neutrons on Diamond-like Carbon". PhD thesis. University Zurich.

Filter, H. (2021). *DHS dDLC storage time*. Private communication.

Flambaum, V. V. and A. Kozlov (Feb. 2012). "Extension of the Schiff theorem to ions and molecules". In: *Phys. Rev. A* 85 (2), p. 022505. DOI: 10.1103/PhysRevA.85.022505. URL: https://link.aps.org/doi/10.1103/PhysRevA.85.022505.

Frei, A. et al. (2007). "First production of ultracold neutrons with a solid deuterium source at the pulsed reactor TRIGA Mainz". In: *The European Physical Journal A* 34.2, pp. 119–127.

Frei, A. et al. (Dec. 2010). "Understanding of ultra-cold–neutron production in solid deuterium". In: *EPL (Europhysics Letters)* 92.6, p. 62001. DOI: 10.1209/0295-5075/92/62001. URL: https://doi.org/10.1209/0295-5075/92/62001.

Frei, Andreas (May 2021). *UCN Source, Heinz Maier-Leibnitz Zentrum*.

Fukuyama, T. (2012). "SEARCHING FOR NEW PHYSICS BEYOND THE STANDARD MODEL IN ELECTRIC DIPOLE MOMENT". In: *International Journal of Modern Physics A* 27.16, p. 1230015. DOI: 10.1142/S0217751X12300153. eprint: http://www.worldscientific.com/doi/pdf/10.1142/S0217751X12300153. URL: http://www.worldscientific.com/doi/abs/10.1142/S0217751X12300153.

Gawlik, Wojciech and Szymon Pustelny (2017). "Nonlinear Magneto-Optical Rotation Magnetometers". In: *High Sensitivity Magnetometers*. Cham: Springer International Publishing, pp. 425–450. ISBN: 978-3-319-34070-8. DOI: 10.1007/978-3-319-34070-8_14. URL: https://doi.org/10.1007/978-3-319-34070-8_14.

GmbH, Heraeus Quarzglas (2021). URL: https://www.heraeus.com/en/hca/fused_silica_quartz_knowledge_base_1/properties_1/properties_hca.html#tabs-608478-8.

Golub, R. (1979). "On the storage of neutrons in superfluid 4He". In: *Physics Letters A* 72.4, pp. 387–390. ISSN: 0375-9601. DOI: https://doi.org/10.1016/0375-9601(79)90505-X. URL: https://www.sciencedirect.com/science/article/pii/037596017990505X.

Golub, R. and S. K. Lamoreaux (1993). "NEUTRON ELECTRIC-DIPOLE MOMENT, ULTRACOLD NEUTRONS AND POLARIZED 3He". In: *Physics Reports* 237.1, p. 62.

Golub, R. and J.M. Pendlebury (1975). "Super-thermal sources of ultra-cold neutrons". In: *Physics Letters A* 53.2, pp. 133–135. ISSN: 0375-9601. DOI: https://doi.org/10.1016/0375-9601(75)90500-9. URL: https://www.sciencedirect.com/science/article/pii/0375960175905009.

– (1977). "The interaction of Ultra-Cold Neutrons (UCN) with liquid helium and a superthermal UCN source". In: *Physics Letters A* 62.5, pp. 337–339. ISSN: 0375-9601. DOI: https://doi.org/10.1016/0375-9601(77)90434-0. URL: https://www.sciencedirect.com/science/article/pii/0375960177904340.

Golub, R., J. D Richardson, and S. K. Lamoreaux (1991). *Ultra-Cold Neutrons*. Adam Hilger, Bristol, Philadelphia and New York.

Grinten, Maurits van der et al. (1999). "Charakterization and development of diamond-like carbon coatings for storing ultracold neutrons". In: *Nucl Instrum Methods Phys Res A* 423, pp. 421–427.

Group, Particle Data et al. (Aug. 2020). "Review of Particle Physics". In: *Progress of Theoretical and Experimental Physics* 2020.8. 083C01. ISSN: 2050-3911. DOI: 10.1093/ptep/ptaa104. URL: https://doi.org/10.1093/ptep/ptaa104.

Gutsmiedl, E. et al. (2011). "Production of ultra-cold neutrons in solid alpha-oxygen". In: *EPL (Europhysics Letters)* 96.6. ISSN: 0295-5075 1286-4854. DOI: 10.1209/0295-5075/96/62001.

Happer, W. (Apr. 1972). "Optical Pumping". In: *Rev. Mod. Phys.* 44 (2), pp. 169–249. DOI: 10.1103/RevModPhys.44.169. URL: http://link.aps.org/doi/10.1103/RevModPhys.44.169.

Harris, P. G. and J. M. Pendlebury (2006). "Dipole-field contributions to geometric-phase-induced false electric-dipole-moment signals for particles in traps". In: *Physical Review A* 73.1. ISSN: 1050-2947 1094-1622. DOI: 10.1103/PhysRevA.73.014101.

Harris, P. G. et al. (Feb. 1999). "New Experimental Limit on the Electric Dipole Moment of the Neutron". In: *Phys. Rev. Lett.* 82 (5), pp. 904–907. DOI: 10.1103/PhysRevLett.82.904. URL: https://link.aps.org/doi/10.1103/PhysRevLett.82.904.

Heil, Werner (2017). "Helium Magnetometers". In: *High Sensitivity Magnetometers*. Cham: Springer International Publishing, pp. 493–521. ISBN: 978-3-319-34070-8. DOI: 10.1007/978-3-319-34070-8_16.

Hingerl, J. (2019). "A Versatile Device for Studying Ultracold Neutrons and Testing Cryogenic Storage Volumes". Thesis. Technical University Munich.

Hirose, S. et al. (May 2017). "Measurement of the τ Lepton Polarization and $R(D^*)$ in the Decay $\overline{B} \to D^*\tau^-\overline{\nu}_\tau$". In: *Phys. Rev. Lett.* 118 (21), p. 211801. DOI: 10.1103/PhysRevLett.118.211801. URL: https://link.aps.org/doi/10.1103/PhysRevLett.118.211801.

Hopf, Lucas (2020). "Aspects of the high voltage system of the PanEDM experiment". MA thesis. TUM.

ILL (2021). URL: https://www.ill.eu/users/instruments/instruments-list.

Ito, T. M. et al. (Jan. 2018). "Performance of the upgraded ultracold neutron source at Los Alamos National Laboratory and its implication for a possible neutron electric dipole moment experiment". In: *Phys. Rev. C* 97 (1), p. 012501. DOI: 10.1103/PhysRevC.97.012501. URL: https://link.aps.org/doi/10.1103/PhysRevC.97.012501.

Janosek, Michal (2017). "Parallel Fluxgate Magnetometers". In: *High Sensitivity Magnetometers*. Cham: Springer International Publishing, pp. 41–61. ISBN: 978-3-319-34070-8. DOI: 10.1007/978-3-319-34070-8_2. URL: https://doi.org/10.1007/978-3-319-34070-8_2.

Jenke, Tobias (May 5, 2021). personal communication.

Kai, Tetsuya et al. (2004). "Coupled hydrogen moderator optimization with ortho/para hydrogen ratio". In: *Nuclear Instruments and Methods in Physics Research Section A: Accelerators, Spectrometers, Detectors and Associated Equipment* 523.3, pp. 398–414.

Karch, J. et al. (2014). "Performance of the solid deuterium ultra-cold neutron source at the pulsed reactor TRIGA Mainz". In: *The European Physical Journal A* 50.4. ISSN: 1434-6001 1434-601X. DOI: 10.1140/epja/i2014-14078-9.

Kimball, D. F. J. and D. Budker, eds. (2013). *Optical Magnetometry*. Cambridge University Press.

Kobayashi, Makoto and Toshihide Maskawa (Feb. 1973). "CP-Violation in the Renormalizable Theory of Weak Interaction". In: *Progress of Theoretical Physics* 49.2, pp. 652–657. ISSN: 0033-068X. DOI: 10.1143/PTP.49.652. eprint: https://academic.oup.com/ptp/article-pdf/49/2/652/5257692/49-2-652.pdf. URL: https://doi.org/10.1143/PTP.49.652.

Lamoreaux, S. K. and R. Golub (2009). "Experimental searches for the neutron electric dipole moment". In: *Journal of Physics G: Nuclear and Particle Physics* 36.10. ISSN: 0954-3899 1361-6471. DOI: 10.1088/0954-3899/36/10/104002.

Lauer, T. (2010). "Investigation of a superthermal ultra old neutron sour e based on a solid deuterium onverter for the TRIGA Mainz rea tor". PhD thesis. Johannes Gutenberg-Universitaet Mainz.

Lees, J. P. et al. (Oct. 2013). "Measurement of an excess of $\overline{B} \to D^{(*)}\tau^-\overline{\nu}_\tau$ decays and implications for charged Higgs bosons". In: *Phys. Rev. D* 88 (7), p. 072012. DOI: 10.1103/PhysRevD.88.072012. URL: https://link.aps.org/doi/10.1103/PhysRevD.88.072012.

Li, Yingchuan, Stefano Profumo, and Michael Ramsey-Musolf (2009). "Bino-driven electroweak baryogenesis with highly suppressed electric dipole moments". In: *Physics Letters B* 673.1, pp. 95–100.

Lins, Tobias (2016). "High Precision Physics in Low Magnetic Fields: Implementation of a Sub-Nanotesla Field with Femtotesla Temporal Stability". PhD thesis. Technical University Munich.

Liu, C. Y. and A. R. Young (2004). *Ultra-cold Neutron Production in Anti-ferromagnetic Oxygen Solid*. arXiv: nucl-th/0406004 [nucl-th].

Liu, C. Y., A. R. Young, and S. K. Lamoreaux (2000). "Ultracold neutron upscattering rates in a molecular deuterium crystal". In: *Physical Review B* 62.6.

Lushchikov, V. I. et al. (Jan. 1969). "OBSERVATION OF ULTRACOLD NEUTRONS." In: *JETP Lett. (USSR) (Engl. Transl.), 9: 23-6(Jan. 5, 1969)*. URL: https://www.osti.gov/biblio/4744673.

Luty, Markus A. (Jan. 1992). "Baryogenesis via leptogenesis". In: *Phys. Rev. D* 45 (2), pp. 455–465. DOI: 10.1103/PhysRevD.45.455. URL: https://link.aps.org/doi/10.1103/PhysRevD.45.455.

Macaluso, D. and Corbino O. (1898). "Sopra una nuova azione che la luce subisce attraversando alcuni vapori metallici in un campo magnetico". In: *Nuovo Cimento* 8, pp. 257–258.

Maki, Ziro, Masami Nakagawa, and Shoichi Sakata (Nov. 1962). "Remarks on the Unified Model of Elementary Particles". In: *Progress of Theoretical Physics* 28.5, pp. 870–880. ISSN: 0033-068X. DOI: 10.1143/PTP.28.870. URL: https://doi.org/10.1143/PTP.28.870.

Masuda, Yasuhiro et al. (2012). "Neutron electric dipole moment measurement with a buffer gas comagnetometer". In: *Physics Letters A* 376.16, pp. 1347–1351.

May, D. J. R. (1998). "A high precision comparison of the gyromagnetic ratios of the 199- Hg atom and the neutron". PhD thesis. University of Sussex.

Meichelböck, J. (2019). "Neutron Detection for the PanEDM Experiment". MA thesis. Technical University Munich.

Morris, C. L. et al. (2002). "Measurements of ultracold-neutron lifetimes in solid deuterium". In: *Phys Rev Lett* 89.27, p. 272501.

Neulinger, T. et al. (2021). *Experimental report for proposal 3-14-404 - PanEDM storage times and emptying efficiency*. Tech. rep. TUM/ILL.

Pattie, R.W. et al. (2017). "Evaluation of commercial nickel-phosphorus coating for ultracold neutron guides using a pinhole bottling method". In: *Nuclear Instruments and Methods in Physics Research Section A: Accelerators, Spectrometers, Detectors and Associated Equipment* 872, pp. 64–73. ISSN: 0168-9002. DOI: https://doi.org/10.1016/j.nima.2017.07.051. URL: https://www.sciencedirect.com/science/article/pii/S0168900217308082.

Patton, B. (Feb. 2012). "The Nonlinear Zeeman Effect in ^{87}Rb, ^{85}Rb, and ^{133}Cs". Internal document.

– (2015). *Layout Cs sensor*. Private communication.

Patton, B. et al. (2013). "An All-Optical Cesium Magnetometer for Neutron Electric Dipole Moment Experiments". In: *21st International Conference on Laser Spectroscopy JUNE 9-14, 2013 University of California, Berkeley, Berkeley, California USA POSTER ABSTRACTS*.

Pendlebury, J. M. et al. (Sept. 2004). "Geometric-phase-induced false electric dipole moment signals for particles in traps". In: *Phys. Rev. A* 70 (3), p. 032102. DOI: 10.1103/PhysRevA.70.032102. URL: http://link.aps.org/doi/10.1103/PhysRevA.70.032102.

Pendlebury, J. M. et al. (Nov. 2015). "Revised experimental upper limit on the electric dipole moment of the neutron". In: *Phys. Rev. D* 92 (9), p. 092003. DOI: 10.1103/PhysRevD.92.092003. URL: https://link.aps.org/doi/10.1103/PhysRevD.92.092003.

Phan, N. S. et al. (2021). "A study of DC electrical breakdown in liquid helium through analysis of the empirical breakdown field distributions". In: *Journal of Applied Physics* 129.8. DOI: https://doi.org/10.1063/5.0037888.

Piegsa, F. M. (2013). "New concept for a neutron electric dipole moment search using a pulsed beam". In: *Physical Review C* 88.4. ISSN: 0556-2813 1089-490X. DOI: 10.1103/PhysRevC.88.045502.

Piegsa, F. M. et al. (July 2014). "New source for ultracold neutrons at the Institut Laue-Langevin". In: *Phys. Rev. C* 90 (1), p. 015501. DOI: 10.1103/PhysRevC.90.015501. URL: https://link.aps.org/doi/10.1103/PhysRevC.90.015501.

Pieler, M. (2021). "UCN Detection System for the PanEDM Experiment". MA thesis. Technischen Universität Wien.

Pignol, Guillaume (2019). "A magic magnetic field to measure the neutron electric dipole moment". In: *Physics Letters B* 793, pp. 440–444. ISSN: 0370-2693. DOI: https://doi.org/10.1016/j.physletb.2019.05.014. URL: https://www.sciencedirect.com/science/article/pii/S0370269319303235.

Pignol, Guillaume and Stephanie Roccia (2012). "Electric-dipole-moment searches: Re-examination of frequency shifts for particles in traps". In: *Physical Review A* 85.4.

Pokotilovski, Yu N. (2005). "UCN anomaly and the possibility for further decreasing neutron losses in traps". In: *Nuclear Instruments and Methods in Physics Research Section A: Accelerators, Spectrometers, Detectors and Associated Equipment* 554.1-3, pp. 356–362. ISSN: 01689002. DOI: 10.1016/j.nima.2005.07.026.

Pontus, Nordin (2021). "Neutron reflectormeter measurements". Private communication.

Pospelov, Maxim and Adam Ritz (Sept. 1999). "Theta-Induced Electric Dipole Moment of the Neutron via QCD Sum Rules". In: *Phys. Rev. Lett.* 83 (13), pp. 2526–2529. DOI: 10.1103/PhysRevLett.83.2526. URL: https://link.aps.org/doi/10.1103/PhysRevLett.83.2526.

Purcell, E. M. and N. F. Ramsey (June 1950). "On the Possibility of Electric Dipole Moments for Elementary Particles and Nuclei". In: *Phys. Rev.* 78 (6), pp. 807–807. DOI: 10.1103/PhysRev.78.807. URL: https://link.aps.org/doi/10.1103/PhysRev.78.807.

Qi, X. Y. et al. (2011). "Enhanced electrical conductivity in polystyrene nanocomposites at ultra-low graphene content". In: *ACS Appl Mater Interfaces* 3.8, pp. 3130–3.

Raghunathan, A. et al. (2010). "Theoretical Model of Temperature Dependence of Hysteresis Based on Mean Field Theory". In: *IEEE Transactions on Magnetics* 46.6, pp. 1507–1510. ISSN: 0018-9464. DOI: 10.1109/tmag.2010.2045351.

Ramsey, Norman F. (1955). "Resonance Transitions Induced by Perturbations at Two or More Different Frequencies". In: *Physical Review* 100.4, pp. 1191–1194.

Riley, William and David Howe (2008). *Handbook of Frequency Stability Analysis*. en. URL: https://tsapps.nist.gov/publication/get_pdf.cfm?pub_id=50505.

Roehrer, Florian (2019). "Development of the Experiment Control Software and a Data Simulation and Analysis Package for the PanEDM Experiment". MA thesis. Technical University Munich.

Rosner, M. (2021). *Allan devianten Cs sensor. Measured BMSR-II, Berlin, Juli 2021.* Private communication.

Rosner, Martin (2021). "T.B.A". Dissertation. Munich: Technical University Munich.

Ruhstorfer, Daniel (2014). "A setup for coating ultracold neutron guides with deuterated polyethylene". MA thesis. TUM.

Sakharov, A. D. (1967). "Violation of CP Invariance, C asymmetry, and baryon asymmetry of the universe". In: *Pisma Zh. Eksp. Teor. Fiz.* 5, pp. 32–35. DOI: 10.1070/PU1991v034n05ABEH002497.

Schiff, L. I. (Dec. 1963). "Measurability of Nuclear Electric Dipole Moments". In: *Phys. Rev.* 132 (5), pp. 2194–2200. DOI: 10.1103/PhysRev.132.2194. URL: https://link.aps.org/doi/10.1103/PhysRev.132.2194.

Serebrov, A. P. et al. (2003). "Depolarization of ultracold neutrons during their storage in material bottles". In: *Physics Letters A* 313.5-6, pp. 373–379. ISSN: 03759601. DOI: 10.1016/s0375-9601(03)00848-x.

Serebrov, A. P. et al. (2005). "Superconducting UCN polarizer for a new EDM spectrometer". In: *Nuclear Instruments and Methods in Physics Research Section A: Accelerators, Spectrometers, Detectors and Associated Equipment* 545.1-2, pp. 490–492. ISSN: 01689002. DOI: 10.1016/j.nima.2005.01.316.

Serebrov, A. P. et al. (2009). "Ultracold-neutron infrastructure for the PNPI/ILL neutron EDM experiment". In: *Nuclear Instruments and Methods in Physics Research Section A: Accelerators, Spectrometers, Detectors and Associated Equipment* 611.2-3, pp. 263–266. ISSN: 01689002. DOI: 10.1016/j.nima.2009.07.084.

Serebrov, A. P. et al. (2015). "New search for the neutron electric dipole moment with ultracold neutrons at ILL". In: *Physical Review C* 92.5.

Serebrov, A. P. et al. (2016a). "PNPI differential EDM spectrometer and latest results of measurements of the neutron electric dipole moment". In: *Physics of Atomic Nuclei* 78.14, pp. 1601–1605. ISSN: 1063-7788 1562-692X. DOI: 10.1134/s1063778815130293.

– (2016b). "PNPI differential EDM spectrometer and latest results of measurements of the neutron electric dipole moment". In: *Physics of Atomic Nuclei* 78.14, pp. 1601–1605.

Shapiro, F. L. (Jan. 1968). "ELECTRIC DIPOLE MOMENTS OF ELEMENTARY PARTICLES." In: *Usp. Fiz. Nauk, 95: 145-58(May 1968).* DOI: 10.1070/PU1968v011n03ABEH003840. URL: https://www.osti.gov/biblio/4493828.

Sixdenier, Fabien et al. (2016). "Temperature-Dependent Extension of a Static Hysteresis Model". In: *IEEE Transactions on Magnetics* 52.3, pp. 1–4. ISSN: 0018-9464 1941-0069. DOI: 10.1109/tmag.2015.2481090.

Steyerl, A. (1969). "Measurements of total cross sections for very slow neutrons with velocities from 100 m/sec to 5 m/sec". In: *Physics Letters B* 29.1, pp. 33–35. ISSN: 0370-2693. DOI: https://doi.org/10.1016/0370-2693(69)90127-0. URL: https://www.sciencedirect.com/science/article/pii/0370269369901270.

Steyerl, A. (2020). *Ultracold Neutrons*. World Scientific Publishing Company. ISBN: 9811212708.

Steyerl, A. et al. (1986). "A new source of cold and ultracold neutrons". In: *Physics Letters A* 116.7, pp. 347–352. ISSN: 0375-9601. DOI: https://doi.org/10.1016/0375-9601(86)90587-6. URL: https://www.sciencedirect.com/science/article/pii/0375960186905876.

Stuiber, Stefan (Apr. 2018). "Creation of ultra-low remanent fields and homogeneous NMR fields for precision experiments". PhD thesis. Technical University Munich.

Sturm, Michael (2020). "A highly drift stable and fully optical Cs atomic magnetometer for a new generation nEDM experiment". Dissertation. Munich: Technical University Munich. URL: http://nbn-resolving.de/urn/resolver.pl?urn:nbn:de:bvb:91-diss-20200507-1536319-1-6.

Swallows, M. (2007). "A search for the permanent electric dipole moment of mercury-199". PhD thesis. University of Washington.

Tang, Z. et al. (2016). "Measurement of spin-flip probabilities for ultracold neutrons interacting with nickel phosphorus coated surfaces". In: *Nuclear Instruments and Methods in Physics Research Section A: Accelerators, Spectrometers, Detectors and Associated Equipment* 827, pp. 32–38. ISSN: 01689002. DOI: 10.1016/j.nima.2016.04.098.

Taubenheim, Bernd (Sept. 2017). "Mercury Vapor Magnetometry in Fundamental Physics". PhD thesis. Technical University Munich.

Trinks, U et al. (2000). "Concepts of UCN sources for the FRM-II". In: *Nuclear Instruments and Methods in Physics Research Section A: Accelerators, Spectrometers, Detectors and Associated Equipment* 440.3, pp. 666–673. ISSN: 0168-9002. DOI: https://doi.org/10.1016/S0168-9002(99)01059-1. URL: https://www.sciencedirect.com/science/article/pii/S0168900299010591.

Turchin, V.F. (1965). *Slow Neutrons.pdf*. Israel Program for Scientific Translations.

Tureanu, Anca (Nov. 2013). "CPT and Lorentz Invariance: Their Relation and Violation". In: *Journal of Physics: Conference Series* 474, p. 012031. DOI: 10.1088/1742-6596/474/1/012031. URL: https://doi.org/10.1088/1742-6596/474/1/012031.

Wei, Wanchun (2020). "A new neutron lifetime experiment with cold neutron beam decay in superfluid helium-4". In: *Journal of Physics G: Nuclear and Particle Physics* 47.12. ISSN: 0954-3899 1361-6471. DOI: 10.1088/1361-6471/abacdb.

Weis, Antoine, Georg Bison, and Zoran D. Grujić (2017). "Magnetic Resonance Based Atomic Magnetometers". In: *High Sensitivity Magnetometers*. Cham: Springer International Publishing, pp. 361–424. ISBN: 978-3-319-34070-8. DOI: 10.1007/978-3-319-34070-8_13. URL: https://doi.org/10.1007/978-3-319-34070-8_13.

Windmayer, Dominik J. (2016). "Using Deuterated Polyethylene Coatings for Manipulating Ultra-Cold-Neutrons in Different Applications". MA thesis. TUM.

Wurm, David (2015). "Towards a Fiberized All Optical Cs Magnetometer". MA thesis. TUM.

Wurm, David et al. (2019). "The PanEDM neutron electric dipole moment experiment at the ILL". In: *EPJ Web of Conferences* 219. ISSN: 2100-014X. DOI: 10.1051/epjconf/201921902006.

Zechlau, Thorsten Sven (Oct. 2016). "Ultra-Cold Neutron Transport and Spin Manipulation System for the Measurement of the Neutron Electric Dipole Moment". PhD thesis. Technical University Munich.

Zel'dovich, Y. (1959). "COLD NEUTRON STORAGE". In.

Zimmer, O. (2017). *New superfluid-helium based UCN sources at ILL and status of the HOPE neutron lifetime experiment*. Unpublished Work.

Zimmer, O. and R. Golub (July 2015). "Ultracold neutron accumulation in a superfluid-helium converter with magnetic multipole reflector". In: *Phys. Rev. C* 92 (1), p. 015501. DOI: 10.1103/PhysRevC.92.015501. URL: https://link.aps.org/doi/10.1103/PhysRevC.92.015501.

Zimmer, O. et al. (Sept. 2007). "Superfluid-Helium Converter for Accumulation and Extraction of Ultracold Neutrons". In: *Phys. Rev. Lett.* 99 (10), p. 104801. DOI: 10.1103/PhysRevLett.99.104801. URL: https://link.aps.org/doi/10.1103/PhysRevLett.99.104801.

Zimmer, Oliver (2004). *Fundamental physics with slow neutrons - Notes of a lecture held at the TUM*.

– (2016). "SuperSUN - new infrastructure for experiments with ultracold neutron". In: Physics of fundamental Symmetries and Interactions - PSI2016.

Zimmer, Oliver, Florian M. Piegsa, and Sergey N. Ivanov (Sept. 2011). "Superthermal Source of Ultracold Neutrons for Fundamental Physics Experiments". In: *Phys. Rev. Lett.* 107 (13), p. 134801. DOI: 10.1103/PhysRevLett.107.134801. URL: https://link.aps.org/doi/10.1103/PhysRevLett.107.134801.